Chem Soc Rev

REVIEW ARTICLE

View Article Online
View Journal | View Issue

Cite this: *Chem. Soc. Rev.*, 2022, **51**, 9262

Rare-earth based tetrapyrrolic sandwiches: chemistry, materials and applications

Alexander G. Martynov, [a] Yoji Horii, [b] Keiichi Katoh, [c] Yongzhong Bian, [de] Jianzhuang Jiang, *[de] Masahiro Yamashita*[f] and Yulia G. Gorbunova *[ag]

Received 5th July 2022

DOI: 10.1039/d2cs00559j

rsc.li/chem-soc-rev

The unique properties of natural tetrapyrrolic compounds have inspired the rapid growth of research interest in the design and synthesis of artificial porphyrinoids and their metal complexes as a basis of modern functional materials. A special role in the design of such materials is played by sandwich complexes formed by tetrapyrrolic macrocycles with rare earth elements, especially lanthanides. The development of synthetic approaches to the functionalization of tetrapyrrolic compounds and their rare earth complexes has facilitated the intensive development of new applications over the last decade. As a way of expanding the functionalities of rare earth complexes, sophisticated examples have been obtained, including mixed-ligand complexes, π-extended analogues, covalently linked and fused sandwiches, complexes with less-common tetrapyrrols, sandwiches with non-tetrapyrrolic macrocycles and even complexes containing up to six stacked ligands. This review intends to offer a general overview of the preparation of such sophisticated REE tetrapyrrolic sandwiches over the last decade as well as emphasizes the current challenges and perspectives of their application in areas such as single-molecule magnetism (SMM), organic field-effect transistors (OFET), conductive materials and nonlinear optics (NLO).

[a] *A.N. Frumkin Institute of Physical Chemistry and Electrochemistry, Russian Academy of Sciences, 119071 Leninskiy pr., 31, bldg.4, Moscow, Russia*
[b] *Department of Chemistry, Faculty of Science, Nara Women's University, Nara 630-8506, Japan*
[c] *Department of Chemistry, Graduate School of Science, Josai University, 1-1 Keyakidai, Sakado, Saitama 350-0295, Japan*
[d] *Beijing Key Laboratory for Science and Application of Functional Molecular and Crystalline Materials, Department of Chemistry, School of Chemistry and Biological Engineering, University of Science and Technology Beijing, Beijing, China*
[e] *Daxing Research Institute, and Beijing Advanced Innovation Center for Materials Genome Engineering, University of Science and Technology Beijing, Beijing, China. E-mail: jianzhuang@ustb.edu.cn*
[f] *Department of Chemistry, Graduate School of Science, Tohoku University, 6-3 Aramaki-Aza-Aoba, Aoba-Ku, Sendai 980-8578, Japan. E-mail: yamasita@agnus.chem.tohoku.ac.jp*
[g] *N.S. Kurnakov Institute of General and Inorganic Chemistry, Russian Academy of Sciences, 119991 Leninskiy pr., 31, Moscow, Russia. E-mail: yulia@igic.ras.ru*

Alexander G. Martynov

Alexander G. Martynov graduated from the Higher Chemical College of the Russian Academy of Sciences in 2006. He received his PhD and Dr Hab. degrees in 2008 and 2020. In 2022 he was awarded the Moscow government prize for young scientists. In 2022 he became a Professor of the Russian Academy of Sciences. Currently he is a leading researcher at the Frumkin Institute of Physical Chemistry and Electrochemistry RAS. His research interests are in the areas of spectroscopy of tetrapyrrolic macrocycles and tetrapyrrol-based materials with tuneable properties including REE sandwich complexes for magnetic applications, agents for photodynamic therapy and carbene transfer catalysts.

Yoji Horii

Yoji Horii was born in Gumma, Japan in 1989. He received his Bachelor's (2012), Master's (2014) and PhD (2017) degrees at Tohoku University under the supervision of Professor Masahiro Yamashita. He worked on magnetism and electronic states of phthalocyaninato-lanthanide single-molecule magnets. He moved to Osaka University as the postdoctoral fellow in April 2017. In 2019, he moved to Tohoku University as a postdoctoral fellow. Since April 2020, he has been working as an assistant professor at Nara Women's University. His current research interests include molecular magnetism, two dimensional nanomaterials and soft materials.

1. Introduction

Just as it is difficult to overestimate the role of natural porphyrins in the functioning of living beings, it is also difficult to disagree with the fact that synthetic porphyrinoids have greatly contributed to the development of modern materials science. In particular, this has been made possible by a variety of unique photophysical, electrochemical, catalytic, magnetic, and other properties provided by both the tetrapyrroles themselves and the metal ions placed in their cavities.

Among various coordination compounds formed by tetrapyrrole macrocycles, the complexes with rare earth elements (REE) attract special attention.[1–6] Due to large ionic radii and high coordination numbers, these elements form sandwich

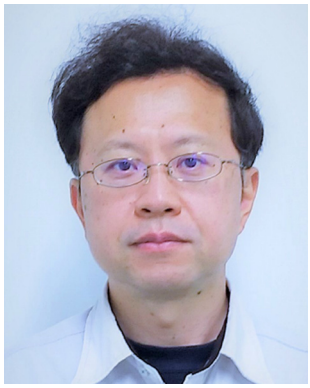

Keiichi Katoh

Keiichi Katoh is currently an associate professor in the Department of Chemistry of Josai University where he is leading research activities in inorganic chemistry and magnetism. He received his PhD in 2003 from the Graduate University for Advanced Studies (Institute for Molecular Science). After being a post-doctoral fellow at Hokkaido University (Research Institute for Electronic Science) until 2004, he worked as a post-doctoral fellow at Kyoto University (Institute for Chemical Research) until 2008, and he joined the Prof. Yamashita group as a post-doctoral fellow at Tohoku University in 2008. From 2009 to 2020, he was appointed to an assistant professor in the Department of Chemistry of Tohoku University. He works on the development of solid state spin systems based on molecular magnetic materials.

Yongzhong Bian

Yongzhong Bian was born in Shanxi, China. He received his BSc (1998) and PhD (2005) (with Prof. Jiangzhuang Jiang) from Shandong University. He carried out a JSPS postdoctoral fellowship (2005–2007) at the University of Tokyo with Prof. Takuzo Aida. He became an associate professor at Shandong University in 2007, and moved to the University of Science and Technology Beijing as a full professor in 2009. His current research centers on porphyrin chemistry, encompasses applications in Fluorescent chemosensing and bioimaging, photodynamic therapy, photochemical catalysis and molecular recognition.

Jianzhuang Jiang

Jianzhuang Jiang was born in Heilongjiang, China. He received his BSc (1985), MSc (1988), and PhD (1993) (with Tsinglien Chang) from the Peking University. During his doctoral study (1990–1992), he obtained a Fellowship from the Ministry of Culture, Science, and Sport of Japan and carried out his PhD work at the Osaka University under the guidance of Kenichi Machida and Ginya Adachi. He became a Postdoctoral Fellow at Peking University with Tsinglien Chang (1993–1994), a Visiting Scholar at The Chinese University of Hong Kong with Dennis K. P. Ng and Thomas C. W. Mak (1995–1996), and a Postdoctoral Fellow at the Queensland University of Technology with Dennis P. Arnold (1998–2000). He joined Shandong University and the University of Science and Technology Beijing in 1996 and 2008, respectively. He has been working on porphyrin- and phthalocyanine-based materials for more than thirty years to develop new single-molecule magnets, organic field-effect transistors, optical materials, energy materials, and porous materials.

Masahiro Yamashita

Masahiro Yamashita received his BSc degree in 1977, MSc in 1979, and DSc in 1982 from Kyushu University. After his graduation, he joined the Institute for Molecular Science (IMS). In 1983, he was appointed as an Assistant Professor at Kyushu University. In 1988, he was appointed as an Associate Professor at Nagoya University, and he was promoted to a full Professor at the same university in 1998. He was a full Professor at Tokyo Metropolitan University from 2000 to 2004. He moved to Tohoku University as a full professor in 2005. He has been honored with the Inoue Scientific Award (2002), the Chemical Society of Japan Award for Creative Work (2005), the Award of Japan Society of Coordination Chemistry (2014), Mukai Award (2019), and the Chemical Society of Japan Award (2020). He is now an Associate Member of the Science Council of Japan. He is a Fellow of the Royal Society of Chemistry (FRSC).

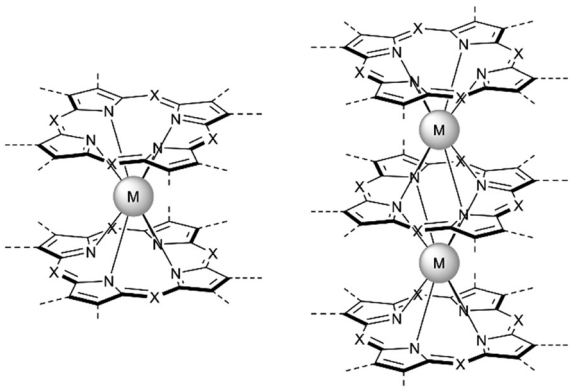

Fig. 1 Double- and triple-decker sandwich complexes formed by REE ions with tetrapyrrolic macrocycles, X = C-Ar, C-Alk, and N.

double- and triple-decker complexes with porphyrins (Por), phthalocyanines (Pc) and related macrocycles (Fig. 1), which, with some exceptions, are not observed for the other metals of the periodic table. Tightly coupled π-systems of stacked aromatic macrocycles provide these sandwiches with unique optical and electrochemical properties, and the presence of 4f-electron shells in paramagnetic lanthanide (Ln) metal centres expands the area of their application to the actively developing and promising fields of molecular magnetism and spintronics.[7–11]

Interestingly, the somewhat detective chemistry of sandwich complexes with tetrapyrrolic ligands started almost simultaneously with rise of phthalocyanines, although the first element to form double-decker complexes – tin(IV) – did not belong to rare earth elements. The synthesis of its bisphthalocyaninate, **Sn(Pc)$_2$**, was reported in 1936 by Linstead *et al.*[12] The authors used the reaction of **(Pc)SnCl$_2$** and **Na$_2$(Pc)**, and this raise-by-one-story approach much later became the main way to various heteroleptic and mixed ligand sandwiches.

Much later, in 1965 Kirin and Moskalev *et al.* reported seminal work on the template reaction between REE acetates and melted phthalonitrile.[13] The authors isolated surprisingly stable green and blue complexes, where metal ions were sandwiched between two Pc ligands – **M(Pc)$_2$**; however, at that time the details of their electronic structure and the nature of the intriguing redox behaviour remained unclear. In particular, thin films formed by bisphthalocyaninates were able to reversibly change colour when a potential was applied or when these films were treated with volatile oxidants and reducing agents. The electrochromic behaviour of bisphthalocyaninates was explained in 1979 by Corker *et al.*[14] who used UV-Vis and EPR spectra to show that **M(Pc)$_2$** undergoes ligand-centred redox-triggered interconversion between three forms of trivalent metal complexes – anionic $[M^{3+}(Pc^{2-})_2]^-$, neutral $[(Pc^{-\bullet})M^{3+}(Pc^{2-})]^0$ and cationic $[M^{3+}(Pc^{-})_2]^+$ forms. Due to the pronounced difference in spectral signatures these three forms possessed different colours, and for many years they were known as blue, green and red forms, respectively. Apart from changes in UV-Vis spectra, switching between redox states caused modulation of NIR absorbance, and the nature of NIR bands of neutral green complexes, has been discussed in the works of Simon *et al.*,[15] Aroca *et al.*,[16] Tomilova and Lukyanets *et al.*[17]

Importantly, under harsh conditions of template condensation, apart from double-decker complexes, REE ions can also form blue triple-decker sandwiches **M$_2$(Pc)$_3$**,[18,19] where Pc ligands are isoelectronic with those in blue forms of bisphthalocyaninates. Because of the similarity of their optical properties and lack of available mass-spectral characterization these complexes were sometimes mistaken for each other. These contradictions have been eliminated by single-crystal X-ray assignment performed in 1980 for neodymium bisphthalocyaninate, **Nd(Pc)$_2$** by Kasuga *et al.*,[20] and in 1999 for dilutetium tris-(tetra-15-crown-5-phthalocyaninate), **Lu$_2$[(15C5)$_4$Pc]$_3$** by Troyanov *et al.*[21]

The survey for milder conditions where double- and triple-deckers could be selectively obtained, afforded several convenient protocols, which are commonly used in synthetic practice nowadays. These protocols include template condensation of phthalonitriles and REE salts in high boiling alcohols in the presence of DBU as a phthalonitrile activator as suggested by De Cian *et al.*,[22] and also direct reactions of pre-synthesized phthalocyanine ligands with metal salts as suggested by Takahashi *et al.*[23,24] While the former method yields double-decker sandwiches, the latter method furnishes both double- and triple-decker complexes, and later studies showed that the selectivity of complex formation can be governed either by the presence or absence of DBU, respectively.[25,26]

Yulia G. Gorbunova

Yulia G. Gorbunova is a Full member of Russian Academy of Sciences (2022) and main researcher at the Russian Academy of Sciences (Kurnakov Institute of General and Inorganic Chemistry RAS (IGIC RAS) and Frumkin Institute of Physical Chemistry and Electrochemistry RAS). She graduated in Chemistry from the Lomonosov Moscow State University and received her PhD (1995) and habilitation (2006) from IGIC RAS. Her current research interests are related to the chemistry of tetrapyrrolic compounds as the basis of functional materials, including molecular switchers, nonlinear optics, electrochromic materials, SMM, sensors and hybrid organo-inorganic nanomaterials. She was a recipient of the Award of European Academy of Science for young researcher (2001), the Russian Government prize in the field of science and techniques (2002) and the Chugaev Award in coordination chemistry (2010). In 2016 Prof. Gorbunova was awarded by order ''Chevalier dans l'Ordre national des Palmes Academiques'' by the Government of France.

In the case of phthalocyanines both template and direct methods are equally applicable for the synthesis of REE sandwiches, however, in the case of porphyrins only direct method can be used to synthesize double- and triple-decker complexes. First example of homoleptic REE bisporphyrinates was reported in 1977 by Buchler *et al.* with the example of quadrivalent cerium complex **Ce(TTP)$_2$** formed upon the reaction of Ce(acac)$_3$ with tetra-*p*-tolylporphyrin, **H$_2$(TTP)** in refluxing 1,2,4-trichlorobenzene (TClB).[27] The authors noticed a remarkable analogy between the structure and the redox-properties of this complex and the ''special pair'' formed by chlorophyl molecules in the photosynthetic systems of green plants.[28] Later more double- and triple-decker porphyrinates were isolated and characterized,[29–31] and it was found that porphyrin ligands tended to form sandwiches only with early and middle lanthanides, while Pc ligands could form sandwiches with all REE ions, including the relatively small Sc^{3+} ions.[32,33]

Finally, REE complexes provided the marriage of porphyrins and phthalocyanines in mixed ligand sandwiches, where both types of ligands are combined and strongly coupled due to intramolecular orbital interactions providing them with peculiar optical properties of panchromatic absorbers. Synthesis and crystallographic characterization of the first example of such complexes were reported in 1986 by Moussavi *et al.* with the example of mixed ligand triple-decker complexes with tetra-*p*-anisylporphyrin **(Pc)M(Pc)M(TAnP)**, where M = Nd, Eu, and Gd.[34]

The rapid development of the chemistry of sandwich REE complexes was driven both by advances in spectroscopy and physicochemical characterization of these challenging objects and breakthrough discoveries which affected many areas of modern chemistry. Among them we should inevitably mention the first organic semiconductor – lutetium bisphthalocyaninate, **Lu(Pc)$_2$**, described for the first time in 1987 by Turek *et al.*,[35] and especially the first example of a 4f single molecule magnet – terbium(III) bisphthalocyaninate, **Tb(Pc)$_2$**, reported in 2003 by Ishikawa *et al.*[36]

Because of this, the largely fundamental interest in these compounds was gradually replaced by a focus on applied research where archetypal double- and triple-decker complexes **M(Pc)$_2$** and **M$_2$(Pc)$_3$** coexist with more sophisticated compounds, including mixed-ligand complexes, π-extended analogues, covalently linked and fused sandwiches, complexes with less-common tetrapyrrols, sandwiches with non-tetrapyrrolic macrocycles and even complexes containing up to six stacked ligands obtained by coordination or supramolecular bonding. Moreover, these complexes have been recognized as molecular switches whose properties can be altered by the reversible self-assembly processes, protonation, redox reactions, *etc.*, opening the way to the creation of ''smart'' materials.

These sophisticated complexes began to attract the most attention over the last decade; thus, the aim of the present review is mainly to summarize the advances in the chemistry of REE tetrapyrrolic sandwiches over this period to supplement the previously published comprehensive reviews[1–6] with new data. Another goal of this review is to emphasize the current challenges and perspectives of sandwich complex application in various fields such as single-molecule magnetism (SMM), organic field-effect transistors (OFET) and conductive materials, and nonlinear optics (NLO).

2. Advances in the synthesis of functionalized multiple-decker sandwiches

2.1 New homo- and heteroleptic double- and triple-decker complexes bearing symmetrically substituted tetrapyrolic ligands

From the synthetic viewpoint, sandwich complexes with symmetrically substituted tetrapyrrolic ligands are the most available objects, particularly due to facile synthesis and separation procedures. The following section will include various classes of homo- and heteroleptic sandwiches with symmetrical ligands. In the latter case, ligands belong to the same classes of tetrapyrrolic macrocycles.

2.1.1 Aryloxy- and aryl-substituted sandwich phthalo- and naphthalocyaninates. Over the last decade among other sandwich complexes with symmetrical ligands special attention was paid to aryloxy-substituted phthalocyaninates, particularly due to high solubility, which contributes to the processing of thin-film materials and devices. Aryloxy-groups reveal electron-withdrawing behaviour,[37] making their reduction easier and their oxidation more difficult. Finally, these substituents participate in the molecular packing of complexes governing conductivity and other useful properties of materials based on them.

For example, Kong *et al.* used template condensation of 4,5-di(α-naphthoxy)phthalonitrile with Eu(acac)$_3$ and DBU in refluxing *n*-PentOH to make a double-decker complex **Eu[(NaphO)$_8$Pc]$_2$** (Scheme 1) which was used as a component of a flexible ambipolar OFET,[38] and it also revealed sensing properties towards NO_2 and NH_3 (*cf.* Section 4).[39] To synthesize a triple-decker complex **Eu$_2$[(NaphO)$_8$Pc]$_3$**, raise-by-one-story approach was applied, namely octa-naphthyloxy-phthalocyanine was condensed with the double-decker complex (Scheme 1).[40] The resulting trisphthalocyaninate could form self-assembled microstructures whose morphology and n-/p-mobilities could be controlled by solvent–vapour annealing procedure (*cf.* Section 4.2). Similar approaches were used to synthesize various examples of other aryloxy-substituted sandwiches, including heteroleptic complexes, which were designed as high-performance air-stable ambipolar organic thin film transistors,[41–44] optical limiters[45–48] and single molecule magnets.[49]

Phenyl-substituted phthalo- and naphthalocyanines were used by Dubinina *et al.* for the synthesis of REE complexes.[50,51] The selectivity of complex formation upon direct metalation of these ligands depended on conditions affording either monophthalo- and naphthalocyaninates or sandwich complexes (Scheme 2). While double-decker complexes were obtained for both types of macrocycles,

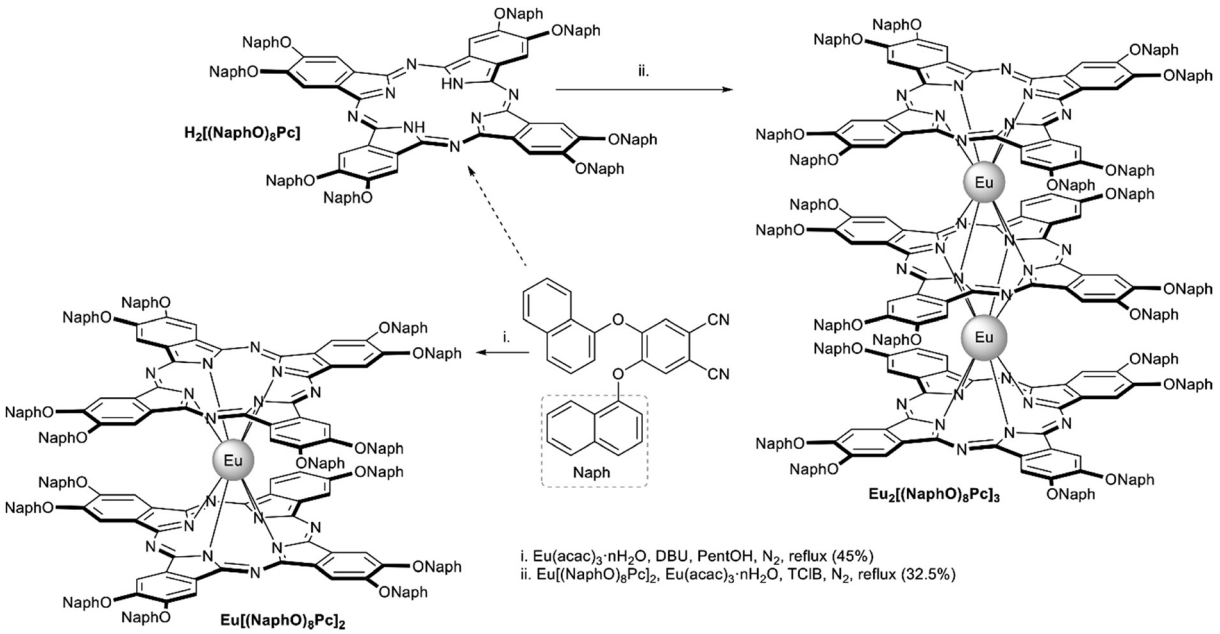

Scheme 1 Synthesis of α-naphthyloxy-substituted Eu(III) bis- and trisphthalocyaninates.[38,40]

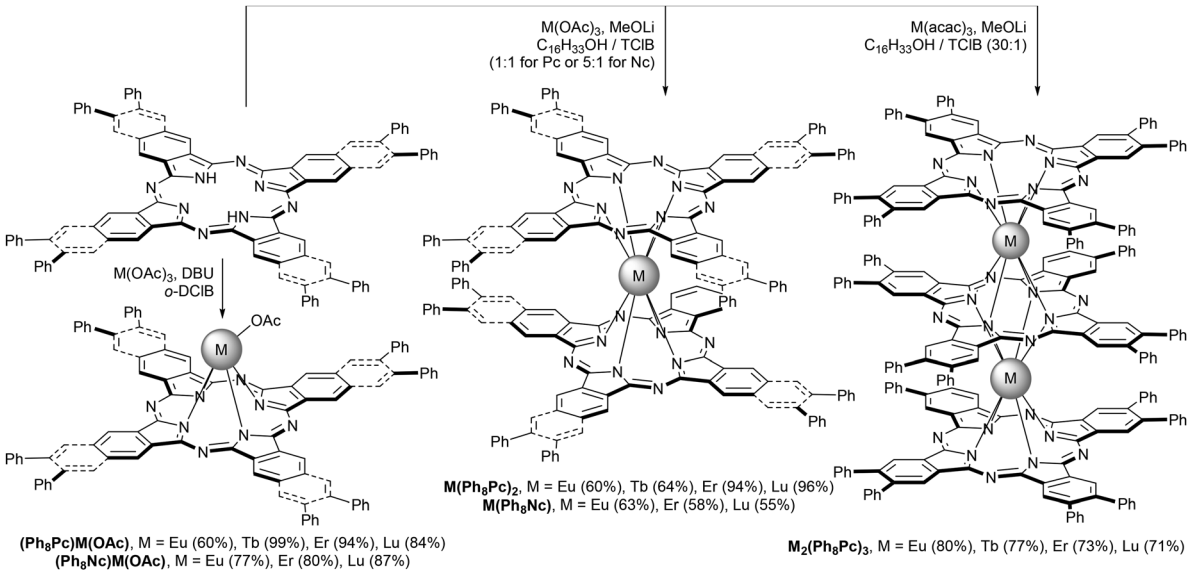

Scheme 2 Synthesis of lanthanide complexes with phenyl-substituted phthalo- and naphthalocyanines.[50,51]

triple-decker complexes could be obtained by only using phthalocyanine ligands.

Single-crystal XRD studies of **Lu(Ph$_8$Pc)$_2$** revealed intramolecular edge-to-face π–π stacking interactions between peripheral phenyl groups, reinforcing the overall intramolecular interactions between Pc ligands (Fig. 2).[50] In turn, it resulted in a strong hypsochromic shift of NIR bands in UV-Vis-NIR spectra of bisphthalocyaninates – for example the intervalence band shifted from 1575 nm in the spectrum of **Tb(*t*Bu$_4$Pc)$_2$** to 1433 nm in the spectrum of **Tb(Ph$_8$Pc)$_2$**. In contrast, benzoannelation going from phthalo- to naphthalocyaninates caused bathochromic shifts of intervalence bands by *ca.* 200 nm.

Measurements of conductivity of thin drop-casting films formed by phenyl-substituted terbium(III) phthalocyaninates showed that in the series of mono-, bis- and trisphthalocyaninates the complex **Tb(Ph$_8$Pc)$_2$** had the largest conductivity of 5×10^{-10} S cm^{-1}, which is however much smaller than the values obtained for unsubstituted double-deckers.[51] Optical microscopy data showed that such a low conductivity value was partially caused by film inhomogeneity. AFM studies of films, formed by triple-decker complex **Tb$_2$(Ph$_8$Pc)$_3$** showed that it forms ring-shaped nanostructures – nano-coffee rings, which appear due to an increase in the surface tension of the solutions of this complex in comparison with mono- and

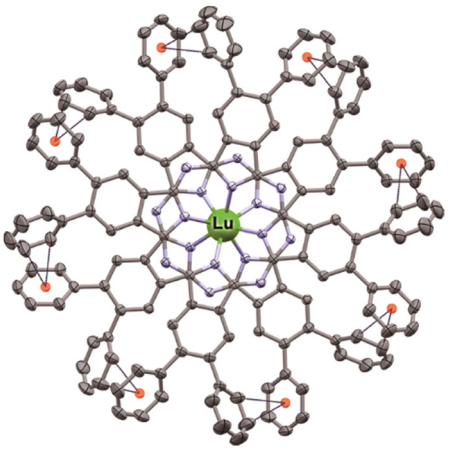

Fig. 2 Top view of the X-ray structure of **Lu(Ph$_8$Pc)$_2$** (CCDC PIXGUA). Dark blue lines show edge-to-face π-stacking interactions.[50]

bisphthalocyaninates. This feature can be used for nanopatterning of various substrates.

2.1.2 Crown-substituted sandwich phthalocyaninates. Crown-phthalocyanines still attract continuing interest, although they are known since late 1980s,[52,53] and lutetium(III) bis(tetra-15-crown-5)phthalocyaninate, **Lu[(15C5)$_4$Pc]**, was actively studied in 1990s as a potential component of ionoelectronic materials.[54,55] In subsequent years, homoleptic crown-substituted double-deckers were synthesized by Gorbunova *et al.* for almost all rare earth elements including the smallest Sc^{3+} ions.[56,57] The availability of this series allowed the smooth changes of major physical-chemical properties following *f*-contraction to be revealed,[58] although discrepancy was observed in the case of cerium complexes which can exist in tri- and quadrivalent states of metal centres.[59]

Attention to crown-substituted sandwiches was attracted mainly in the context of fabrication of electronic devices due to their ability to form thin films with well-defined morphology.[58,60] While investigating the formation of ultrathin Langmuir films by crown-substituted bisphthalocyaninates, Selektor *et al.* discovered the phenomenon of orientation-induced redox isomerism in planar supramolecular systems with **Ce[(15C5)$_4$Pc]$_2$** as the example.[61] Depending on the surface pressure at the water/air interface the complex underwent valence tautomeric interconversion: $Ce^{4+}[L^{2-}]_2 \leftrightarrow [L^{2-}]Ce^{3+}[L^{\bullet-}]$; moreover, films with different redox states of metal centres could be transferred from water to solid surfaces to characterize the valence state by various spectroscopic techniques. The phenomenon was also found to be general for most of bisphthalocyaninates, which are formed by lanthanides exhibiting di- and trivalent states – Sm, Eu, Er, Tm, and Yb.[62,63]

Homonuclear trisphthalocyaninates of strongly paramagnetic lanthanides – **Ln$_2$[(15C5)$_4$Pc]$_3$**, Ln = Tb, Dy, Ho, and Tm were studied by variable-temperature NMR showing the possibility of their application as thermosensors in the physiological temperature range (303–323 K)[64,65] due to the sensitivity of lanthanide-induced shifts to temperature. The Tb(III) complex was found to have the highest sensitivity of this shift among the reported paramagnetic complexes of 4f and d elements with polydentate ligands in organic media.

Several types of crown-substituted complexes were synthesized to study single-molecule magnetism,[66,67] which is particularly interesting for this type of REE sandwiches since it can be tuned by the interaction of crown-ether macrocycles with alkali metal cations. Such tuning was demonstrated for the first time by Horii *et al.*[67] with heteroleptic terbium(III) complex **[(15C5)$_4$Pc]Tb(Pc)** synthesized from **(Pc)Tb(acac)**, 4′,5′-dicyanobenzo-15-crown-5 and DBU in hexanol as the example (*cf.* Section 3.3.1 for more details on SMM studies).

Alternative one-pot strategy towards this complex was proposed by Martynov *et al.*[68] It was based on the generation of **(Pc)Tb(acac)** by transmetalation of a lanthanum(III) complex **La(Pc)$_2$** with Tb(acac)$_3$·*n*H$_2$O and the reaction of this intermediate with tetra-15-crown-5-phthalocyanine, **H$_2$[(15C5)$_4$Pc]**, in the presence of DBU in refluxing 1-chloronaphthalene (ClN) and OctOH mixture (Scheme 3a). The yield of the complex was 24%, and the presence of DBU was shown to be crucial for the formation of the double-decker complex – in the absence of DBU the mixtures of homonuclear triple-decker complexes **(Pc)Tb[(15C5)$_4$Pc]Tb(Pc)** and **[(15C5)$_4$Pc]Tb[(15C5)$_4$Pc]Tb(Pc)** were obtained.[69,70]

Original variant of the raise-by-one-story approach was proposed to synthesize heteronuclear triple-decker complexes, **[(15C5)$_4$Pc]M*[(15C5)$_4$Pc]M(Pc)**, using **La(Pc)$_2$** as a donor of unsubstituted phthalocyaninate-dianion (Scheme 3b).[71,72] Thus, its reaction with crown-substituted bisphthalocyaninates, **M*[(15C5)$_4$Pc]$_2$** and M(acac)$_3$·*n*H$_2$O, in refluxing ClN resulted in remarkably rapid – 10–15 min – formation of the target heteronuclear complexes with a wide range of pairs of dia- and paramagnetic metal centers (M ≠ M* = Nd, Sm, Eu, Gd–Yb, Y) in high yields. SMM properties of homonuclear diterbium(III) complex and heteronuclear terbium(III)/yttrium(III) complexes were studied and the effects of intramolecular ferromagnetic interactions together with the impact of coordinating surrounding were revealed.[66]

A heteroleptic octopus-type Tb(III) bisphthalocyaninate bearing a 15-crown-substituted ligand and a ligand with eight thioacetate-terminated flexible tentacles was synthesized by Shokurov *et al. via* the raise-by-one-story approach starting from tetrahydropyranyl-protected phthalocyanine and half-sandwich Tb(III) crown-phthalocyaninate followed by the cleavage of protective groups, the introduction of iodine atoms and their nucleophilic substitution with thioacetate residues (Scheme 4).[73] The resulting octopus formed a self-assembled monolayer (SAM) on gold with a face-to-face orientation of the molecules, serving as an anchor for further surface modification, namely the binding of additional crown phthalocyanine molecules *via* potassium ion bridges. The enhanced redox-switching ability of the bilayer thus formed was demonstrated (*cf.* Section 4.3).

2.1.3 Chiral sandwich phthlocyaninates. An interesting example of aryloxy-substituted sandwiches was synthesized by Zhou *et al. via* template condensation of phthalonitrile,

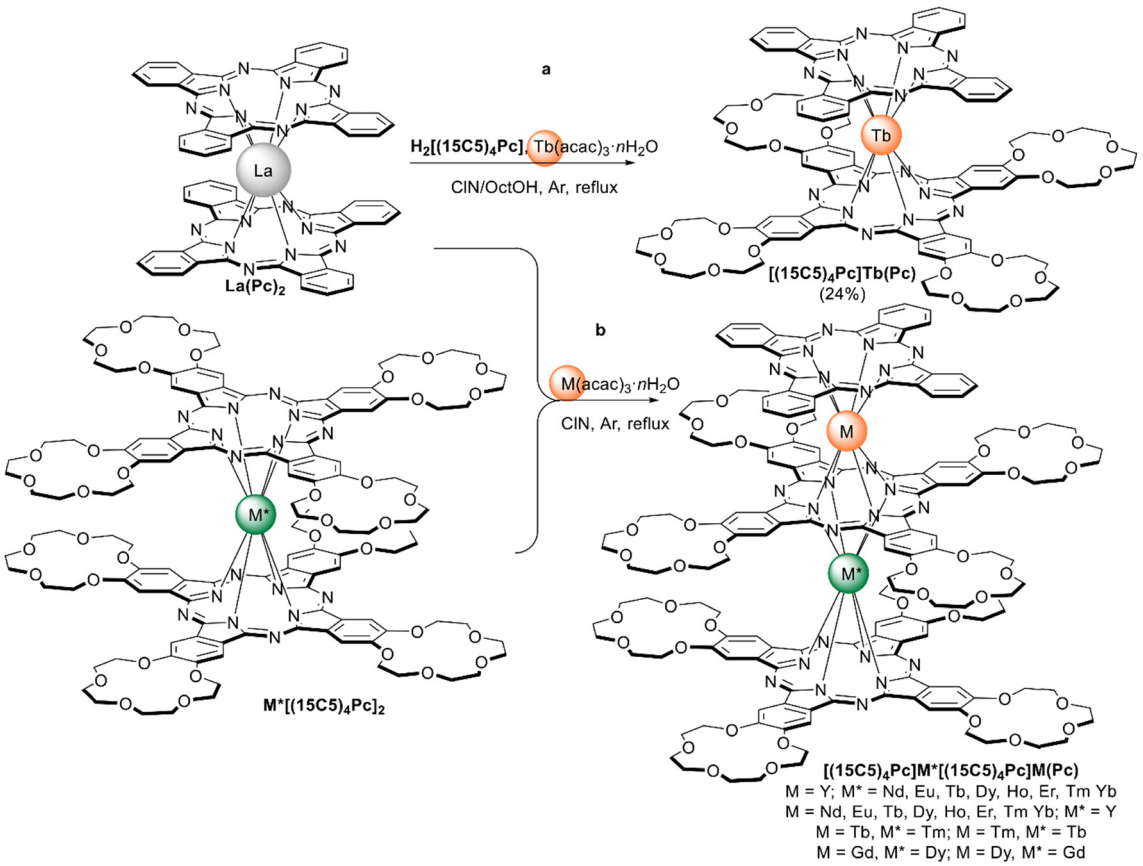

Scheme 3 Transmetalation of **La(Pc)$_2$** in the synthesis of heteroleptic crown-substituted bisphthalocyaninates (a) and heteronuclear trisphthalocyaninates (b).[66,68,71,72]

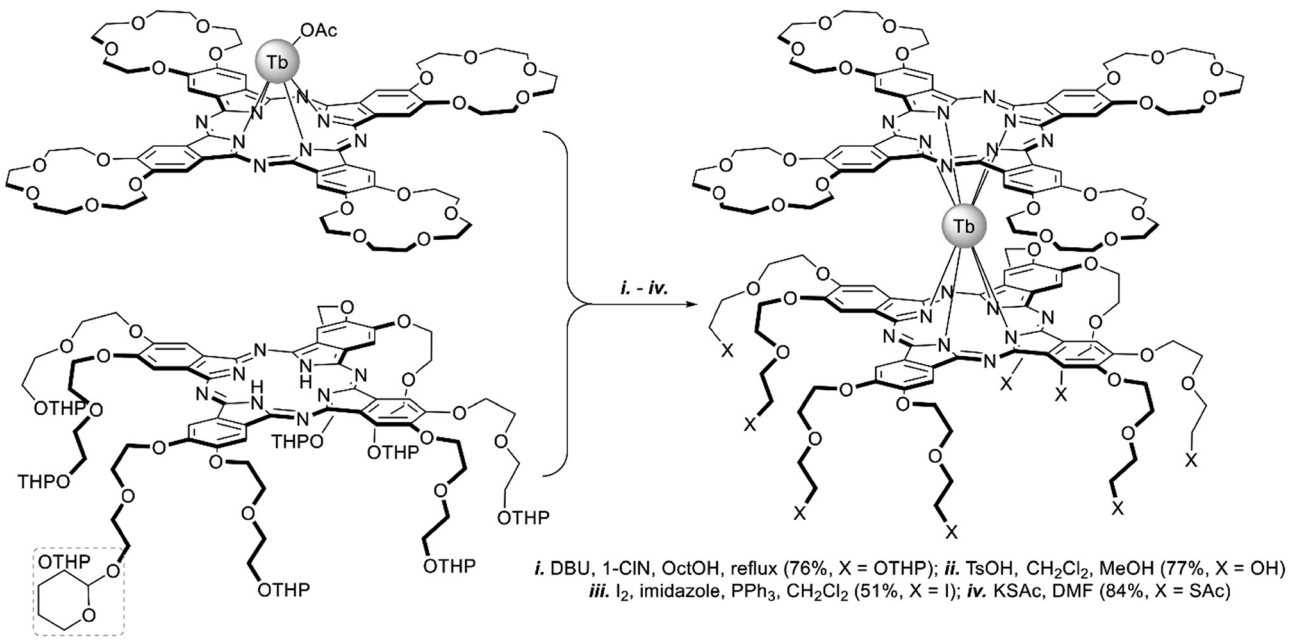

Scheme 4 Synthesis of heteroleptic octopus-type Tb(III) bisphthalocyaninate.[73]

annelated with enantiomerically-pure *R*- or *S*-binaphthyloxy (BNPO) groups (Scheme 5a).[74] Studies of the resulting complexes **Y[(*R*-/*S*-BNPO)$_4$Pc]$_2$** using CD-spectroscopy revealed efficient transfer of chiral information from periphery to

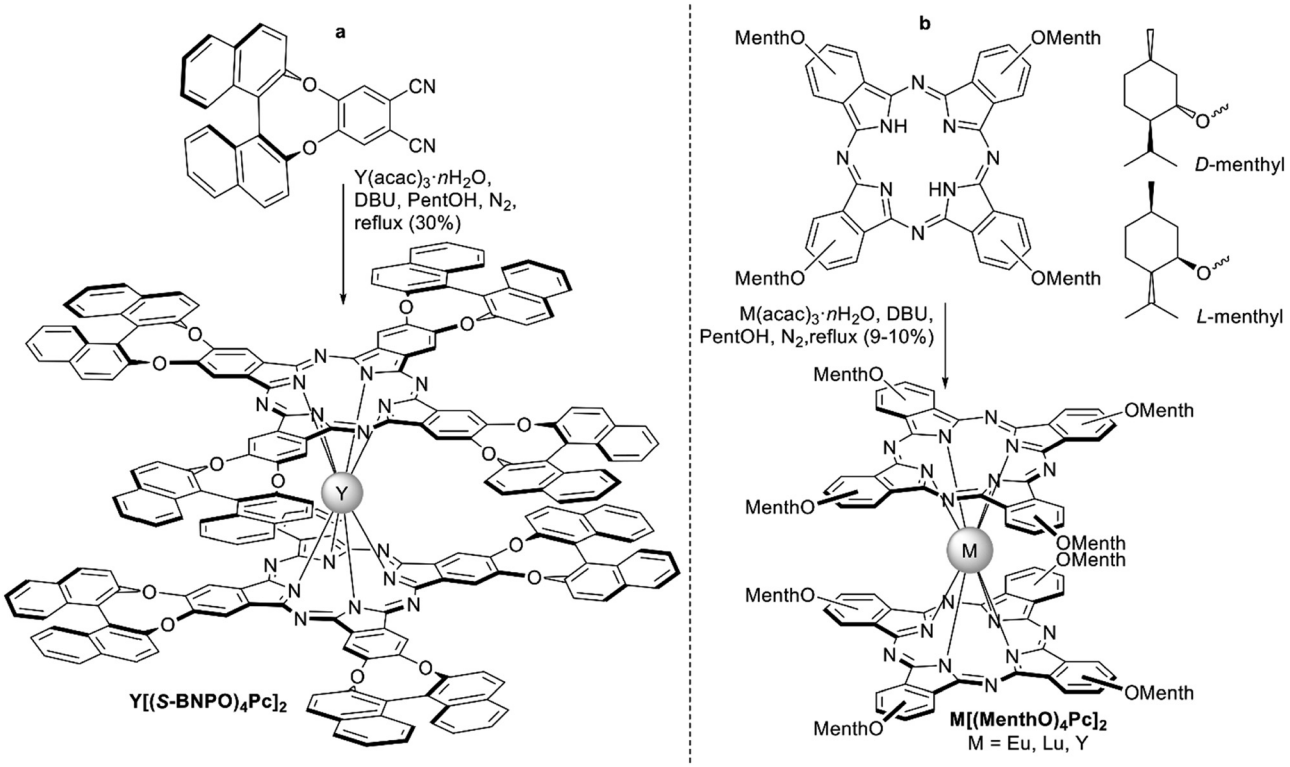

Scheme 5 Synthesis of chiral bisphthalocyaninates on the examples of **Y[(BNPO)$_4$Pc]$_2$** (a, only *S*-enantiomer is shown),[74] and menthyl-substituted bisphthalocyaninates **M[(MenthO)$_4$Pc]$_2$** (b).[75]

phthalocyanine chromophores, and the efficiency of this transfer was much more pronounced in comparison with another example of chiral bisphthalocyaninates, **M[(MenthO)$_4$Pc]$_2$**, bearing D- or L-menthyl groups (Scheme 5b).[75] The latter complexes were prepared by Lv *et al. via* direct metalation of the corresponding methyl-substituted phthalocyanines with M(acac)$_3$·*n*H$_2$O (M = Eu, Lu, Y) in *n*-PentOH. The latter example also emphasized the role of intramolecular π–π interaction since the monomeric chiral ligand **H$_2$[(D-/L-MenthO)$_4$Pc]** was CD-inactive.

Another naturally occurring chiral terpene, (−)-myrtenal, was used by Zheng *et al.* to synthesize the dicyanobenzo-annelated pinene derivative which underwent template condensation to furnish double-decker complexes **M[(pinene)$_4$Pc]$_2$**, M = Eu, Er, and Lu (Scheme 6).[76] Introduction of bulky conformationally rigid hydrocarbon substituents was made with the aim to decrease both inter- and intramolecular interactions between Pc ligands. Such tuning of intermolecular interactions decreased the aggregation of complexes and enhanced their film-forming ability. Decrease of intramolecular interactions resulted in a significant red shift of the intervalence band in the NIR region in comparison with other double-decker complexes, improving the electrochromic properties of compounds thus modified. Finally, chirality of complexes was manifested in their CD-spectra.

Terbium(III) bisphthalocyaninate substituted with chiral (*S*)-2-(dodecyloxy)propoxy groups was synthesized by Gonidec *et al.* as a liquid crystalline material with tuneable magnetic

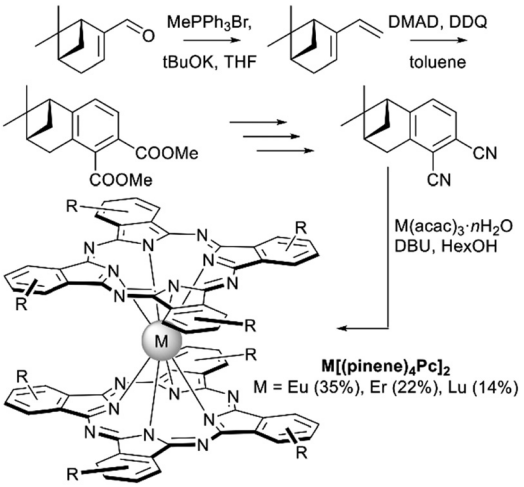

Scheme 6 Key steps leading to pinene-annelated phthalonitrile and bisphthalocyaninates (DMAD – dimethyl acetylene dicarboxylate). Only one isomer of double-decker complexes is shown.[76]

properties.[77] This double-decker complex was synthesized by the direct metalation of the corresponding phthalocyanine (Scheme 7) with lithium bis(trimethylsilyl)amide as a basic reagent promoting complex formation. Similar to mentyl-substitued complexes, the metal-free ligand was CD-silent, while the double-decker complex showed a pronounced CD signal in the Q-band region. Also, the complex showed mesogenic behaviour and both crystalline and disordered states of

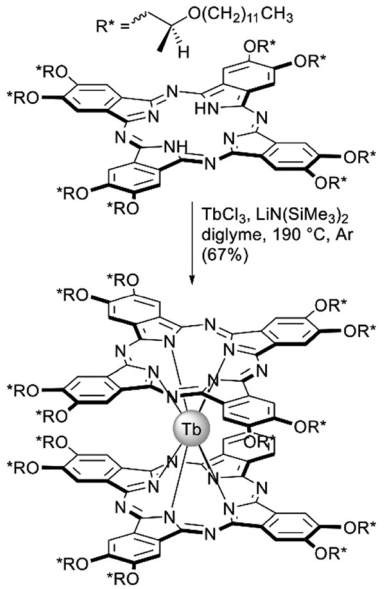

Scheme 7 Synthesis of mesogenic terbium(III) bisphthalocyaninate, bearing (*S*)-2-(dodecyloxy)propoxy-substituents.[77]

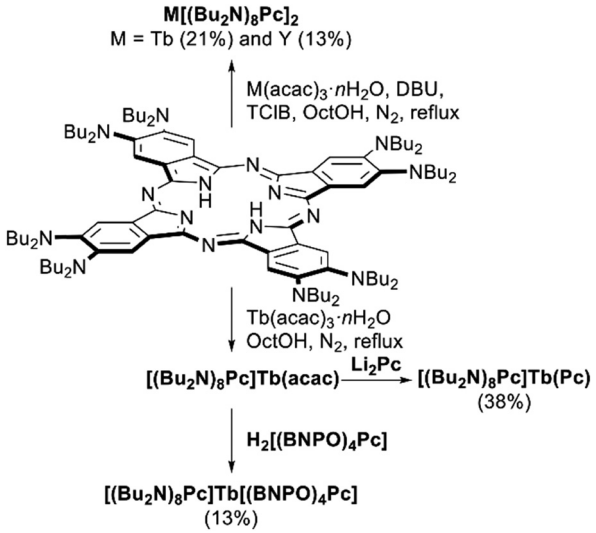

Scheme 8 Synthesis of bisphthalocyaninates based on octa-(di-*n*-butylamino)phthalocyanine.[81,82]

the same specimen could be kinetically trapped upon measurements of SMM behaviour at low temperatures. Both structural states showed markedly different magnetization dynamics revealing important influence of the structural environment of a single-molecule magnet taking advantage of its phase behaviour.

2.1.4 Sandwich phthalocyaninates bearing strong electron donors. High sensitivity of phthalocyanines to electronic effects of peripheral substituents allows the tuning of the properties of their complexes, thus over the last decade extreme samples have been reported, bearing particularly strong electron donors or acceptors.[78] Among the former, the introduction of di-*n*-butylamino-groups had a profound effect on the electronic structure of phthalocyanines – for example, octa-substituted metal-free ligand **H_2[(Bu_2N)$_8$Pc]** revealed a significant decrease by 0.26–0.35 V for the HOMO–LUMO gap in comparison with **H_2(Pc)** due to the effective p–π conjugation between the peripheral nitrogen atoms and the Pc chromophore.[79] This phthalocyanine was also used to synthesize various double-decker complexes (Scheme 8). Its direct metalation with M(acac)$_3$·*n*H_2O, in the TClB/OctOH (5 : 1 v/v) mixture yielded double-decker complexes in mediocre yields.[80]

The complex **Tb[(Bu_2N)$_8$Pc]$_2$** revealed excellent SMM behaviour which could be further improved by the synthesis of a heteroleptic complex **[(Bu_2N)$_8$Pc]Tb(Pc)** (*cf.* Section 3.2.2).[81] This complex was synthesized by the raise-by-one-story approach involving the metalation of **H_2[(Bu_2N)$_8$Pc]** with Tb(acac)·*n*H_2O in refluxing OctOH and *in situ* reaction of the generated Tb(III) monophthalocyaninate with **Li_2(Pc)**. In the same manner, erbium(III) complex **[(Bu_2N)$_8$Pc]Er(Pc)** was also synthesized and its anionic form was a first sandwich-type phthalocyanine-based erbium(III) compound with field-induced slow relaxation.[82]

Chiral heteroleptic complex was synthesized in a similar manner by the reaction of **[(Bu_2N)$_8$Pc]Tb(acac)** with **H_2[(BNPO)$_4$Pc]**,[83] and it also revealed excellent SMM characteristics. Such superior SMM behaviour of amino-substituted complexes was explained using DFT calculations in terms of the electrostatic effects of electron-rich ligands.

2.1.5 Sandwich phthalocyaninates bearing strong electron acceptors. Apart from spectacular red–green–blue colour change upon oxidation and reduction of sandwich Pcs rendering them as components of electrochromic materials, switching between redox states of sandwiches can be used to tune their magnetic properties.[84,85] Thus, introduction of strong electron acceptors into double-decker complexes was used to stabilize their reduced forms and study their SMM performance. Starting from a series of dicyanophthalimides Gonidec *et al.* synthesized electron-deficient double-decker complexes stabilized in their anionic forms **Tb[(R-imide)$_4$Pc]$_2^-$TBA$^+$** (Scheme 9).[86] Their SMM properties were virtually identical to those of the parent **Tb(Pc)$_2^-$TBA$^+$** complex. However, while the anionic forms of unsubstituted double-decker can be readily oxidized, often not on purpose, the imide-substituted compounds were stable in the anionic forms in a wide range of potentials, rendering them as components of hybrid magnetic materials without undesired charge transfer interactions between the substrates and SMMs.

Another extremely electron-deficient Tb(III) bis(octa-isopropyl)phthalocyaninate where all hydrogen atoms were replaced with fluorine atoms was studied by Gonidec *et al.*[87] It could be electrochemically reduced to di- and trianionic forms, and magnetic characteristics of these forms were studied by low-temperature MCD (*cf.* Section 3.4).

2.1.6 Halogenated sandwich phthalocyaninates. Several examples of halogenated sandwich complexes were synthesized by template condensation of the corresponding phthalonitriles in the presence of metal salts. For example, the short-run reaction of 4-iodophthalonitrile with lanthanide acetates in

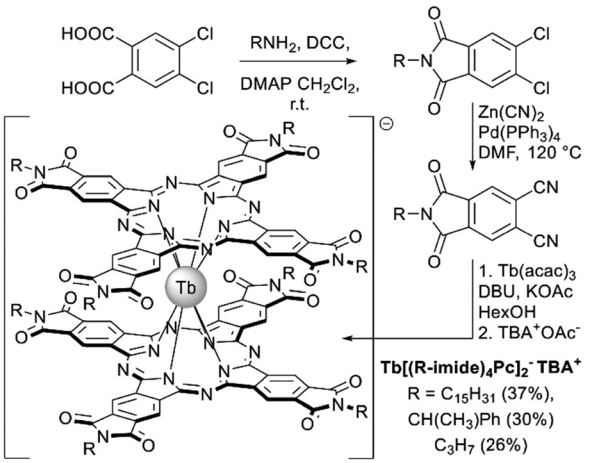

Scheme 9 Synthesis of the imide substituted double-decker complexes.[86]

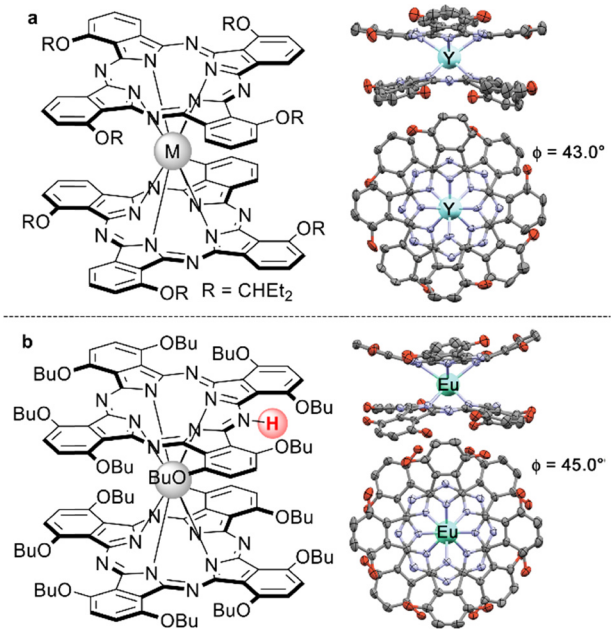

Fig. 3 Homoleptic nonperipherally-substituted bisphthalocyaninates: (a) C_{4h} isomer of **M[(α-$C_5H_{11}O$)$_4$Pc]$_2$** and X-ray structure of the Y(III) complex (CCDC NAZTEO),[93] and (b) *meso*-protonated complex **HM[(α-BuO)$_8$Pc]$_2$** with the X-ray structure of the Eu(III) complex (CCDC XUXCOJ01).[95] Substituents in the X-ray structures are truncated to oxygen atoms; hydrogen atoms are omitted.

melt at 380 °C for 5–6 min yielded a series of iodinated complexes **M(I$_4$Pc)$_2$**, M = Sm-Dy in 13–25% yields; the ability of complexes to absorb gaseous NH_3 was studied by Şenocak *et al.*[88] The yield of **Tb(I$_4$Pc)$_2$** could be improved to 42% when 4-iodophthalonitrile was condensed in the presence of Tb(acac)$_3$·nH$_2$O and DBU in refluxing PentOH. Under the same conditions, condensation of this phthalonitrile with terbium(III) monophthalocyaninate **[(*t*BuPhO)$_8$Pc]Tb(acac)** yielded the heteroleptic complex **(I$_4$Pc)Tb[(*t*BuPhP)$_8$Pc]**. Functionalization of iodinated sandwich using the Sonogashira reaction with 4-pentyn-1-ol was also studied.[89]

Neodymium(III) bis(octachlorophthalocyaninate), **Nd(Cl$_8$Pc)$_2$**, was synthesized by Kuzmina *et al. via* two alternative strategies. Template condensation of 4,5-dichlorophthalonitrile with Nd(OAc)$_3$·H$_2$O and DBU in refluxing PentOH yielded only 10% of the target complex; however, its yield could be improved to 87% using the raise-by-one-story reaction between **H$_2$(Cl$_8$Pc)** and **(Cl$_8$Pc)Nd(OAc)** and MeOLi in a refluxing mixture of trichlorobenzene and cetyl alcohol. This sandwich complex revealed improved optical limiting behaviour in comparison with nonhalogenated derivatives due to the heavy atom effect, although halogenated monophthalocyaninates turned out to be better optical limiters in comparison with sandwich complexes.[90] Interestingly, 4,5-dibromophthalonitrile did not yield any traces of double-decker complexes under the conditions of template synthesis.[91]

2.1.7 Sandwich phthalocyaninates with substituents in nonperipheral positions. All the aforementioned sandwiches contained substituents in the peripheral positions of the Pc rings, while nonperipherally-substituted complexes still remain relatively unexplored, although sterical hindrance caused by proximate nonperipheral substituents can have a profound influence on the structure and properties of such complexes, including particularly strong basicity of *meso*-nitrogen atoms and near-IR absorbance.[92]

Sandwiches based on tetra-α-substituted Pc ligands were reported for the first time by Wang *et al.* in 2005 with tetra-[α-(3-pentyloxy)]phthalocyaninates, **M[(α-Et$_2$CHO)$_4$Pc]$_2$**, M = Eu, Lu, and Y as examples (Fig. 3a).[93] These complexes were synthesized in a straightforward manner by the reaction of metal-free phthalocyanine with the corresponding M(acac)$_3$·nH$_2$O in refluxing OctOH, and the major C_{4h} isomer of europium(III) complex was characterized using XRD, which showed its elegant pinwheel-like structure. SMM behaviour of terbium(III) complex was also studied, showing the clear dependence of the magnetic properties of the complex on its redox state (*cf.* Section 3.4).[94]

The synthesis of complexes with octa-α-substituted ligands (Fig. 3b) turned out to be more challenging. In 2010 Gao *et al.* showed that the reaction of **H$_2$[(α-BuO)$_8$Pc]** with M(acac)$_3$·nH$_2$O and DBU in OctOH did not yield any traces of sandwich complexes; however, it was found that crown-ethers catalyse this reaction, and the best yield of the complex **HM[(α-BuO)$_8$Pc]$_2$** – 36.5% – was obtained in the presence of dibenzo-18-crown-6.[95] Crystallographic characterization of this complex revealed severe distortion of Pc ligands because of the sterical hindrance, caused by the eight proximate butoxy-groups as well as the presence of a proton at one of *meso*-nitrogen atoms. Localization of this proton in solution was shown by Damjanović *et al.* using the ^{1}H-NMR study of the paramagnetic terbium(III) complex **HTb[(α-BuO)$_8$Pc]$_2$**,[96] and the impact of protonation on the SMM behaviour of this complex was also demonstrated by Horii *et al.* (*cf.* Section 3.5).[97]

2.2 Sandwich complexes with low-symmetry phthalocyanine ligands

Lowering the symmetry of phthalocyanines is a powerful tool to tune their physical-chemical properties,[98] which is particularly

important in the field of nonlinear optics as well as in the fabrication of hybrid materials, where it allows the introduction of anchor groups which afford immobilization of complexes on various supports.

2.2.1 Rational template synthesis of A_7B-type bisphthalocyaninates. While low-symmetry phthalocyanines are typically synthesized by template cross-condensation of two different phthalonitriles, this approach has only limited applicability in the case of sandwich complexes since such condensation leads to enormous number of various products; however, it still can be applied when only the A_7B scaffold is required. This was showed for the first time with A_7B-type complex **[(15C5)Pc]Lu(Pc)** as the example, which was synthesized in a small yield of 3% by cross-condensation of unsubstituted and 15-crown-5-substituted phthlonitriles.[99]

This approach was optimized by Alpugan *et al.* with the example of europium(III)-templated cross-condensation of 4,5-di(*n*-hexylthio)phthalonitrile as component **A** with phthalonitriles, bearing one or two 5-hydroxypentylthio-groups as component **B** (Scheme 10).[100] Using the stoichiometric ratio of precursors yielded a mixture of six products with laborious separation issues. However, due to similar reactivities of both components, the distribution of products is expected to be close to statistical, thus increasing the ratio of **A** : **B** the yield of products, containing more than one **B** unit can be decreased, and the optimal ratio of 10 : 1 was selected to obtain two main products – complexes **$Eu(A_4)_2$** and **$(A_4)Eu(A_3B)$**, whose separation was facilitated by increased polarity of the asymmetric compound. Reproducible 10–12% yields were obtained for A_7B-type complexes based on hydroxylated phthalonitrile. Further functionalization of complexes was achieved by their mesylation and substitution of mesyl groups with azide as a possible substrate for *click*-chemistry.

2.2.2 Direct synthesis of homoleptic complexes with low-symmetry tetrapyrrolic ligands. Application of template reactions for the preparative synthesis of sandwich phthalocyaninates with more than one low-symmetry ligand is prohibitive, thus their synthesis is performed by the direct metalation of low-symmetry ligands.

Direct metalation of A_3B-type ligand was attempted by Oluwole *et al.* for the synthesis of homoleptic europium(III) bis- and trisphthalocyaninates bearing diethyleneglycol chains with terminal OH groups (Scheme 11).[101] Unexpectedly, direct metalation of this ligand with $Eu(OAc)_3$ in refluxing OctOH neither in the absence nor in the presence of DBU failed to produce target sandwiches, likely due to side processes associated with the interaction of diethyleneglycol groups with Eu^{3+} ions. However, protection of OH-groups with dihydropyran in starting phthalocyanine prior to complex formation allowed smooth conversion of the protected derivative into double-decker and triple-decker complexes, and the selectivity was controlled by the addition of DBU. Deprotection of THPO-groups yielded OH-substituted sandwiches, which were immobilized on the surface of quantum dots to give the first examples of hybrid optical limiters based on sandwich REE complexes.

A similar necessity to introduce protective groups was observed by Pushkarev *et al.* with the example of metalation of the phthalocyanine ligand bearing one phenolic OH group

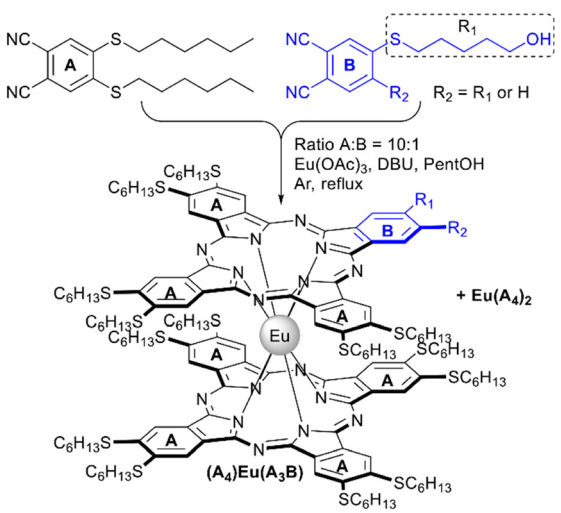

Scheme 10 Selective synthesis of a functionalized A_7B-type europium(III) bisphthalocyaninate.[100]

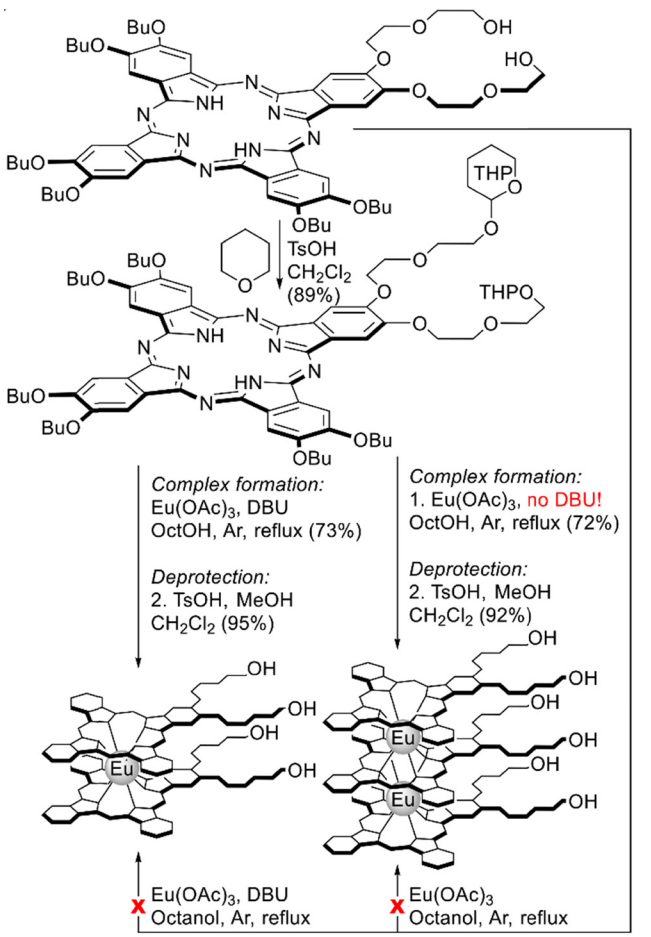

Scheme 11 Synthesis of sandwich europium(III) complexes bearing diethyleneglycol substituents with terminal OH-groups.[101]

conjugated with the Pc system (Scheme 12a).[102] Degradation of the unprotected ligand was observed upon metalation with europium and lutetium acetylacetonates in high boiling solvents; however, the benzylated derivative smoothly produced double-decker complexes where benzyl protections were removed by treatment with sulphuric acid.

This approach allowed Pedrini *et al.* to synthesize homoleptic terbium(III) bisphthalocyaninate with A_3B-type ligands bearing undec-10-en-1-yloxy groups, which were used to obtain covalent 1D architectures using diene metathesis (Scheme 12b).[103] This reaction turned out to be concentration-dependent – the product of intramolecular cyclisation of two ω-alkenyl chains was obtained when metathesis was performed in dichloromethane solution at 2.4 mM concentration. Increasing the concentration by an order of magnitude afforded the mixture of oligomers containing species from dimer to pentamer according to MALDI TOF mass-spectrometry. Importantly, the magnetic properties of this mixture were only slightly modified after the formation of the bond between molecules, highlighting the potential of this reaction scheme to form multinuclear magnetic assemblies.

Studies of metalation of covalently bonded dimeric phthalocyanines in the synthesis of sandwich complexes revealed that this reaction can proceed either in the intra- or intermolecular mode leading to mononuclear complexes or oligomeric assemblies (Scheme 13).

For example, clamshell-type diphthalocyanine **H_4[c-Pc_2]** with an *o*-xylyl bridge studied by Pushkarev *et al.* underwent mainly intracavity metalation upon interaction with lanthanide acetylacetonates (Scheme 13a), although some oligomers were detected by MALDI TOF mass-spectrometry.[104] To form well-defined dimeric bisphthalocyaninates the starting clamshell ligand can be treated with lanthanide monophthalocyaninates.[105,106] With a diterbium complex **(*t*Bu_4Pc)Tb[c-Pc_2]Tb(*t*Bu_4Pc)** as the example ferromagnetic intermetallic interactions were observed leading to elongation of magnetic relaxation times in comparison with the monomeric terbium complex **Tb(*t*$Bu_4$$Pc)_2$** (*cf.* Section 3.3.1).[105]

The balance of intra- *vs.* intermolecular complexation was studied by Birin *et al.* for butoxy-substituted diphthalocyanine with 24-crown-8 bridge **H_4[(24C8)Pc_2]**.[107] Its interaction with $M(acac)_3$, M = La, Ce, and Eu, and DBU in ClN yielded mixtures of mononuclear complexes and olygomers, and the yields of monomeric intercavity complexes (Scheme 13b) increased with the decrease of the metal size, gaining 40% for the Ce(IV) complex. The latter complex revealed unusual solvatochromic behaviour when going from chloroform to toluene, which was not observed in the case of homoleptic symmetrical **Ce[$(15C5)_4$$Pc]_2$**. Such behaviour was also studied by NMR spectroscopy which revealed solvent-induced changing of sandwich conformation.

Intracavity complexes of cerium(IV) with diporphyrins with chiral BINOL bridges **Ce[(BINOL-*n*)Por_2]**, *n* = 1 or 2 (Scheme 13c), were synthesized by Lu *et al.* using metalation of the corresponding ligands with cerium(III) acetylacetonate in trichlorobenzene in the presence of metal lithium, which was

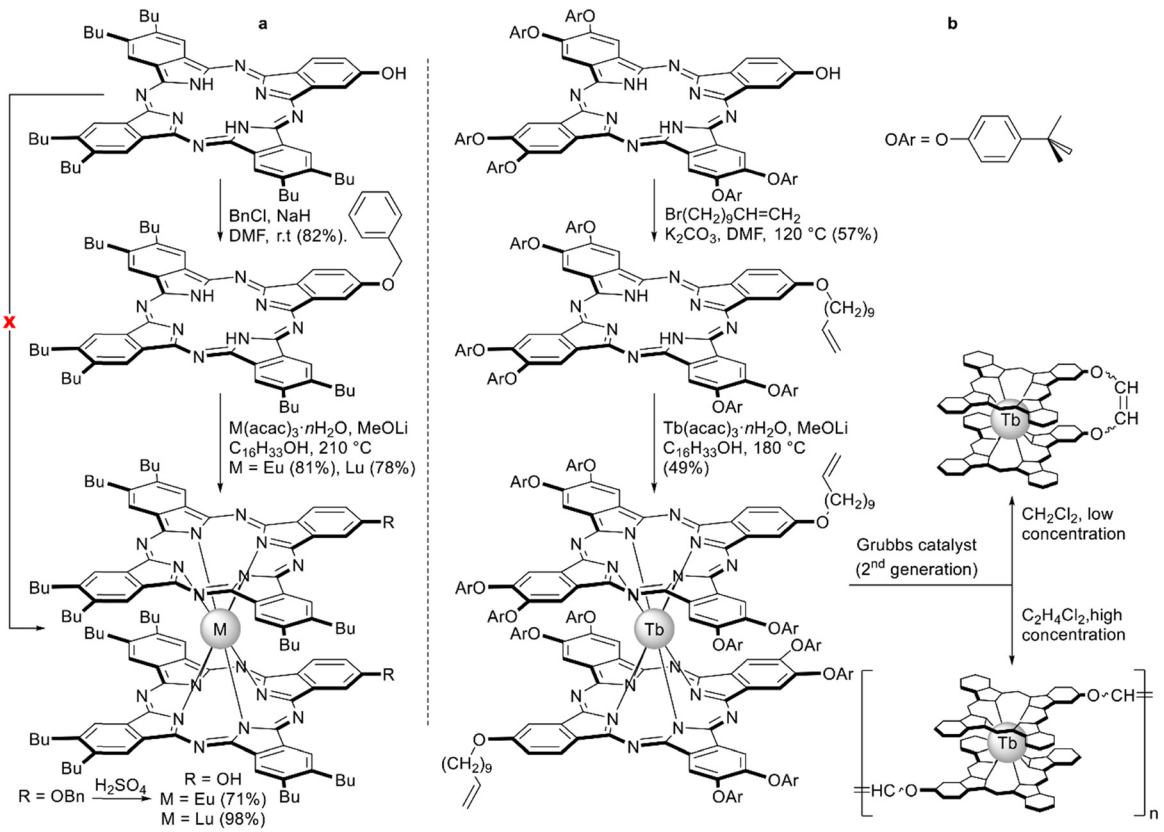

Scheme 12 Synthesis of sandwich complexes starting from hydroxy-substituted phthalocyanine ligands.[102,103]

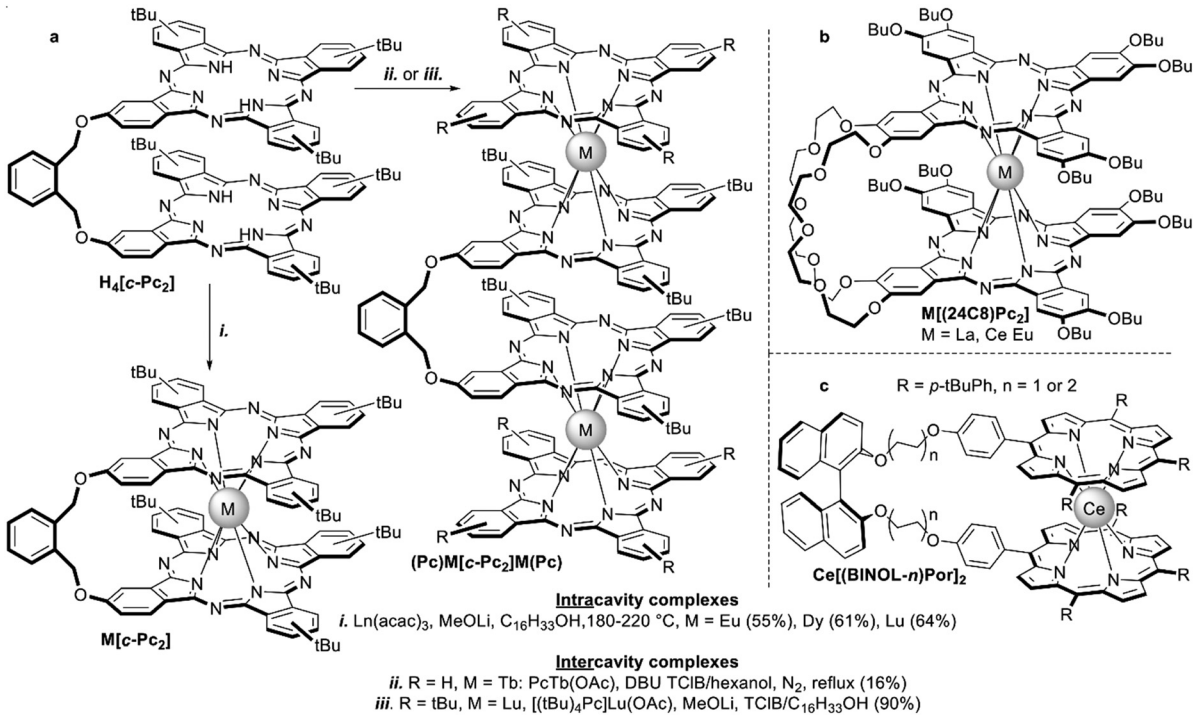

Scheme 13 Examples of sandwich complexes formed with dimeric tetrapyrrols: (a) intra-[104] *vs.* intermolecular[105,106] binding of lanthanides with clamshell-phthalocyanine **H_4[c-Pc_2]**; (b) 24-crown-8-interlocked bisphthalocyaninates **M[(24C8)Pc_2]**;[107] and (c) binaphthol-strapped chiral bis(porphyrinato)cerium(IV) complexes.[108]

added to activate the porphyrin.[108] CD measurements evidenced that (*R*)- and (*S*)-BINOL-strapped complexes formed perfect mirror spectra with negative and positive signs in the Soret band regions respectively. This observation suggests that the C_2-chirality of a BINOL strap is transcribed to the double-decker core as a defined chiral twist in the inter-porphyrin arrangement. The intensity of signals also depended on the length of the aliphatic bridge – $(CH_2CH_2)_n$ between BINOL and $CePor_2$ units, indicating the possibility to tune the efficiency of the intramolecular chirality transfer.

Homoleptic complexes with low-symmetric ABAB-type Pc ligands have been designed as NLO materials, bearing in mind the concept of octupolar molecules, which can be approximated by a cube with alternating donor and acceptor groups in the corners (Scheme 14). With this aim, double-deckers were synthesized by direct metalation of the corresponding Pcs bearing either four hexylthio-groups – **H_2[(SHex)$_4$Pc]**,[109,110] or alternating pairs of α-PentO and β-Cl substituents **H_2[(α-PentO)$_4$Cl$_4$Pc]**.[111,112]

Homoleptic terbium(III) bis-porphyrinate **HTb(DADAPor)$_2$** was synthesized by the reaction of metal-free tetra-*meso*-substituted porphyrin bearing alternating donor- and acceptor *p*-diphenylamino-phenyl and *p*-carboxymethylphenyl-ethynyl groups (Scheme 15).[113] Although X-ray structure of this complex was not obtained, DFT calculations suggested that intramolecular interactions between donor and acceptor

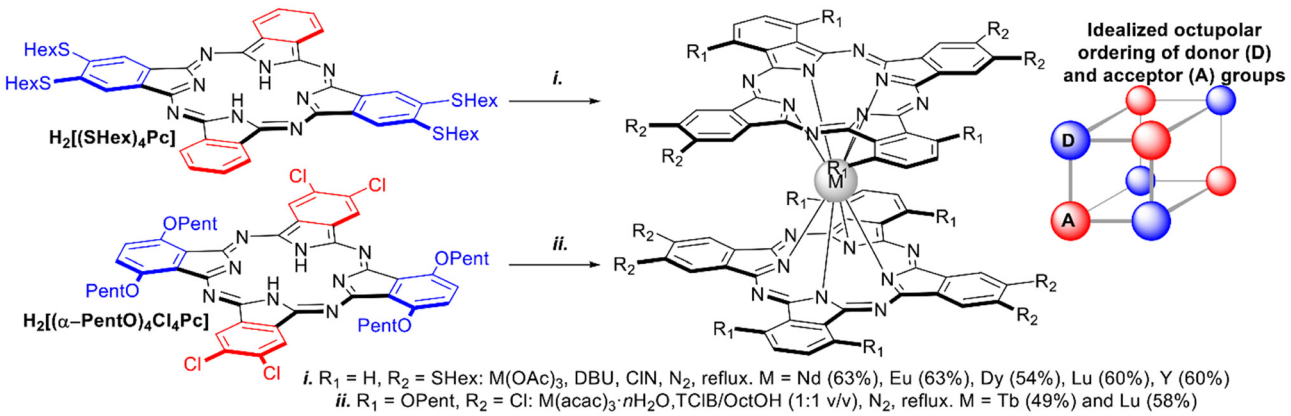

Scheme 14 Synthesis of octupolar bisphthalocyaninates based on ABAB-type ligands.[109–112]

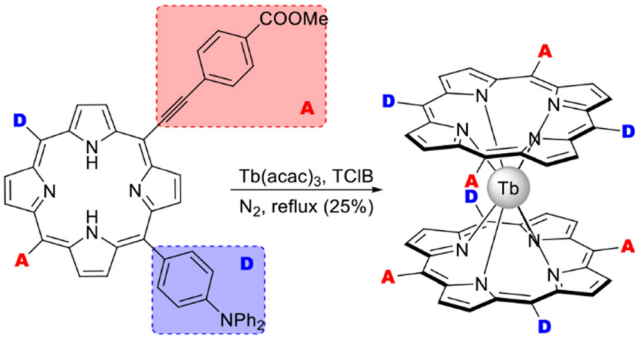

Scheme 15 Synthesis of octupolar bisporphyrinate with ABAB-type ligands.[113]

fragments should stabilize distorted cuboid conformation of this sandwich with a twist angle near 17°. This structural feature provided the studied complex with the largest off-resonant first hyperpolarizability as evaluated by harmonic light scattering measurements. Details on NLO studies of synthesized octupolar sandwiches are given in Section 5.1.

2.2.3 Heteroleptic complexes with low-symmetry phthalocyanine ligands. Heteroleptic complexes bearing only one low-symmetry ligand are convenient components of covalent or supramolecular assemblies with nanomaterials. Their synthesis is typically accomplished *via* the raise-by-one-story approach, where monophthalocyaninate with one ligand reacts either with another ligand or with phthalocyanine precursors.

For example, bisphthalocyaninates bearing one pyrene-containing A_3B ligand were synthesized by Klyatskaya *et al.* starting from **Li_2(Pc)** which was treated with $M(acac)_3$ in ClN generating **(Pc)M(acac)** species, M = Tb, Dy, and Ho.[114,115] Their further interaction with dilithium complex of pyrenyl-substituted phthalocyanine **Li_2[(Pyrene)Pc]** yielded 20–24% of the target heteroleptic complexes **[(Pyrene)Pc]M(Pc)**, which were separated from homoleptic complexes by column chromatography (Scheme 16). Isolation of the heteroleptic triple-decker terbium(III) complex with one terminal unsubstituted ligand and two adjacent pyrenyl-substituted ligands was also reported; the order of ligands was determined by collision induced dissociation using Fourier transform ion cyclotron resonance and an Orbitrap mass spectrometer.[116]

Due to the presence of pyrenyl group in the double-decker terbium(III) complex, it could be anchored to the surface of carbon nanotubes *via* π–π interactions. The anisotropy energy barrier and the magnetic relaxation time of the resulting conjugate are both increased compared with those of pure crystalline **[(Pyrene)Pc]Tb(Pc)**.[114] Also this conjugate behaved as an original spin-valve device, where localized magnetic moments lead to a magnetic field dependence of the electronic transport through single-walled carbon nanotubes, resulting in magnetoresistance ratios up to 300% at temperatures lower than 1 K (*cf.* Section 3.8).[117]

Interestingly, the ability of the pyrenyl group to participate in stacking interactions governed the crystal packing of the **[(Pyrene)Pc]Tb(Pc)** complex – its molecules formed head-to-tail dimers with the shortest intermolecular distances of 3.345–3.369 Å which is in good agreement with the general values observed for π–π stacking (Fig. 4).[115]

Heteroleptic bisphthalocyaninates, bearing one fullerene-appended ligand, were synthesized by Ballesteros *et al.* starting from a A_3B-type ligand with one benzylic alcohol group

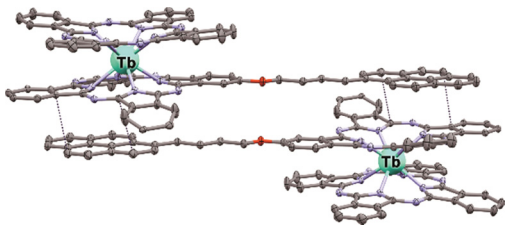

Fig. 4 Structure of a head-to-tail supramolecular dimer, formed in crystal packing by molecules of **[(Pyrene)Pc]Tb(Pc)** (CCDC LOGBEQ).[115] Hexyl substituents, hydrogen atoms and solvate molecules are omitted for clarity. The shortest intermolecular distances are shown with blue dotted lines.

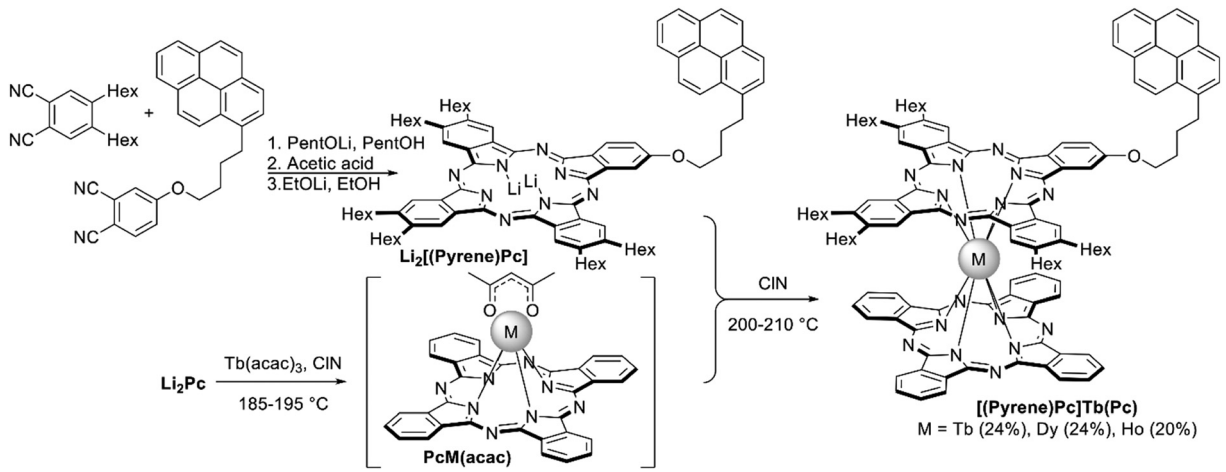

Scheme 16 Synthesis of pyrenyl-substituted bisphthalocyaninates **[(Pyrene)Pc]M(Pc)**.[114,115]

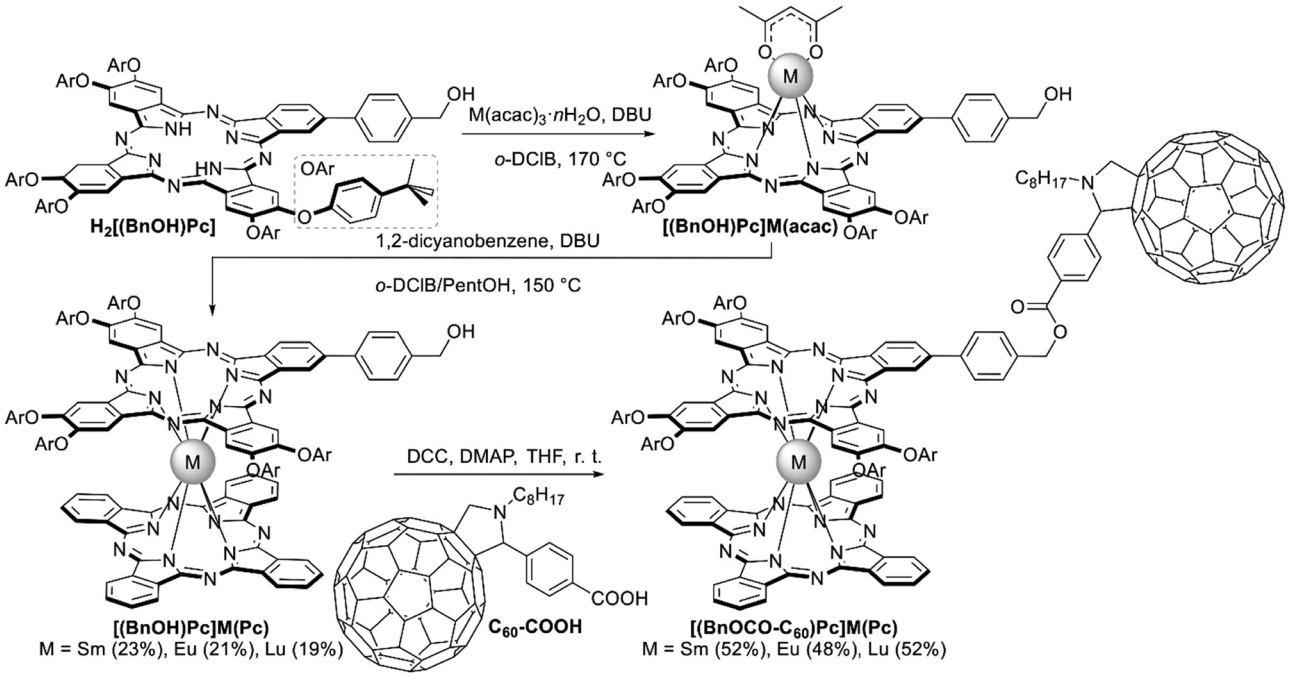

Scheme 17 Synthesis of fullerene-substituted bisphthalocyaninates **[(BnOCO-C_{60})Pc]M(Pc)**.[118]

H_2[(BnOH)Pc] whose reaction with acetylacetonates in *o*-dichlorobenzene yielded the corresponding monophthalocyaninates **[(BnOH)Pc]M(acac)**, M = Sm, Eu and Lu (Scheme 17).[118] These complexes were used as templates in reactions with phthalonitrile to construct unsubstituted Pc ligands yielding heteroleptic sandwiches which were esterified with fulleropyrrolidine carboxylic acid **C_{60}-COOH**. Photophysical characterization of the resulting complexes **[(BnOCO-C_{60})Pc]M(Pc)** showed that their components totally lack electronic interactions in the ground state; however, photoexcitation of the C_{60} fragment at 387 nm lead to a fast and long-lived charge transfer from $M(Pc)_2$ to C_{60} π-systems. In contrast, the short-lived nature of the bisphthalocyaninate excited states fails to trigger analogous charge-transfer reactions upon photoexcitation of this moiety.

Monophthalocyaninates can act as templates in cross-condensation of pairs of different phthalonitriles A and B paving the way to heteroleptic complexes where one of the ligands is represented by various combinations A_nB_{4-n}, n = 0–4. This one-pot approach was used by Pan *et al.* to synthesize a series of tetrathiafulvalene(TTF)-fused heteroleptic europium(III) double-deckers **[$(TTF)_n$Pc]Eu(Pc)**.[119] With this aim **(Pc)Eu(acac)** reacted with the mixture of unsubstituted and TTF-fused phthalonitriles (Scheme 18) and the mixture of the resulting complexes could be successfully separated by size-exclusion chromatography together with chromatography on silica to separate the *cis*- and *trans*-isomers of **[$(TTF)_2$Pc]Eu(Pc)**. Introduction of the TTF units onto double-decker complexes had strong effects on their UV-Vis spectra and electrochemical properties, revealing the significant contribution of these units to the electronic structure of double-deckers.

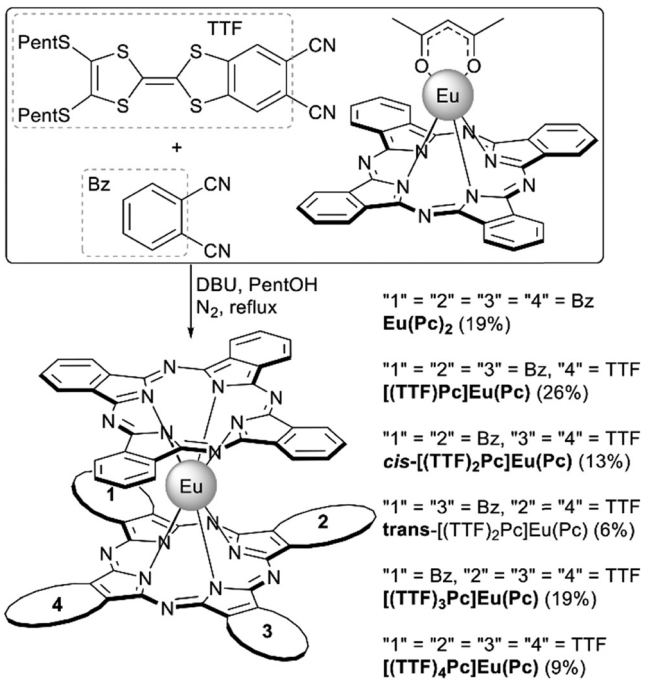

Scheme 18 One-pot synthesis of a series of tetrathiafulvalene (TTF)-fused bisphthalocyaninates **[$(TTF)_n$Pc]Eu(Pc)**, n = 0–4.[118]

Unprecedent heteroleptic complexes with open-chain triisoindole-1-one ligands **(R-TIO)Lu(Pc)**, R = Me or iPr, were unexpectedly isolated by Wang *et al.* from the conventional raise-by-one-story synthesis of heteroleptic bisphthalocyaninates *via* template condensation of bulky diaryloxy-phthalonitriles with

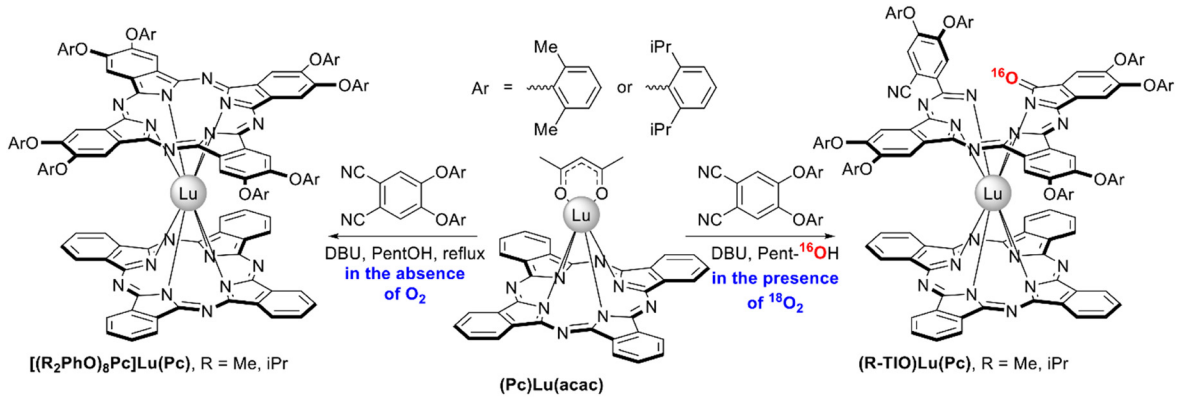

Scheme 19 Synthesis of heteroleptic double-deckers with triisoindole-1-one ligands.[120]

lutetium(III) monophthalocyaninate and DBU in refluxing pentanol (Scheme 19).[120] It was found that the target **[(R$_2$PhO)$_8$Pc]Lu(Pc)** complexes were sole products of template condensation only when it was performed under strictly anaerobic conditions. However, the presence of even 5 ppm of oxygen in inert gas media terminated the reaction at the stage of uncyclized isoindole oligomeric derivatives rather than the phthalocyanine chromophores. The yields of TIO-containing sandwiches could be increased up to 25.8% when the reactions were performed in a pure oxygen atmosphere. Experiments with labeled $^{18}O_2$ showed that the carbonyl group in the TIO ligand contains ^{16}O atom, suggesting that it comes from the solvent. TIO ligands were stabilized both by bulky aryloxy-groups as well as by half-sandwich part of the molecule, and demetalation of these complexes resulted in complete degradation of triisoindole-1-ones.

2.3 Mixed ligand sandwich complexes

In hierarchy of sandwich complexes mixed ligand double- and triple-deckers combining tetrapyrrolic macrocycles from different families (Por, Pc, Nc, *etc.*) attract special attention due to wider possibilities of tuning of both structural and functional characteristics in comparison with homoligand complexes. Among the most important features in the context of the present review we should mention specific acid–base equilibria in double-decker Por-Pc complexes (*cf.* Section 3.5). Panchromatic absorbance appearing from orbital interactions between stacked ligands is particularly important for the elaboration of broadband light harvesting materials.[121] Combination of ligands with different sterical demands in sandwich complexes also affords precise control of twist angles between these ligands which in turn rules the shape of the coordination polyhedron of the metal centre bound to these ligands and affects its SMM behaviour (*cf.* Section 3.2.1).

2.3.1 Mixed complexes containing porphyrin and phthalocyanine ligands. Mixed ligand sandwiches containing both porphyrin and phthalocyanine macrocycles have been known for several decades starting from the seminal work of Moussavi *et al.* in 1989.[34] A new round of interest in these complexes began in 2012 when Sakaue *et al.* reported the synthesis, structural characterization and magnetic relaxation studies of homo- and heteronuclear triple-deckers **(TAnP)M*(Pc)M(Pc)**, M* = M = Tb and M* ≠ M = Tb/Y.[122] These complexes were prepared in modest yields of 2.3–4.2% by generation of REE monoporphyrinates from tetra-*p*-anisyl-porphyrin **H$_2$(TAnP)** and M*(acac)$_3$ with subsequent interaction with **M(Pc)$_2$** in refluxing trichlorobenzene (Scheme 20). XRD characterization of complexes revealed different symmetries of coordination surrounding of metal centres M and M*, which has a profound effect on the dynamics of magnetization relaxation (*cf.* Section 3.2.1).

Interest in studies of mixed ligand sandwiches requires efficient synthetic pathways with improved yields, which can be realized either by optimization of experimental protocols, or by application of auxiliary functionalities in macrocycles, governing the regioselectivity of complex formation.

With the aim to synthesize early lanthanide complexes based on tetra-*meso*-aryl-porphyrins and crown-phthalocyanine Birin *et al.* proposed one-pot procedures implying reactions between corresponding porphyrins, M(acac)$_3$ and 15-crown-5-phthalonitrile, the latter undergoes template

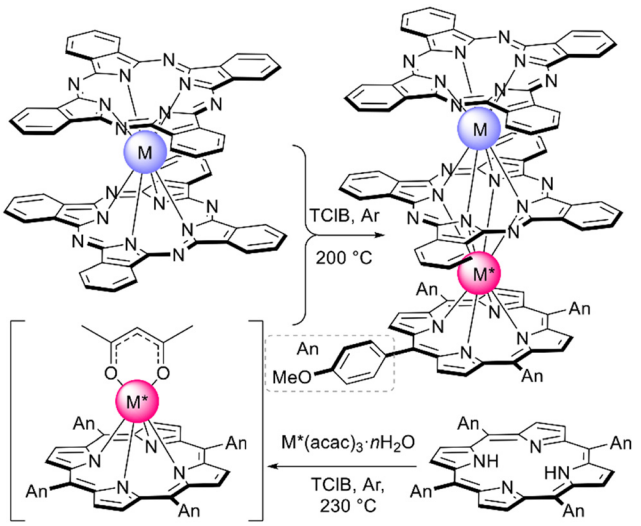

Scheme 20 Synthesis of homo- and heteronuclear mixed ligand complexes **(TAnP)M*(Pc)M(Pc)**, M* = M = Tb or M* ≠ M = Tb/Y.[122]

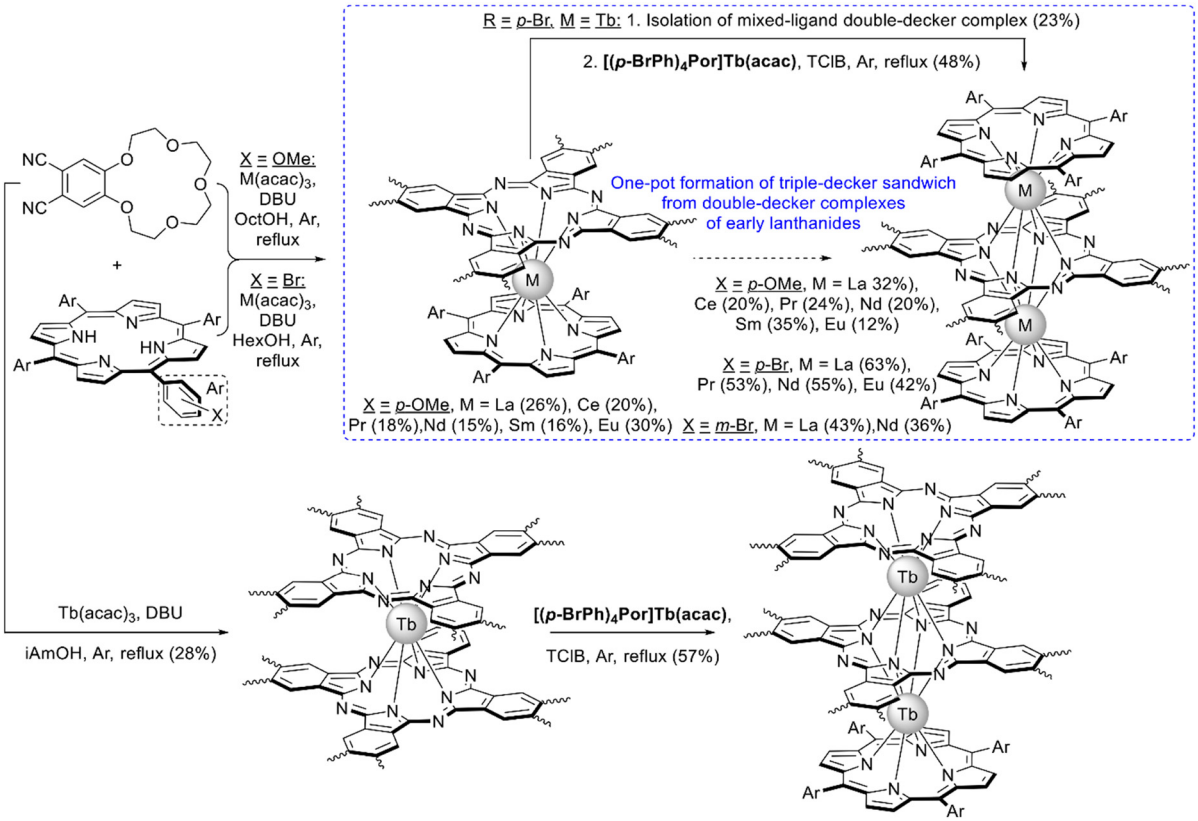

Scheme 21 Synthesis of crown-substituted mixed ligand sandwich complexes.[123–129]

condensation with simultaneous formation of sandwich complexes (Scheme 21).[123–126] The balance of concurrent stages was studied[127] and the optimal conditions were found leading either to mixtures of double- and triple-decker complexes or selectively to triple-decker complexes with a Por–Pc–Por ligand arrangement. The crucial role of electron-donating crown-ether groups in the synthesis of such triple-deckers was demonstrated, when unsubstituted phthalonitrile was used instead of crown-substituted precursor; the synthesis terminated at the step of mixed-ligand double-decker complex.[128] Going from early to late lanthanides drastically decreased the yield of triple-deckers, thus, to synthesize a terbium(III) complex it was necessary to use the raise-by-one procedure with the addition of terbium(III) porphyrinates to pre-synthesized double-decker complexes.[129]

Classical conditions of the raise-by-one-story approach to Por–Pc–Pc mixed ligand complexes *via* the interaction of monoporphyrinates with bisphthalocyaninates in high-boiling solvents turned out to be inapplicable in the synthesis of complexes with phthalocyanines bearing bulky substituents. To circumvent this drawback Jin *et al.* used microwave activation, the thus optimized conditions allowed the synthesis of series of complexes in high yields (Scheme 22).[130] Importantly, MW activation allowed the speeding-up of the synthetic procedures, thereby minimizing possible thermolysis of labile compounds. This benefit allowed the synthesis of complex with free *meso*-positions in porphyrin ligands, while under classical

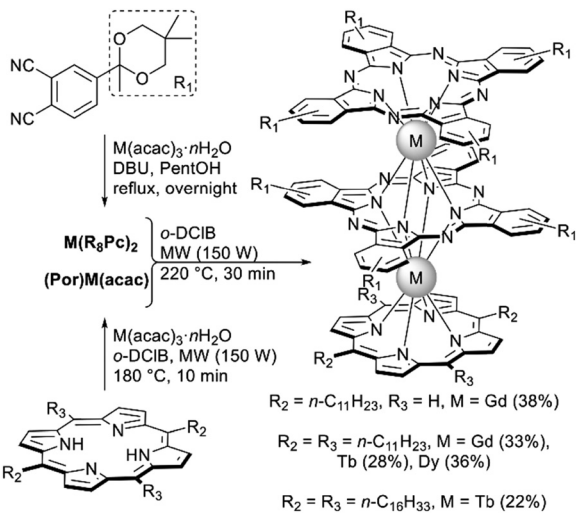

Scheme 22 Microwave-mediated synthesis of lanthanide porphyrin/phthalocyanine triple-deckers bearing bulky substituents.[130]

solvothermal synthesis of similar complexes starting from 5,15-diphenylporphyrin its degradation was observed under prolonged refluxing of reaction mixtures.[128]

Straightforward synthesis of mixed ligand triple-deckers leading to the regioselective Por–Pc–Por arrangement of ligands was achieved by González-Lucas *et al.*[131] who applied a diporphyrin with a flexible decamethylene spacer (Scheme 23). This

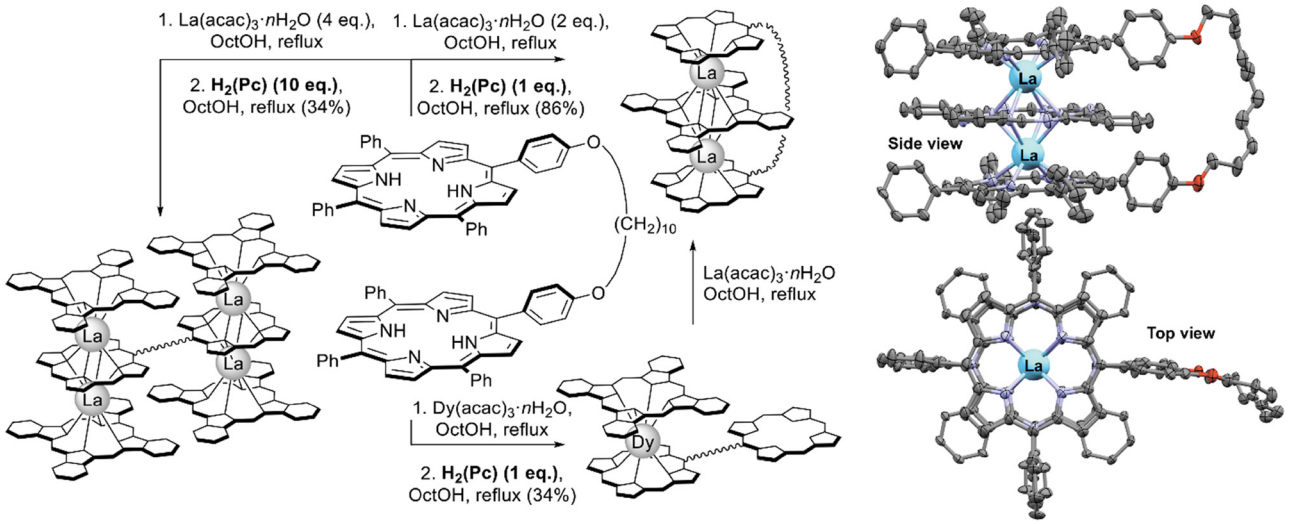

Scheme 23 Synthesis of sandwich mixed ligand complexes with spacered diporphyrin and X-ray structure of dilanthanum(III) complex (CCDC LUVWUX). Only one of the symmetry-imposed disorder components is shown. Hydrogen atoms and solvent molecules have been omitted for clarity.[131]

pincer ligand sequentially captures lanthanide ions and phthalocyanines to efficiently form desired triple-decker complexes in high yield when it reacts with stoichiometric amounts of $La(acac)_3$ and **H_2(Pc)**. In a similar manner, complexes with Pr(III), Nd(III), Sm(III) and Eu(III) were synthesized; however, attempts to synthesize complexes with a smaller metal centre – Dy(III) resulted in the formation of a double-decker complex linked with a free-base porphyrin residue. Reaction of this complex with $La(acac)_3$ resulted in the formation of an intermediate heteronuclear La(III)/Dy(III) complex which however underwent complete transmetalation with the formation of a homonuclear lanthanum(III) complex.

To broaden the range of useful properties of mixed ligand complexes, they can be functionalized with redox-active groups or hydrogen-bond donors which can form supramolecular aggregates of various architectures *via* self-assembling processes.

A series of ferrocene-decorated mixed ligand sandwiches were synthesized by Zhu *et al.* using the raise-by-one-story approach starting from 5,15-diferrocenylporphyrin in 20–5% yields for double-decker complexes and 70% for a triple-decker sandwich (Fig. 5).[132] Electrochemical studies of these complexes revealed two consecutive Fc-based one-electron oxidation waves, suggesting the effective electronic coupling between these units which could be finely tuned by structural modifications of the sandwich framework. Thus, the separation between these waves increased with the decrease of the REE ionic radius, but it decreased when going from a double- to triple-decker complex.

Mixed ligand europium(III) double-deckers bearing from one to four *n*-octylamino-groups (Fig. 6) were synthesized and used as tectons for self-assembled nanostructures, formed upon injection of concentrated solutions of complexes in toluene into excess of methanol.[133,134] The morphology of the resulting aggregates was studied by various methods, and it was

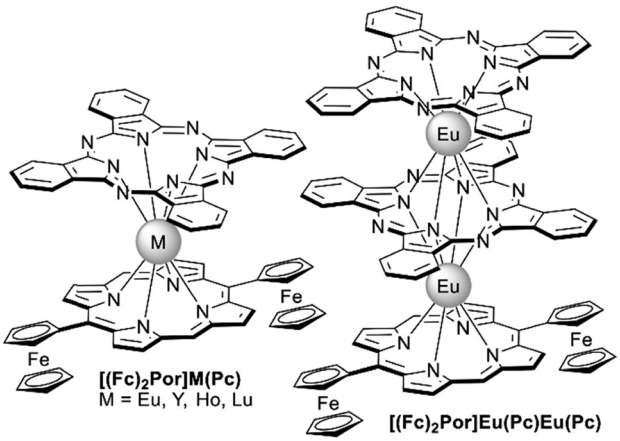

Fig. 5 Ferrocene-decorated double- and triple-decker mixed ligand complexes.[132]

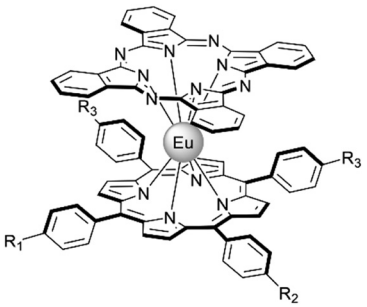

Fig. 6 Amino-substituted mixed ligand complexes **(A_1-TPP)Eu(Pc)**: R_1 = NHOct, R_2 = R_3 = H; **(A_2-TPP)Eu(Pc)**: R_1 = R_2 = NHOct, R_3 = H; **(A_4-TPP)Eu(Pc)**: R_1 = R_2 = R_3 = NHOct.[133,134]

demonstrated that it governed their functional characteristics. For example, in the case of **(A_1-TPP)Eu(Pc)** and **(A_4-TPP)Eu(Pc)** this procedure resulted in the fabrication of uniform well-

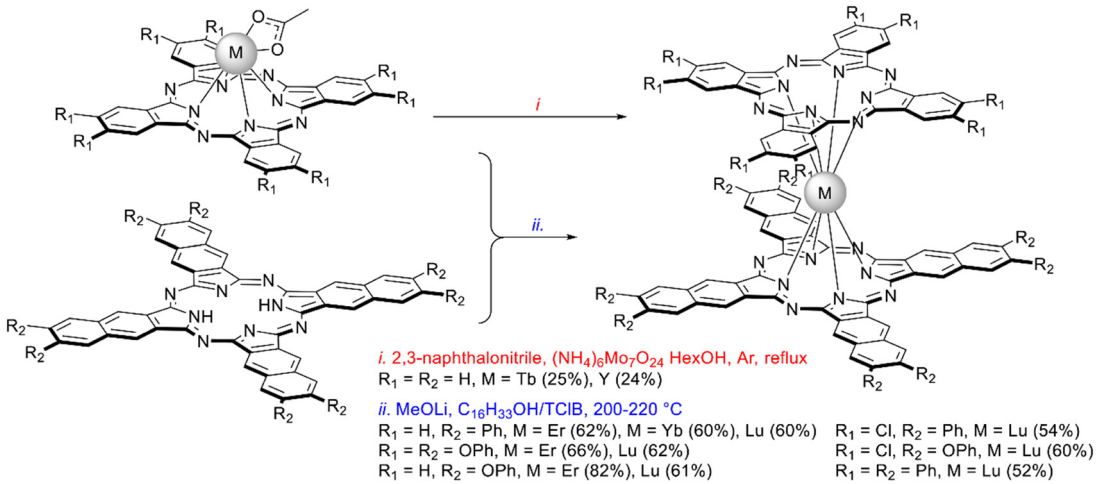

Scheme 24 Template (i) *vs.* direct (ii) synthesis of complexes containing phthalo- and naphthalocyanine ligands.[43,136,137]

defined nano-rods and nano-sheets with conductivities of 3.85×10^{-5} and 2.48×10^{-5} S m^{-1}, respectively. This difference was attributed mainly to the more effective intermolecular π-electron delocalization in nano-sheets which was concluded from the analysis of X-ray diffraction patterns of the nanostructures.[134]

2.3.2 Mixed ligand complexes with naphthalocyanines. Introduction of naphthalocyanines into mixed ligand complexes affords strong dissymmetrisation of electronic density due to anisotropic expansion of the π-system, which can be used for grafting of molecules in a well-defined fashion on various supports. For example, Komeda *et al.* absorbed **(Nc)Tb(Pc)** on the Au(111) surface in segregated Pc- or Nc-up modes to study Kondo resonance originating from interactions between conduction electrons and a localized spin (*cf.* Section 3.7).[135] Katoh *et al.* showed that the cationic complex **(Nc)Tb(Pc)$^+$PF$_6^-$** forms tetragonal crystals with perfect collinear arrangement of metal centres with efficient intermolecular ferromagnetic coupling (*cf.* Section 3.3.3).[136]

Mixed-ligand Pc–Nc complexes can be synthesized using the raise-by-one-story approach. Thus, neutral complex **(Nc)Tb(Pc)** was synthesized in a mediocre yield by template condensation of 2,3-naphthalonitrile in the coordination sphere of terbium(III) monophthalocyaninate in the presence of DBU and ammonium molybdate (Scheme 24i).[136] High quality crystals of its cationic complex were obtained by the electrochemical oxidation of neutral **(Nc)Tb(Pc)^0** in dichloromethane in the presence of NBu_4PF_6 electrolyte.

The interaction of naphthalocyanine ligands with monophthalocyaninates using lithium methoxide in the mixture of TClB and cetyl alcohol allowed Dubinina *et al.* to optimize the synthesis of mixed ligand phthalo-/naphthalocyaninates (Scheme 24ii).[43,137] It afforded a series of complexes containing various substituents in both Pc and Nc rings, and the yields of sandwiches were high even for the late lanthanides. AFM studies of thin films formed by lutetium(III) Pc–Nc complexes evidenced that their tendency to aggregate depended on the

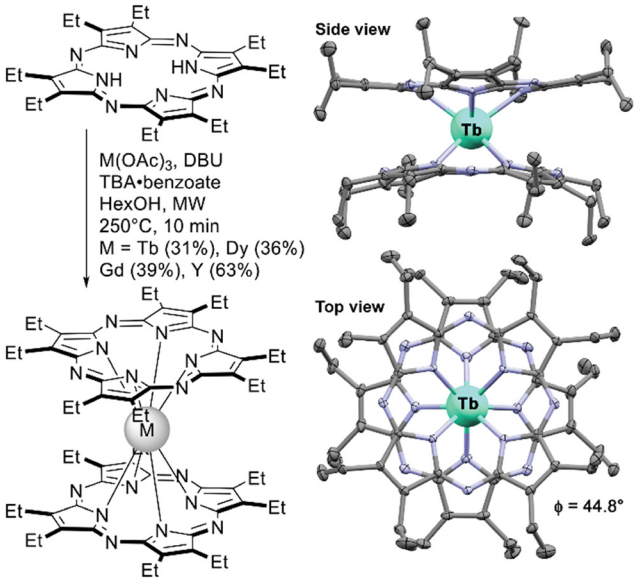

Scheme 25 Synthesis of double-decker complexes with octaethylporphyrazine and the X-ray structure of the complex **Tb(OEPz)$_2$** (CCDC QOQPIX).[140] Hydrogen atoms and solvate molecules are not shown for clarity.

substitution patterns, gaining maximum for **(Ph$_8$Nc)Lu(Ph$_8$Pc)**, and in general the series of complex behaved as semiconductors with small activation energy.[43]

A mixed ligand europium(III) complex with decylthio-substituted naphthalocyanine and push-pull porphyrin (Fig. 7a) was synthesized by Stefak *et al.*, who used the template condensation of 6,7-di(*n*-decylthio)-2,3-naphthalonitrile in the presence of the corresponding monoporphyrinate.[138] This complex was suggested as a rotor which can be absorbed on the Cu(111) surface in a porphyrin-up fashion, forming a network where molecules undergo simultaneous and coordinated rotational switching under the influence of an STM tip-induced electric field by applying biases above 1 V at 80 K (Fig. 7b).[139]

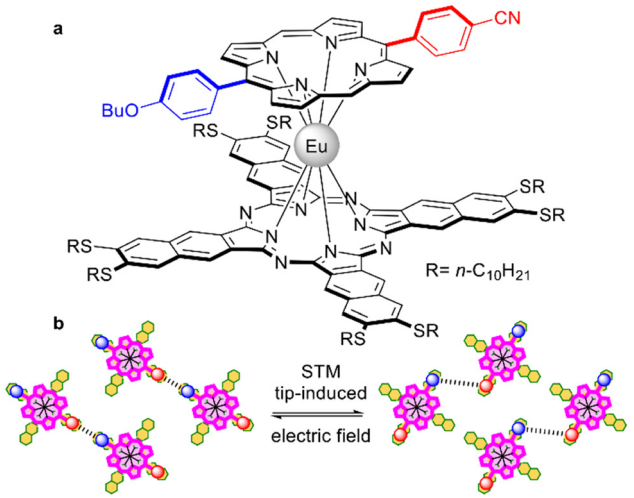

Fig. 7 (a) Donor–acceptor porphyrinate rotor mounted on a naphthalocyaninato-europium(III) complex.[138] (b) Behaviour of a supramolecular network of a donor–acceptor double-decker complex in monolayer, formed by complex on the Cu(111) surface.[139]

2.4 Sandwiches with less-common tetrapyrrolic ligands

Advances in the synthesis of novel tetrapyrrolic ligands were often followed by the introduction of these ligands into the chemistry of sandwich REE complexes. The following section will include examples of double- and triple-deckers with porphyrazines including hetero-annulated derivatives, tetrabenzoporphyrins, and core-modified macrocycles – tetrabensotriazaporphyrins (TBTAP), corroles and *N*-confused porphyrins. Most of these complexes are yet to be comprehensively explored in terms of applicability, thus this section can give a summary inspiring their further study.

2.4.1 Sandwich complexes with porphyrazine ligands. In contrast to porphyrins and especially phthalocyanines attention to porphyrazines in context of sandwich REE complexes still remains very modest.

A series of neutral double-decker complexes with an octaethylporpyrazine ligand (OEPz) with Tb(III), Dy(III), Gd(III) and Y(III) metal centres was reported in 2014 by Giménez-Agulló *et al.* Sandwiches were synthesized starting from **H_2(OEPz)** using microwave activation.[140] Interestingly, the synthetic protocol included the necessity to add tetrabutylammonium benzoate as an auxiliary reagent – in its absence double-decker complexes could not be obtained. The authors claimed that this salt was needed to stabilize the intermediate – anionic form **$[M^{3+}(OEPz^{2-})_2]^-TBA^+$**, which underwent oxidation to the neutral radical form during reaction workup.

X-ray structure of the complex showed that the molecule adapts staggered conformation with SAP surrounding of the metal centre which is a prerequisite of SMM behaviour of Tb(III) and Dy(III) complexes. Indeed, AC magnetometry showed that **$Tb(OEPz)_2$** is characterized by high value of magnetization relaxation barrier comparable with the value of **$Tb(Pc)_2$**.

Sandwich REE complexes with heterocycle-annelated macrocycles were reported for the first time by Tarakanova *et al.* in 2014[141] with complexes with tetradiazepinoporphyrazine (DZPz) ligands as examples. High CH-acidity of the peripheral diazepine rings made them efficient hydrogen bond donors thus the macrocycles themselves were found to form highly stable dimers in solutions.[142] Staggered conformations of these dimers reminded the arrangement of tetrapyrrols in REE sandwiches; therefore, additional stabilization of a double-decker scaffold could be expected.[143] And indeed, it was shown that direct metalation of **H_2[(*t*BuPh)$_8$DZPz]** with M(acac)$_3$ and DBU (Scheme 26a) smoothly yielded double-decker complexes at the temperature of refluxing *o*-dichlorobenzene (180 °C), where classical phthalocyanines selectively form only monophthalocyaninates.[141,143–145] Importantly, diazepine rings were susceptible to hydrolysis in alkaline media, which made template synthesis of REE complexes with DZPz ligands less efficient than direct metalation.[141] DFT modelling of the resulting double-deckers suggested the presence of

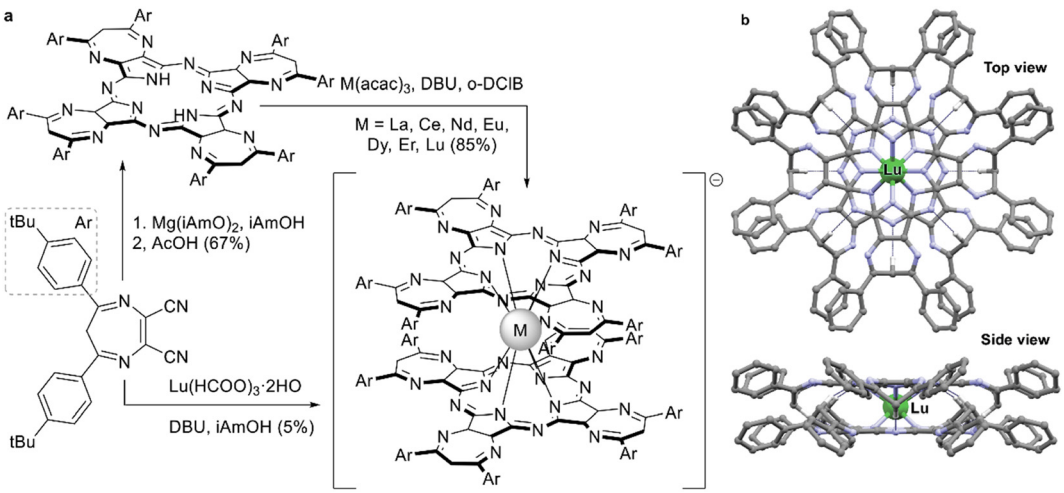

Scheme 26 (a) Synthesis of double-decker complexes with tetradiazepinoporphyrazine ligands. (b) Optimized structure of **Lu(Ph$_8$DZPz)$_2^-$** in top and side views, showing hydrogen bonds between CH_2 groups of diazepine rings and *meso*-N atoms. Other hydrogen atoms are omitted for clarity. Model was built using Cartesian coordinates, provided in the ESI in ref. 143.

intramolecular hydrogen bonds between endocyclic CH-groups of diazepine rings and *meso*-nitrogen atoms of opposite ligands (Scheme 26b).

Among other differences in the reactivity of DZPz and Pc ligands the stabilization of anionic forms of double-decker complexes should be emphasized. In contrast to $\mathbf{M(Pc)_2}^-$ which readily undergoes aerobic oxidation to neutral forms, the synthesized complexes $\mathbf{M[(\mathit{t}BuPh)_8DZPz]_2}^-$ remained in this form during chromatographic purification, and the addition of strong oxidants like bromine was needed to generate neutral forms which revealed characteristic intervalence bands in the NIR region.[143] The cerium complex fell out of this trend and its double-decker complex was stabilized in the neutral form with a quadrivalent metal centre.[145] Its electrochemical reduction to trivalent state was characterized by slow electron transfer kinetics which was explained by strong structural rearrangement of the sandwich molecule following the electron transfer step as well as shielding of the metal center by the bulky macrocycles.

Interestingly, solutions of anionic double-deckers with DZPz ligands were stable for several months showing no evidence of aggregation or decomposition; however, in the case of neutral forms evolution of their UV-Vis spectra was observed, depending on the nature of the metal centre. First of all, upon storage of solutions of $\mathbf{M[(\mathit{t}BuPh)_8DZPz]_2}^{0\bullet}$ in CH_2Cl_2 the hypsochromic shift and broadening of Q-bands were observed, and DLS studies of aged solutions revealed the formation of aggregates with a hydrodynamic radius of 20 nm. The tendency of neutral forms to aggregate was explained by the possibility of inversion of diazepine moieties leading to the reorientation of the intramolecular hydrogen bonds in the double-decker followed by the formation of intermolecular hydrogen bonds. In turn, it weakened the stabilizing effect of intramolecular H-bonding, and it resulted in lowering of stability in early lanthanide complexes – slow demetalation of $\mathbf{La[(\mathit{t}BuPh)_8DZPz]_2}^{0\bullet}$ was observed even after 1 day of solution storage, while lutetium(III) complex was stable towards demetalation ever after five days.[143]

In the case of mixed ligand complexes $\mathbf{[(\mathit{t}BuPh)_8DZPz]M(Pc)}$, M = La, Eu and Lu, spontaneous aggregation due to inversion of diazepine ring was observed even for anionic forms.[146] In contrast to homoleptic complexes these double-deckers could form only dimeric species, which were observed by NMR spectroscopy. Tendency to aggregation followed the growth of the ionic radius of lanthanide ion due to an increase of interligand distance, weakening of intramolecular CH...N interactions and facilitation of diazepine ring inversion. The same trend was observed in the case of neutral forms generated during spectroelectrochemical studies. Thus, the intermolecular self-assembly of sandwich complexes containing DZPz decks can be controlled by changing the nature of both peripheral substituents and REE ions.

Soluble tetrathieno[2,3-*b*]porphyrazine annelated with cyclohexane rings was used by Dubinina *et al.* to synthesize lutetium(III) complexes expecting that the presence of sulphur-containing heterocycles can provide the resulting complexes

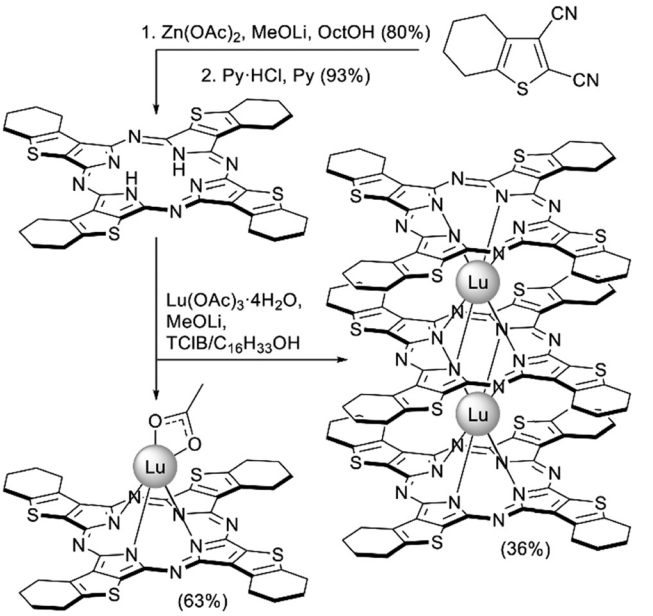

Scheme 27 Synthesis of lutetium(III) complexes with substituted tetrathieno[2,3-*b*] porphyrazine.[147]

with improved NLO properties.[147] Starting metal-free ligand was synthesized from tiophenedicarbonitrile by Zn-templated condensation and demetalation. Reactivity of the resulting ligand was quite unusual – upon its reaction with $Lu(OAc)_3 \cdot 4H_2O$ and MeOLi in refluxing mixture of TClB and cetyl alcohol only mono- and triple-decker complexes were obtained, which were separated by preparative TLC (Scheme 27). Although the formation of double-decker was detected by mass-spectrometry, it could not be isolated because of its low stability associated with the presence of π-radical.

2.4.2 Sandwich complexes with tetrabenzoporphyrin and tetrabenzocorrin ligands. Tetrabenzoporphyrins (TBP) were known since 1938;[148] however, their complexes with REE were described for the first time only in 2012. The studies were inspired by interest in the properties of porphyrin complexes with an expanded aromatic system. These and more recent results are summarised in Scheme 28.

Thus, interaction of tetra(bicyclo[2.2.2])octadienoporphyrin with $Gd(OAc)_3$ in refluxing TClB was studied by Xu and Liu *et al.*[149] Under these conditions metalation of tetrapyrrolic macrocycles was accompanied by retro Diels-Alder aromatization producing TBP ligands. Heating of the reaction mixture for 15–17 h resulted in the formation of a double-decker complex $\mathbf{Gd(TBP)_2}$, and increase of the reaction time to 45–48 h resulted in the predominant formation of a triple-decker complex $\mathbf{Gd_2(TBP)_3}$.[150,151] Magnetic properties of complexes were studied revealing antiferromagnetic interactions between π- and f-electrons in $\mathbf{Gd(TBP)_2}$ and between two Gd^{3+} ions in the case of $\mathbf{Gd_2(TBP)_3}$.

Interaction of tetrabenzoporphyrin $\mathbf{H_2(TBP)}$ itself with $M(acac)_3$, M = La, Nd, Gd, Dy, and Lu was used by Galanin *et al.* to generate half-sandwich complexes **(TBP)M(acac)** which reacted with $\mathbf{Li_2(Pc)}$ to form mixed ligand double-deckers

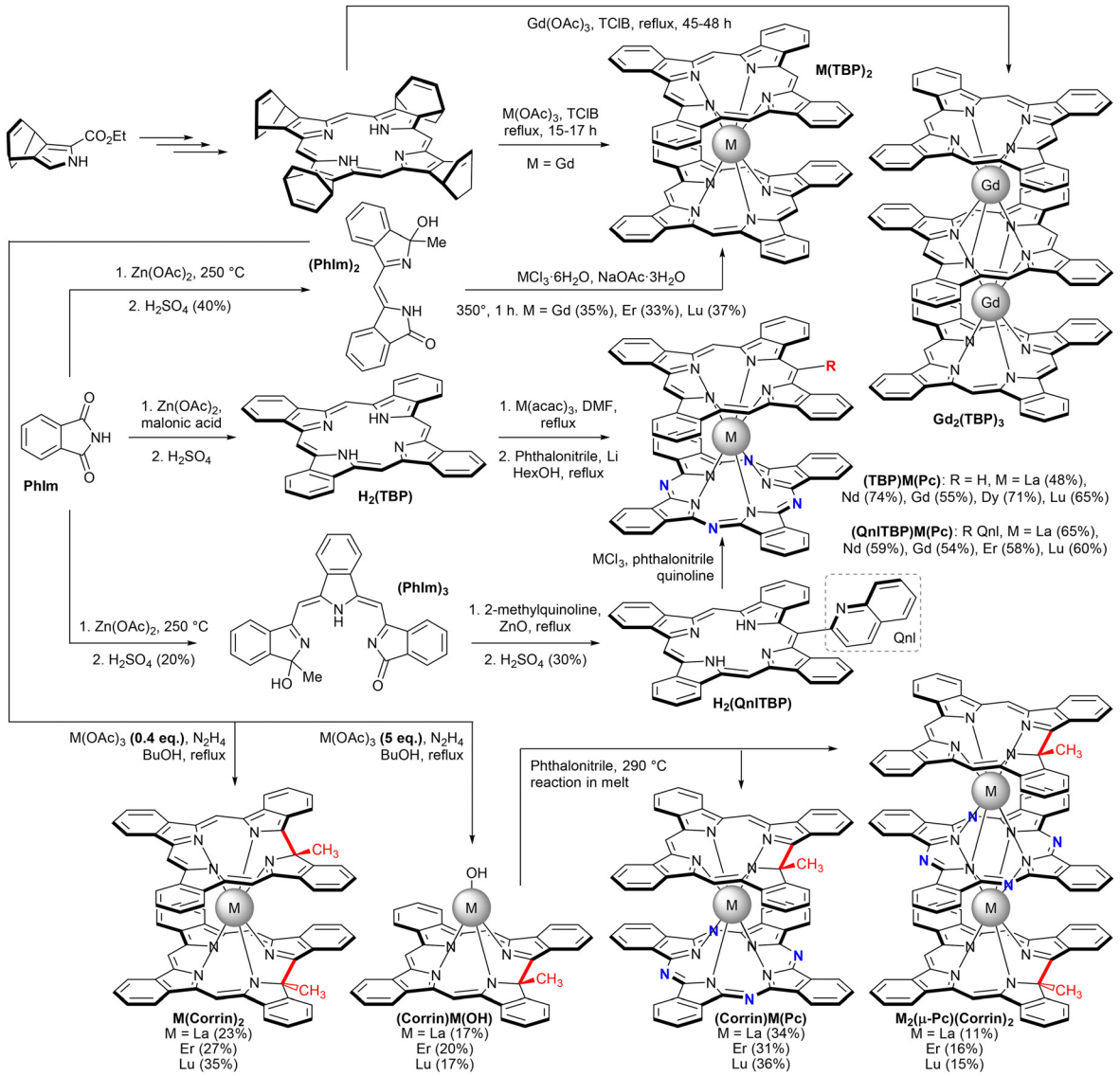

Scheme 28 Synthetic pathways to sandwich complexes with benzoporphyrin and corrin ligands.

(TBP)M(Pc) in 48–74% yields.[152] A similar strategy was applied to synthesize complexes starting from *tert*-butyl-substituted benzoporphyrin **H_2[(*t*Bu)$_4$TBP]**.[153]

Original strategy leading to homoleptic complexes **M(TBP)$_2$**, M = Gd, Er, and Lu, was proposed using a dipyrrolic precursor **(PhIm)$_2$** prepared from readily available phthalimide **PhIm**.[154] This procedure compares favourably with the time-consuming protocol using tetra(bicyclo[2.2.2])octadienoporphyrin due to the availability of starting compounds.

Application of acyclic olygopyrrolic precursors affords more options in the synthesis of various porphyrinoid derivatives. Condensation of 2-methylquinoline with a tripyrrolic compound **(PhIm)$_3$** prepared from phthalimide afforded *meso*-(quinolin-5-yl)tetrabenzoporphyrin **H_2(QnlTBP)** which was also used to synthesize mixed ligand complexes.[155] The aforementioned dipyrrolic compound **(PhIm)$_2$** can be dimerized in the presence of lanthanide acetates and hydrazine with the formation of complexes with the 1-tethyltetrabenzo-octadehydrocorrin ligand.[156] Depending on the ratio of reagents, either half-sandwiches or homoleptic double-decker complexes could be obtained. The reaction of the former complex with phthalonitrile can be used to synthesize phthalocyanine-corrin mixed ligand double- and triple-decker complexes.

2.4.3 Sandwich complexes with tetrabenzotriazaporphyrin ligands. The tetrabenzotriazporphyrin (TBTAP) ligands are intermediate macrocycles between classical porphyrins and phthalocyanines, possessing a permanent dipole moment, which may be responsible for the emergence of new properties. REE complexes with these ligands were reported by Pushkarev *et al.* on the examples of homo- and heteroleptic lutetium(III)[157,158] and europium(III) double-decker complexes which were synthesized by direct metalation of *meso*-phenyl-TBTAP macrocycle using lithium methoxide as a basic reagent (Scheme 29a). Apart from a homoleptic double-decker complex, small amount of

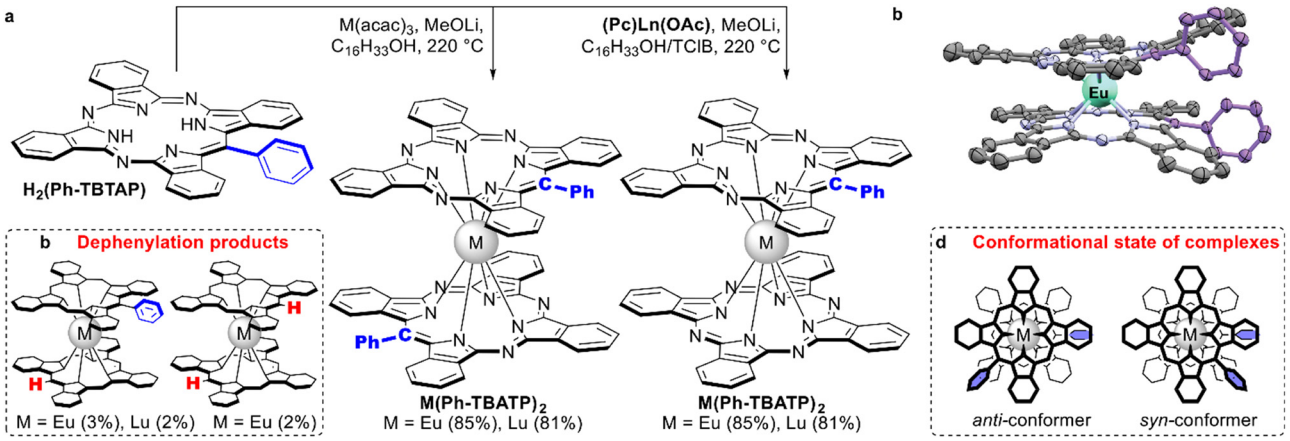

Scheme 29 (a) Synthesis of homo- and heteroleptic complexes with *meso*-phenyl-tetrabenzotriazaporphyrin, **H_2(Ph-TBTAP)**.[157,158] (b) Side products of dephenylation. (c) X-ray structure of the complex **Eu(Ph-TBTAP)$_2$** (CCDC ZUNJID).[158] Hydrogen atoms are not shown for clarity, *meso*-phenyl groups are highlighted with blue colour. (d) *Anti- vs. syn*-conformers of **M(Ph-TBTAP)$_2$** complexes.

triple-decker sandwich was isolated in the course of synthesis of **Eu(Ph-TBTAP)$_2$**, and moreover, prolonged heating of reaction mixtures resulted in partial dephenylation of TBTAP ligands (Scheme 29b), which was never observed previously in the chemistry of *meso*-aryl-substituted tetrapyrroles.

Comparison of UV-Vis spectra of **M(Pc)$_2$**, **(Ph-TBTAP)M(Pc)** and **M(Ph-TBTAP)$_2$** revealed that replacement of one or two *meso*-nitrogen atoms with C-Ph groups resulted in gradual perturbation of electronic systems, leading to complicated spectral patterns with split Q- and intervalence bands, which is not typical for symmetrical complexes. Electrochemical studies of new complexes evidenced that the introduction of two bulky phenyl rings has a profound effect on frontier orbital levels due to weakening of the intramolecular interaction between macrocyclic ligands.

Single-crystal X-ray characterization of **Eu(Ph-TBTAP)$_2$** showed that the molecule adapt *syn*-conformation (Scheme 29c and d), although conformational analysis performed by DFT calculations suggested that *anti*-form should be more stable and this form is observed as a sole state in solution according to NMR studies. Thus, a less stable conformer is formed in the solid state due to the advantage in energy of the molecular packing.

2.4.4 Sandwich complexes with corrole ligands. Corroles as ring-contracted porphyrinoids have been known since 1964; however, their fascinating properties were revealed mainly in the 1990s when straightforward synthetic procedures towards this class of macrocycles were proposed by the groups of Gross and Paolesse.[159,160]

First examples of REE complexes with corroles were synthesized only in 2013 by Buckley *et al.* either by metalation of tris-*meso*-aryl-corrole with M[N(SiMe$_3$)$_2$]$_3$, M = La and Tb or by the reaction of lithium corrolate with GdCl$_3$.[161] In both the cases half-sandwiches were isolated, where the coordination sphere of lanthanide ions was saturated with neutral ligands – dimethoxyethane or trimethyltriazanonane. A similar procedure was used to synthesize cerium complexes with corrole ligands and axial ligand-dependent self-assembling of the resulting half-sandwiches was studied.[162]

Mixed ligand complexes containing corroles and phthalocyanine ligands were synthesized by the reaction of pre-synthesized monophthalocyaninates with corroles in the presence of DBU in octanol (Scheme 30).[163–168] Several substituted macrocycles were introduced into this reaction, but invariantly on substituents and REE ions in all cases mixed ligand triple-deckers were isolated with inner Cor and terminal Pc ligands. Moreover, reaction of half-sandwich corrole complex with metal-free phthalocyanine and one-pot reaction of corrole, metal-free Pc and metal salts both yielded the identical triple-deckers and their yields were systematically larger than that when the first method was used.[166]

Some of the synthesized complexes were characterized by XRD revealing that in contrast to other symmetrical triple-deckers two outer phthalocyanine ligands were not staggered, and coordination polyhedra of two metal centres were slightly different, although in all cases they were close to distorted square prisms.[163,164,167] This distortion of coordination surrounding manifested in fast relaxation of magnetization because of QTM (the quantum tunnelling of the magnetisation; *cf.* Section 3.1), as evidenced from AC magnetic susceptibility measurements performed for dysprosium(III) complexes **Dy$_2$[(PentO)$_8$Pc]$_2$[(*p*-XPh)$_3$Cor]**, X = F or Cl.[164]

The presence of three protons in corroles suggests that the closed-shell form of triple-decker complexes should be anionic in nature, which makes them different from trisphthalocyaninates, where the charge of two trivalent REE ions is balanced by the charge of three dianionic ligands. Thus, to stabilize the negative charge of the $(M^{3+})_2(Cor^{3-})(Pc^{2-})_2$ species a counterion is needed. NMR studies of the europium(III) complex suggested that the charge is balanced by a proton, which is likely to be delocalized over the isoindoline nitrogen atoms of one of the phthalocyanine ligands.[163] Air oxidation of the protonated forms with the formation of paramagnetic complexes with delocalized π-electron was observed, which was followed by disappearance of NMR spectra and appearance of intervalence bands in UV-Vis-NIR spectra at *ca.* 2000 nm.[167]

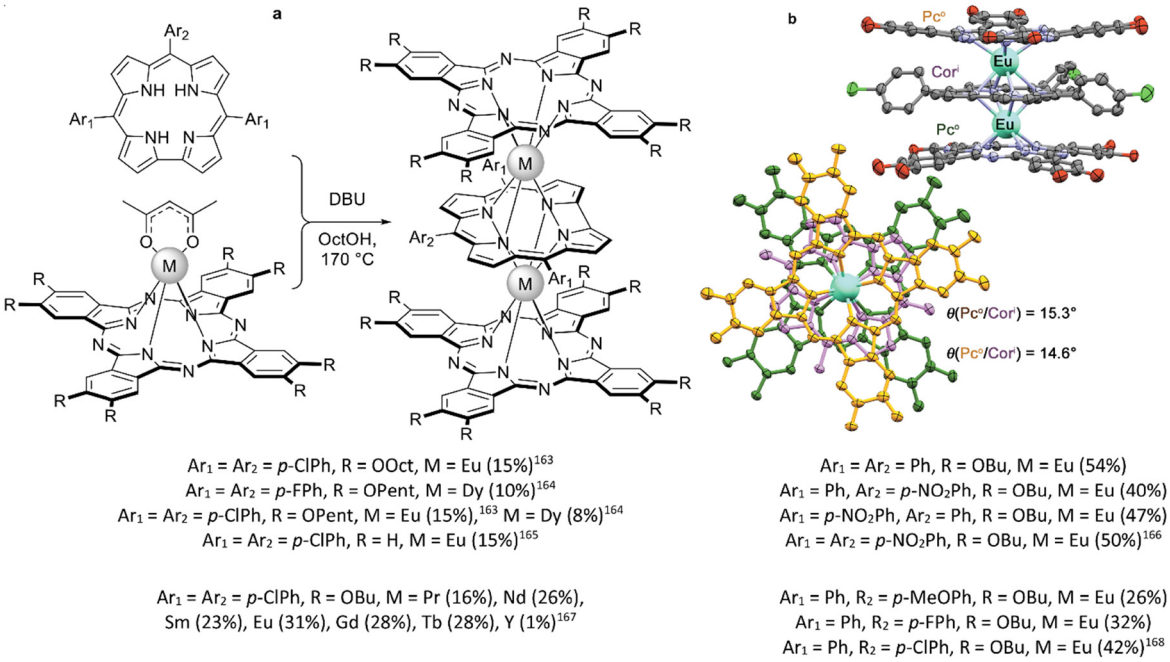

$Ar_1 = Ar_2 = p$-ClPh, R = OOct, M = Eu (15%)[163]
$Ar_1 = Ar_2 = p$-FPh, R = OPent, M = Dy (10%)[164]
$Ar_1 = Ar_2 = p$-ClPh, R = OPent, M = Eu (15%),[163] M = Dy (8%)[164]
$Ar_1 = Ar_2 = p$-ClPh, R = H, M = Eu (15%)[165]

$Ar_1 = Ar_2 = p$-ClPh, R = OBu, M = Pr (16%), Nd (26%), Sm (23%), Eu (31%), Gd (28%), Tb (28%), Y (1%)[167]

$Ar_1 = Ar_2$ = Ph, R = OBu, M = Eu (54%)
Ar_1 = Ph, $Ar_2 = p$-NO_2Ph, R = OBu, M = Eu (40%)
$Ar_1 = p$-NO_2Ph, Ar_2 = Ph, R = OBu, M = Eu (47%)
$Ar_1 = Ar_2 = p$-NO_2Ph, R = OBu, M = Eu (50%)[166]

Ar_1 = Ph, $R_2 = p$-MeOPh, R = OBu, M = Eu (26%)
Ar_1 = Ph, $R_2 = p$-FPh, R = OBu, M = Eu (32%)
Ar_1 = Ph, $R_2 = p$-ClPh, R = OBu, M = Eu (42%)[168]

Scheme 30 (a) Synthesis of mixed ligand complexes with phthalocyanine and corrole macrocycles. (b) X-ray structure of the complex **$Eu_2[(OctO)_8Pc]_2[(p\text{-ClPh})_3Cor]$** (CCDC HOKQOP).[163] Hydrogen atoms and substituents in top views are not shown for clarity.

Rich electrochemistry of studied complexes was demonstrated, and up to five oxidized states and three reduced states were observed rendering them as potential molecular materials for information storage devices.[163,166–168] The potentials of redox transitions could be finely tuned both by variation of metal centres and substituents in the *para*-positions of *meso*-phenyl groups, due to linear correlations between the sums of Hammett constants σ of these substituents and electrochemical characteristics of complexes.[168]

Comparative studies of self-assembling of two europium(III) complexes **$Eu_2(R_8Pc)_2[(p\text{-ClPh})_3Cor]$**, where R = H or octyl revealed that substituents in Pc ligands affected the morphology of aggregates formed by the phase transfer method upon mixing of solutions of complexes in chloroform with excess of methanol.[165] TEM and SEM studies of the resulting aggregates showed that the complex with unsubstituted Pc ligands forms nanobelts of 1.5–2.0 μm length and 100 nm width, while the octyloxy-substituted complex forms large scale sheet-like nanostructures with an average length of *ca.* 500 nm and a width of 300 nm. NLO studies of these complexes showed significant nonlinear reverse saturation absorption and self-defocusing behaviour.

Altogether, these results suggest that these corrole-containing mixed-ligand complexes can be considered as promising candidates for future nano-electronic and optical device applications.

2.4.5 Sandwich complexes with *N*-confused porphyrin ligands and heteroanalogues of porphyrins. Among core-modified derivatives of porphyrins special attention is paid to *N*-confused (or inverted, iPor) analogues with endocyclic CH and exocyclic NH groups. They have been known since the seminal work of Furuta *et al.* reported in 1994,[169] and these macrocycles found application in the construction of multinuclear assemblies due to their versatile binding modes.[170]

First REE sandwiches with *N*-confused porphyrins were synthesized in 2012 by Cao *et al.* on the examples of mixed ligand double-deckers of iPor-Pc type using the typical raise-by-one-story approach with monophthalocyaninate and metal-free *N*-confused porphyrin (Scheme 31a).[171] For the comparison of spectral properties, *N*-methylated iPor complex was also synthesized.

In 2014 cross-condensation of common and *N*-confused porphyrins with La(III) and Pr(III) acetylacetonates was reported, leading to heteroleptic double-decker complexes of Por-iPor type (Scheme 31b).[172] Homoleptic bisporphyrinates were isolated as side products, while formation of homoleptic complexes with *N*-confused ligands was not observed. Interestingly, heteroleptic complexes exhibited NIR band at *ca.* 850 nm, which was absent in homoleptic bisporphyrinates.

Another type of porphyrin core modification, namely replacement of one of pyrrolic nitrogen atoms with oxygen or sulphur was used for spectacular tuning of magnetic properties of mixed ligand double-deckers. This was demonstrated on the examples of dysprosium(III) complexes with phthalocyanine and oxa- or thiaporphyrin ligands **$[(t\text{BuPh})_4\text{XPor}]\text{Dy(Pc)}$**, X = O or S (Scheme 32).[173] It was demonstrated that although Dy–X bonds are longer than Dy–N bonds, the symmetries of coordination polyhedra did not change upon going from classical porphyrin to its oxa- and thia-analogues. However, the replacement of one of heteroatoms significantly enhanced the anisotropy of the Dy(III) ion providing the complex with one of the

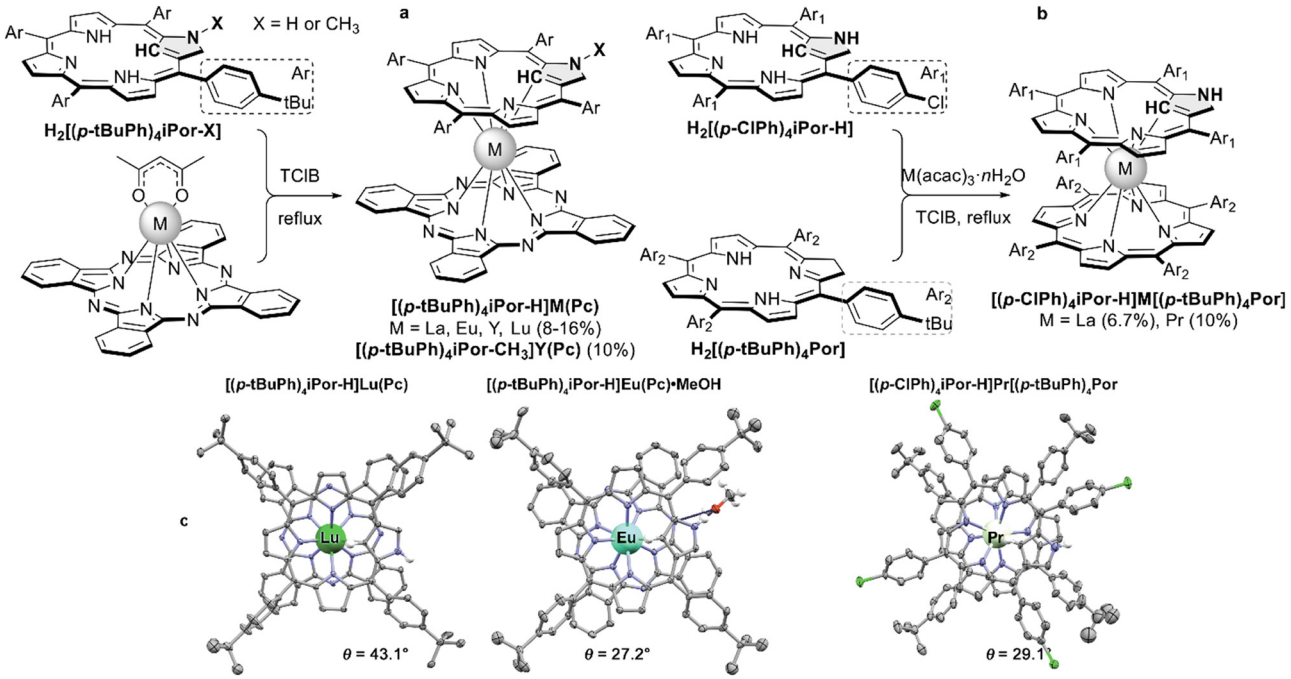

Scheme 31 (a and b) Synthesis of heteroligand double-decker complexes with *N*-confused ligands. (c) X-ray structures of **[(*t*BuPh)$_4$iPorH]Lu(Pc)** (CCDC YEFZIU), **[(*t*BuPh)$_4$iPorH]Eu(Pc)·MeOH** (CCDC YEFZAM)[171] and **[(*p*-ClPh)$_4$iPorH]Pr[(*t*BuPh)$_4$Por]** (CCDC BODFIL).[172] Solvate molecules and most of hydrogen atoms are not shown for clarity.

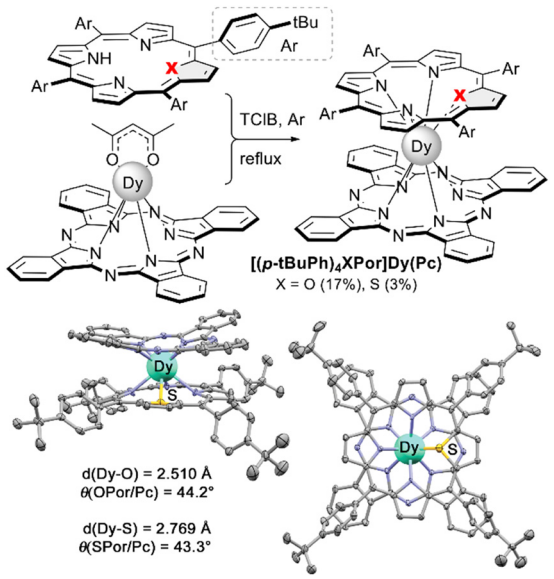

Scheme 32 Synthesis of mixed ligand double-decker complexes with oxa- and thiaporphyrin ligands and X-ray structure of **[(*t*BuPh)$_4$SPor]-Dy(Pc)** (CCDC AHOPUK).[173] Hydrogen atoms and solvent molecules are not shown for clarity.

largest barriers ever reported for dysprosium(III) complexes with tetrapyrrolic ligands (*cf.* Section 3.2.2).

2.5 Complexes based on half-sandwiches with axially coordinated non-tetrapyrrolic ligands

Due to large coordination numbers of REE ions, their half-sandwich complexes tend to have labile coordination spheres. This phenomenon is at the heart of the raise-by-one-story approach leading to the aforementioned heteroleptic and mixed ligand sandwiches, but it is possible to combine ligands of completely different natures in a molecule as part of this approach.

Thus, the present section will include sandwich REE complexes, where porphyrin or phthalocyanine ligands coexist with ligands of non-tetrapyrrolic nature. Although they only resemble sandwich structures of archetypal double- and triple-decker complexes, we included them in this section due to the increasing interest in such type of objects providing pathways to novel fluorescent materials, optical limiters, molecular magnets, *etc.* Finally, some of the structures are curious by themselves, broadening the rich coordination chemistry of both REE and tetrapyrrolic macrocycles.

2.5.1 Sandwich complexes with Schiff bases axially coordinated to REE monophthalocyaninates. Starting from 2013 the scope of sandwich-type tetrapyrrole-based rare-earth molecular materials was extended by monophthalocyaninates with axially-coordinated Schiff base (SB) ligands. The summary of the reaction studied on the example of the ligand, based on *o*-phenylenediamine and methoxy-substituted salicylic aldehyde, **H$_2$(SB)** is given in Scheme 33.

First examples of such complexes were prepared by Wang *et al.* from **(Pc)M(acac)**, M = Dy and Y and **H$_2$(SB)**.[174] Depending on the base used for deprotonation of **H$_2$(SB)** complexes of different nuclearities were obtained. Performing this reaction with $Ca(OH)_2$ afforded a quadruple-decker complex where the $[Ca(MeOH)_2]^{2+}$ group bridged two **(Pc)M(SB)**$^-$ units (Scheme 33a), while dinuclear double-deckers **(Pc)M[(SB)K(MeOH)]** was isolated in the

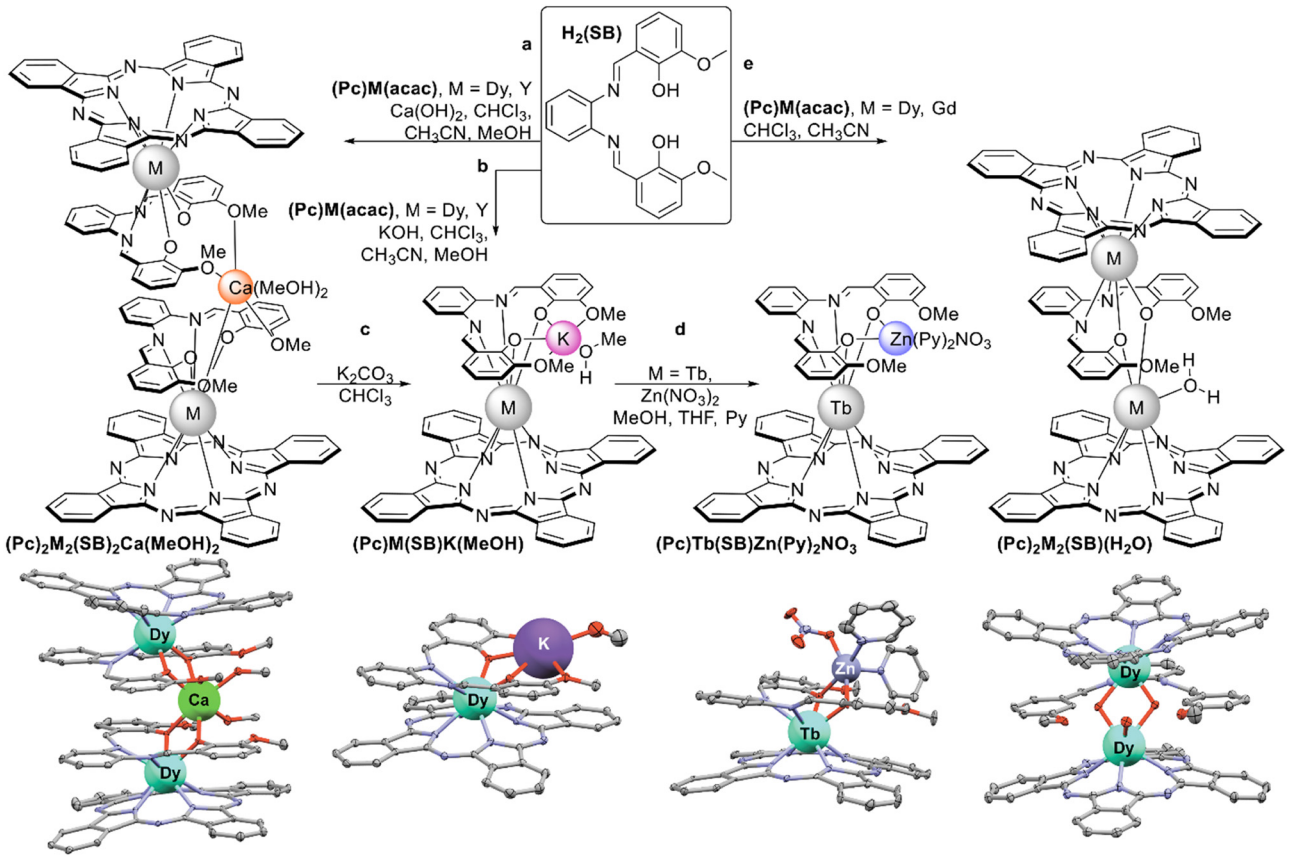

Scheme 33 Synthesis of mixed-ligand complexes based on half-sandwich phthalocyaninates and Schiff base **H_2(SB)** with X-ray structures of the corresponding complexes – from the left to the right: **(Pc)$_2$Dy$_2$(SB)$_2$Ca(MeOH)$_2$** (CCDC FEVDOB),[174] **(Pc)Dy(SB)K(MeOH)** (CCDC FEVDUH),[174] **(Pc)Tb(SB)Zn(Py)$_2$NO$_3$** (CCDC YIMMUE)[175] and **(Pc)$_2$Dy$_2$(CB)(H$_2$O)** (CCDC XILTOD).[176]

presence of KOH (Scheme 33b). The latter complex dissociated with the formation of double-decker species upon treatment with K_2CO_3 (Scheme 33c). Fast QTM relaxation was observed in zero-field AC magnetic susceptibility measurements for dysprosium(III) complexes of both types, although long-distance magnetic interactions between two paramagnetic centres in quadruple-decker complex was detected (*cf.* Section 3.2.2).

Later, Ma *et al.* synthesized terbium(III) complexes with all alkali metal cations **[(SB)M(MeOH)]Tb(Pc)**, M = Li^+ to Cs^+ and the possibility to exchange these cations with the Zn^{2+} ion was demonstrated (Scheme 33d), providing an interesting example of polyfunctional complex with tuneable properties.[175]

Slow diffusion of the acetonitrile solution of **H_2(SB)** into the solution of **(Pc)M(acac)**, M = Gd and Dy, in chloroform afforded another type of triple-decker complex with bridging **$(SB)^{2-}$** unit and chemically non-equivalent REE ions – **M$_2$(Pc)$_2$(SB)(H$_2$O)** (Scheme 33e).[176] One of metal centres was in octahedral surrounding and another one was hepta-coordinated by four isoindole nitrogen atoms of **$(Pc)^{2-}$**, two oxygen atoms of a Schiff-base ligand, and one oxygen atom of water molecule. Homoleptic binuclear dysprosium(III) complex with the **H_2(SB)** ligand had the same binding mode; however, incorporation of the phthalocyanine ligand had a profound effect on SMM properties of the mixed-ligand sandwich in comparison with **Dy$_2$(SB)$_3$(H$_2$O)** in terms of ferromagnetic coupling between paramagnetic ions and energy barrier, U_{eff}.

Analogous binuclear complexes were synthesized by Li *et al.* based on a family of chiral ligand prepared by the condensation of 1,2-diphenylethylenediamine and 5-chlorosalicylic aldehyde. Photophysical characterization of such complexes showed their potential in future nonlinear optical applications such as wavelength conversion and optical switching.[177,178]

By varying the ratio of half-sandwich phthalocyaninate and Schiff base, complexes with different stoichiometries of ligands can be obtained. This was shown by Gao *et al.* on the example of the reaction between one equivalent of dysprosium(III) phthalocyaninate and two equivalents of tetrathiafulvalene-fused Schiff base **H_2(SB-TTF)** yielding a binuclear complex **Dy$_2$(Pc)(SB-TTF)$_2$(MeOH)** (Scheme 34a).[179] Due to the intrinsic dipole moment, this complex could be absorbed on the surface of HOPG either in Pc-up or S-TTF-up fashion depending on the applied potential, which was demonstrated by scanning tunneling microscopy at the single molecule level, rendering this compound as a component of functional materials fabricated by self-assembly.

Gao *et al.* used dysprosium(III) or erbium(III) monophthalocyaninates generated *in situ* as templates for condensation of 2,6-diformyl-4-methylphenol and 1,3-diaminopropane to form

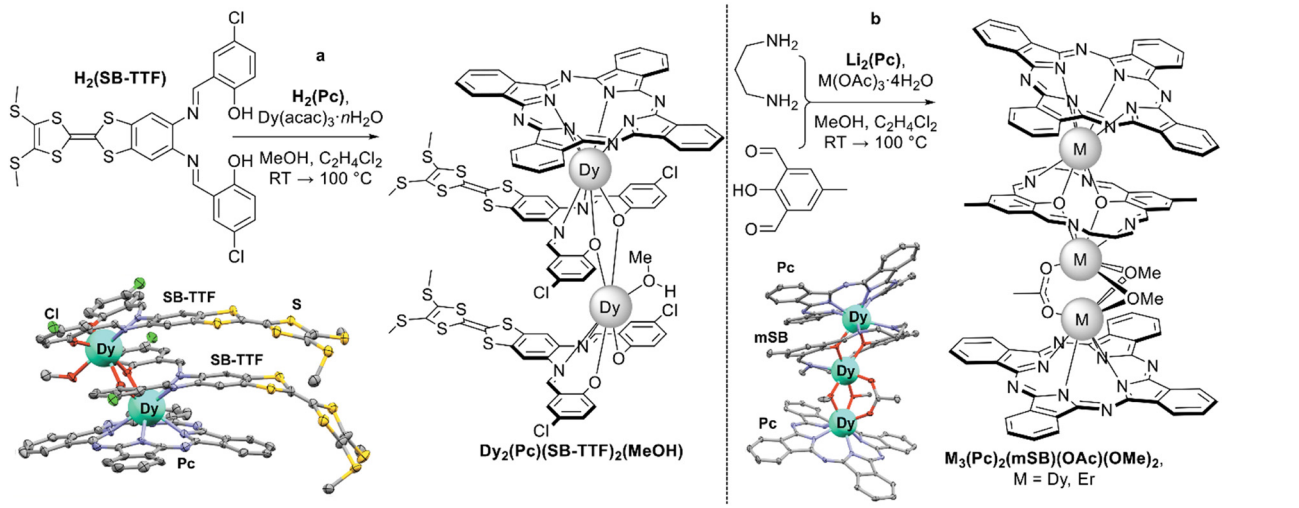

Scheme 34 (a) Synthesis of a mixed-ligand complex with tetrathiafulvalene-fused Schiff base with the X-ray structure of complex **$Dy_2(Pc)(SB\text{-}TTF)_2(MeOH)$** (CCDC WONKIV).[179] (b) Synthesis of sandwiches based on closed-macrocyclic Schiff base and REE monophthalocyaninates with the X-ray structure of complex **$Dy_3(Pc)_2(mSB)(OMe)_2$** (CCDC IKAQAO, only one of two crystallographically independent molecules is shown).[180] Hydrogen atoms are omitted for clarity.

unusual trinuclear triple-decker sandwiches with a macrocyclic Schiff ligand and bridging acetate and methoxide counterions **$M_3(Pc)_2(mS)(OAc)(OMe)_2$** (Scheme 34b).[180] Interestingly, in the crystal lattice these complexes existed as pairs of symmetrically unrelated molecules with slightly different symmetries of coordination polyhedra. This feature resulted in multiple magnetic relaxation modes found by AC magnetic susceptibility measurements of the dysprosium(III) complex. Pronounced intramolecular interactions between proximal metal centres was observed – ferromagnetic in the case of dysprosium and antiferromagnetic in the case of erbium (*cf.* Section 3.2.2).

2.5.2 Monoporphyrinato- and monophthalocyaninato-complexes with axially coordinated cyclic ligands. Sandwiches formed by heavy lanthanide monoporphyrinates[181] and monophthalocyaninates[182] with cyclen ligands coordinated to metal centres were reported by Santria and Kizaki *et al.* These complexes with well-defined coordination spheres of metal ions were synthesized by simple reactions of **(TPP)MCl** or **(Pc)MCl**, M = Tb–Yb and Y with excess of cyclen in methanol or THF, respectively (Scheme 35), and single crystals of all complexes were characterized by XRD to show that outer-sphere chloride anions do not bind to metal ions, thus, they adapt a tetragonal SAP symmetry of coordination polyhedra formed solely by pairs of N_4 ligands. The smooth changes of structural parameters of both families of complexes depending on the ionic radii of M^{3+} were demonstrated.

Ground multiplet states of a series of porphyrin complexes **$[(TPP)M(Cyclen)]^+Cl^-$** were determined by NMR and magnetic susceptibility data together with CASSCF calculations, giving insight into their electronic structures.[183] Intramolecular magnetic interactions between localized 4f-electronic systems and photoexcited Por or Pc π-systems in terbium(III) Por/cyclen and Pc/cyclen complexes was studied by variable-temperature variable-field magnetic circular dichroism spectroscopy

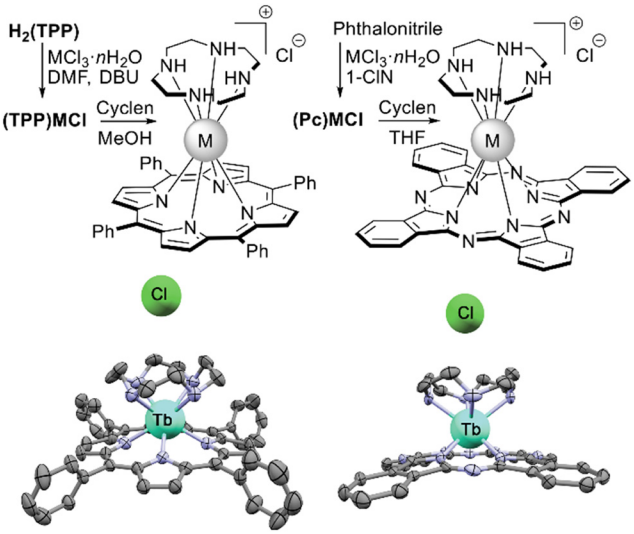

Scheme 35 Synthesis of REE porphyrinates and phthalocyaninates with axially-coordinated cyclen ligands with X-ray structures of **$[(TPP)Tb(Cyclen)]^+Cl^-$** (CCDC LEBMUD) and **$[(Pc)Tb(Cyclen)]^+Cl^-$** (CCDC WENBID).[181,182] Hydrogen atoms are omitted for clarity.

providing experimental data to validate the theoretical models describing such interactions.[184,185]

Interesting sandwich complexes with η^5-Cp and η^5-Me_5Cp ligands sitting-atop scandium(III) phthalocyaninate were synthesized from **(Pc)ScCl** by Platel *et al.* (Scheme 36).[186] As a first step of this work, template condensation of phthalonitrile in the presence of $ScCl_3$ in ClN was performed, yielding inseparable mixture of target **(Pc)ScCl** with *ca.* 15% of unreacted $ScCl_3$. Treatment of this mixture with $LiCH(TMS)_2$ in THF afforded the formation of a soluble binuclear complex **$(Pc)ScCl_2Li(THF)_2$** which could be crystallized as an individual compound. Its reaction with NaCp or LiCp* in THF provided

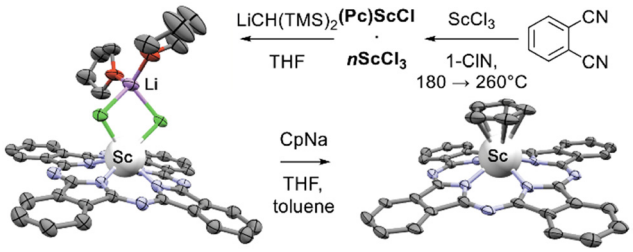

Scheme 36 Synthesis of scandium phthalocyaninates – **(Pc)ScCl$_2$Li(THF)$_2$** (CCDC DUDTED) and **(Pc)Sc(Cp)** (CCDC DUDTIH).[186] Hydrogen atoms are omitted for clarity.

(Pc)Sc(Cp) and **(Pc)Sc(Cp*)**, respectively, as first representatives of metallophthalocyanine-ocenes.

Another class of macrocyclic ligands which was recently introduced into sandwich REE chemistry is hemiporphyrazin, Hp. Synthesis of this 20π-electron antiaromatic relative of azaporphyrins was reported for the first time in 1952 by Elvidge and Linstead.[187] However, REE complexes with Hp were reported for the first time only in 2017.[188] The complexes **(HHp)M(Pc)**, M = Eu, Lu, were obtained by Liu *et al.* using reactions of the corresponding **(Pc)M(acac)** with **H$_2$(Hp)** and DBU in refluxing pentanol. Metalation of hemiporpyrazine with M(acac)$_3$·*n*H$_2$O under the same conditions yielded double-decker complex **(HHp)M(Hp)**. ESR and NMR studies of the resulting sandwiches evidenced that they were diamagnetic in contrast to most bisphthalocyaninates existing as free radicals. The proton needed for such state was localized by NMR spectroscopy, XRD and quantum-chemical calculations – all methods evidenced that the proton is bound to the pyridine nitrogen atom. Quantum-chemical calculations of shielding surfaces of both types of complexes revealed that in homoleptic complexes hemiporphyrazine ligands retained their antiaromatic nature; however, combination of antiaromatic Hp and aromatic Pc species provided molecules with overall aromatic behaviour.

XRD characterization of both types of Hp complexes revealed nearly ideal SAP surrounding of metal centres, although somewhat distorted because of the protonation of one of the pyridine groups. Nevertheless, measurements of magnetic properties of **(HHp)Dy(Pc)** and **(HHp)Dy(Hp)** revealed excellent SMM properties (*cf.* Section 3.2.2).

2.5.3 Heteronuclear complexes with metalloligands. Half-sandwich porphyrinates and phthalocyaninates were used to form heteronuclear complexes with metalloligands. For example, in 2013 Gao *et al.* reported solvothermal one-pot reactions of metal-free **H$_2$(TPP)** or **H$_2$(Pc)** with Gd(III), Tb(III), Dy(III) and Ho(III) acetylacetonates, and sodium salt of Kläui's, **Na[(η^5-Cp)Co{P(=O)(OEt)$_2$}$_3$]**.[190] These reactions yielded seven-coordinate complexes with axial tripodal ligands (Scheme 38a and b). Tb(III) and Dy(III) complexes showed field-induced slow relaxation of magnetization; these complexes were convenient models demonstrating the correlation between the magnetic relaxation properties and subtle distortions of the coordination geometry of the paramagnetic lanthanide ions (*cf.* Section 3.2.2).

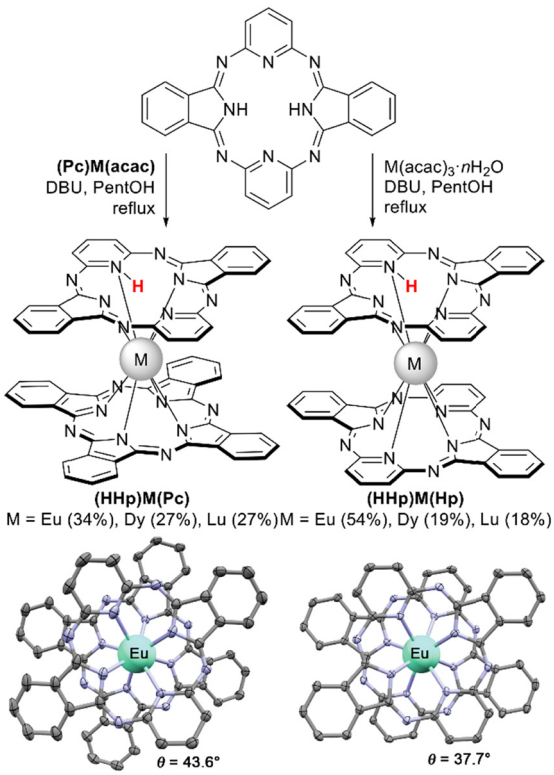

Scheme 37 Synthesis of complexes with hemiporphyrazine ligand[188,189] and X-ray structures of **(HHp)Eu(Pc)** (CCDC GAWCAL) and **(HHp)Eu(Hp)** (CCDC GAVXUZ).[188] Hydrogen atoms are omitted for clarity.

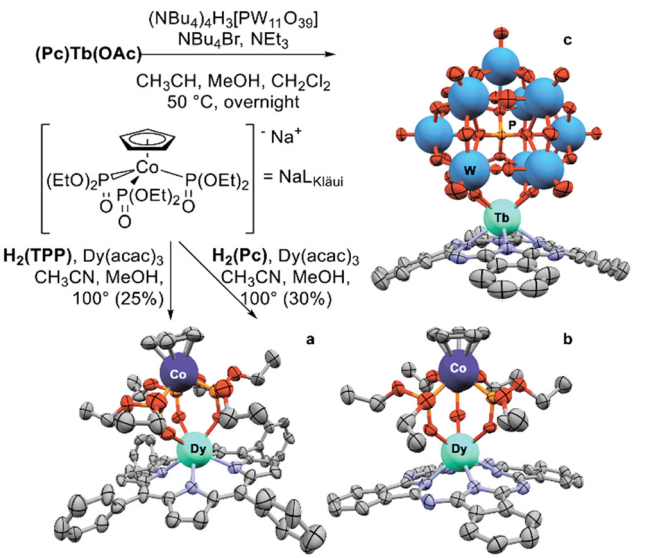

Scheme 38 Synthesis of heteronuclear complexes based on REE half-sandwiches. (a and b) Synthesis of Dy(III) porphyrinate (CCDC LIMDOC) and phthalocyaninate (CCDC LIMCUH) with a Kläui ligand. (c) Synthesis of Tb(III) phthalocyaninate bearing a polyoxotungstate ligand **(Pc)M-(PW$_{11}$O$_{39}$)$^{6-}$(NBu$_4^+$)$_6$** (CCDC GUZFOZ), and the X-ray structure of anionic part of the complex **(Pc)Tb[PW$_{11}$O$_{39}$]$^{6-}$**. Solvate molecules, hydrogen atoms and counterions are omitted for clarity.

Later, half-sandwich Yb(III) with porphyrin derivatives and axial Kläui's ligands attracted great interest as highly near-IR emissive complexes with unprecedented quantum yields up to 63%,[191] which contributes to the design of molecular probes for near-IR imaging.[192]

In 2020 Sarwar *et al.* reported the synthesis of Tb(III), Dy(III) and Y(III) phthalocyaninates with a monolacunary α-Keggin polyoxotungstate ligand $[P^{V}W^{VI}_{11}O_{39}]^{7-}$.[193] With this aim, the corresponding monophthalocyaninates **(Pc)M(OAc)** reacted with $(NBu_4)_4H_3[PW_{11}O_{39}]$ in the presence of triethylamine and NBu_4Br under mild conditions, yielding anionic complexes with tetrabutylammonium counterions **(Pc)M-$(PW_{11}O_{39})^{6-}$-$(NBu_4^+)_6$** (Scheme 38c). Their characterisation included high resolution mass spectrometry, synchrotron-based single-crystal X-ray diffraction and magnetic studies revealing slow relaxation of the magnetisation for the Dy(III) derivate (*cf.* Section 3.2.2).

2.5.4 Inverted sandwich complexes. Final class of complexes in the following section – inverted sandwiches do not refer to sandwich complexes in the common sense, since they contain only one phthalocyanine ligand as a bridge between two $M(dpm)_2^+$ groups, where dpm^- – dipivaloylmethanate anion. The term "inverted" refers to the fact that one macrocycle is sandwiched between two REE ions, as opposed to the conventional sandwiching of metal ions between two macrocycles.

Thus, these complexes were reported for the first time in 1983 in a short communication by Sugimoto *et al.*, describing the reaction between **Li_2(Pc)** and $M(dpm)_3$ in refluxing THF under anaerobic conditions.[194] This reaction afforded a series of **(μ-Pc)[M(dpm)$_2$]$_2$**, where M = Sm to Yb and Y. The X-ray structure of the samarium(III) complex with benzene solvate molecules was determined (Fig. 8), showing the extremely rare representative of binuclear complexes formed by a single tetrapyrrolic macrocycle. A bit later magnetic properties of these unique complexes were studied by Maeda *et al.*, showing the first evidence of intramolecular spin–spin exchange interaction between trivalent REE ions.[195,196] However, for many years that followed, these complexes attracted no attention.

Only in 2014 detailed characterization of magnetic properties of **(μ-Pc)[M(dpm)$_2$]$_2$**, M = Tb and Dy, was performed by Tsuchiya *et al.*, showing their striking difference from common binuclear triple-deckers.[197] Unexpectedly, antiferromagnetic interaction between metal centres was found in contrast to ferromagnetic coupling in the corresponding trisphthalocyaninates. NMR studies showed that aromatic proton resonances were shifted down-field – again, it was in sharp contrast with **M_2(Pc)$_3$** with large up-field lanthanide-induced shifts. These intriguing results were explained assuming the ligand field potential of the inverted-sandwich complexes gave strong easy-plain-type magnetic anisotropy, where the J_z value of the lowest sublevel has a small value, while trisphthalocyaninates have a strong easy-axis-type magnetic anisotropy. The benzene solvates **(μ-Pc)[M(dpm)$_2$]$_2$·2C_6H_6** showed interesting behaviour with respect to desolvation and exchange of solvation molecules to dichloromethane, affording the pathway for fine tuning of magnetic properties (*cf.* Section 3.6).[198–200]

Interesting properties of inverted sandwiches could encourage synthetic studies to broaden this class of REE complexes; however, to date, only dpm ligands could stabilize their unusual architecture. To the best of our knowledge, the sole reported attempt to exchange these anions was made by Ge *et al.* when the complex **(μ-Pc)[Dy(dpm)$_2$]$_2$** was treated with 3-methoxy- or 3-ethoxysalicyllic aldehydes **H(LR)**, R = OMe, OEt.[201] However, it resulted in the deterioration of the inverted sandwich scaffold with the formation of a new type of triple-deckers **(μ-LR)$_2$Dy$_2$(Pc)$_2$(H_2O)** where two **(DyPc)$^+$** units were bridged by a pair of coplanar deprotonated **LR$^-$** ligands (Scheme 39a). Although at the first glance both complexes had similar structures invariant to substituents in bridging ligands, their magnetic properties were markedly different. Magnetic studies indicated that the MeO-substituted complex behaved as a zero-field single-molecule magnet with a higher energy barrier, while EtO-substituted complex exhibited a fast tunneling relaxation process (*cf.* Section 3.2.2). Detailed analysis of the XRD data revealed that one of MeO-groups

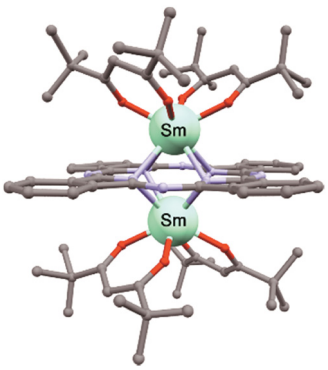

Fig. 8 X-ray structure of **(μ-Pc)[Sm(dpm)$_2$]$_2$** (CCDC CALWIV).[194] Solvate molecules and hydrogen atoms are not shown.

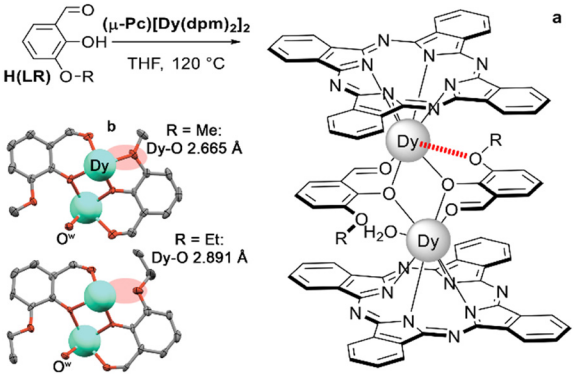

Scheme 39 (a) Transformation of inverted sandwich **(μ-Pc)[Dy(dpm)$_2$]$_2$** into a triple-decker mixed ligand complex **(μ-LR)$_2$Dy$_2$(Pc)$_2$(H_2O)** upon interaction with 3-alkoxysalicylic aldehydes, **H(LR)**, R = OMe, OEr. (b) Structure of the middle layers formed by deprotonated ligands **LR$^-$**, coordinated to dysprosium ions (CCDC MESMIJ, R = Me and MESMOP, R = Et).[201]

coordinated to dysprosium(III) ion, while oxygen atoms of both ethoxy-groups remained in the non-coordination mode (Scheme 39b). This difference in the substitution of ligands in the middle layer leads to perturbation of the main magnetic axes, consequently changing the coupling interaction and modulating the magnetic behaviour for this Dy2 system.

2.6 Sandwich complexes that go beyond triple-deckers

Simple electrostatic considerations suggest that triple-deckers formed by doubly-deprotonated porphyrins and phthalocyanines with a pair of trivalent REE cations are the largest possible electroneutral species. However, there is interest in larger sandwiches, which can fill in the gap between discrete double-/triple-decker complexes and infinite lattices formed by these complexes in solid functional materials. The following section will describe some approaches which were developed over the last decade to obtain discrete multideckers, avoiding electrostatic limitations.

2.6.1 Discrete sandwiches containing from four to six decks bridged through REE(III) and Cd(II) metal centres. From the electrostatic viewpoint electroneutral trisphthalocyaninates can be considered as complexes formed by anionic double-deckers $[M(Pc)_2]^-$ and cationic half-sandwiches. Thus, binding of two $[M(Pc)_2]^-$ species with an appropriate divalent cation could be used as a pathway to a quadruple-decker complex. In 2010 this idea was realized by Fukuda *et al.* on the example of the reaction between $\mathbf{[Lu(Pc)_2]^-(NBu)_4}$ and cadmium acetate (Scheme 40a).[202] Heating of solid reagents at 400 °C followed by chromatographic separation afforded 3.4% of a quadruple-decker complex **(Pc)Lu(Pc)Cd(Pc)Lu(Pc)**, which was characterized by elemental analysis, mass-spectrometry and NMR spectroscopy. The complex underwent eight reversible one-electron redox-processes – four oxidation reactions and four reduction reactions, while the parent lutetium bisphthalocyaninate showed only two oxidation reactions and three reduction reactions in the same potential range; moreover, in this case the gap between first reduction and oxidation potentials was wider than in the case of a quadruple-decker complex, revealing the stacking effect which stabilized the redox forms of the extended complex. Spectroelectrochemical studies also revealed exceptionally low-lying π–π* excited states of the oxidized form of a quadruple-decker complex – the corresponding absorbance bands appeared at *ca.* 1000 cm^{-1}, where normally only finger-print vibration bands are observed in IR spectra.[203] These experimental observations were interpreted using molecular orbital calculations.[204]

Both stability and yields of quadriphthalocyaninates could be improved when electron-rich BuO-substituted ligands were used instead of unsubstituted phthalocyaninates. Thus, Wang *et al.* showed that the reaction of neutral $\mathbf{Dy[(BuO)_8Pc]_2}$ with $Cd(OAc)_2{\cdot}2H_2O$ in refluxing TClB afforded target substituted quadruple-decker complex $\mathbf{Dy_2Cd[(BuO)_8Pc]_4}$ in yield as high as 43% (Scheme 40b).[205] In a similar manner, Eu(III) complex with *n*-hexylthio-substituents $\mathbf{Eu_2Cd[(HexS)_8Pc]_4}$ was synthesized starting from the corresponding double-decker in 84% yield (Scheme 40c).[206] Both the OFET and gas sensing properties were studied on the self-assembled film of the latter complex (*cf.* Section 4).

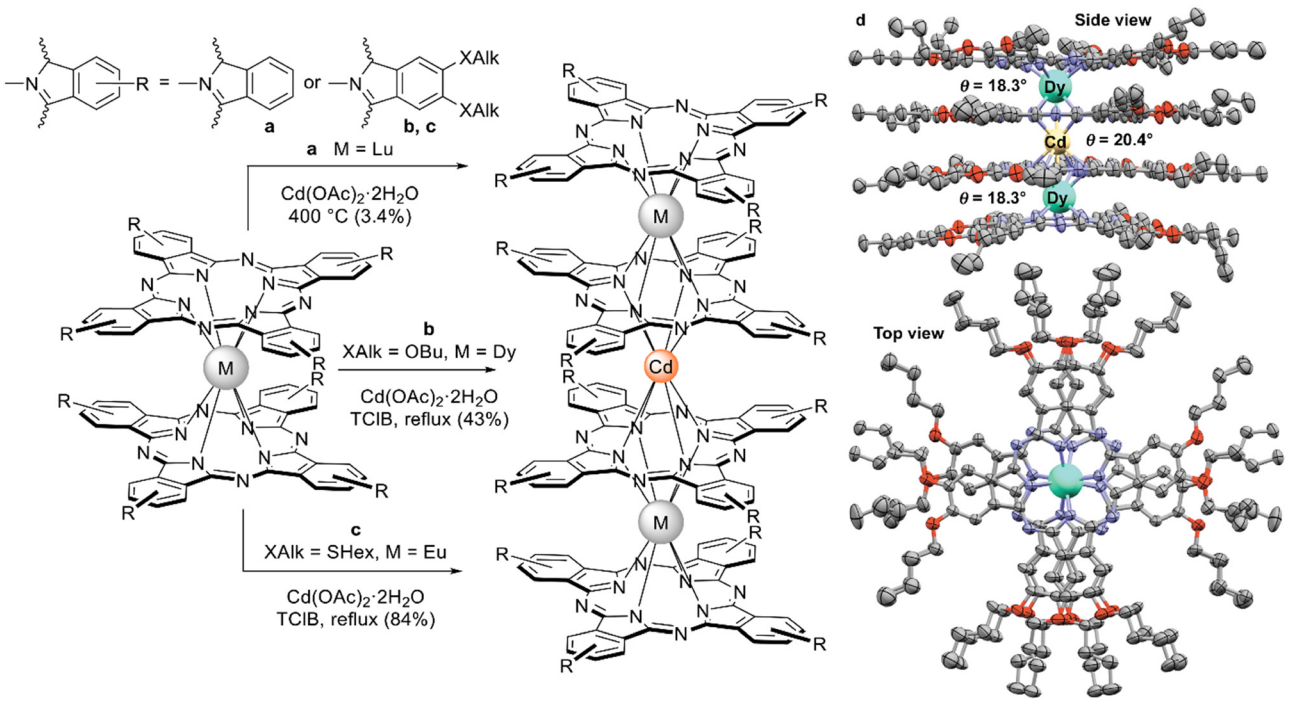

Scheme 40 (a–c) Synthesis of discrete quadruple-decker complexes $\mathbf{Lu_2Cd(Pc)_4}$,[202] $\mathbf{Dy_2Cd[(BuO)_8Pc]_4}$,[205] and $\mathbf{Eu_2Cd[(HexS)_8Pc]_4}$[206] *via* connection of two double-decker molecules with Cd(II) ions. (c) Structure of complex $\mathbf{Dy_2Cd[(BuO)_8Pc]_4}$ (CCDC IYOCIJ),[205] the structure of only one of two crystallographically independent molecules is shown, hydrogen atoms and solvent molecules are omitted.

Single crystals of the Dy(III) complex were obtained by Wang *et al.*, and XRD provided a first ultimate proof of a quadruple-decker structure (Scheme 40d).[205] Separation between Dy(III) ions – *ca.* 6.65 Å was expectedly much larger than in triple-decker complexes; however, it was still enough to detect notable intramolecular interaction between paramagnetic metal centres, which was responsible for the fast quantum tunnelling of magnetization in a zero DC field (*cf.* Section 3.2.4). Interestingly, introduction of alkoxy and alkylthio groups provided complexes with different conformations. In the case of the BuO-substituted complex both Dy(III) and Cd(II) metal centres were in distorted prismatic surrounding with a twist angle of *ca.* 20°,[205] while in HexS-substituted complex Eu(III) and Cd(II) had lightly deviated SAP coordination geometries with twist angles of *ca.* 43 and 39°.[206]

The capability of cadmium bridge to connect pairs of different double-deckers was tested by Wang *et al.* on the example of homoleptic bisphthalocyaninates **M(Pc)$_2$** and mixed-ligand complexes **(TClPP)M(Pc)**, M = Eu and Y.[207] In principle, this reaction could lead to isomeric quadruple-decker complexes with different sequences of tetrapyrrols – Pc–Pc–Pc–Por or Pc–Pc–Por–Pc, but both NMR and X-ray crystallography showed that only one type of complex with terminal porphyrin ligand was formed. The complexes were isolated in 9–14% yields. Similarly to homoleptic quadriphthalocyaninates, the synthesized mixed-ligand complex had rich electrochemistry associated with four ligand-centred oxidation and three reduction processes, whose potentials showed dependence on the metal centre.

No surprise, extended sandwiches became attractive objects to study long-distance interactions between paramagnetic metal ions in the context of elaboration of SMM materials and understand mechanisms or magnetization relaxation. Thus, the approach to quadriple-deckers was extended to even higher sandwiches. Wang *et al.* showed that reactions of **M[(BuO)$_8$Pc]$_2$** with one or two equivalents of **H$_2$[(BuO)$_8$Pc]** and Cd(OAc)$_2$·2H$_2$O allowed the introduction of one or two additional phthalocyanine layers between REE-containing moieties, affording therefore quintuple- and sextuple-decker sandwiches (Scheme 41).[208,209] Moreover, this strategy allowed the synthesis of heteroleptic quintuple-decker sandwiches with precise sequences of unsubstituted and octa-pentyloxy-substituted ligands – either Pc–Pc–Pc*–Pc–Pc or Pc–Pc*–Pc*–Pc*–Pc.[210] Single-crystal XRD studies of complexes evidenced of smooth elongation of distances between REE ions going from triple- to sextuple-deckers, providing more objects for studies of long-range magnetic interactions (*cf.* Section 3.2.4).[211–214]

In principle, this approach can be used to obtain multi-decker complexes with any number of tetrapyrrolic ligands, since further sequential addition of "CdPc" fragments does not violate the electroneutrality requirement in the resulting extended sandwiches. However, the problems with isolation of required multi-decker from the mixture of complexes are highly likely to arise.

2.6.2 Sandwich complexes based on fused dimeric tetrapyrrols. Synthesis of binuclear fused phthalocyanines **[f-Pc$_2$]** sharing common benzene rings was reported for the first time by Kobayashi *et al.* in 1994 *via* the cross-condensation of diiminoisoindolines derived from phthalonitriles and pyromellitic tetranitriles.[215] Almost 20 years later Wang *et al.* recognized *f*-Pc ligand as a convenient scaffold to form biradical sandwich complexes which can be used to clarify the role of radicals in 2p–4f integrated systems and study the magnetic properties of polynuclear systems (*cf.* Section 3.3.2).[216]

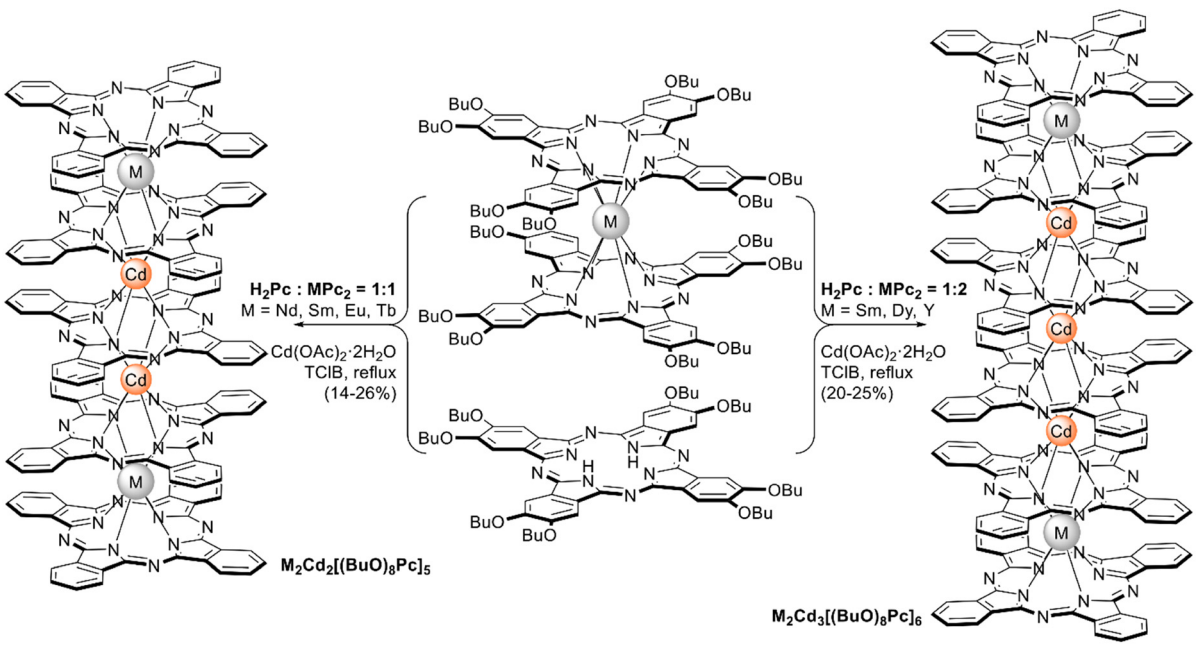

Scheme 41 Synthesis of discrete quintuple-decker complexes **M$_2$Cd$_2$(Pc)$_5$**[208] and sextuple-decker complexes **M$_2$Cd$_3$[(BuO)$_8$Pc]$_6$**.[209] Butoxy-groups in resulting multi-deckers are not shown.

Thus, in 2013 Wang *et al.* showed that Y(III)- or Dy(III)-templated cross-condensation of bis(diiminoisoindoline) with 4,5-dibutoxyphthalonitrile in refluxing pentanol in the presence of DBU furnished target fused bisphthalocyaninates **(Pc)M[f-Pc$_2$]M(Pc)^{OBu}** in 2.0–4.3% yields (Scheme 42a).[216] In the same manner Tb(III) complex was synthesized by Morita *et al.* in 2.5% yield using hexanol as a solvent for template condensation.[217] Using 4,5-di(ethylthio)phthalonitrile in this procedure allowed Wei *et al.* to increase the yield of the fused bisphthalocyaninate **(Pc)M[f-Pc$_2$]M(Pc)^{SEt}** to 24.8% (Scheme 42b).[218]

Fused complexes with higher nuclearity could be synthesized using variants of the raise-by-one-story approach. Thus, Motita and Katoh *et al.* treated metal-free BuO-substituted fused phthalocyanine **H$_4$[f-Pc$_2$]^{OBu}** with double-deckers and Tb(III) or Dy(III) acetylacetonates in TClB to synthesize tetranuclear Tb(III)[219] and Dy(III)[220] complexes **(Pc)$_2$M$_2$-[f-Pc$_2$]M$_2$(Pc)$_2^{OBu}$** (Scheme 42c). Alternatively, Wei *et al.* treated SEt-substituted fused Eu(III) bisphthalocyaninate with **H$_2$[(SEt)$_8$Pc]** and Eu(acac)$_3$ to synthesize tri- and tetranuclear complexes **(Pc)M[f-Pc$_2$]M$_2$(Pc)$_2^{SEt}$** and **(Pc)$_2$M$_2$[f-Pc$_2$]M$_2$(Pc)$_2^{SEt}$** which could be separated by chromatography (Scheme 42d).[218] In all cases the yields of isolated complexes were relatively small, yet, it was enough to characterize their properties and demonstrate their applicability.

Fused bi-, tri- and tetranuclear substituted complexes were used as redox-active components in sensors to NO_2 and NH_3 revealing excellent sensitivity to these gasses.[218,221] The film formed by the tetranuclear SEt-substituted complex was one of the best gas sensors obtained so far for all solution-processed organic semiconductor films in dry air at room temperature.[218] Binuclear SEt-substituted complex was also used as a component of an electrochemical sensor for simultaneous detection of acetaminophen and ascorbic acid.[222] SHex-substituted tetranuclear complex was found to form well-defined single crystal microsheets upon self-assembling in solution, which were used to fabricate OFET with high hole and electron mobilities of 18 and 0.3 $cm^2\ V^{-1}\ s^{-1}$, respectively, representing the best result for phthalocyanine-based OFETs at that time (*cf.* Section 4).[223]

A unique example of fused bisporphyrinate synthesized from β-β/*meso*–*meso*/β-β triply-linked diporphyrin **H$_4$[f-Por$_2$]** was reported by Lee *et al.* in 2019.[224] Starting ligand was treated with LiHMDS to generate a tetralithium intermediate which reacted with half-sandwiches **(TPP)M(acac)** to furnish fused sandwiches **(TPP)M[f-Por$_2$]M(TPP)**, M = Tb and Y in small yields (Scheme 43). Complexes were isolated in neutral states exhibiting an open shell biradical character, as determined from magnetic susceptibility measurements and theoretical calculations. The Tb(III) complex exhibited rich electrochemistry, having more than eight clear peaks in the voltammetry curves;

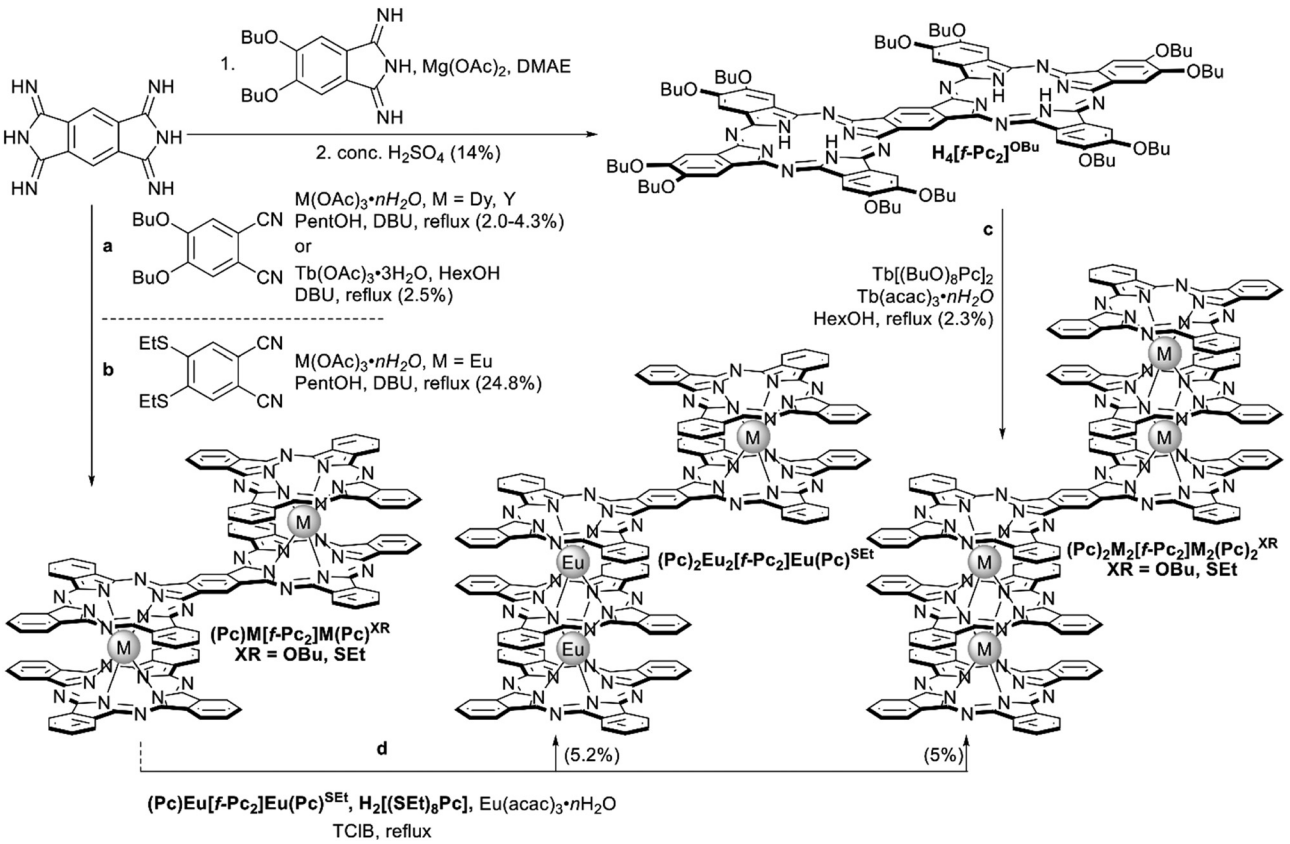

Scheme 42 Synthesis of fused sandwich phthalocyaninates. (a and b) Binuclear complexes **(Pc)M[f-Pc$_2$]M(Pc)^{XR}**, XR = OBu or SEt. (c) Tetranuclear complexes **(Pc)$_2$M$_2$[f-Pc$_2$]M$_2$(Pc)$_2^{OBu}$**. (d) Tri- and tetranuclear complexes **(Pc)$_2$M$_2$[f-Pc$_2$]M(Pc)^{SEt}** and **(Pc)$_2$M$_2$[f-Pc$_2$]M$_2$(Pc)$_2^{SEt}$**. Superscripts ^{OBu} and ^{SEt} indicate that all accessible peripheral positions of the benzene rings contain the corresponding substituents.

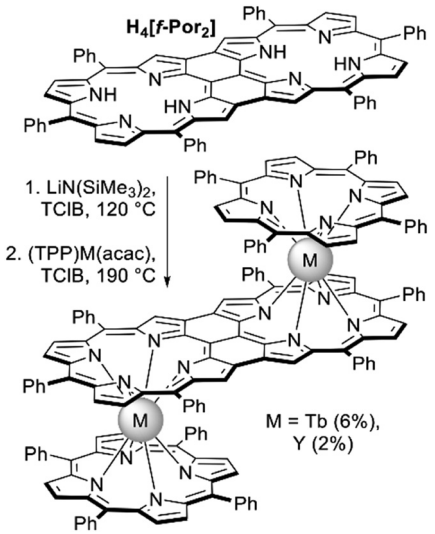

Scheme 43 Synthesis of fused sandwich bisporphyrinates **(TPP)M[f-Por$_2$]M(TPP)**.[224]

moreover, it has a very small HOMO–LUMO energy gap as evidenced from optical (3700 nm, 0.33 eV) and electrochemical measurements (3400 nm, 0.36 eV). These features together with high stability render these biradicals as promising candidates for use in molecular electronics, optics, and spintronics.

3. Development of the functionalities of sandwich tetrapyrrole rare-earth single-molecule magnets

In this section, we will provide a comprehensive survey of several types of sandwich tetrapyrrole rare-earth (RE) single-molecule magnets (SMMs) that use a supramolecular approach, combined with a discussion of their functionalities. Importantly, the properties of these molecules are changed significantly by the formation of associations among such molecules. The chemical and physical properties of molecular assemblies composed of a finite number of molecules are also affected by various intermolecular interactions. Currently, researchers are also conducting studies on applying self-assembly strategies that actively apply coordination bonds to molecular magnetic materials. In 2002, Wernsdorfer *et al.* reported that the introduction of hydrogen bonds and van der Waals forces into a tetranuclear Mn complex SMM (abbreviated as **[Mn$_4$O$_3$Cl$_4$(O$_2$CEt)$_3$(py)$_3$] = Mn$_4$**) resulted in dimers of the type **Mn$_4$···Mn$_4$**, which exhibit superexchange interactions and suppress the quantum tunnelling of magnetisation (QTM; *cf.* Section 3.1).[225] This phenomenon was achieved *via* the superexchange interaction between the SMMs, which act as an exchange bias ($H_{bias} \approx \pm M_2 J/g\mu_B$) on the QTM that occurs at a zero magnetic field, resulting in a spin-sublevel energy mismatch. Thus, the magnetic interaction acts as a perturbation between the SMMs that affects the QTM that occurs at a near-zero magnetic field. In other words, it is also possible to control the properties of SMMs using intra/intermolecular magnetic interactions between SMMs. Moreover, to control the magnetic interactions between SMMs, it is possible to use not only hydrogen bonds but also π–π interactions, CH–π interactions, and inclusion (host–guest) interactions associated with ion and molecular recognition. Controlling the spin relaxation time (τ) by utilizing the interactions between the infinite number of intramolecular vibrational modes of SMMs and spin excitation is essential for spintronics. SMMs (molecular crystal) have weak intermolecular interaction and low phonon energy in the acoustic mode. Therefore, the spin-acoustic mode interaction is restricted. On the other hand, by introducing a strong intermolecular interaction into the SMMs, the phonon energy in the acoustic mode can be increased, and interaction with the spin can be expected. In other words, from the viewpoint of controlling magnetic relaxation, the approach of introducing a molecular assembly structure into SMMs is one method (*vide infra*).

Furthermore, ligand modifications, protonation–deprotonation reactions, and redox reactions also cause dramatic changes in SMM characteristics by inducing substantial changes in their coordination environments. Sandwich tetrapyrrole rare-earth-type SMMs have attracted attention for potential use in the fields of spintronic devices and/or quantum technology (QT). However, the performance of these devices depends on the nature of the ground-state electronic structures of the SMM units. By using supramolecular approaches to prepare sandwich tetrapyrrole rare-earth-type SMMs, their ground-state electronic structures and functionality can potentially be controlled (Fig. 9).

3.1 Brief outline of single-molecule magnets

In 1993, Sessoli, Gatteschi, and co-workers reported that the cluster **[Mn$_{12}$O$_{12}$(AcO)$_{16}$(H$_2$O)$_4$]·2AcOH** with $S = 10$ (henceforth abbreviated as **Mn$_{12}$**; Fig. 10a), which contains twelve Mn ions (eight Mn^{3+} with $S = 2$ and four Mn^{4+} with $S = 3/2$), exhibited superparamagnetic properties; they referred to **Mn$_{12}$** as an SMM because it exhibited both single molecule properties and ferromagnetic properties (Fig. 10c).[226,227] However, REE-type SMMs are fundamentally different from transition-metal (TM) SMMs, because their SMM behaviour originates from the f electrons (Fig. 10b). Since the orbital angular momentum L does not disappear for f electrons, ground-state multiplets exhibit a total angular momentum J due to spin–orbit coupling (SOC). When the ground-state multiplet is placed in a ligand field (LF) environment, the degeneracy splits into the $2J + 1$ sublevels (Fig. 10d). As a result, double-well potentials form, and SMM behaviour emerges (*vide infra*).[36,226] In general, the sublevel splitting in REE-type SMMs (10^2–10^3 cm^{-1})[5] is much larger than that of TM-type SMMs (*ca.* 70 cm^{-1}),[228] indicating that REE-type SMMs are more useful in terms of their SMM characteristics, such as large magnetic anisotropy and U_{eff} (Fig. 10c and d).[229,230]

In the last 20 years, SMMs with high operating temperature have been synthesized by controlling the LF and/or crystal field (CF) around the metal ion, even in single-ion magnets (SIMs).[234] Since the **Mn$_{12}$** cluster complex has been shown to

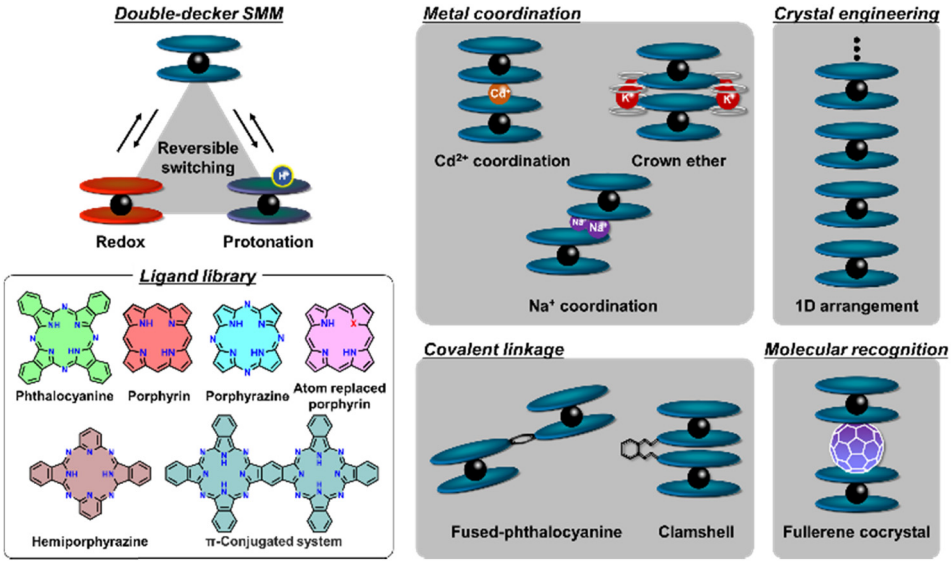

Fig. 9 Brief overview of rare-earth sandwich tetrapyrrole SMMs. Double-decker complexes with various kinds of porphyrinoids act as SMMs. The magnetic properties of the double-decker SMMs can be reversibly tuned by redox reactions and protonation–deprotonation reactions. Various approaches for connecting/arranging SMMs have been used to introduce Ln–Ln interactions and tune the coordination environment.

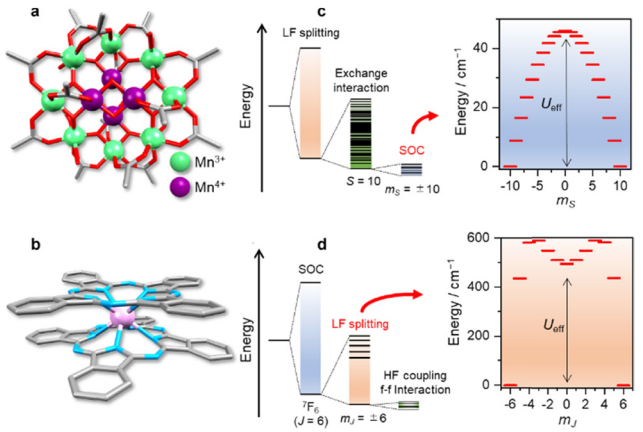

Fig. 10 Molecular structures of (a) **Mn_{12}** and (b) **$Tb(Pc)_2$** based on the cif files from ref. 231 and 232. Schematic energy diagrams of (c) **Mn_{12}** and (d) **$Tb(Pc)_2$**. In the case of **Mn_{12}**, eight Mn^{3+} and four Mn^{4+} ions with d-orbital splitting (LF splitting) couple with each other (exchange interactions) to form an $S = 10$ state. The L of Mn^{3+} and Mn^{4+} is quenched due to the large LF splitting. The zero-field splitting ($D = -0.46$ cm^{-1}) of $S = 10$, which mainly originates from second-order SOC, results in a U_{eff} of *ca.* 40 cm^{-1} for spin reversal between $m_S = +10$ and $m_S = -10$. In the case of **$Tb(Pc)_2$**, $S = 3$ and $L = 3$ couple with each other (first-order SOC) to form $^7F_6$. LF splitting of the Tb^{3+} centre results in a U_{eff} of *ca.* 400 cm^{-1} for spin reversal between $m_J = +6$ and $m_J = -6$. m_J *vs.* energy plots were constructed from ref. 233.

exhibit the SMM phenomena, 3d to 5f metal complexes have been investigated as SMMs (henceforth, the term SMM will be used to refer to SIMs as well).[228,230,235–244] SMMs have a fixed number of metal ions and an ordered magnetic ion structure, and exhibit uniaxial magnetic anisotropy due to the introduction of an LF and SOC.[226,227,229,245] A brief description of magnetic anisotropy is given here. When a magnetic material is magnetised in various directions, there are directions in which it is easy to magnetise (easy axis of magnetisation) and difficult to magnetise (hard axis of magnetisation). When the direction is in one direction (uniaxial), it is called "uniaxial magnetic anisotropy". This magnetic anisotropy is caused by the orientation of magnetic moments of the atoms which have the CF and SOC that make up the magnetic material. That is, the stable direction of orbital angular momentum in the crystal affects the direction of spin, which is the source of magnetism. As described later, the 4f orbital shape of rare earth metal ions has a very strong directivity, so it is possible to control the magnetic anisotropy by controlling the appropriate CF (*cf.* Section 3.2). A characteristic of **Mn_{12}** is that the Jahn-Teller axis of Mn^{3+} ions with magnetic anisotropy is almost parallel to the S_4 axis, showing large uniaxial magnetic anisotropy as a single molecule.[226] It is possible to control the magnetic properties of metal complexes, such as their electronic state, LF, and magnetic anisotropy, by changing the metal ions and coordinating ligands. In particular, it has been shown that the LF directly affects the magnetic properties. Classical magnets exhibit large magnetisation *via* three-dimensional interactions among the electron spins of the metal ions, but SMMs involve the uniaxial magnetic anisotropy of one molecule. It is thought that SMMs are also "single-domain magnets", as intermolecular magnetic interactions are ignored.

Using the effective spin Hamiltonian, we discuss the uniaxial magnetic anisotropy and U_{eff} in SMMs. The concept of effective spin Hamiltonian $(\hat{\mathcal{H}})$ was introduced by M. H. L. Pryce which has only the spin operator being considered. When incorporating the CF and SO into the effective spin Hamiltonian, it can be expressed by D (uniaxial crystal field constant) and E (biaxial crystal field constant). Here, the spin Hamiltonian is given by $\hat{\mathcal{H}} = D\hat{S}_z^2$ with the D. In the absence of an

external DC magnetic field (H = 0; H and H_{dc} are used interchangeably), the Zeeman term goes to zero, so Dm_S^2 (m_S is the z-component of S) is the splitting energy at zero magnetic field (zero-field splitting, ZFS). For the reasons mentioned above, the splitting width of the ground and highest energy levels is defined as $U_{eff} = |D|S^2$ for TM-type SMMs, where the D value is the "zero-field splitting constant" and the S is the spin quantum number of the ground state, which mainly originates from second-order SOC (the U_{eff} of REE-type SMMs is explained in the next section). For SMMs, the degeneracy of the total spin state S_{total} is split into $2S + 1$ by LF and SOC, a quantized double-well potential is formed by the uniaxial magnetic anisotropy, and the spin inversion between spin-up and spin-downstate caused by the spin sublevel shows Arrhenius-like relaxation ($\tau = \tau_0 \exp(U_{eff}/T)$, Fig. 10c). Here, τ represents the magnetic relaxation time, τ_0 is the frequency factor, U_{eff} is the energy barrier associated with spin inversion, and T is the temperature. At temperatures higher than U_{eff} associated with spin inversion, the SMM behaves as a paramagnetic material, but when the temperature decreases and the U_{eff} cannot be overcome, the magnetic moment (spin) is frozen. The temperature at which the τ reaches 100 s is defined as the blocking temperature (T_B). SMMs behave like a magnet which shows magnetic hysteresis with coercivity (H_C) below T_B due to long τ values. In addition, the field cooled (FC) and zero-field cooled (ZFC) measurements of the SMM diverge at T_B. The magnitude of magnetic anisotropy is possible to estimate from the M *versus* HT^{-1} plot at different T values. If SMMs have large uniaxial magnetic anisotropies and/or the population of low-lying excited states, M *versus* HT^{-1} shows non-superposed magnetisation curves.

The temperature change in the spin system reaches thermal equilibrium through heat exchange between the spin and the lattice, and finally moves to the heat bath. Therefore, the information for slow magnetic relaxation can be obtained from alternating current (AC) magnetic measurements. The measurement data are analyzed by using a generalized Debye model containing the dispersion coefficient α. It is possible to estimate values of τ. The magnetic relaxation undergoes a single relaxation process at α = 0, a Cole–Cole plot (χ'' *versus* χ' plot) is semicircular.[246] In addition, magnetic relaxation is a phenomenon associated with spin–phonon coupling, in which the lattice vibration of the molecular crystal is mainly dominated by intramolecular vibration. SMMs undergo three types of magnetic relaxation processes due to spin–lattice interactions, *i.e.*, (1) direct, (2) Raman, and (3) Orbach processes.[247] The direct process is caused by the absorption or emission of a phonon ($\hbar\omega$), while the Raman process is due to phonon scattering between the ground state and the virtual transition to higher energy levels.[248–250] Numerical simulation of the T dependence of τ is carry out using a combination of the magnetic relaxation processes.[247,251,252]

Furthermore, at extremely low temperatures (*e.g.* 40 mK), spin inversion *via* QTM occurs due to the quantum tunneling effect when the energies of the spin sublevels are equal, and the steps in the magnetic hysteresis curves (M *versus* H) are observed using a micro-SQUID (Fig. 12c).[227,245,253] The origin of QTM in SMMs can be understood *via* an energy level diagram for a system with a tunnelling gap (ΔE_{tunnel}) by the hyperfine (hf) interaction between the electronic spin and the nuclear spin I. QTM is complicated due to the interactions of the ground state with the I, which cause energy level crossing (Fig. 12b).[253–255] It is possible to explain QTM using the Landau–Zener–Stückelberg (LZS) model to the ground state $\pm m_S$ levels.[245] Quantum phenomena, such as the QTM observed in SMMs, have been studied in relation to the field of quantum logic (*e.g.*, quantum spin coherence,[256] quantum phase transition,[257] Berry phase interference,[258] and quantum computers[259]). Interest in the use of molecules as spin qubits is growing rapidly, and several perspective articles and reviews focusing on such molecules have been published recently.[260–263] Using SMMs in information storage devices would allow memory capacity to be expanded quite dramatically. Thus, the development of multi-functional SMMs can be expected to continue for several years to come.[264] In addition, single-crystal X-ray diffraction analysis and/or theoretical calculations (DFT and *ab initio*; *e.g.* CASSCF/RASSI-SO/SINGLE_ANISO calculations)[265] for the structure optimisation and the ground state are the most effective methods for investigating the coordination environment of Ln^{3+} ions in SMMs. Additionally, electron spin resonance (ESR), nuclear magnetic resonance (NMR), inelastic neutron scattering, and muon spin relaxation (μSR) are useful in the investigation of the SMM phenomena.[245] It is possible to evaluate the SMM characteristics by using a variety of measurements together with magnetic measurements. Thus, the field of molecular magnetism, which includes SMMs, has been extensively studied recently in physics and nanotechnology contexts, particularly in the areas of molecular spintronics and quantum technology (QT) (Fig. 11).[266]

For more information, several books and reviews suggested by the authors are included in the reference. In particular, D. Gatteschi, R. Sessoli and J. Villain have published a groundbreaking book on SMMs in 2006, which covers everything from basic principles of physical phenomena to measurement techniques.[245]

3.2 Brief overview of rare-earth sandwich tetrapyrrole single-molecule magnets

Phthalocyanines feature prominently in diverse research fields, including molecular conductors, solar cells, liquid crystals, pharmaceuticals, and biological chemistry,[271,272] as they are highly soluble in several organic solvents, chemically stable and robust, as well as commercially available.[273–275] In addition, in recent years, tetrapyrrole has attracted attention as a ligand for SMMs.[9,36]

In order to identify an underlying cause for SMM properties, we review the coordination environment and SMM properties of **Ln(Pc)$_2$** with a D_{4d} symmetry. The LF potential around a Tb^{3+} ion ($^7F_6$) with a total angular momentum (J) of 6 splits the ground-state multiplet so that the lowest sublevel has the largest z-component of J ($m_J = \pm 6$) and a large energy gap (*ca.* 400 cm^{-1}) to the next-closest sublevel ($m_J = \pm 5$), which is correlated with U_{eff} (Fig. 10d).[36] In 2003, Ishikawa *et al.* first

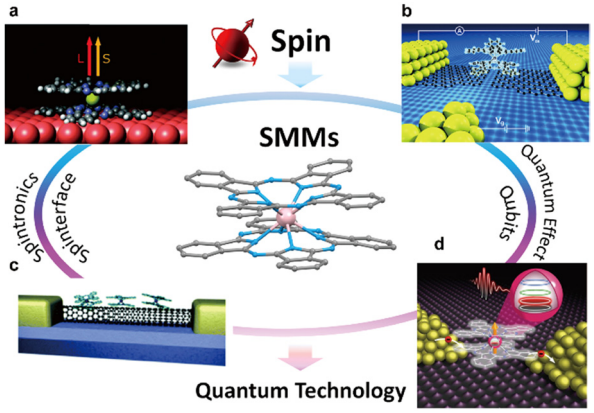

Fig. 11 Quantum technology actively using SMMs. Rare-earth sandwich tetrapyrrole SMMs (**Tb(Pc)$_2$**) have excellent chemical and physical stability, which make it possible to use them in quantum devices. Reprinted with permission from (a) ref. 267. Copyright 2010, American Chemical Society. Reprinted from (b) ref. 268. Copyright 2016, Royal Society of Chemistry. Reprinted from (c) ref. 269. Copyright 2011, MDPI. Reprinted with permission from (d) ref. 270. Copyright 2014, American Association for the Advancement of Science.

reported the SMM properties of **(NBu$_4^+$)[Tb(Pc)$_2$]$^-$**, which contains a single rare-earth 4f ion (U_{eff} = 230 cm^{-1}; τ_0 = 6.25 × 10^{-8} s; H_C ≈ 0.01 T@0.04 K).[36,276] For the neutral (one-electron-oxidized) species **Tb(Pc)$_2^0$** with an unpaired π-radical (S = 1/2) on the Pc ligands, the U_{eff} is 410 cm^{-1}.[277] In comparison to **(NBu$_4^+$)[Tb(Pc)$_2$]$^-$** and **Tb(Pc)$_2^0$**, the cationic species **Tb[(EtO)$_8$Pc]$_2^+$** has a much larger U_{eff} (550 cm^{-1}).[84] The cationic species has a shorter interligand distance than the neutral and anionic ones because the electrons are removed from antibonding molecular orbitals.[84] In addition, structural changes in **Tb[(BuO)$_8$Pc]$_2^+$** are induced by oxidation from its neutral/anionic species, whereby the interligand distance decreases upon oxidation (*cf.* Section 3.4).[278] Thus, LF contractions cause strong LF splitting, which directly affects the U_{eff} value. This result quantified LF contractions in the cationic species. Later, the group of complexes that exhibits SMM characteristics with a mononuclear d/f metal ion also became known as single-ion magnets (SIMs). In particular, **Ln(Pc)$_2$**-based SMMs are attractive complexes that can be developed using various approaches, because it is possible to control the distance between the Ln^{3+} ions, the coordination environment, and the electronic state by chemically modifying the Pc ligands.[3,4,279] It should be mentioned here that the relationship between the magnitude of the LF splittings and the U_{eff} is not straightforward. In case of **Tb(Pc)$_2$**, the U_{eff} coincides with the energy difference between ground m_J = ±6 and 1st excited m_J = ±5 states (Fig. 10d). The reason why the magnetic relaxations *via* 2nd or higher LF level as seen in **Mn$_{12}$** do not occur in the series of **Tb(Pc)$_2$** remains unclear to date. However, recent research studies on the SMMs indicate the importance of the vibrations of atoms and molecules in the crystalline lattice.[248,280,281] For instance, SMMs with a high U_{eff} (1541 cm^{-1}) and record T_B value (80 K) were reported by Guo *et al.* in 2018, which was achieved by modifying the vibrational modes upon ligand modification of the [Dy(Cp)$_2$]$^+$ (Cp = cyclopentadienyl) complex.[234,282,283] The high U_{eff} of this complex originates from the Orbach process *via* 4th excited LF levels, meaning that those *via* lower excited states are effectively suppressed. The control of the coupling between spin and vibrations is therefore extremely important for achieving high-performance SMMs.

There have been many attempts, both experimental and theoretical, to elucidate the relationship between coordination geometry and LF parameters, which have a great influence on the ground-state multiplet structure and magnetic anisotropy (*cf.* Sections 3.2.1 and 3.2.2).[229] Contractions of square antiprismatic (SAP) coordination environments affect the LF of Ln^{3+} ions, thus bringing about highly significant changes in the SMM properties.[36,84,233,242,252,276,284–287] In general, the LF (or CF) parameter in the Hamiltonian is defined as follows:

$$\hat{H}_{LF} = \sum_{k=2}^{6} \sum_{q=-k}^{k} B_k^q \hat{O}_k^q,$$

where B_k^q is the LF parameter and $\hat{O}_k^q$ is the Stevens operator.[288–291] There are noticeable differences in SMM properties due to the presence or absence of particular off-diagonal LF terms (B_k^q, k = 2, 4, 6; $q \neq 0$), which are the non-axial LF parameters. As a specific example, it has been reported that the LF parameters of the square prismatic (SP) coordination structure with D_{4h} symmetry and those of the ideal SAP coordination structure with D_{4d} symmetry are different. In the SAP geometry, only the axial anisotropy LF parameters occur (B_k^q, k = 2, 4, 6; q = 0).[252,276,284,288,291–293] On the other hand, the SP geometry contributes not only to the axial LF parameters, but also to the transverse anisotropy LF parameters B_4^4 and B_6^4. In the case of **[Tb(Pc)$_2$]$^-$**, the LF parameters (B_k^q/cm^{-1}) are as follows: real geometry (B_2^0 = 414, B_4^0 = −228, B_6^0 = 33, B_4^4 = 10)[252] and ideal geometry (B_2^0 = 574, B_4^0 = −116, B_6^0 = 20).[292] In the case of **[Dy(Pc)$_2$]$^-$**, the B_k^q are as follows: real geometry (B_2^0 = 395, B_4^0 = −220, B_6^0 = 40, B_4^4 = 10).[284,287] The fourth-range extradiagonal parameters (B_4^4 and/or B_6^4) exert a greater influence on both the hyperfine structure of the ground state and the ground-state multiplet structure.[122,276,294–296] Moreover, as the structure deviates from D_{4d} symmetry, the twist angle (θ) and the zenithal angles (φ) between the C_4 axis and the direction of the Ln^{3+}–N$_{iso}$ coordination bond exert great influence on the ground state and the first excited state of the octacoordination geometry of the **Ln(Pc)$_2$** complex as determined using the theoretical approach.[286,287] Several groups have reported the m_J ground states for different φ and Ln^{3+}–N$_{iso}$ distances. It is clear that the Tb^{3+} ground-state doublet will be $|m_J|$ = 6 at φ < 55°. However, taking a Ln^{3+}–N$_{iso}$ distance of 2.3 Å as an example, the $|m_J|$ = 15/2 ground state of Dy^{3+} will no longer be the lowest at φ > 49°.[286] Previous studies have reported that the lowest $|m_J|$ ground state of the **Tb(Pc)$_2$** system is the $|m_J|$ = 6 state, and that of the **Dy(Pc)$_2$** system is the $|m_J|$ = 13/2 state.[233] These high-$|m_J|$ ground states have high magnetic anisotropy, which is

advantageous for SMM design. Consequently, the distortion of the coordination environment is reflected in the SMM characteristics of rare-earth sandwich tetrapyrrole SMMs. The protonation–deprotonation reactions of the double-decker SMMs cause significant changes in the coordination environment around the Ln^{3+} ions, enabling reversible switching of the SMM properties (*cf.* Section 3.5).[297] The SMM properties of Ln^{3+} sandwich complexes are also sensitive to the nuclear spins of the Ln^{3+} ions (*cf.* Section 3.2.3)[276] and Ln–Ln magnetic interactions (f–f interactions; *cf.* Sections 3.2.4 and 3.3).[298] Various approaches are available to induce f–f interactions to improve SMM properties (*cf.* Sections 3.3.1–3.3.4).

Ln(Pc)$_2$ exhibits excellent thermal stability and is attracting attention as an SMM to which the vacuum deposition method can be applied; they can be deposited on various substrates in an ultra-high vacuum (UHV) environment. **Ln(Pc)$_2$**-based SMMs have excellent physical and chemical stability, and many groups, including ours, are investigating these SMMs as molecular-memory and spintronic device materials (*cf.* Section 3.8).[117,135,232,267,299–306] The unpaired π-radical (S = 1/2) on the Pc ligands in **Tb(Pc)$_2$** interacts with the conduction electrons, and Kondo resonance has been observed using scanning tunnelling spectroscopy (STS).[302] Furthermore, the Kondo resonance largely depends on the twist angle (θ) of the tetrapyrrole ligand and the electronic structure due to the delocalized π spin state, demonstrating the manipulation of a single spin with a conduction electron.[135,302,307] In addition, Ln-Pc-based SMMs are attractive materials for quantum mechanical devices that can be developed based on the separation between the ground-state doublet m_J and the excited states, as well as the hyperfine (hf) interaction between the electronic spin and the nuclear spin I, because it is possible to control the hyperfine QTM (hf-QTM).[269,270,303,308–315] The important point here is that each spin (S, J, I) in **Tb(Pc)$_2$** shows a cascade phenomenon through spin interactions. Here, **Tb(Pc)$_2$** incorporated in a transistor structure is in contact with the source, drain, and gate electrode. The various spins (S, J, I) interact with the injected conduction electrons *via* the delocalized π electrons, and the conduction electrons recognize changes in the hf-QTM state during magnetic field sweeps.[270] This represents a readout mechanism for the nuclear spin state, in which the transport properties of **Tb(Pc)$_2$** are controlled by the conduction electrons. Thus, **Tb(Pc)$_2$** SMMs have all the properties necessary to serve as a functional component of quantum-mechanical devices (Fig. 12).

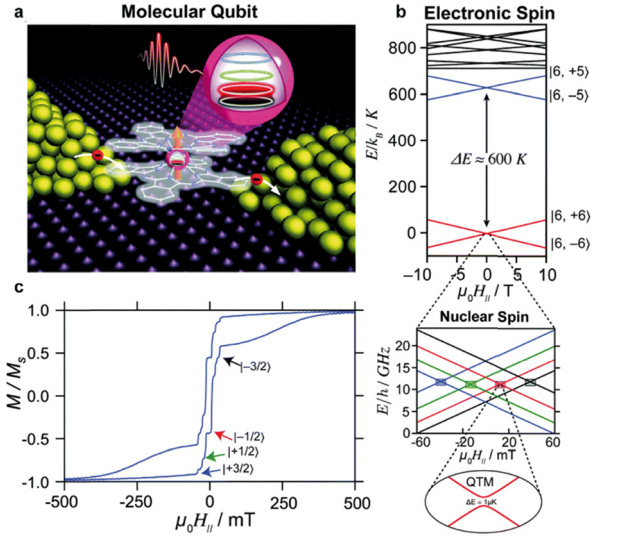

Fig. 12 Molecular qubit based on a **Tb(Pc)$_2$** SMM. (a) Schematic diagram of the qubit detection. **Tb(Pc)$_2$** is placed between Au electrodes. (b) In the Zeeman diagram of **Tb(Pc)$_2$**, the strong hyperfine coupling between the m_J = ±6 and the nuclear spin (I = 3/2) forms four avoided level crossings with a tunnel gap ($\Delta E \approx 1$ μK) and four different qubit states (|−3/2⟩, |−1/2⟩, |+1/2⟩, and |+3/2⟩). (c) Quantum tunnelling phenomenon due to hyperfine coupling in which the nuclear spin is observed in the magnetisation curve of **Tb(Pc)$_2$**. Reprinted from ref. 308 with permission from the Royal Society of Chemistry.

3.2.1 Effect of the coordination environment around the Ln^{3+} ions on the SMM properties. In this section, we summarize the theoretical and experimental research that has elucidated the relationship between the coordination geometries around the Ln^{3+} ions and the properties of the resulting SMMs. Ishikawa *et al.* reported that the wavefunctions of the LF sublevels, which are strongly correlated with the SMM properties, are sensitive to the coordination geometry around the Ln^{3+} ions.[233] In double-decker complexes, a Ln^{3+} ion is coordinated by the eight pyrrole N atoms of the porphyrinoids, and the coordination geometries are evaluated *via* the twist angle θ between the upper and lower ligands. In this case, there are two extreme coordination geometries, *i.e.*, the square-prism (SP) geometry ($\theta = 0°$) and square antiprism (SAP) geometry ($\theta = 45°$). In the case of the SP geometry, the LF Hamiltonian $\hat{H}_{LF}$ contains non-zero $B_4^4\hat{O}_4^4$ and $B_6^4\hat{O}_6^4$ terms:

$$\hat{H}_{LF} = B_2^0\hat{O}_2^0 + B_4^0\hat{O}_4^0 + B_4^4\hat{O}_4^4 + B_6^0\hat{O}_6^0 + B_6^4\hat{O}_6^4$$

where the B_k^q terms represent the LF parameters and the $\hat{O}_k^q$ terms represent the Stevens operators. Stevens operators with non-zero q values act to mix $|m_J\rangle$ and $|m_J \pm q\rangle$. Therefore, the $B_4^4\hat{O}_4^4$ and $B_6^4\hat{O}_6^4$ terms mix the $|m_J\rangle$ and $|m_J \pm 4\rangle$; this mixing enhances the QTM. In contrast, the $\hat{H}_{LF}$ of the ideal SAP geometry does not contain an operator that gives off-diagonal terms between $|m_J\rangle$ and $|m_J'\rangle (m_J \neq m_J')$:

$$\hat{H}_{LF} = B_2^0\hat{O}_2^0 + B_4^0\hat{O}_4^0 + B_6^0\hat{O}_6^0.$$

Therefore, there is no mixing between $|m_J\rangle$ and $|m_J'\rangle$ in the ideal SAP geometry, suppressing QTM. It is not easy to construct the SP geometry in double-decker complexes without replacing the Ln^{3+} ions.[316] Instead, SP and SAP geometries around Ln^{3+} ions have been realized by using porphyrinato–phthalocyaninato triple-decker complexes (Fig. 13).

In 2012, Sakaue *et al.* reported the crystal structure and SMM properties of the heteroligand triple-decker complex **(TAnP)Ln(Pc)Ln*(Pc)**, Ln* = Ln = Tb, or Ln* ≠ Ln = Tb, Y (Scheme 20 and Fig. 13a).[122] The metal center sandwiched by two Pc ligands (Ln*) shows SAP geometry, whereas that sandwiched by Pc and TAnP, namely, Ln, shows SP geometry. It is possible to synthesize heterometal complexes **(TAnP)Y(Pc)Tb(Pc)** and **(TAnP)Tb(Pc)Y(Pc)**, in which one of the

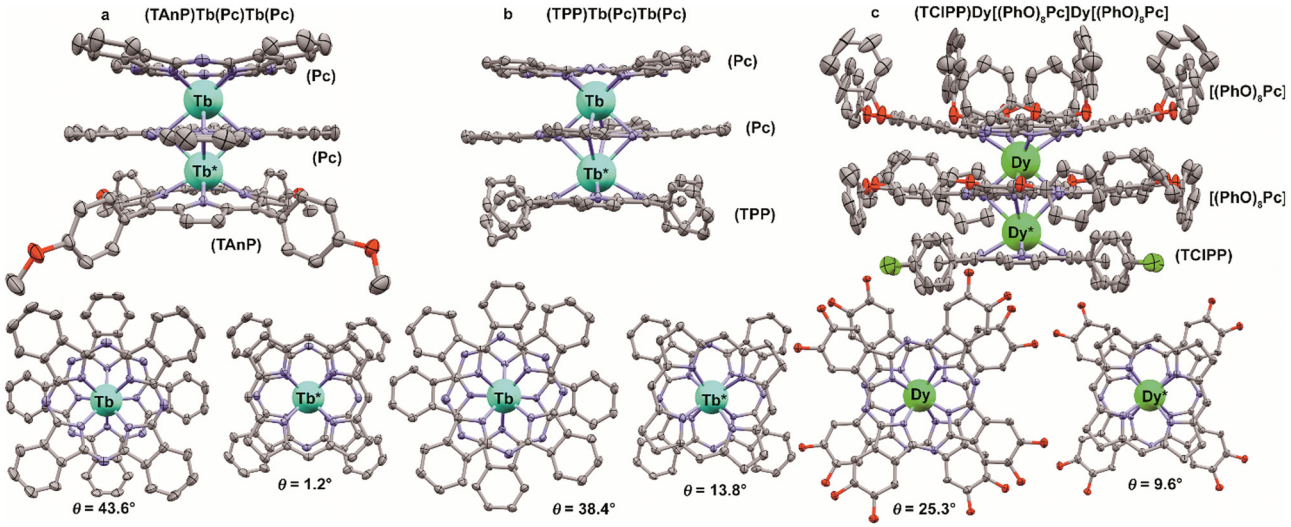

Fig. 13 X-ray structures of mixed ligand complexes, showing coordination surrounding symmetries for different metal centres: (a) **(Pc)Tb(Pc)Tb(TAnP)** (CCDC SAZLIQ);[122] (b) **(TPP)Tb(Pc)Tb(Pc)** (CCDC IJOSUX)[317] and (c) **(TClPP)Dy[(PhO)$_8$Pc]Dy[(PhO)$_8$Pc]** (CCDC MIKSEG).[318] Hydrogen atoms and solvate molecules are omitted for clarity.

metal ions is replaced with a diamagnetic and isostructural Y^{3+} ion. The Tb^{3+} ion of **(TAnP)Y(Pc)Tb(Pc)** adopts SAP geometry, whereas that of **(TAnP)Tb(Pc)Y(Pc)** adopts SP geometry. The maxima of the imaginary part of the AC magnetic susceptibility (χ_M'') for **(TAnP)Y(Pc)Tb(Pc)** occur at much lower frequencies than those of **(TAnP)Tb(Pc)Y(Pc)** (Fig. 14b). In other words, **(TAnP)Y(Pc)Tb(Pc)** shows much longer τ values than **(TAnP)Tb(Pc)Y(Pc)**. These differences have been ascribed to the differences in the coordination geometry around the Tb^{3+} ions. As the Tb^{3+} ion of **(TAnP)Y(Pc)Tb(Pc)** adopts SAP geometry, mixing between LF sublevels and the accompanying QTM is suppressed, which results in long τ values.

In 2016, Katoh *et al.* reported a detailed study on the crystal structures and the SMM properties of triple-decker complexes composed of two Tb^{3+} ions, TPP ligands, and Pc.[317] In case of the triple-decker complex **(TPP)Tb(Pc)Tb(TPP)**, the coordination geometry of the two Tb^{3+} ions is close to the SP geometry (θ = 4°), and the U_{eff} is *ca.* 50 cm^{-1}. Another triple-decker complex, **(Pc)Tb(Pc)Tb(TPP)**, showed two different types of coordination geometry around the Tb^{3+} ions (Fig. 14b), and thus two peaks in the $\chi_M''T$ *vs.* T plots. The coordination geometry around the Tb^{3+} (Fig. 13b) sandwiched by two Pc ligands is similar to the SAP geometry (θ = 38°), whereas that of the Tb^{3+} sandwiched by a TPP and a Pc ligand is similar to the SP geometry (θ = 14°). The θ value of the phthalocyaninato triple-decker complex **Tb$_2$[(BuO)$_8$Pc]$_3$** is 32°.[319] By comparing the magnetic properties of this series of triple-decker complexes, Katoh *et al.* demonstrated the existence of a linear relationship between the U_{eff} and θ values (Fig. 14b). This result is consistent with the degree of mixing of the off-diagonal LF terms ($B_4^4\hat{O}_4^4$ and $B_6^4\hat{O}_6^4$) due to the deviation from the SAP geometry.

The trend for Dy^{3+} complexes is similar to that for Tb^{3+} complexes. In 2013, Kan *et al.* reported a series of Dy^{3+} triple-decker complexes composed of phthalocyaninato and porphyrinato ligands (Fig. 13c).[318] The θ value of the Ln^{3+} between a phthalocyaninato and a porphyrinato ligand is narrow (10°), whereas the θ value of Ln^{3+} surrounded by two phthalocyaninato ligands is wide (25°). The mono-Dy^{3+} complex with a wide θ value, **(TClPP)Y[(PhO)$_8$Pc]Dy[(PhO)$_8$Pc]**, shows slow magnetic relaxation without a bias DC magnetic field. In contrast, **(TClPP)Dy[(PhO)$_8$Pc]Y[(PhO)$_8$Pc]** does not show slow magnetic relaxation even in a DC field. The homonuclear Dy^{3+} complex **(TClPP)Dy[(PhO)$_8$Pc]Dy[(PhO)$_8$Pc]** shows field-induced SMM properties. These results demonstrate that wider θ values improve the τ values.

In 2012, Wang *et al.* reported the structural and magnetic properties of the Dy^{3+} double-decker complexes **(TClPP)Dy(Pc)** and **(TClPP)Dy[(α-Et$_2$CHO)$_4$Pc]** (Fig. 15).[320] The θ value of **(TClPP)Dy(Pc)** is 44°, whereas that of **(TClPP)Dy[(α-Et$_2$CHO)$_4$Pc]** is 38°. **(TClPP)Dy(Pc)** shows clear peaks in the χ_M'' *vs.* T plots in comparison with **(TClPP)Dy[(α-Et$_2$CHO)$_4$Pc]**,

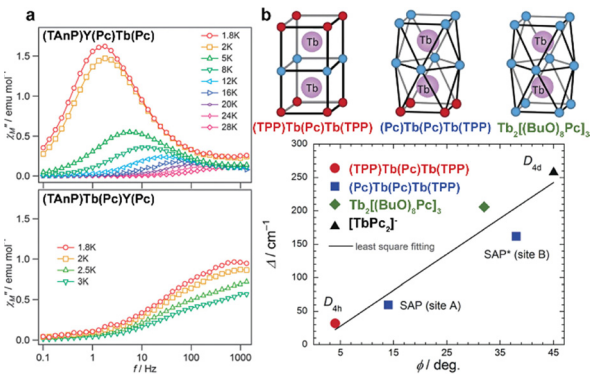

Fig. 14 (a) χ_M'' *vs.* frequency plots for **(TAnP)Y(Pc)Tb(Pc)** (upper) and **(TAnP)Tb(Pc)Y(Pc)** (lower). (b) Coordination geometry and θ *vs.* U_{eff} plots for the series of Tb^{3+} triple-decker complexes. Reproduced from (a) ref. 122 and (b) ref. 317 with permission from the Royal Society of Chemistry.

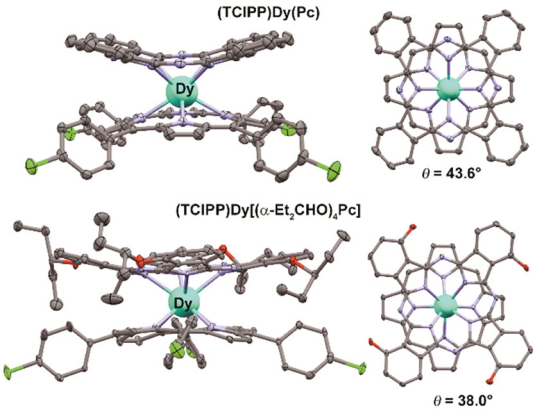

Fig. 15 X-ray structures of mixed ligand complexes **(TClPP)Dy(Pc)** (CCDC MAVQIL)[317] and **(TClPP)Dy[(α-Et2CHO)$_4$Pc]** (CCDC MAVQOR)[321] together with the symmetries of coordination surrounding lanthanide ions. Hydrogen atoms and solvate molecules are omitted for clarity.

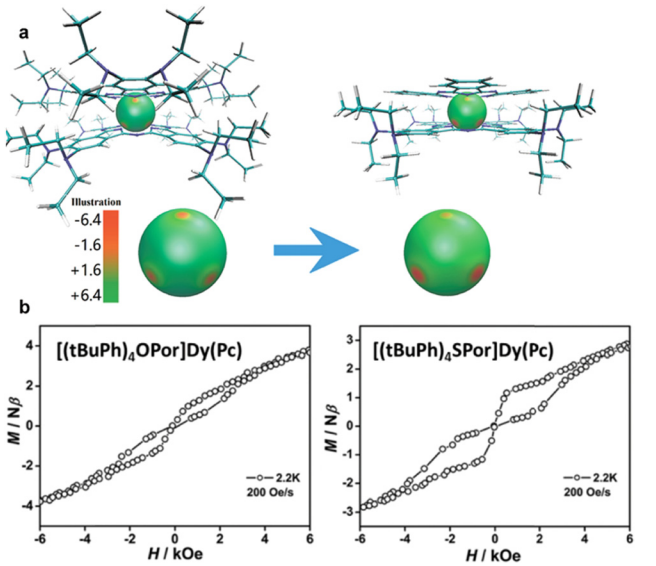

Fig. 16 (a) Electrostatic potential around Tb^{3+} in the **Tb[(Bu$_2$N)$_8$Pc]$_2$** and **[(Bu$_2$N)$_8$Pc]Tb(Pc)** double-decker complexes. (b) Magnetic hysteresis curves for atom-replaced double-decker complexes. **[(*t*BuPh)$_4$SPor]-Dy(Pc)** show larger magnetic hysteresis (right) than **[(*t*BuPh)$_4$OPor]Dy(Pc)** (left) at a sweep rate of 200 Oe s^{-1}. Adapted with permission from (a) ref. 81. Copyright 2017, American Chemical Society. Reproduced from (b) ref. 173 with permission from the Royal Society of Chemistry.

indicating that QTM is suppressed in **(TClPP)Dy(Pc)** due to the SAP coordination geometry.

3.2.2 Effect of peripheral and coordinating atom substitution on the SMM properties. Atom substitution at the peripheral positions of the porphyrinoid ligands affects the SMM properties through changing the coordination geometry and electrostatic potential of the coordinating N atoms.

In 2013, Ganivet *et al.* reported a series of Tb^{3+} double-decker complexes composed of octa(*p-tert*-butyl phenoxy)phthalocyanine **H$_2$[(*t*BuPhO)$_8$Pc]**, tetra(*tert*-butyl)phthalocyanine **H$_2$(*t*Bu$_4$Pc)** and unsubstituted phthalocyanine **H$_2$(Pc)**.[49] The heteroleptic ligand complexes in which one of the Pc ligands is unsubstituted show higher U_{eff} values (642–652 cm^{-1}) than the homoleptic ones (394–504 cm^{-1}). Ganivet *et al.* proposed that electron-donating substituents increase the Tb–N distances, thus pushing the Tb^{3+} toward the unsubstituted phthalocyanine and hence increasing the U_{eff}. This concept was subsequently extended by Chen *et al.* in 2017. These authors reported a high U_{eff} value (652 cm^{-1}) and a magnetic hysteresis of up to 30 K at a sweep rate of 200 Oe s^{-1} for the double-decker complex **[(Bu$_2$N)$_8$Pc]Tb(Pc)**, in which one of the Pc ligands is substituted with alkylamino groups (Scheme 8).[81] DFT calculations of the optimized structures for **[(Bu$_2$N)$_8$Pc]Tb(Pc)** and the corresponding homoligand complex **Tb[(Bu$_2$N)$_8$Pc]$_2$** revealed that the electrostatic potential of $(Bu_2N)_8Pc$ is greater in the heteroligand Pc/$(Bu_2N)_8Pc$ complex than in the homoligand $(Bu_2N)_8Pc$ complex (Fig. 16a). This result supports the enhancement of U_{eff} in heteroligand complexes.

The SMM properties of the porphyrazine (Pz)-based double-decker complexes **Tb(OEPz)$_2$** and **Dy(OEPz)$_2$** were reported by Gimnez *et al.* (Scheme 25).[140] The U_{eff} values of **Tb(OEPz)$_2$** (266 cm^{-1}) and **Dy(OEPz)$_2$** (22 cm^{-1}) are similar to those of their Pc analogues. However, Pz complex benefits from its Pc counterpart due to easier processing. They have a higher solubility of up to 50 mM in CH_2Cl_2 and they can be readily sublimed under relatively mild conditions, that is, 360 °C and 10 mbar. **Tb(OEPz)$_2$** and **Dy(OEPz)$_2$** were evaporated using organic molecular beam epitaxy at 550 K and absorbed intact on the surfaces of Au(111), Ag(111) and Cu(111) in a flat-on fashion, forming hexagonal close-packed layers.[322] Systematic STM studies with multi- and monolayer XPS and complementary DFT calculations were performed showing the preservation of the electronic properties of both ligands and lanthanide centres upon adsorption. Persistence of slow dynamics in **Tb(OEPz)$_2$** single molecule magnets embedded in conducting polymers was confirmed by muon spin relaxation on the example of thin films of PEDOT:PSS mixed with the complex, suggesting that the resulting hybrid material can be interesting for organic spintronics.[323]

Replacing the coordinating N atoms of the porphyrinoid with another element modulates the LF splitting of the Ln^{3+} ions. In 2015, Cao *et al.* reported the magnetic properties of **[(*t*BuPh)$_4$OPor]Dy(Pc)** and **[(*t*BuPh)$_4$SPor]Dy(Pc)**, in which one of the coordinating N atoms of the porphyrin unit is replaced with an O or an S atom, respectively (Scheme 32 and Fig. 16b).[173] Importantly, the U_{eff} values of **[(*t*BuPh)$_4$OPor]Dy(Pc)** (95 cm^{-1}) and **[(*t*BuPh)$_4$SPor]Dy(Pc)** (135 cm^{-1}) are larger than those of the non-replaced analogue **[(*t*BuPh)$_4$Por]Dy(Pc)** (U_{eff} = 28 cm^{-1}). In addition, the U_{eff} of **[(*t*BuPh)$_4$SPor]Dy(Pc)** is the largest among the Dy^{3+}-porphyrinoid sandwich complexes. The difference in the U_{eff} values between **[(*t*BuPh)$_4$OPor]Dy(Pc)** and **[(*t*BuPh)$_4$SPor]Dy(Pc)** are also evidenced by the magnetic hysteresis curve, in which the latter complex exhibits larger magnetic hysteresis than former complex does (Fig. 16c). *Ab initio* calculations revealed that the ground-state doublet of **[(*t*BuPh)$_4$Por]-Dy(Pc)** has the second largest m_J value of ±13/2, whereas those of **[(*t*BuPh)$_4$OPor]Dy(Pc)** and **[(*t*BuPh)$_4$SPor]Dy(Pc)** have an m_J

value of ±15/2. The coordination of the O and S atoms to Dy^{3+} is weaker than that of the N atoms, as evident from the experimental bond lengths and calculated charge distributions. The decrease in the LF along the Dy^{3+}–X (X = O, S) direction stabilizes the m_J = ±15/2 states and thus enhances the SMM properties.

In 2018, the SMM properties of hemiporphyrazinato double-decker complexes (Scheme 37) were reported by Liu *et al.*[189] The homoleptic bis(hemiporphyrazinato) complex **(HHp)Dy(Hp)** and heteroleptic complex **(HHp)Dy(Pc)** show U_{eff} values of 56 cm^{-1} and 40 cm^{-1}, respectively. These U_{eff} values are larger than those of Pc-based Dy^{3+} double-decker complexes. The lone electron pair on N in the pyridine in Hp is more localized in comparison with that of the isoindole N atom of Pc. As a result of the stronger LF of Hp compared to that of Pc, the SMM properties of the Hp-based complexes are superior to those of the Pc-based complexes.

SMMs that combine porphyrinoid and non-porphyrinoid ligands are rare. In 2013, Wang *et al.* reported triple-decker SMMs composed of Pc and the Schiff-base ligand **SB**. Reaction of the half-sandwich complex **[(Pc)Dy(acac)]** with **H_2(SB)** affords the triple-decker complex **$(Pc)_2Dy_2(SB)(H_2O)$** (Scheme 33), which shows a U_{eff} value of 19.8 cm^{-1}.[176] The two Dy^{3+} ions of **$(Pc)_2Dy_2(SB)(H_2O)$** are crystallographically independent, whereby one adopts a SAP geometry that comprises four N atoms of Pc and two N and two O atoms of SB, while the other adopts a seven-coordinated geometry constructed by four N atoms of Pc, two O atoms of SB, and one oxygen atom of a water molecule. In 2014, Gao *et al.* reported a similar triple-decker SMM, **Dy_2(Pc)(SB-TTF)$_2$(MeOH)** (Scheme 34a), with a U_{eff} value of 20 cm^{-1}, which forms assembled structures on highly oriented pyrolytic graphite (HOPG).[179] The same author reported the SMM properties of the trinuclear Dy^{3+} complex **$Dy_3(Pc)_2$(mS)(OAc)(OMe)$_2$** (Scheme 34b) composed of two Pc ligands and macrocyclic Schiff base liagnd(mS), which exhibits zero-field SMM behavior with a U_{eff} value of 42 cm^{-1} and ferromagnetic interactions. In contrast, its Er^{3+} analogue **$Er_3(Pc)_2$(mS)(OAc)(OMe)$_2$** exhibts neither SMM properties nor ferromgnetic interactions.[180] A similar analogue of the dinuclear Dy^{3+} complexes **(μ-LR)$_2Dy_2(Pc)_2(H_2O)$** composed of salicyclic aldehydes **H(LR)** (R = OMe and OEt) and Pc reported by Ge *et al.* (Scheme 39) exhibits zero-field SMM behavior with the U_{eff} values ranging from 27 (R = OEt in the presence of a DC magnetic field) to 47 cm^{-1} (R = OMe).[201] The MeO-substituted complex exhibits better SMM properties than the EtO-subsituted one does because coordination geometry of the latter one deviates from the SAP geometry, which is caused by a long bond length between the ethocy O atom and Dy^{3+} ion. As the result of difference in coordination geometry and LF, methoxy-substituted complex exhibits intramolecular ferromagnetic interactions between two Dy^{3+} ions. Reaction of the half-sandwich complex **[Dy(Pc)(OAc)]** with the polyoxotungstate $[PW_{11}O_{39}]^{6-}$ affords **(Pc)Dy[$PW_{11}O_{39}$]$^{6-}$(NBu_4^+)$_6$,** which shows a U_{eff} value of 34 cm^{-1} at a bias DC field of 500 Oe (Scheme 38c).[193] SMMs composed of Kläui's tripodal ligand and a porphyrinoid, **(L^{Co})Ln(Pc)** and **(L^{Co})Ln(TPP)** (Ln = Tb and Dy) (Scheme 38a and b), were reported by Gao *et al.*,[190] and their U_{eff} values ranged from 6 to 17 cm^{-1}.

3.2.3 Quantum tunnelling of the magnetisation driven by nuclear spin. Quantum tunnelling of magnetisation (QTM) is an emblematic phenomenon originating from the quantum mechanical properties of SMMs. QTM was observed for the first time in the Mn_{12} cluster SMM.[255] This cluster has a total spin quantum number S = 10, and its degree of degeneracy is 21, *i.e.*, 21 of the magnetic states mix with each other at a certain magnetic field. The occurrence of QTM was observed as steps in the magnetic hysteresis curve of the Mn_{12} cluster. The energy separation of 21 of the magnetic states of the Mn_{12} cluster is only a few wavenumbers (Fig. 10c). Therefore, the application of a relatively weak magnetic field can induce the mixing of magnetic states, making it possible to observe the steps in the hysteresis curve of the Mn_{12} cluster. In contrast, the energy separation of the LF sub-levels of **[Tb(Pc)$_2$]$^-$** (and **[Dy(Pc)$_2$]$^-$**) is too great (several hundred wavenumbers) for mixing to be induced between the 13 (16 for **[Dy(Pc)$_2$]$^-$**) m_J states (Fig. 10d). In contrast, Ishikawa *et al.* reported that doping excess amounts of the tetrabutylammonium (Bu_4N^+) salts of **[Tb(Pc)$_2$]$^-$**, **[Dy(Pc)$_2$]$^-$**, and **[Ho(Pc)$_2$]$^-$** into a diamagnetic matrix (**[Y(Pc)$_2$]$^-$**) led to the observation of steps in the magnetic hysteresis at dozens of millikelvin (Fig. 12c).[276,324] These steps originate from the QTM among the ground-state LF sublevels coupled with the nuclear spins of Ln^{3+} (hyperfine coupling). In the case of **[Tb(Pc)$_2$]$^-$**, the lowest energy doublet $|m_J\rangle = |\pm 6\rangle$ couple with the nuclear spin I = 3/2 of ^{159}Tb (natural abundance of 100%) to form the $|m_J,m_I\rangle$ (m_I = ±3/2, ±1/2) states (Fig. 12b). The steps in the magnetic hysteresis of **[Tb(Pc)$_2$]$^-$** originate from the QTM among those eight hyperfine states. The steps in the magnetic hysteresis curves of **[DyPc$_2$]$^-$** are complicated and unclear compared to those of **[TbPc$_2$]$^-$** due to the seven isotopes of Dy, namely, ^{156}Dy, ^{158}Dy, ^{160}Dy, ^{161}Dy, ^{162}Dy, ^{163}Dy, and ^{164}Dy. Moreno-Pineda *et al.* reported the magnetic hysteresis of **(Et_4N^+)[$^{163}Dy_{0.05}Y_{0.95}$(Pc)$_2$]$^-$** (I = 5/2) and **(Et_4N^+)[$^{164}Dy_{0.05}Y_{0.95}$(Pc)$_2$]$^-$** (I = 0).[311] ^{163}Dy has a nuclear spin, whereas ^{164}Dy does not. The magnetic hysteresis curves of **(Et_4N^+)[$^{163}Dy_{0.05}Y_{0.95}$(Pc)$_2$]$^-$** show clearer steps compared to those of the mixture of nuclear isomers (Fig. 17a). Moreover, the multiple steps in the hysteresis curves disappear in **(Et_4N^+)[$^{164}Dy_{0.05}Y_{0.95}$(Pc)$_2$]$^-$** (Fig. 17b). This is direct evidence that nuclear spins correlate with the QTMs.

Nuclear-spin-driven QTM has also been observed in the Tb^{3+} triple-decker complex **(Pc)Tb(Pc)Tb[(Hex)$_8$Pc]**, which contains two Tb^{3+} ions (Tb(1) and Tb(2)) (Fig. 17c–f).[314] As will be discussed later, magnetic interactions exist between the Tb^{3+} ions in the triple-decker complex (*cf.* Section 3.2.4). Therefore, QTM occurs among $|m_J^1, m_I^1, m_J^2, m_I^2\rangle$. The number of possible quantum states d for the triple-decker complex ($d = (2I + 1)^2$ = 16) is larger than that for **[Tb(Pc)$_2$]$^-$** ($d = (2I + 1)^1$ = 4). The strategy of using Ln^{3+}–Ln^{3+} interactions is promising for the construction of multiple qubits, which is required for quantum computers.

3.2.4 f–f interactions elucidated using multiple-decker complexes. In addition to double-decker complexes, multiple-

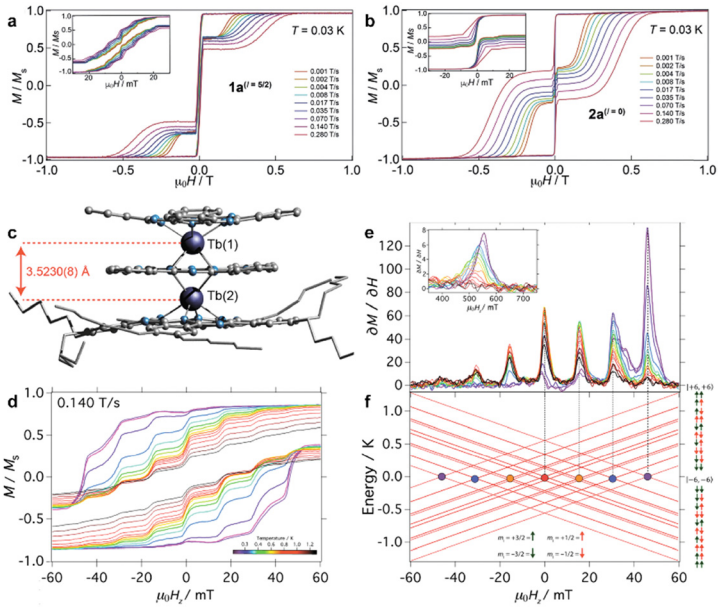

Fig. 17 Field dependence of the magnetisation at 0.03 K with the field applied parallel to the easy axis of magnetisation for (a) $(Et_4N^+)[^{163}Dy_{0.05}Y_{0.95}(Pc)_2]^-$ (I = 5/2) and (b) $(Et_4N^+)[^{164}Dy_{0.05}Y_{0.95}(Pc)_2]^-$ (I = 0). Insets show magnifications in the ±30 mT region. (c) Crystal structure of triple-decker complex **(Pc)Tb(Pc)Tb[(Hex)$_8$Pc]**. (d) Hysteresis loop of **(Pc)Tb(Pc)Tb[(Hex)$_8$Pc]** recorded with a field sweep of 0.140 T s^{-1}. (e) First field derivative for a field sweep from −1 to +1 T of the data in (d), and (f) Zeeman diagram with the field parallel to the magnetic easy axes. Adapted with permission from (a and b) ref. 311. Copyright 2017, Wiley-VCH. Adapted with permission from (c–f) ref. 314. Copyright 2018, American Chemical Society.

decker complexes that contain two lanthanoid ions Ln^{3+} also show SMM properties. The main differences between the double-decker and multiple-decker complexes are the existence of intramolecular Ln^{3+}–Ln^{3+} interactions in the latter case. Magnetic interactions between Ln^{3+} ions in binuclear metal complexes were reported by Ishikawa *et al.*[298] before the first report of rare-earth-based SMMs in 2003.[36] The authors synthesized a series of phthalocyaninato triple-decker complexes **(Pc)Ln(Pc)Ln′[(BuO)$_8$Pc]** (Ln = Ln′ = Tb, Dy, Ho, Er, Tm, Yb), denoted as **[Ln,Ln′]** (Fig. 18). A comparison of the DC magnetic properties of **[Ln,Ln′]**, **[Y,Ln′]**, and **[Ln,Y]** (in the latter two, one Ln^{3+} is replaced with the diamagnetic and isostructural Y^{3+} ion), enables the observation of Ln^{3+}–Ln^{3+} interactions with the increase/decrease in $\Delta\chi_M T$ values:

$$\Delta\chi_M T = \chi_M^{[Ln,Ln']} T - \frac{1}{2}\left\{\chi_M^{[Y,Ln']} T + \chi_M^{[Ln,Y]} T\right\},$$

where $\chi_M^{[Ln,Ln']}$, $\chi_M^{[Y,Ln']}$ and $\chi_M^{[Ln,Y]}$ represent the χ_M values for **[Ln,Ln′]**, **[Y,Ln′]**, and **[Ln,Y]**, respectively. Ishikawa *et al.* revealed that the behaviour of the $\Delta\chi_M T$ values can be explained solely by the magnetic dipolar term, indicating that the magnetic f–f interactions originate from magnetic dipole–dipole interactions. Increases in the $\Delta\chi_M T$ in Tb^{3+}, Dy^{3+}, and Ho^{3+} complexes with decreasing temperature indicate the existence of ferromagnetic interactions. On the other hand, the Er^{3+} and Tm^{3+} complexes show antiferromagnetic interactions, which were observed as decreases in $\Delta\chi_M T$. The $\Delta\chi_M T$ values of the Yb^{3+} complex showed only negligible temperature dependence. This complicated behaviour can be interpreted in terms of dipole–dipole interactions. As discussed in the section on double-decker complexes (*cf.* Section 3.2), Tb^{3+}, Dy^{3+}, and Ho^{3+} ions show easy-axis magnetic anisotropy when sandwiched by Pc ligands. In other words, the magnetic dipoles of these ions in the **[Ln,Ln′]** complexes tend to be aligned along the C_4 axis (perpendicular to the Pc plane). Therefore, head-to-tail ferromagnetic arrangement of the magnetic dipoles is favored in Tb^{3+}, Dy^{3+}, and Ho^{3+} complexes. In contrast, Er^{3+} and Tm^{3+} sandwiched by Pc ligands show easy-plane magnetic anisotropy. As a result, parallel and antiferromagnetic arrangement of the magnetic dipoles is favored in Er^{3+} and Tm^{3+} complexes. The $\Delta\chi_M T$ of the Yb^{3+} complex is less temperature dependent than those of other **[Ln,Ln′]** complexes because of

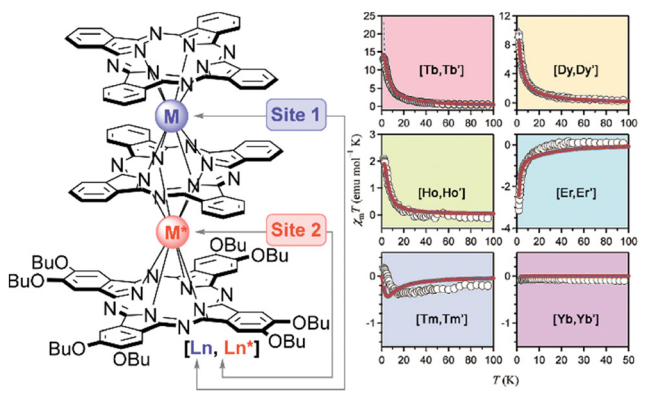

Fig. 18 Molecular structures and $\Delta\chi_M T$ values of **(Pc)Ln(Pc)Ln′[(BuO)$_8$Pc]** denoted as **[Ln,Ln′]**. The red curves show theoretical data. Adapted with permission from ref. 298. Copyright 2003, American Chemical Society.

the weak magnetic anisotropy of Yb^{3+}. The use of diamagnetic and isostructural Y^{3+} ions demonstrated by Ishikawa *et al.* is a smart method to accurately determine the effect of magnetic Ln^{3+}–Ln^{3+} interactions that has been used for a wide variety of Ln^{3+}-based SMMs.

The next question is how long the Ln^{3+}–Ln^{3+} distance must be in order to induce f–f interactions. The Ln^{3+}–Ln^{3+} distance of the Pc triple-decker complex estimated using DFT calculations is 3.57 Å (this value is consistent with the crystal structure analyses for triple-decker analogues).[298] Increasing the Ln^{3+}–Ln^{3+} distance should affect the magnitude of the f–f interactions.

In 2010, Fukuda *et al.* reported the first example of a discrete quadruple-decker complex composed of four Pc ligands.[202] The reaction of the anionic Lu^{3+} double-decker complex $[\mathbf{Ln(Pc)_2}]^-$ with Cd^{2+} acetate afforded **(Pc)Lu(Pc)Cd(Pc)Lu(Pc)**, which is referred to as **[LnCdLn]** (Fig. 19a). As the two Ln^{3+} ions are separated by a diamagnetic Cd^{2+} ion, the Ln^{3+}–Ln^{3+} distance is longer than those in triple-decker complexes. Fukuda *et al.* investigated the Ln^{3+}–Ln^{3+} interactions in **[LnCdLn]** (Ln = Tb, Dy, Er)[325] using the same method as for the series of **[Ln,Ln′]** complexes[298] and revealed the existence of f–f interactions, although their magnitude was low compared to those observed in **[Ln,Ln′]**. In the case of **[TbCdTb]** and **[DyCdDy]**, an increase in $\Delta\chi_M T$ is observed, indicating intramolecular ferromagnetic interactions between the Ln^{3+} ions (Fig. 19b). As discussed in the section on **[Ln,Ln′]**, the head-to-tail arrangement of the magnetic dipoles is stabilized when axially anisotropic Ln^{3+} ions (Tb^{3+} and Dy^{3+}) are involved. On the other hand, **[ErCdEr]** shows a decrease in $\Delta\chi_M T$ due to the easy-plane magnetic anisotropy of the Er^{3+} ions.

Wang *et al.* and Katoh *et al.* have reported the crystal structures of Dy^{3+} and Tb^{3+} quadruple-decker complexes composed of $(BuO)_8Pc$ ligands, $\mathbf{Tb_2Cd[(BuO)_8Pc]_4}$ and $\mathbf{Dy_2Cd[(BuO)_8Pc]_4}$.[205,211] On account of the low solubility of the quadruple-decker complexes composed of unsubstituted Pc ligands, peripheral *n*-butoxy substitution is mandatory to obtain single crystals suitable for X-ray diffraction analysis. The strategy of using Cd^{2+} ions to elongate the stacked π-system was further extended by Wang *et al.* Their group succeeded in obtaining a series of stacked π-systems: the quintuple-decker complexes $\mathbf{Ln_2Cd_2[(BuO)_8Pc]_5}$[208] and sextuple-decker complexes $\mathbf{Ln_2Cd_3[(BuO)_8Pc]_6}$.[209] Horii *et al.* reported the crystal structures of the Dy^{3+} multiple-decker complexes composed of $[(BuO)_8Pc]$ ligands (Fig. 19a) and confirmed that the Dy^{3+}–Dy^{3+} distances are 9.8 Å for the quintuple-decker complex $\mathbf{Dy_2Cd_2[(BuO)_8Pc]_5}$ and 13.0 Å for the sextuple-decker complex $\mathbf{Dy_2Cd_3[(BuO)_8Pc]_6}$.[213,326] Very weak f–f interactions exist in both complexes, as demonstrated by the increase in their $\Delta\chi_M T$ values (Fig. 19a right). These f–f interactions can be used to alter their SMM properties, as discussed in the following section.

3.3 Using f–f interactions to improve SMM properties

In 2002, Wernsdorfer *et al.* reported the magnetic properties of a SMM dimer composed of the TM-based cluster $\mathbf{Mn_4}$.[225] The step at zero DC magnetic field in the magnetic hysteresis curve of the monomeric SMM $\mathbf{Mn_4}$ disappears in the dimerized SMMs $\mathbf{Mn_4}\cdots\mathbf{Mn_4}$ due to the suppression of QTM. The mechanism of the suppression of QTM can be explained as follows. If the probability of QTM between the up ($|\uparrow\rangle$) and down spin

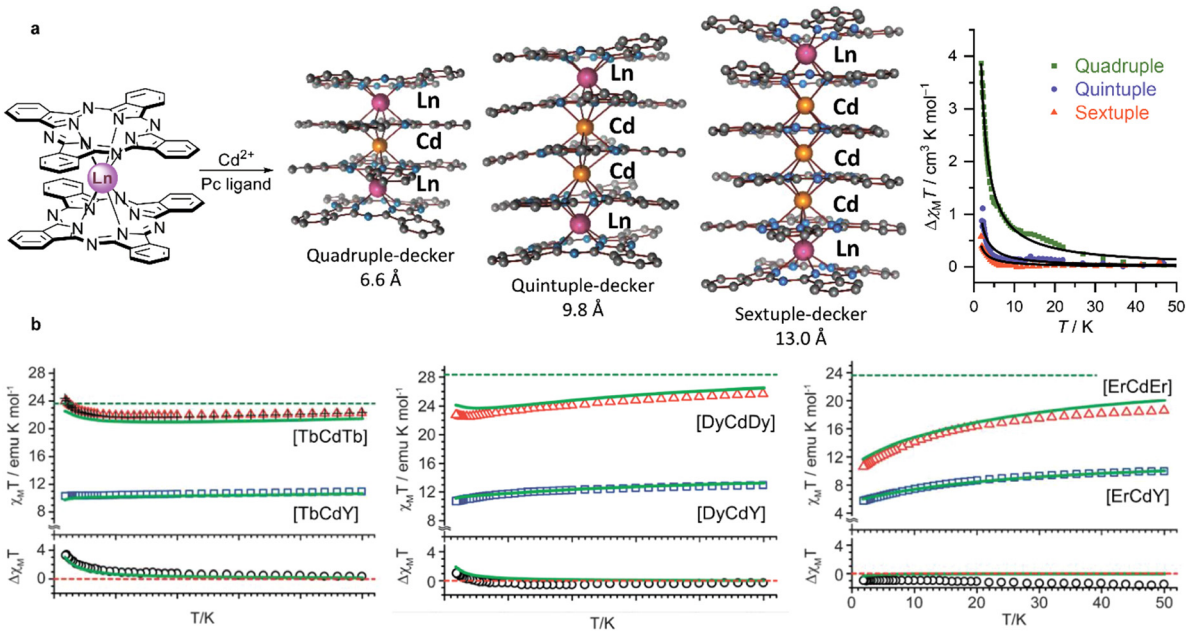

Fig. 19 (a) Synthesis and crystal structures of a series of phthalocyaninato multiple-decker complexes; representative molecular crystal structures of the Dy^{3+} complexes $\mathbf{Dy_2Cd[(BuO)_8Pc]_4}$, $\mathbf{Dy_2Cd_2[(BuO)_8Pc]_5}$ and $\mathbf{Dy_2Cd_3[(BuO)_8Pc]_6}$; *n*-butoxy groups in the crystal structures are omitted for clarity. $\Delta\chi_M T$ *vs.* *T* plots for the Dy^{3+} multiple-decker complexes were constructed using data from ref. 211, 213 and 326. (b) DC magnetic susceptibilities of quadruple-decker complexes that contain Tb^{3+}, Dy^{3+} and Er^{3+} ions. Reproduced from (b) ref. 325 with permission from the Royal Society of Chemistry.

($|\downarrow\rangle$) states of one SMM is P_{QTM}, the QTM probability between the ferromagnetically coupled states ($|\uparrow,\uparrow\rangle$ and $|\downarrow,\downarrow\rangle$) in the SMM dimer is expressed as $P_{QTM}{}^2$, because QTM between these states requires simultaneous spin reversal. Since $P_{QTM}{}^2$ is much smaller than P_{QTM}, QTM between the coupled spin states is a forbidden transition. Therefore, the coupling of two SMMs suppresses the QTM at zero bias DC magnetic field. This strategy (exchange bias effect) is important when considering SMMs as a possible candidate for information storage, because it can improve data stabilisation at zero DC field. The f–f interactions in multiple-decker complexes can also be used as a source of exchange bias. The effect of f–f interactions on the dynamic magnetic properties of rare-earth SMMs was reported by Ishikawa *et al.*[327] They prepared the homodinuclear Tb^{3+} triple-decker complex **(Pc)Tb(Pc)Tb[(BuO)$_8$Pc]** (denoted as **[Tb,Tb]**) and the two heterodinuclear complexes **(Pc)Y(Pc)Tb[(BuO)$_8$Pc]** (denoted as **[Y,Tb]**) and **(Pc)Tb(Pc)Y[(BuO)$_8$Pc]** (denoted as **[Tb,Y]**), as summarized in Fig. 18. The mono-Tb^{3+} complexes **[Y,Tb]** and **[Tb,Y]** show clear DC magnetic field (H_{dc}) dependences in their χ''_M *vs.* T plots; the peak maxima shift to a higher temperature with increasing H_{dc} magnitude (Fig. 20a). In contrast, the χ''_M *vs.* T plots for **[Tb,Tb]** are H_{dc}-independent in the field range of 0 to 3000 Oe (the right side of Fig. 20a). The two peaks in the plots of **[Tb,Tb]** are due to the two inequivalent Tb^{3+} ions. The increase in the temperatures of the maxima of **[Y,Tb]** and **[Tb,Y]** corresponds to the suppression of QTM by applying an H_{dc}. The QTM occurs among the energetically degenerate states. However, applying an H_{dc} resolves the degeneracy of the ground-state doublet $|\pm6\rangle$ due to Zeeman splitting. Therefore, the QTM of **[Y,Tb]** and **[Tb,Y]** is suppressed with increasing H_{dc}, causing the remarkable H_{dc} dependences of χ''_M. In contrast, the Tb^{3+} ions of **[Tb,Tb]** are affected by the magnetic dipolar field from the other Tb^{3+} ion. Therefore, the Tb^{3+} ions of **[Tb,Tb]** act as if a DC magnetic field is applied even in the absence of an external H_{dc}. Therefore, the QTM in **[Tb,Tb]** is suppressed without an H_{dc}, resulting in weak H_{dc} dependence in its χ''_M *vs.* T plots.

The Zeeman diagrams of the triple-decker complexes reported by Sakaue *et al.* aid in the understanding of the relaxation mechanism of **[Tb,Tb]**.[122] Fig. 20b is a schematic illustration of the Zeeman diagrams of various multiple-decker Tb^{3+} complexes.[212] Due to the ferromagnetic dipole–dipole interactions between the Tb^{3+} ions in the triple-decker complex **[Tb,Tb]**, the lowest energy states are $|m_J, m_J\rangle = |\pm6, \pm6\rangle$ at zero H_{dc}. The antiferromagnetically coupled doublet $|\pm6, \mp6\rangle$ is located at *ca.* 3 cm^{-1}. Due to the hyperfine coupling between J and I, the Zeeman diagram of $|\pm6, \pm6\rangle$ and $|\pm6, \mp6\rangle$ shows multiple lines, which are depicted as bands in Fig. 20b. At zero

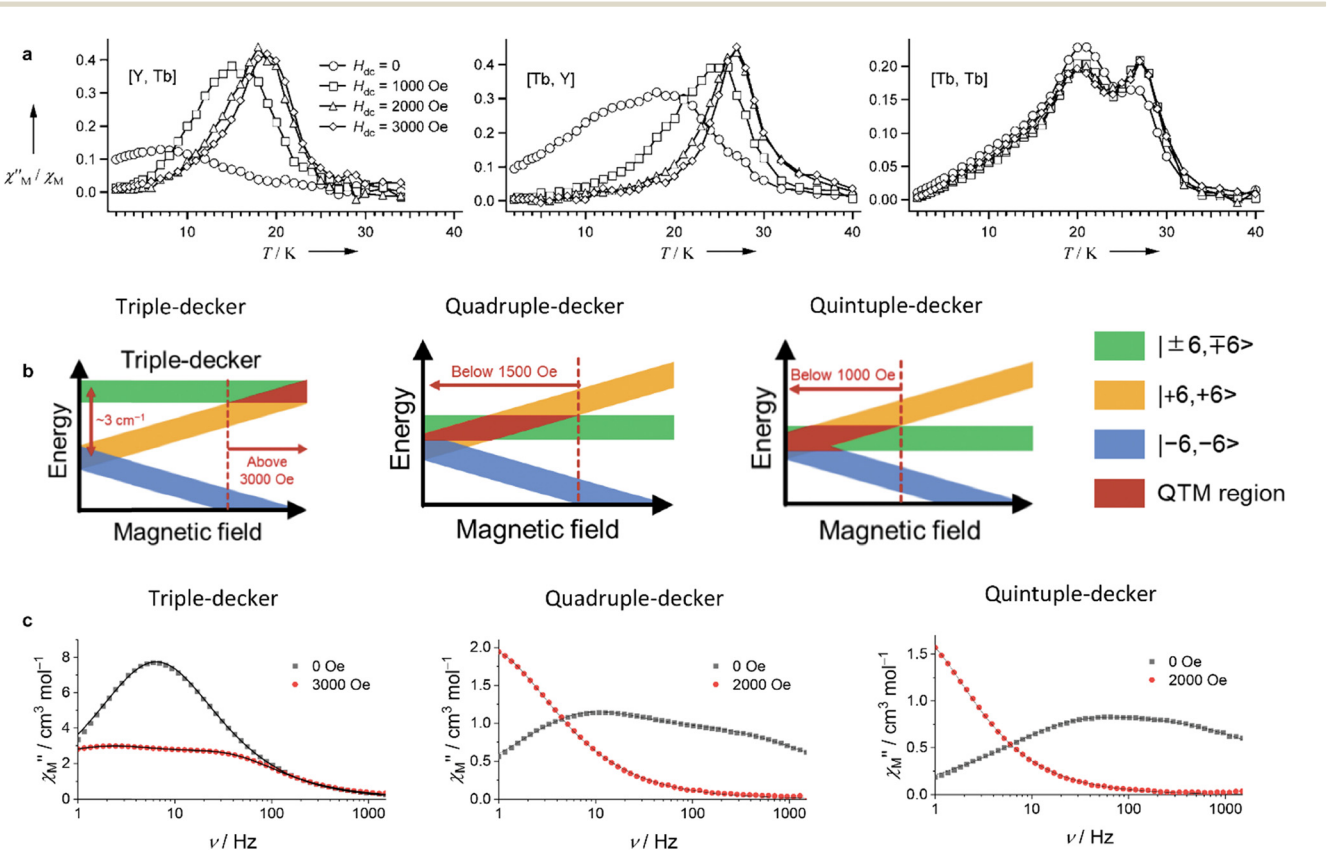

Fig. 20 (a) DC magnetic field (H_{dc}) dependences of the χ''_M *vs.* T plots at an AC frequency of 997 Hz for the triple-decker complexes **[Y,Tb]**, **[Tb,Y]** and **[Tb,Tb]**. (b) Schematic illustration of the Zeeman diagrams of Tb^{3+} multiple-decker complexes. (c) H_{dc} dependences of the χ''_M *vs.* ν plots for the series of butoxy-substituted Tb^{3+} multiple-decker complexes at 4 K based on the data from ref. 319, 328 and 211. Adapted with permission from (a) ref. 327. Copyright 2005, Wiley-VCH.

DC magnetic field, $|+6, +6\rangle$ and $|-6, -6\rangle$ are degenerate. However, QTM between $|+6, +6\rangle$ and $|-6, -6\rangle$ is prohibited because this transition requires simultaneous spin reversal. The Zeeman diagram also predicts energy crossing between $|\pm6, \mp6\rangle$ and $|+6, +6\rangle$ at H_{dc} = ±3000 Oe, indicating that the QTM between $|\pm6, \mp6\rangle$ and $|+6, +6\rangle$ is enhanced at 3000 Oe.

In the case of the quadruple-decker complexes, the magnitude of the f–f interactions decreases and the H_{dc} dependences of τ are changed. Fukuda *et al.* reported the H_{dc} dependences of the τ values for homonuclear (**[TbCdTb]**) and heteronuclear (**[TbCdY]**) quadruple-decker complexes.[329] **[TbCdTb]** has f–f interactions, whereas **[TbCdY]** does not. At zero H_{dc}, **[TbCdTb]** shows longer τ values than **[TbCdY]**. However, at H_{dc} = 1000 Oe, the τ values of **[TbCdTb]** become faster than those of **[TbCdY]**. Further increasing the H_{dc} causes the τ of both complexes to become similar. This complicated modulation of τ can again be explained using a Zeeman diagram. Since the magnetic easy axis of the Tb^{3+} ion in the multiple-decker complex is parallel to the C_4 axis, the ferromagnetic head-to-tail arrangement of the magnetic dipoles is stabilized in **[TbCdTb]**. Therefore, the ground and first excited states of **[TbCdTb]** are $|\pm6, \pm6\rangle$ and $|\pm6, \mp6\rangle$, respectively. Compared to the triple-decker complex, the energy difference between $|\pm6, \pm6\rangle$ and $|\pm6, \mp6\rangle$ is smaller in **[TbCdTb]** due to the weaker f–f interactions. The ground-state doublet $|\pm6, \pm6\rangle$ shows Zeeman splitting, whereas $|\pm6, \mp6\rangle$ does not. Due to the hyperfine interactions, $|\pm6, \pm6\rangle$ and $|\pm6, \mp6\rangle$ are shown as crowded lines. At zero H_{dc}, the QTM in **[TbCdTb]** is suppressed due to the exchange bias effect, which prolongs the τ values. However, $|+6, +6\rangle$ and $|\pm6, \mp6\rangle$ cross at around 1000 Oe (middle plot in Fig. 20b). Therefore, the QTM between these is enhanced, decreasing the τ values of **[TbCdTb]**. This is the reason for the magnetic field dependences of the τ values in **[TbCdTb]** and **[TbCdY]**. A similar trend has also been observed in the Dy^{3+} analogues. Katoh *et al.* reported that the homonuclear Tb^{3+} triple-decker complex **$Tb_2[(BuO)_8Pc]_3$** shows two peaks in the imaginary part of the AC magnetic susceptibility in the presence of a non-zero H_{dc} (3000 Oe) as summarized in the left side of Fig. 20c.[319] In contrast, quadruple-decker **$Tb_2Cd[(BuO)_8Pc]_4$**[328] and quintuple-decker **$Tb_2Cd_2[(BuO)_8Pc]_5$**[211] complexes that contain two Tb^{3+} ions show dual magnetic relaxations at zero H_{dc}. Importantly, the dual magnetic relaxations become a single one in the presence of a non-zero H_{dc} (2000 Oe). The complicated magnetic behaviour in these complexes originates from the differences in the magnitude of the f–f interactions. The dual magnetic relaxations of **$Tb_2[(BuO)_8Pc]_3$** have been observed at 3000 Oe, where level-crossing between $|+6, +6\rangle$ and $|\pm6, \mp6\rangle$ occurs. Therefore, one of the dual magnetic relaxations in **$Tb_2[(BuO)_8Pc]_3$** is attributed to the QTM and spin-lattice relaxations among $|+6, +6\rangle$ and $|\pm6, \mp6\rangle$. In the case of **$Tb_2Cd[(BuO)_8Pc]_4$** and **$Tb_2Cd_2[(BuO)_8Pc]_5$**, $|\pm6, \pm6\rangle$ and $|\pm6, \mp6\rangle$ show crossing at zero H_{dc} because of the weaker f–f interactions (small energy difference between $|\pm6, \pm6\rangle$ and $|\pm6, \mp6\rangle$), as shown in Fig. 20b. Therefore, magnetic relaxations among these states occur and are observed as the dual magnetic relaxations at zero H_{dc}. Increasing H_{dc} resolves the degeneracy of $|\pm6, \pm6\rangle$ and $|\pm6, \mp6\rangle$, resulting in the observation of single magnetic relaxation.

The effect of the f–f interactions on the dynamic magnetic properties has been reported in Dy^{3+} complexes. Katoh *et al.* reported the SMM properties of the triple-decker complexes **$Dy_2[(BuO)_8Pc]_3$** and **$DyY[(BuO)_8Pc]_3$**.[330] Homonuclear **$Dy_2[(BuO)_8Pc]_3$** has intramolecular f–f interactions, whereas **$DyY[(BuO)_8Pc]_3$** does not. The magnetic relaxation time τ of **$Dy_2[(BuO)_8Pc]_3$** is 1.30×10^{-4} s at 1.82 K. This value is one order of magnitude greater than that for **$DyY[(BuO)_8Pc]_3$** (3.20×10^{-5} s at 1.9 K), indicating that f–f interactions act as an exchange bias to suppress the QTM at zero H_{dc}.

Horii *et al.* reported the exchange bias effect in Dy^{3+} quadruple-decker (**$Dy_2Cd[(BuO)_8Pc]_4$**), quintuple-decker (**$Dy_2Cd_2[(BuO)_8Pc]_5$**), and sextuple-decker (**$Dy_2Cd_3[(BuO)_8Pc]_6$**) complexes.[213,326] Similar to the triple-decker complexes composed of two Dy^{3+} ions, the series of multiple-decker complexes shows longer τ values than the mono-Dy^{3+} complex due to the f–f interactions in the former complex. The exchange bias effect is observed in **$Dy_2Cd_3[(BuO)_8Pc]_6$**, in which the intramolecular Dy^{3+}–Dy^{3+} distance is *ca.* 13 Å.

3.3.1 Connecting double-decker SMMs without using Cd^{2+} ions. The exchange bias effects of the multiple-decker complexes prolong the τ values. However, double-decker complexes show longer τ values than multiple-decker complexes. The short τ values in the latter case are associated with the changes in the coordination geometry around Ln^{3+} that are induced by the coordination of the metal ions. In the case of the triple-decker complex, the inner Pc ligand is coordinated by two Ln^{3+} centres. Therefore, the coordination geometry around Ln^{3+} becomes unsymmetrical, enhancing the QTM (P_{QTM} becomes large). Thus, it is desirable to induce the exchange bias effect while keeping the SAP geometry of the double-decker complex (*i.e.*, keeping P_{QTM} small).

The use of the clamshell-type phthalocyanine[331] reported by Tolbin *et al.* enables the construction of a discrete stacked π-system without using metal coordination.[104] Horii *et al.* reported a clamshell-type quadruple-decker complex **(Pc)Tb[c-Pc_2]Tb(Pc)** in which the two Tb^{3+} double-decker units (***t*Bu_4Pc)Tb(Pc)** are connected by a benzyloxy linker (Scheme 13 and Fig. 21a).[105] Ferromagnetic f–f interactions are present between the two double-decker units, as evidenced by the increase in the $\chi_M T$ value at low temperatures because the head-to-tail arrangements of the magnetic dipoles are stabilized. The magnetic hysteresis of **(Pc)Tb[c-Pc_2]Tb(Pc)** at a zero DC magnetic field is wider than that of the monomer double-decker complex (***t*Bu_4Pc)Tb(Pc)**, indicating that the exchange bias is effective in prolonging the τ values. The reaction of **(Pc)Tb[c-Pc_2]Tb(Pc)** with Cd^{2+} acetate affords the Cd^{2+}-containing complex **(Pc)Tb[c-Pc_2Cd]Tb(Pc)**. Although ferromagnetic interactions between the Tb^{3+} ions exist in **(Pc)Tb[c-Pc_2Cd]Tb(Pc)**, it shows a butterfly-shaped magnetic hysteresis curve in which the curve is closed at zero H_{dc}. These results indicate that the QTM is enhanced (increased P_{QTM} value) by the coordination of a Cd^{2+} ion.

Horii *et al.* used supramolecular assembly reported by Ishikawa *et al.*[332] to introduce f–f interactions.[67] The crown-ether-substituted double-decker complex **[(15C5)$_4$Pc]Tb(Pc)** forms a supramolecular quadruple-decker complex **[K$_4${[(15C5)$_4$Pc]-Tb(Pc)}$_2$]$^{4+}$** in the presence of excess potassium acetate (Fig. 21b). Quantitative conversion from **[(15C5)$_4$Pc]Tb(Pc)** to **[K$_4${[(15C5)$_4$Pc]Tb(Pc)}$_2$]$^{4+}$** was confirmed by paramagnetic ^{1}H NMR analysis and absorption spectra. In addition, ferromagnetic Tb^{3+}–Tb^{3+} interactions exist in **[K$_4${[(15C5)$_4$Pc]Tb(Pc)}$_2$]$^{4+}$**. At 1.8 K, the τ value of **[K$_4${[(15C5)$_4$Pc]Tb(Pc)}$_2$]$^{4+}$** is 1000 times longer than that of **[(15C5)$_4$Pc]Tb(Pc)**, indicating that the exchange bias suppresses QTM.

Recently, the crystal structures of the triple-decker complexes dimerized *via* analogous supramolecular associations using crown ethers and K$^+$ ions were elucidated by Martynov *et al.*[333] The triple-decker complex **[(15C5)$_4$Pc]Tb(Pc)Tb(Pc)** forms a supramolecular dimer in the presence of K$^+$ ions (Fig. 22a). Such dimerization did not alter the symmetry of coordination surrounding of metal centres, and the Ln···Ln distances ranging from 3.5 to 13.2 Å renders these complexes as convenient models to study long-range interactions between paramagnetic metal centres aligned in a collinear fashion. In the case of **[(15C5)$_4$Pc]Tb[(15C5)$_4$Pc]Tb(Pc)**, the reaction with four K$^+$ ions does not induce dimerisation but instead changes the coordination geometry of Tb* from SAP to SP which was demonstrated by crystallographic characterization of isostructural Y^{3+} complex and its supramolecular inclusion compound (Fig. 22b).[334] Therefore, the approach of using (15C5)$_4$Pc is promising not only for introducing f–f interactions, but also for directly changing the LF. Although the SMM properties of **[(15C5)$_4$Pc]Tb(Pc)Tb(Pc)** and **[(15C5)$_4$Pc]Tb[(15C5)$_4$Pc]Tb(Pc)** have not yet been reported, modulation of the magnetic anisotropy, which may be correlated with the LF, was demonstrated *via* NMR analyses.

The connection of the double-decker SMM **H[(α-BuO)$_8$Pc]-Tb(Pc)** by Na$^+$ was reported by Chen *et al.* (Fig. 21c).[335,336]

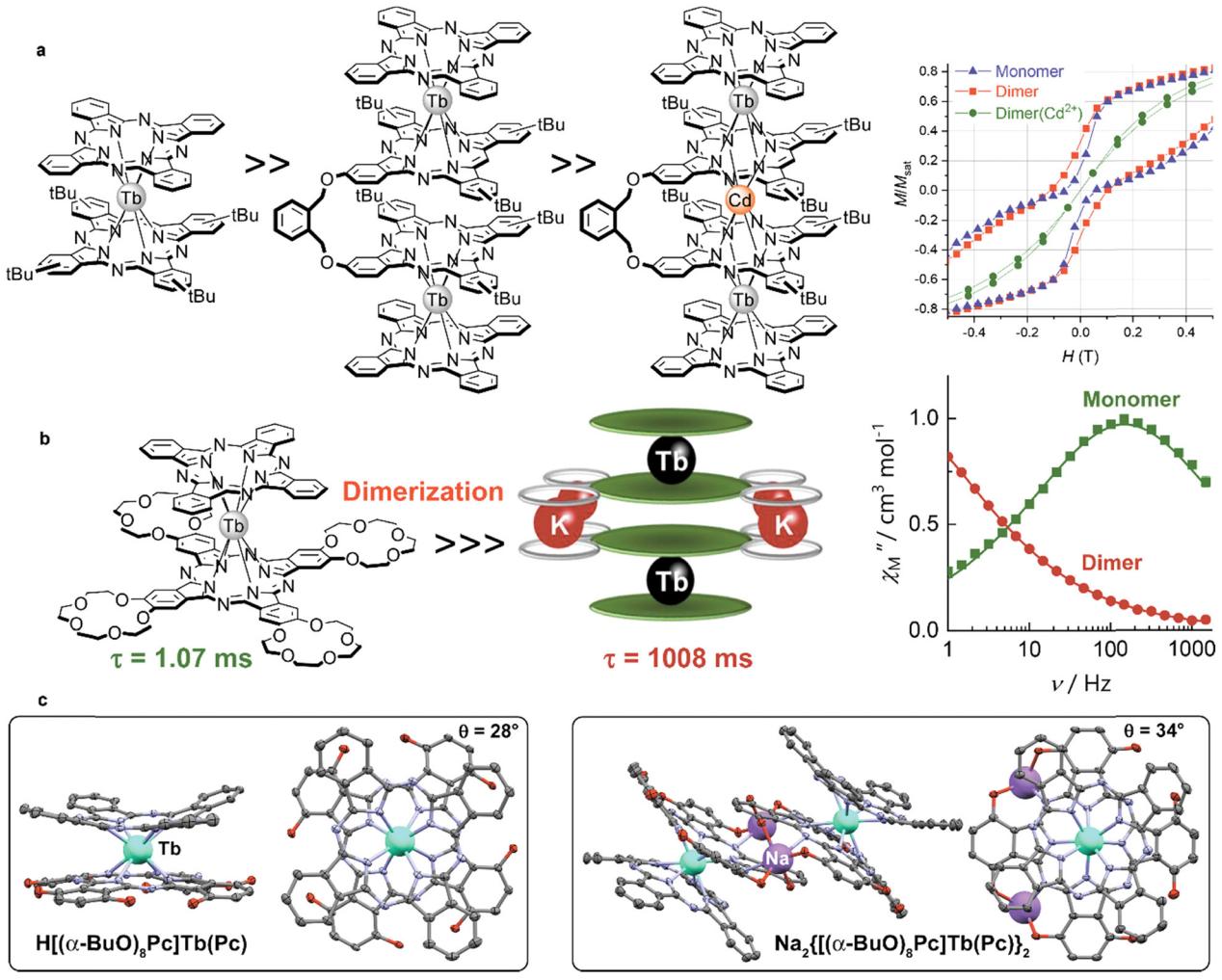

Fig. 21 (a) Molecular structures and magnetic hysteresis curves of the clamshell-type quadruple-decker complexes. (b) Supramolecular dimerisation of the crown-ether-substituted SMM **[(15C5)$_4$Pc]Tb(Pc)**. The maxima in the χ''_M *vs.* ν plots shift toward the low ν region upon dimerisation. (c) Dimerisation of the double-decker SMM **H[(α-BuO)$_8$Pc]Tb(Pc)** (CCDC FIJBEI) by Na$^+$ ions yielding dimer **Na$_2${[(α-BuO)$_8$Pc]Tb(Pc)}$_2$** (CCDC FIJBIM). Reproduced from (a) ref. 105 with permission from the Royal Society of Chemistry. Adapted with permission from (b) ref. 67. Copyright 2018, Wiley-VCH.

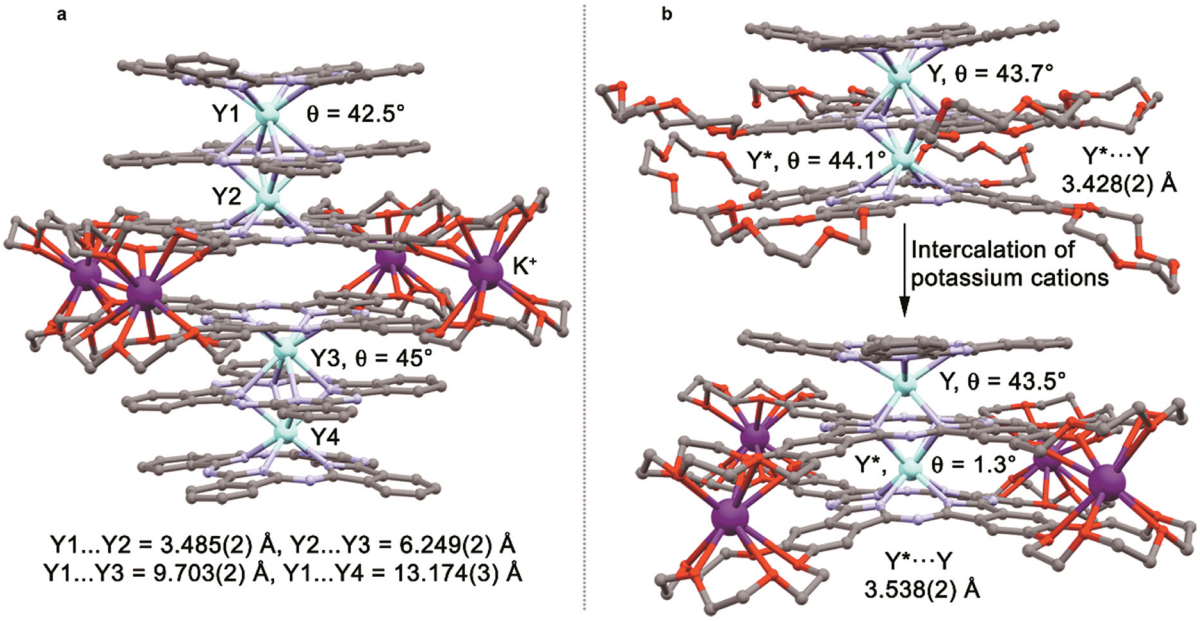

Fig. 22 X-ray structure of the supramolecular assemblies formed by heteroleptic Y^{3+} crown-phthalocyaninates. (a) Dimer formed by **[(15C5)$_4$Pc]Y(Pc)Y(Pc)** (CCDC SULZIL) in the presence of $KBPh_4$. (b) Intercalation of potassium cations between crown-substituted ligands of **[(15C5)$_4$Pc]Y[(15C5)$_4$Pc]Y(Pc)** (CCDC ITUJEP and ITUGUC)[333,334] without the formation of supramolecular dimers. Tetraphenylborate ions, hydrogen atoms and solvent molecules are not shown for clarity.

Compared to the monomeric complex **H[(α-BuO)$_8$Pc]Tb(Pc)** (U_{eff} = 125 cm^{-1}), the corresponding dimer complex **Na$_2${[(α-BuO)$_8$Pc]Tb(Pc)}$_2$** shows a larger U_{eff} value (367 cm^{-1}). The DC magnetic measurements imply that the Tb^{3+}–Tb^{3+} magnetic interactions in **Na$_2${[(α-BuO)$_8$Pc]Tb(Pc)}$_2$** are very weak. Therefore, the change in the stacking angle from $\theta = 28^\circ$ to $\theta = 34^\circ$ upon Na^+ coordination is the main reason for the increase in U_{eff}.

3.3.2 Rare-earth-fused phthalocyaninato sandwich complexes. The distance between spins and their placement are important factors that influence SMM characteristics. QTM can be effectively suppressed by arranging the **Tb(Pc)$_2$** units on the magnetic anisotropy axis (C_4 rotation axis) at the distance at which the magnetic dipole interactions are maximized (closest Tb···Tb distance: *ca.* 0.62 Å).[67,105] To put it simply, the vertical stacking of **Tb(Pc)$_2$** improves SMM characteristics and suppresses the QTM. This raises the naive question, ''How does the geometry of the **Ln(Pc)$_2$/Ln$_2$(Pc)$_3$** units affect the SMM characteristics?'' Klyatskaya *et al.* reported that effective through-space π–π interactions between pyrene-substituted unsymmetrical complexes **[(Pyrene)Pc]Ln(Pc)**, Ln = Tb, Dy, and Ho lead to the formation of head-to-tail π dimers with closest Tb···Tb distance: *ca.* 13.08 Å (Fig. 4).[115] We now summarize the research results related to the effects of through-bond interactions in **Ln^{3+}–Pc** sandwich complexes on their SMM properties.

In 2013, Wang *et al.* prepared the first biradical dinuclear Dy^{3+} triple-decker SMM with a fused phthalocyanine ligand **(Pc)Dy(f-Pc$_2$)Dy(Pc)^{OBu}** (Scheme 42 and Fig. 23a).[328] The distance between the Dy^{3+} ions coordinated to the fused ring Pc^{4-} is 10 Å or more and π–f interactions are observed. The π-bridge

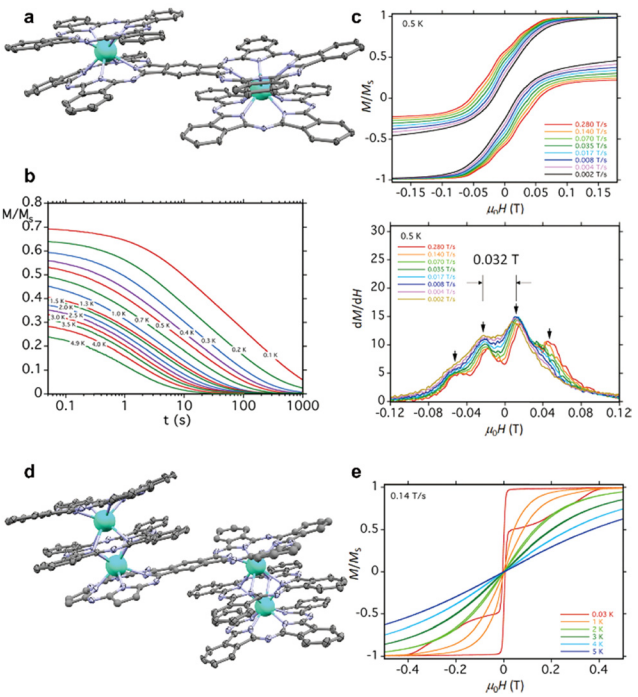

Fig. 23 Crystal structure of (a) **(Pc)Ln(f-Pc$_2$)Ln(Pc)^{OBu}** (Ln^{3+} = Dy and Tb) and (d) **(Pc)$_2$Ln$_2$(f-Pc$_2$)Ln$_2$(Pc)$_2^{OBu}$** (Ln^{3+} = Tb and Dy) and the micro-SQUID-measurement magnetization decay curves (b) and hysteresis loops for oriented crystalline samples of (c) **(Pc)Tb(f-Pc$_2$)Tb(Pc)^{OBu}** and (e) **(Pc)$_2$Dy$_2$(f-Pc$_2$)Dy$_2$(Pc)$_2^{OBu}$**. Molecular structures of (a) and (d) based on the cif files from ref. 217 and 220. Protons and *n*-butoxy groups in **(Pc)Ln(f-Pc$_2$)Ln(Pc)^{OBu}** and **(Pc)$_2$Ln$_2$(f-Pc$_2$)Ln$_2$(Pc)$_2^{OBu}$** are omitted for clarity. Adapted with permission from (a and b) ref. 217. Copyright 2018, American Chemical Society. Adapted with permission from (d and e) ref. 220. Copyright 2018, Wiley-VCH.

delocalized biradical antiferromagnetic interactions effectively suppress the QTM of the Dy^{3+}-ion-based SMMs, and at temperatures of up to 5 K, butterfly-type magnetic hysteresis with H_C was observed.

In 2018, Morita *et al.* prepared the first dinuclear Tb^{3+} fused-Pc^{4-} triple-decker SMM (abbreviated as **(Pc)Tb(f-Pc$_2$)Tb(Pc)^{OBu}**).[217] The complex shows an open hysteresis loop with H_C = 180 Oe at 1.8 K (these values were obtained from the magnetic data for a magnetically diluted sample). From the crystal structure, the twist angle (θ) between the Pc ligands was determined to be 45°, which indicates an SAP coordination environment. The strict SAP coordination caused the absence of the off-diagonal LF terms (B_k^q; $q \neq 0$), which eliminates the tunneling gap (ΔE) *via* level-crossings in the ground state, meaning that QTM processes are suppressed. In addition, solution ^{1}H NMR measurements of **(Pc)Tb(f-Pc$_2$)Tb(Pc)^{OBu}** show that the coordination environment of the Tb^{3+} ions affects the anisotropic magnetic susceptibility (χ_{ax}). Incorporating radicals improves the magnetic properties, as radical-bridged metal complexes exhibit slow magnetic relaxation dynamics due to suppressed QTM, exhibiting high T_B values due to strong exchange coupling J_{ex} in comparison with non-radical systems.[239,337–339] However, it is not necessary to incorporate strong magnetic interactions between the Ln^{3+} ions and radical ligands, as shown by **(Pc)Tb(f-Pc$_2$)Tb(Pc)^{OBu}**. Although the induced intramolecular magnetic interactions using the molecular design of **(Pc)Tb(f-Pc$_2$)Tb(Pc)^{OBu}** are weak, these interactions play a role in suppressing QTM processes. This prediction was supported by DFT calculations, which were used to analyse the exchange couplings in the complex. The obtained results indicated the presence of magnetic interactions among the four spin centres, including indirect Tb^{3+}–Tb^{3+} interactions through π-radicals. On the other hand, hyperfine couplings (0.015 cm^{-1}) were observed for an oriented crystalline sample in micro-SQUID measurements (Fig. 23b and c), indicating that the inter- and intramolecular magnetic interactions were very weak, with smaller couplings than that for **Tb(Pc)$_2^-$** (0.017 cm^{-1}).[276] Magnetic hysteresis loops with H_c = 860 Oe at 1.8 K were observed for a crystalline sample of **(Pc)Tb(f-Pc$_2$)Tb(Pc)^{OBu}** (Fig. 23). Considering the relationship between the molecular arrangement and H_c, the weak intermolecular magnetic interactions are more effective in suppressing QTM. These results indicate that the collinearity of magnetic dipole–dipole interactions strongly affects the suppression of QTM.

In 2013, Morita *et al.* prepared the first tetranuclear Tb^{3+} fused-phthalocyaninato quintuple-decker SMM (Fig. 23c) by using a fused phthalocyaninato ligand to control the spatial arrangement of the Tb^{3+} ions in the SMM **(Pc)$_2$Tb$_2$(f-Pc$_2$)Tb$_2$(Pc)$_2^{OBu}$**.[219] In DC magnetic susceptibility measurements, ferromagnetic interactions among the four Tb^{3+} ions in **(Pc)$_2$Tb$_2$(f-Pc$_2$)Tb$_2$(Pc)$_2^{OBu}$** were observed, with two kinds of magnetic dipole–dipole interactions. **(Pc)$_2$Tb$_2$(f-Pc$_2$)Tb$_2$(Pc)$_2^{OBu}$** can be described as a weakly ferromagnetically coupled dimer of the SMM **Tb$_2$[(BuO)$_8$Pc]$_3$**[319] with strong dipole–dipole interactions in the triple-decker moieties and weak dipole–dipole interactions through the fused-Pc^{4-} linking the two **Tb$_2$[(BuO)$_8$Pc]$_3$** units. Dual magnetic relaxation processes were observed in **(Pc)$_2$Tb$_2$(f-Pc$_2$)Tb$_2$(Pc)$_2^{OBu}$**, similar to those in other dinuclear Tb^{3+}–Pc complexes.[211,317,340] This provides clear evidence that the magnetic relaxation phenomena depend heavily on the magnetic dipole interactions between the Tb^{3+} ions in **(Pc)$_2$Tb$_2$(f-Pc$_2$)Tb$_2$(Pc)$_2^{OBu}$**.

In 2018, Katoh *et al.* reported the magnetic properties and spin-relaxation processes of the tetranuclear Dy^{3+} fused-phthalocyaninato quintuple-decker SMM **(Pc)$_2$Dy$_2$(f-Pc$_2$)Dy$_2$(Pc)$_2^{OBu}$** and its crystal structure (Fig. 23d and e).[220] The structure of **(Pc)$_2$Dy$_2$(f-Pc$_2$)Dy$_2$(Pc)$_2^{OBu}$** can be regarded as a dimer of **Dy$_2$[(BuO)$_8$Pc]$_3$** SMMs[341] with different magnetic relaxation behaviour corresponding to the octacoordination-geometry sites Dy1 with a C_4 symmetry (θ_1 = 23°) and Dy2 with a D_{4d} symmetry (θ_2 = 45°). The lowest Kramers doublet (KD) of **(Pc)$_2$Dy$_2$(f-Pc$_2$)Dy$_2$(Pc)$_2^{OBu}$** is thought to be a mixed state of $m_J = \pm 13/2$ and $\pm 11/2$. At an H_{dc} of 1750 Oe and T range of 1.8–3.75 K, the QTM is suppressed, and the direct process is enhanced; these depend on the different coordination environments. Consequently, the coordination geometry plays a more significant role in the spin-relaxation phenomena of **(Pc)$_2$Dy$_2$(f-Pc$_2$)Dy$_2$(Pc)$_2^{OBu}$** than the dipolar bias between Dy^{3+} ions.[341,342] The different conclusions for the Tb^{3+} and Dy^{3+} systems are attributable to the ground m_J state for their coordination geometries.[36,84,233,242,252,276,284–287]

These studies show that the SMM properties can be fine-tuned by introducing magnetic dipole–dipole interactions in a controlled SMM spatial arrangement. In addition, we can expect to obtain nuclear spin molecular qubits using the spin cascade $|S = 1/2\rangle \| J = 6\rangle \| I = 3/2\rangle$ of the **Tb(Pc)$_2$** system by taking advantage of the more complex intramolecular magnetic interactions in **(Pc)Tb(f-Pc$_2$)Tb(Pc)^{OBu}**.[270,303,308]

3.3.3 Crystal engineering of rare-earth-phthalocyaninato sandwich complexes for one-dimensional spin arrangement. Self-assembly *via* coordination bonds and supramolecular approaches are effective methods of controlling the geometric spin arrangement. It is possible to rationally design molecule-based magnetic materials with zero-dimensional (0D), one-dimensional (1D), two-dimensional (2D), and three-dimensional (3D) structures with a variety of properties, such as electronic and ionic conduction, gas adsorption, and stimulus-induced switching characteristics.[343] This concept has been a huge success in improving the functionalities of **Ln(Pc)$_2$**-based SMMs.

Tb(Pc)$_2^0$ can be used in molecular spintronics due to its SMM characteristics and its physical and chemical stability.[344] Investigating the influence of the direction of the magnetic dipole interactions acting among the **Tb(Pc)$_2^0$** SMMs in the bulk solid on the magnetic relaxation behaviour is important for controlling its magnetic properties, which depend on the molecular arrangement.[345,346] In 2017, Yamabayashi *et al.* showed that the arrangement of the **Tb(Pc)$_2^0$** SMMs in crystals affects the ground state, and that QTM is suppressed at low temperatures.[347] As a result, it has been suggested that QTM depends on the orientation angle (σ) of the uniaxial magnetic anisotropy with respect to the vector connecting the Tb^{3+} ions. In addition, QTM is

suppressed in the **Tb(Pc)$_2$** dimer when the **Tb(Pc)$_2$** units are connected with a spacer acting as a H_{bias} *via* through-space magnetic dipole interactions (dipolar bias).[105] Moreover, it is possible to eliminate the influence of the transverse field by arranging the Tb^{3+} ions in the direction of the C_4 axis.[97] The probability of QTM occurring in one **Tb(Pc)$_2$** unit is P_{QTM}, and the probability of QTM occurring simultaneously in a **Tb(Pc)$_2$** dimer is $P_{QTM}{}^2$, indicating that QTM is effectively suppressed.

Magnetic dipole interactions are dominant in quasi-1D molecular magnetic materials, in which **(Nc)Tb(Pc)** SMM units adopt a structure similar to that of **Tb(Pc)$_2$** SMMs (Fig. 24b). In 2018, Katoh *et al.* reported that the magnetic properties of **(Nc)Tb(Pc)$^{0/+}$** (neutral **(Nc)Tb(Pc)^0**: U_{eff} = 652 cm^{-1} with τ_0 = 2.5 × 10^{-12} s; cationic **(Nc)Tb(Pc)$^+$**: U_{eff} = 584 cm^{-1} with τ_0 = 5.5 × 10^{-12} s) with 1D structures are significantly different from those of a magnetically diluted sample (**(Nc)Tb$_{0.1}$Y$_{0.9}$(Pc)^0**: U_{eff} = 342 cm^{-1} with τ_0 = 1.1 × 10^{-8} s).[136] In particular, the τ of **(Nc)Tb(Pc)$^+$** (22 s at 1.8 K) in the low-temperature region is five orders of magnitude slower than that of **(Nc)Tb$_{0.1}$Y$_{0.9}$(Pc)^0** (1.2 ms at 1.8 K). Furthermore, the H_C of **(Nc)Tb(Pc)$^+$** was retained at temperatures of up to *ca.* 20 K, which is the T_B. The single-ion anisotropy of the Tb^{3+} ions in a 1D structure and the magnetic dipole interactions acting among the molecules determine the direction of the magnetic properties. These results show that the spin dynamics can be improved by manipulating the arrangement of the SMMs in the solid state. There are clear advantages to using quasi-1D SMM systems with magnetic dipole interactions such as **(Nc)Tb(Pc)$^{0/+}$**. This strategy could lead to dramatic changes in the spin-blocking phenomena, because τ is slower at a zero magnetic field. In other words, since the probability of QTM occurring in **(Nc)Tb(Pc)$^+$** is $P_{QTM}{}^n$ ($n > 2$), the QTM is effectively suppressed in a 1D system. Therefore, this relatively simple molecular-design method can be used to construct a variety of **Ln(Pc)$_2$**-SMM-based functional molecular magnetic materials, and new functionalities, such as electronic and ionic conduction, gas adsorption, and various switching characteristics, can be incorporated by controlling the pore size.

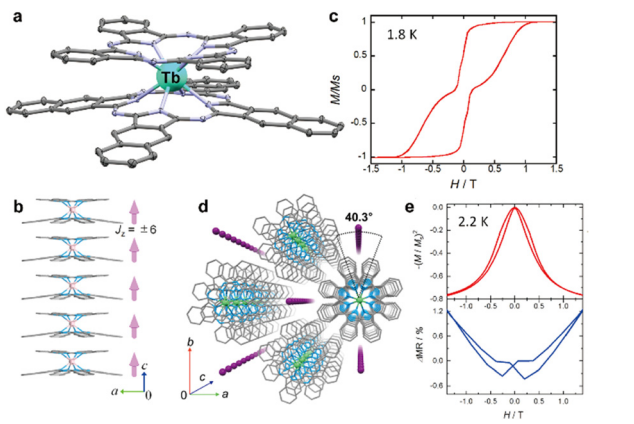

Fig. 24 (a) Crystal structure of **[(Nc)Tb(Pc)]$^+$PF$_6^-$** (CCDC YICQIN). Hydrogen atoms and the PF_6^- anion are omitted for clarity. (b) 1D structure of **[(Nc)Tb(Pc)]$^+$PF$_6^-$** along the *c*-axis. (c) *MH* measurement hysteresis loop with a coercivity (H_C) of 150 mT (1500 Oe) for a single crystal of **[(Nc)Tb(Pc)]$^+$PF$_6^-$** at 1.8 K (*H*//*c*-axis). The data were normalized to the value in a field of 7 T. (d) 1D structure of **[Dy(Pc)$_2$]I$_x$** along the *c*-axis. Hydrogen atoms are omitted for clarity. (e) *MH* curve of **[Dy(Pc)$_2$]I$_x$** for a polycrystalline sample at 2.2 K (top). Magnetoresistance (MR) measurement of **[Dy(Pc)$_2$]I$_x$** for a single crystal at 2.2 K. Adapted with permission from (a–c) ref. 136 and (d and e) ref. 348. Copyright 2018 and Copyright 2021, Wiley-VHC.

These **Ln(Pc)$_2$**-SMM-based materials are expected to exhibit galvanomagnetic effects due to the correlation between the localized f electrons and conduction electrons. There have been several reports of partially oxidized 1D **[Ln(Pc)$_2$]I$_x$** complexes (Ln = Ce, Pr, Sm, Ho, and Yb).[349–353] In 2021, a 1D arrangement of a partially oxidized Dy^{3+} double-decker SMM, **[Dy(Pc)$_2$]I$_x$** (1.95 < *x* < 2.26), was reported by Sato *et al.* (Fig. 24d).[348] Comparison of the Arrhenius plots with those of a magnetically diluted sample **[Dy$_{0.02}$Y$_{0.98}$(Pc)$_2$]I$_x$** revealed that the τ for **[Dy(Pc)$_2$]I$_x$** is four times slower at 1.8 K (**[Dy(Pc)$_2$]I$_x$**: 0.0050 s; **[Dy$_{0.02}$Y$_{0.98}$(Pc)$_2$]I$_x$**: 0.0013 s), and that its QTM at low temperatures is suppressed by the dipolar bias in the 1D array. In **[Dy(Pc)$_2$]I$_x$**, the Pc ligands were partially oxidized, and the I_3^- ion was present as a counter ion. Based on the polarised reflection spectra of **[Dy(Pc)$_2$]I$_x$**, the π-radicals were delocalized in a 1D column and behaved as a conductor even at low temperatures. Given that conductivity was observed at temperatures lower than T_B, the negative magnetoresistance (MR) effects of *ca.* 1% corresponding to the magnetic hysteresis of the SMM were observed when the galvanomagnetic characteristics were investigated at 2.2 K. This indicated that the galvanomagnetic properties between the SMMs and the electrical conduction characteristics due to the π–f interactions could be observed. Our groups are continuing to investigate the galvanomagnetism due to π–f interactions in partially oxidized **[Ln(Pc)$_2$]I$_x$** 1D complexes. This strategy may pave the way for the construction of electro-conductive SMMs as molecular spintronic devices *via* a spin-cascade system.

3.3.4 Cocrystals of rare-earth phthalocyaninato sandwich complexes and fullerenes. In this section, we review the effects of supramolecular assembly with fullerenes on the SMM properties. Supramolecular complexes between porphyrin (Por^{2-}) moieties and (C60-Ih)[5,6]fullerene (C_{60}), and/or fullerene derivatives, have been investigated in detail with respect to host–guest chemistry and electronic structures.[354–359] In fullerene–porphyrin systems, a close contact between the molecules and selective supramolecular interactions is generated. C_{60} regioselectively binds at the centre of the porphyrin complex *via* a molecular recognition process supported by the non-planar deformation of the porphyrin ligand, which matches the convex shape of C_{60}. Since the LF around the Ln^{3+} ions affects their charge density, researchers have focused on ways to control the magnetic properties of Ln^{3+} SMMs *via* supramolecular assembly with a fullerene. The coordination geometry significantly affects the spin-relaxation phenomena of **Ln^{3+}–Pc/Por** multiple-decker complexes.[105,122,317,341] In particular, **Ln$_2$(Pc)$_3$** complexes have an important advantage over **Ln(Pc)$_2$** complexes as the magnetic relaxation processes

correspond to the Zeeman splitting when two 4f spin systems are present.[67,211,219,220,319,326,330,340–342]

In 2014, Wang *et al.* reported cocrystals of C_{60} with the SMM **(Pc)Dy(TCIPP)**, along with the relationship among the coordination environment, intermolecular interactions, and the SMM behaviour.[360] Focusing on the twist angle θ between the ligands, it has been reported that the initial angle (43.60° for **(Pc)Dy(TCIPP)**) does not change dramatically after co-crystallisation (41.22°/44.45° for **(Pc)Dy(TCIPP)·0.5C$_{60}$**, 44.41° for **(Pc)Dy(TCIPP)·C$_{60}$**, and 44.35° for **(Pc)Dy(TCIPP)·2C$_{60}$**). However, the frequency (ν) dependences of the alternating current (AC) measurements changed due to the different molecular arrangements, depending on the number of incorporated C_{60} molecules.

Combining a triple-decker SMM with C_{60} can be expected to reduce the overall symmetry and thus reveal the effects of the LF term. In 2020, Katoh *et al.* reported the dinuclear Tb^{3+} triple-decker complex **(TPP)Tb(Pc)Tb(TPP)**, which contains porphyrin units on the outside to bind with C_{60} (henceforth abbreviated as **[(TPP)Tb(Pc)Tb(TPP)]·C$_{60}$**).[321] The supramolecular complex **[(TPP)Tb(Pc)Tb(TPP)]·C$_{60}$** (Fig. 25a and b) was prepared by assembling C_{60} with the dinuclear Tb^{3+} triple-decker complex **(TPP)Tb(Pc)Tb(TPP)** with quasi-D_{4h} symmetry to investigate the relationship between the coordination symmetry and SMM properties (Fig. 25e and f). The two Tb^{3+} sites of **(TPP)Tb(Pc)Tb(TPP)** are equivalent, and θ was determined to be 3.62° (Fig. 25d). On the other hand, the two Tb^{3+} sites of **[(TPP)Tb(Pc)Tb(TPP)]·C$_{60}$** are not equivalent. The θ values for sites Tb1 and Tb2 were determined to be 3.67° and 33.8°, respectively, due to a change in the coordination symmetry of **(TPP)Tb(Pc)Tb(TPP)** upon association with C_{60} (Fig. 25c). At 1.8 K, **(TPP)Tb(Pc)Tb(TPP)** and **[(TPP)Tb(Pc)Tb(TPP)]·C$_{60}$** undergo different magnetic relaxations, and the changes in the ground state affect the spin dynamics. **(TPP)Tb(Pc)Tb(TPP)** and **[(TPP)Tb(Pc)Tb(TPP)]·C$_{60}$** relax *via* QTM at zero H_{dc}, and the H dependences of their τ values are similar at $H > 1500$ Oe. On the other hand, at $H < 1500$ Oe, their τ values show different behaviour, since the off-diagonal terms (B_k^q; $q \neq 0$) affect the magnetic relaxation mechanism. Based on the temperature and H dependences of τ, the spin dynamics can be explained by spin–phonon interactions together with the direct and Raman mechanisms. Thus, a supramolecular approach can be used to control the magnetic anisotropy along the C_4 rotation axis and the spin-dynamic properties in **Ln^{3+}–Pc** multiple-decker complexes.

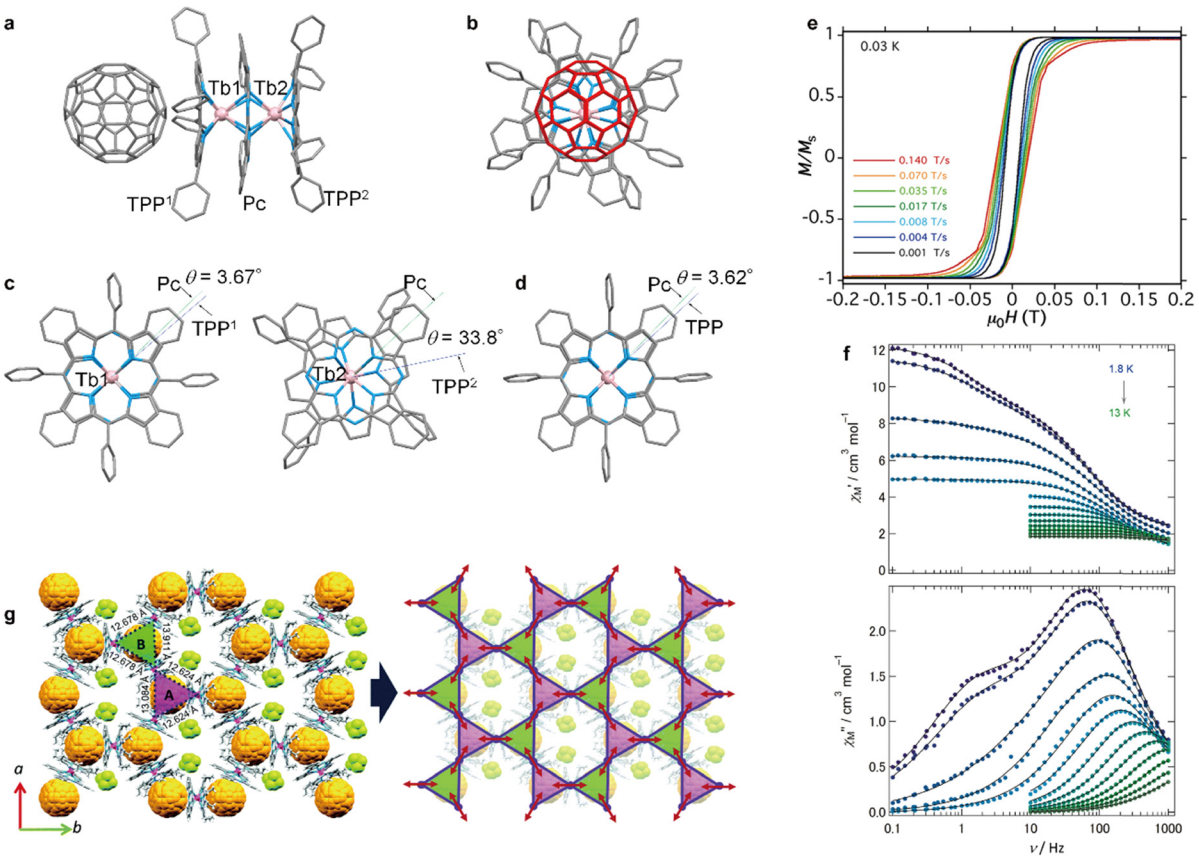

Fig. 25 Cocrystals of rare-earth phthalocyaninato sandwich complexes and fullerene derivatives. (a–c) Crystal structure of **[(TPP)Tb(Pc)Tb(TPP)]·C$_{60}$**. The inclusion of C_{60} changes the coordination environment of the Tb^{3+} ion and affects the SMM characteristics. (d) Coordination environment of **(TPP)Tb(Pc)Tb(TPP)** before the subsumption of C_{60}. The micro-SQUID-measurement hysteresis loops (e) and alternating current (AC) magnetic susceptibility data (f) of **[(TPP)Tb(Pc)Tb(TPP)]·C$_{60}$**. (g) The cocrystal **[(Pc)Tb(OEP)]$_3$(Li$^+$@C$_{60}$·PF$_6^-$)$_2$** forms a quasi-kagome lattice due to the two kinds of isosceles triangles (A and B). Protons and crystal solvents of **[(TPP)Tb(Pc)Tb(TPP)]·C$_{60}$** and **[(Pc)Tb(OEP)]$_3$(Li$^+$@C$_{60}$·PF$_6^-$)$_2$** are omitted for clarity. Adapted with permission from (a–f) ref. 321. Copyright 2020, Wiley-VHC. Reproduced from (g) ref. 361 with permission from the Royal Society of Chemistry.

In 2020, Iwami *et al.* reported the cocrystallisation of a lithium-ion-encapsulating fullerene ($Li^+@C_{60}$), C_{60} and C_{70} with a **(Pc)Tb(OEP)** SMM (Fig. 25g).[361] The OEP unit interacted with the fullerene derivatives to form five different cocrystals: **[(Pc)Tb(OEP)]$_3$($Li^+@C_{60}\cdot PF_6^-$)$_2$**, **[(Pc)Tb(OEP)]($Li^+@C_{60}\cdot BF_4^-$)**, **[(Pc)Tb(OEP)]$C_{70}\cdot C_6H_{14}$**, **[(Pc)Tb(OEP)]$C_{60}\cdot C_6H_{14}$**, and **[(Pc)Tb(OEP)]-$C_{60}\cdot Et_2O$**. For the cocrystals containing $Li^+@C_{60}$ (**[(Pc)Tb(OEP)]$_3$-($Li^+@C_{60}\cdot PF_6^-$)$_2$** and **[(Pc)Tb(OEP)]($Li^+@C_{60}\cdot BF_4^-$)**), the use of different counter anions resulted in different crystal packings. In particular, **[(Pc)Tb(OEP)]$_3$($Li^+@C_{60}\cdot PF_6^-$)$_2$** was found to have a unique quasi-kagome lattice packing that induces intermolecular ferromagnetic interactions. Depending on the crystallisation conditions, different packings, *i.e.*, 1D column packings for **[(Pc)Tb(OEP)]($Li^+@C_{60}\cdot BF_4^-$)** and **[(Pc)Tb(OEP)]$C_{70}\cdot C_6H_{14}$** and AABB-type arrays of **(Pc)Tb(OEP)** and C_{60} dimers for **[(Pc)Tb(OEP)]$C_{60}\cdot C_6H_{14}$** and **[(Pc)Tb(OEP)]$C_{60}\cdot Et_2O$**, were formed. In addition, the magnetic properties of the **(Pc)Tb(OEP)** units were modulated *via* cocrystallisation.

The relationship between the changes in the coordination geometry of the same molecule and the SMM properties induced *via* a supramolecular approach was also investigated. The corresponding results showed that the magnetic anisotropy along the C_4 rotation axis of the metal sites in the dinuclear **Ln^{3+}–Pc** multiple-decker complexes could be controlled by forming a supramolecular complex, which could lead to switchable SMMs.

3.4 Correlation between redox states and SMM properties

Porphyrinoids are redox-active ligands due to their extended π-systems and high redox stability. Therefore, sandwich complexes composed of porphyrinoids are also redox active. In this section, we will explain the relationship between redox states and SMM properties. The Ln^{3+} ions (except for Ce^{3+}) are in essence redox inert. Therefore, the redox reactions of the sandwich complexes presented here occur on the porphyrinoid ligands.

Ishikawa and Takamatsu *et al.* reported that the U_{eff} values of the anionic forms of the double-decker complexes **(NBu_4^+)-{Tb[$(EtO)_8Pc]_2$}$^-$** and **(NBu_4^+){Dy[$(EtO)_8Pc]_2$}$^-$** are enhanced in their corresponding cationic forms, **{Tb[$(EtO)_8Pc]_2$}$^+$($SbCl_6^-$)**[84] and **{Dy[$(EtO)_8Pc]_2$}$^+$($SbCl_6^-$)**.[362] The mechanism of the structural changes due to the redox reactions can be explained using molecular orbital theory[363] (Fig. 26a and b). As was briefly introduced in Section 3.2, the oxidized species of Tb^{3+}–Pc and Dy^{3+}–Pc double-decker complexes tend to show improved SMM properties compared to the reduced ones due to the short ligand-to-metal distance in the oxidized form, which result in greater LF splitting and U_{eff} values. The molecular orbitals of the sandwich complexes are constructed from the combination of the Pc ligands. The stacked dimerisation shown in the double-decker complexes constructs the antibonding HOMO orbital and the bonding HOMO−1 orbital (Fig. 26a). The removal of electrons (oxidation of the complex) increases the bond order between the ligands, causing axial compression and a decrease in the interligand distance. Although this mechanism is widely accepted, recent *ab initio* calculations based on

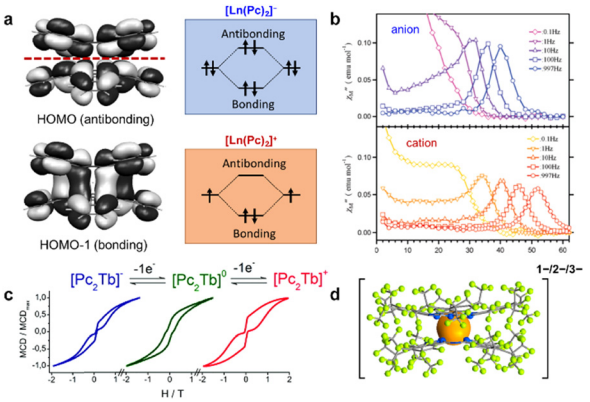

Fig. 26 (a) Molecular orbitals of **[Ln(Pc)$_2$]$^-$**. Removal of two electrons from the antibonding HOMO affords the cationic form **[Ln(Pc)$_2$]$^+$** with a shorter Ln^{3+}–Pc distance. (b) χ_M'' *vs.* *T* plots for anionic (**(NBu_4^+){Tb[$(EtO)_8Pc]_2$}$^-$**) and cationic (**{Tb[$(EtO)_8Pc]_2$}$^+$($SbCl_6^-$)**) Tb^{3+} double-decker complexes. (c) Magnetic hysteresis behaviour of a Tb^{3+} double-decker complex in a series of redox states (**[Tb(iprPc)$_2$]$^{-/0/+}$**) as captured using MCD spectroscopy. (d) Structure of the perfluoro double-decker complexes **[Tb(F64Pc)$_2$]$^{-/2-/3-}$**. Adapted with permission from (a) ref. 363. Copyright 2006, Elsevier Ltd. Adapted with permission from (b) ref. 84 (c) ref. 366 and (d) ref. 87. Copyright 2007, Copyright 2010 and Copyright 2013, American Chemical Society.

the CASSCF/RASSI-SO method have indicated that the magnitude of the LF splitting does not strongly depend on the structural changes induced by the redox reactions, and that the calculated energy levels of the first excited doublets ($|m_J\rangle$ = $|\pm5\rangle$) for Tb^{3+} double-decker complexes are *ca.* 300 cm^{-1}.[293,364,365] Therefore, the 8% increase in the U_{eff} of **(NBu_4^+){Tb[$(EtO)_8Pc]_2$}$^-$** due to oxidation may arise from thermally assisted QTM *via* higher excited LF sublevels.

In 2010, Gonidec *et al.* reported the magnetic properties of the various redox states of the double-decker complex **[Tb(iprPc)$_2$]$^{-/0/+}$** (iprPc = 2,3,9,10,16,17,23,24-octa(isopropylidenedioxy)phthalocyaninato) as detected using magnetic circular dichroism (MCD) spectroscopy (Fig. 26c).[366] The advantage of MCD is the measurement of the magnetic properties of the specimen in frozen solution states. Therefore, the effects of the intermolecular magnetic interactions and crystal packing, which could potentially affect the magnetic properties, can be minimized. The MCD intensity *vs.* magnetic field plots at 1.5 K show magnetic hysteresis for all redox states due to magnetisation blocking. **[Tb(iprPc)$_2$]$^-$** and **[Tb(iprPc)$_2$]$^+$** show butterfly-shaped hysteresis curves, and the opening of the curve is larger in **[Tb(iprPc)$_2$]$^+$**. Importantly, **[Tb(iprPc)$_2$]^0** (a ligand π-radical complex) shows clear opening of the hysteresis curve at zero DC magnetic field. These results clearly indicate that the ligand π-radical suppresses QTM.[277]

In 2010, the same group reported the magnetic properties (MCD spectra) of the highly reduced double-decker complex **[Tb($F_{64}Pc$)$_2$]$^{-/2-/3-}$** ($F_{64}Pc$ = 1,4,8,11,15,18,22,25-octakis-fluoro-2,3,9,10,16,17,23,24-octakis-perfluoro(isopropyl)phthalocyaninato) stabilized by electron-withdrawing fluoro groups (Fig. 26d).[87] Magnetic hysteresis behaviour was observed in all the reduced states. Among these, **[Tb($F_{64}Pc$)$_2$]$^{2-}$** showed the

largest magnetic hysteresis. The non-π-radical complexes ($[Tb(F_{64}Pc)_2]^-$ and $[Tb(F_{64}Pc)_2]^{3-}$) showed narrowing of the hysteresis curve at zero DC magnetic field, whereas the π-radical species $[Tb(F_{64}Pc)_2]^{2-}$ did not show such behaviour. Accordingly, the results of this study corroborate suppression of the QTM at the zero DC field due to a ligand π radical.

The first crystal structure characterisation of the dianionic double-decker complex $[Cryptand(Na^+)]_2[Tb(Pc)_2]^{2-}$ was reported by Konarev *et al.* in 2019.[85] The existence of the ligand π-radical was confirmed based on near-IR absorption and EPR analyses. The interligand distance in $[Cryptand(Na^+)]_2[Tb(Pc)_2]^{2-}$ (3.258 Å) is shorter than that (3.294 Å) in the monoanionic form $(PPN^+)[Tb(Pc)_2]^-$ (PPN^+ = bis(triphenylphosphoranylidene)ammonium). Interestingly, $[Cryptand(Na^+)]_2[Tb(Pc)_2]^{2-}$ does not show slow magnetic relaxation or magnetic hysteresis at 1.9 K, which may be related to the relatively strong intermolecular antiferromagnetic interactions confirmed by the DC magnetic susceptibility measurements.

In 2020, Horii *et al.* reported a comprehensive study on the structural and magnetic properties of multiple-decker Tb^{3+}-$(BuO)_8Pc$ complexes (triple- ($Tb_2[(BuO)_8Pc]_3$), quadruple-($Tb_2Cd[(BuO)_8Pc]_4$), and quintuple-decker ($Tb_2Cd_2[(BuO)_8Pc]_5$) complexes) in highly oxidized states.[214] Crystal structure analyses and DFT calculations revealed that the multiple-decker complexes show decreasing interligand distances with successive oxidations. More importantly, paramagnetic NMR analyses in the solution state revealed that the axial component of the magnetic susceptibility (χ_{ax}) also decreases with successive oxidation (Fig. 27a). This behaviour stands in clear contrast to that of the double-decker complexes, in which χ_{ax} increases with oxidation.[278] In other words, the Tb^{3+} ions in the multiple-decker complexes show decreased magnetic anisotropy upon oxidation. A similar trend was confirmed in the AC magnetic measurements of the oxidized species characterized by X-ray analyses (Fig. 27b). In the case of the triple-decker complex $Tb_2[(BuO)_8Pc]_3$, the oxidation from the neutral to the two-electron-oxidized state $\{Tb_2[(BuO)_8Pc]_3\}^{2+}(SbCl_6^-)_2$ shifts the maxima of the χ_M'' *vs.* AC frequency (ν) plots to higher ν. In addition, the U_{eff} decreases from 233 cm^{-1} ($Tb_2[(BuO)_8Pc]_3$) to 167 cm^{-1} ($\{Tb_2[(BuO)_8Pc]_3\}^{2+}(SbCl_6^-)_2$) upon oxidation. In the case of the multiple-decker complexes, oxidation causes a decrease in the interligand distances as well as a decrease in the intermetal distances (Fig. 27c). Due to the approach of the positively charged metal ions along the axial direction, the axial LF is decreased. This is the reason for the decrease in U_{eff} upon oxidation of the multiple-decker complexes.

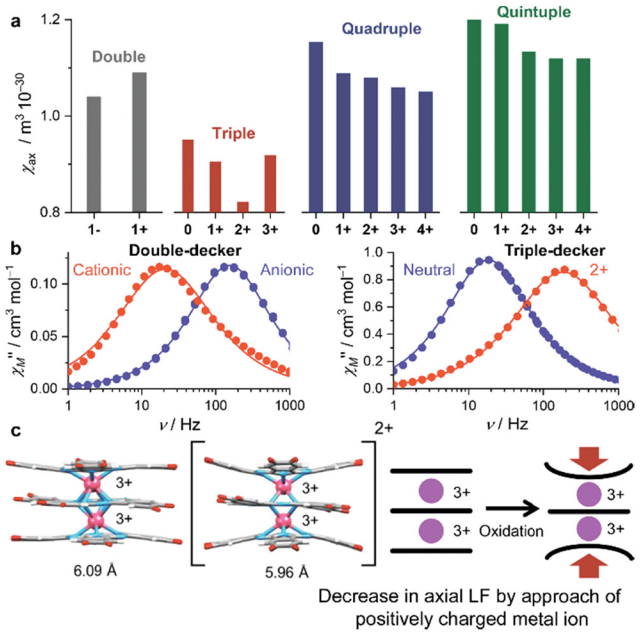

Fig. 27 (a) χ_{ax} values for the oxidation states of a $(BuO)_8Pc$ multiple-decker complex. (b) χ_M'' *vs.* frequency (ν) plots for the redox series of double and triple-decker complexes ($Tb_2[(BuO)_8Pc]_3$ and $\{Tb_2[(BuO)_8Pc]_3\}^{2+}(SbCl_6^-)_2$). (c) Crystal structures of $Tb_2[(BuO)_8Pc]_3$ and $\{Tb_2[(BuO)_8Pc]_3\}^{2+}(SbCl_6^-)_2$ from the cifs in ref. 319 and 214. *n*-Butoxy groups are omitted for clarity. The triple-decker complex shows a decrease in axial magnetic anisotropy upon oxidation due to the decrease in the LF with the approach of a positively charged Ln^{3+} ion along the axial direction. Adapted with permission from (a) ref. 214. Copyright 2020, Wiley-VHC.

3.5 Proton-induced switching of the SMM properties

Switching of the SMM properties *via* external stimuli has great importance for the use of SMMs as information-storage devices due to the requirement to eventually erase stored information.

Tanaka and Inose *et al.*[297,367] reported the switching of SMM properties *via* the protonation/deprotonation of the Tb^{3+}-porphyrinato double-decker complex $HTb(TPP)_2$. In the protonated form of $HTb(TPP)_2$, H^+ coordinates to one pyrrole N atom (Fig. 28a). The distance between Tb^{3+} and the protonated N atom is 2.840 Å; this value is significantly longer than the bond lengths between Tb^{3+} and the non-protonated N atoms (2.430–2.627 Å). In other words, the Tb^{3+} ion in $HTb(TPP)_2$ adopts a heptacoordinated structure. The significant deviation from the SAP geometry in $HTb(TPP)_2$ results in the absence of SMM behaviour. When the coordinated proton is removed by DBU (1,8-diazabicyclo[5.4.0]undec-7-ene), the deprotonated form $(HDBU^+)[Tb(TPP)_2]^-$ is obtained. $(HDBU^+)[Tb(TPP)_2]^-$ crystallizes in the space group I_4/mmm, and the eight N atoms coordinating to the Tb^{3+} ion are crystallographically equivalent. Therefore, the Tb^{3+} of $(HDBU^+)[Tb(TPP)_2]^-$ adopts an octacoordinated SAP geometry, which is one of the most ideal symmetries for SMMs. As a result, $(HDBU^+)[Tb(TPP)_2]^-$ shows slow magnetic relaxations and butterfly-shaped hysteresis, which are characteristics of SMMs. The conversion from $(HDBU^+)[Tb(TPP)_2]^-$ to $HTb(TPP)_2$ is achieved by the addition of acetic acid. Therefore, the protonation/deprotonation process is reversible, enabling the reversible switching of the SMM properties by a single proton.

The protonation/deprotonation of the phthalocyaninato-porphyrinato heteroligand double-decker complex H(Pc)Tb(TPP) was reported by Tanaka *et al.* (Fig. 28b).[368] This complex is obtained as the protonated form H(Pc)Tb(TPP), in which the proton coordinates to the *meso*-N of the Pc ligand. Since the

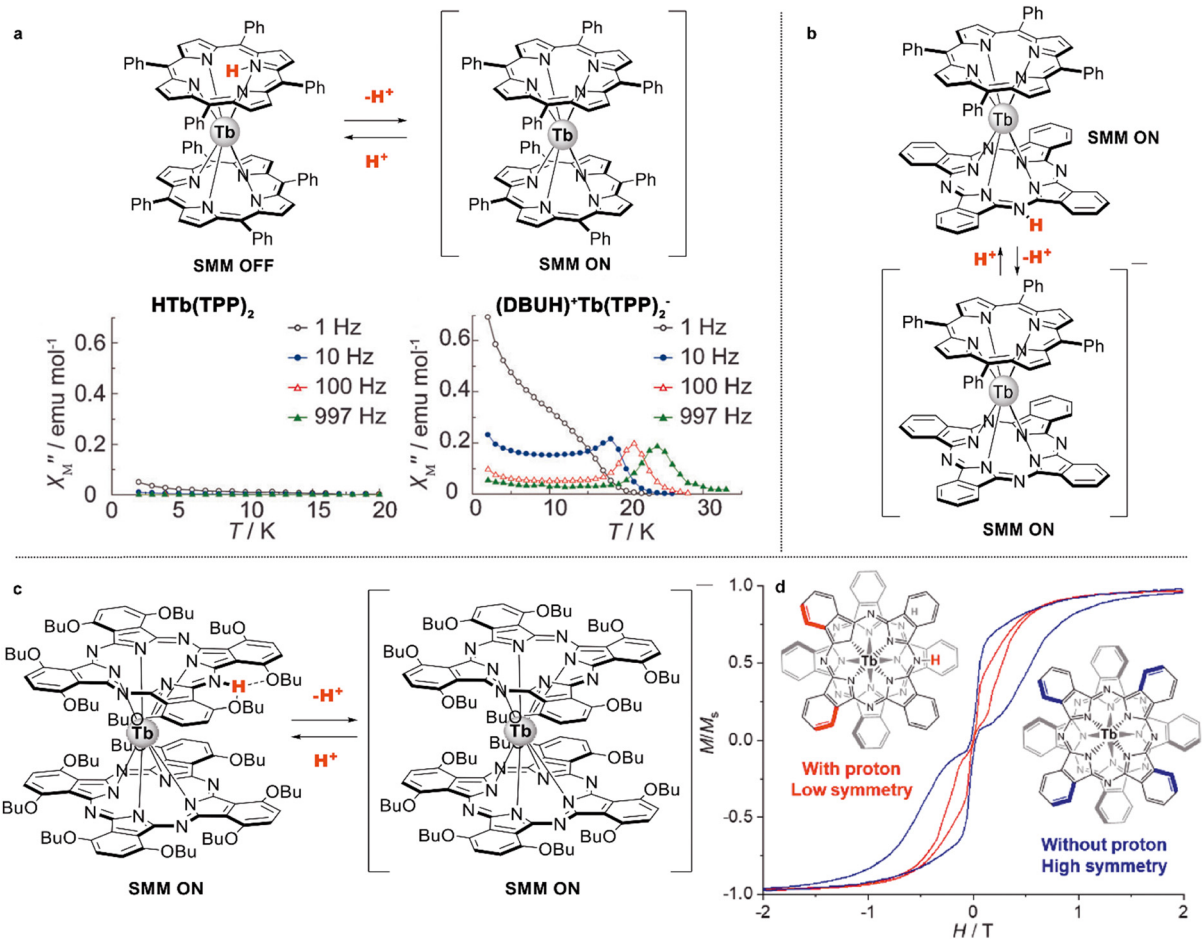

Fig. 28 (a) Proton-induced on/off switching of SMM properties (**HTb(TPP)$_2$** and **(HDBU$^+$)[Tb(TPP)$_2$]$^-$**). (b) Protonation/deprotonation of the porphyrinato–phthalocyaninato Tb^{3+} double-decker complex **H(Pc)Tb(TPP)** and (c) phthalocyaninato–phthalocyaninato double-decker complex **HTb[(α-BuO)$_8$Pc]$_2$**. (d) Magnetic hysteresis curves of the protonated (**HTb[(α-BuO)$_8$Pc]$_2$**) and deprotonated form (**(HDBU$^+$){Tb[(α-BuO)$_8$Pc]$_2$}$^-$**) of the double-decker complex. Reproduced from (a) ref. 297 with permission from the Royal Society of Chemistry. Adapted with permission from (d) ref. 97. Copyright 2018, American Chemical Society.

protonation/deprotonation occurs on the non-coordinating N atom, the changes in the SMM properties induced by deprotonation are not significant compared to those of the homoporphyrinato complexes. However, the protonated form shows additional magnetic relaxations at low temperatures.

The protonated forms of homo-phthalocyaninato Ln^{3+} double-decker complexes (Fig. 3) were obtained using the [(α-BuO)$_8$Pc] ligand,[95] which has eight *n*-butoxy groups at the nonperipheral positions of Pc, causing a saddle-shaped distortion of the π-structure (Fig. 3). This distortion causes the *meso*-N atoms of [(α-BuO)$_8$Pc] to be more basic than those in [(β-BuO)$_8$Pc]. In 2018, Horii *et al.* reported the modulation of the SMM properties of **HTb[(α-BuO)$_8$Pc]$_2$** *via* a protonation/deprotonation reaction (Fig. 28c).[97] The protonation of the *meso*-N atoms in **HTb[(α-BuO)$_8$Pc]$_2$** causes asymmetric distortion as well as a low-symmetry structure, whereas deprotonation using DBU affords **(HDBU$^+$){Tb[(α-BuO)$_8$Pc]$_2$}$^-$**, which is distorted in a highly symmetric windmill-like fashion. The deprotonated form shows larger magnetic hysteresis than the protonated one does. Similar trends were observed in magnetically diluted samples, indicating that the differences between the magnetic properties of the protonated and deprotonated forms originate from the molecular structures rather than the intermolecular magnetic interactions.

The following two examples also show changes in their SMM properties as a result of deprotonation. However, oxidation from the anionic (and protonated) form to the neutral (and deprotonated) form is the driving force for the deprotonation. In 2019, Chen *et al.* reported the magnetic properties of **HTb[(α-C$_5$H$_{11}$O)$_4$Pc]$_2$** with 3-pentyloxy-substituents (Fig. 3a).[94] The U_{eff} value for **HTb[(α-C$_5$H$_{11}$O)$_4$Pc]$_2$** is 300 cm^{-1}. On the other hand, the U_{eff} value for the neutral and deprotonated form **Tb[(α-C$_5$H$_{11}$O)$_4$Pc]$_2$** obtained using 2,3-dichloro-5,6-dicyano-1,4-benzoquinone (DDQ) is 324 cm^{-1}, indicating that the SMM properties are enhanced by deprotonation. In contrast to the previous examples, the presence of the ligand π-radical in **Tb[(α-C$_5$H$_{11}$O)$_4$Pc]$_2$** was confirmed by absorption spectroscopy. Therefore, Chen *et al.* concluded that the enhancement of the

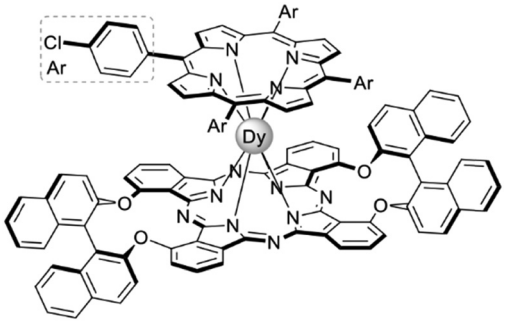

Fig. 29 Molecular structures of **Dy[(BNPO)$_2$Pc](TClPP)**.

SMM properties stems from the radical–f interactions and enhanced LF due to the shorter ligand-to-metal distances in the neutral form.

In 2019, Sun *et al.* reported the negative effect of deprotonation on SMM properties by comparison of the chiral (phthalocyaninato)(porphyrinato) Dy^{3+} double-decker complexes **(*R*)/(*S*)-H[(BNPO)$_2$Pc]Dy(TClPP)** and the corresponding neutral unprotonated species **(*R*)/(*S*)-[(BNPO)$_2$Pc]Dy(TClPP)** (Fig. 29).[369] The AC magnetic susceptibilities of the protonated form **(*R*)/(*S*)-[(BNPO)$_2$Pc]Dy(TClPP)** show clear frequency dependences, whereas **(*R*)/(*S*)-[(BNPO)$_2$Pc]Dy(TClPP)** shows no frequency dependence even under a bias DC field (H_{dc} = 2000 Oe). DFT calculations of **(*R*)/(*S*)-H[(BNPO)$_2$Pc]Dy(TClPP)** and **(*R*)/(*S*)-[(BNPO)$_2$Pc]Dy(TClPP)** revealed that the ionic part of the N–Dy bond decreases due to oxidation (deprotonation). This decrease in the electrostatic interactions between the ligand and Dy^{3+} decreases the uniaxial magnetic anisotropy of **(*R*)/(*S*)-[(BNPO)$_2$Pc]Dy(TClPP)**.

3.6 Influence of solvation effects in the crystal lattice on SMM properties

The benzene solvates **(μ-Pc)[Ln(dpm)$_2$]$_2$·2C$_6$H$_6$** showed interesting behaviour with respect to desolvation and exchange of solvation molecules. Thus, heating of solvates with Ln = Sm, Tb, Dy[198] and Er[199] at 100 °C was shown to cause desolvation without disintegration of crystals. This procedure had dramatic influences on the structural and magnetic properties of complexes which were demonstrated on a dysprosium analogue. The solvated complex contains one crystallographically independent metal center, which exhibits a single magnetic relaxation process with an energy barrier (U_{eff}) of 39 cm^{-1}. When desolvated, the complex had two different types of metal centres with slightly different surrounding, and it exhibited field-induced SMM behaviour with two thermally activated magnetic relaxation processes with U_{eff} which reach 44 cm^{-1} and 76 cm^{-1}, respectively. Soaking of desolvated crystals in benzene recovered **(μ-Pc)[Ln(dpm)$_2$]$_2$·2C$_6$H$_6$** which was confirmed by X-ray powder diffractions and elemental analyses.

This work confirmed that the solvated molecules can finely tune the magnetic relaxation mechanisms. Further development of this approach by Ge *et al.* showed that benzene can be replaced with dichloromethane in the course of "crystal to crystal" transformation.[200] Again, the change of solvation state had influence on the magnetic properties, which was demonstrated on the example of **(μ-Pc)[Er(dpm)$_2$]$_2$·2C$_6$H$_6$** undergoing transformation to **(μ-Pc)[Er(dpm)$_2$]$_2$·2CH$_2$Cl$_2$**.[200] Magnetic susceptibility measurements showed that the two solvates exhibited dramatically different relaxation behaviour (Fig. 30). While benzene solvate exhibited fast relaxation and an estimated energy barrier of 2.6 cm^{-1} under 600 Oe DC field, the dichloromethane solvate behaved as a field-induced SMM with a higher energy barrier (U_{eff}) of 34.3 cm^{-1}. The source of these magnetic differences was tentatively assigned to subtle structural differences caused by the change of the crystal lattice, as confirmed by *ab initio* calculations.

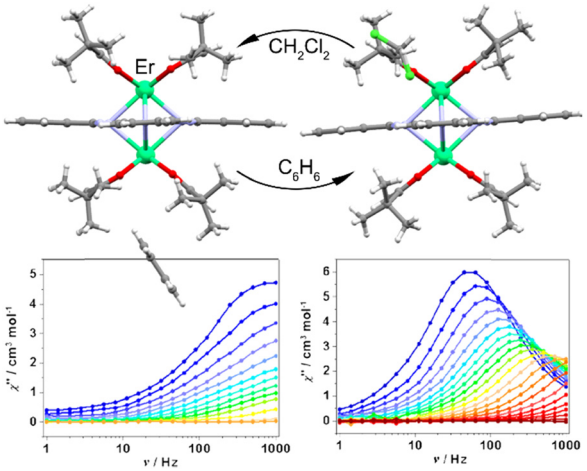

Fig. 30 Interconversion between solvates **(μ-Pc)[Er(dpm)$_2$]$_2$·2C$_6$H$_6$** (CCDC 1494900) and **(μ-Pc)[Er(dpm)$_2$]$_2$·2CH$_2$Cl$_2$** (CCDC 1494901) causing drastic change of magnetic relaxation as seen from the corresponding out-of-phase (χ'') AC susceptibility plots under 600 Oe DC field. Adapted with permission from ref. 200. Copyright 2017, American Chemical Society.

Ruan *et al.* showed that crystallization of **Tb(Pc)$_2$** from $CHCl_3$/MeOH or CH_2Cl_2/MeOH mixtures afforded orthorhombic crystals **Tb(Pc)$_2$** (space group $P2_12_12_1$) and **Tb(Pc)$_2$·CH$_2$Cl$_2$** (*Pnma*) solvates respectively.[370] Although the structural differences in magnetically active sandwich molecules were only subtle, absorption of CH_2Cl_2 in the crystal lattice had a profound effect on magnetic relaxation, resulting in a butterfly-shaped hysteresis loop in the case of solvate up to 10 K, while **Tb(Pc)$_2$** showed almost no opening even at 2 K. These results are consistent with the conclusions of Yamabayashi *et al.*, shown in Section 3.3.3.[347]

In the context of this result, an important study by Dailey and Besson on the selective crystallization of four possible polymorphs of **M(Pc)$_2$** complexes should be mentioned.[371] The authors proposed reproducible and selective crystallization techniques affording pure α-, γ- and δ-phases together with the CH_2Cl_2 solvate of complexes depending on the solvent, applied for crystallization. Systematic crystallographic and UV-Vis characterization of complexes allowed some of the confusion over chemical composition in previously published literature

associated with interconversion between neutral and ionic forms of bisphthalocyaninates to be explained.

3.7 Magnetic studies on surfaces

The properties of molecules significantly change not only through aggregation but also through the interface of organic–inorganic hybrid materials. One of the goals of the research involving sandwich-type tetrapyrrole rare-earth metal–inorganic hybrid materials is their application in spintronic devices.[344] In the case of **Tb(Pc)$_2^0$**, the magnetic species are composed of the f electron of the central Tb^{3+} ion and the π radical on the Pc ligands. The Pc ligands are almost flat, and the direction of the magnetic moment (axis of easy magnetisation) of the Tb^{3+} ion is perpendicular to the Pc ligand with uniaxially anisotropy, indicating that they are single-molecule magnets.[36] Furthermore, since they are thermally stable, they can be deposited on various substrates in an ultra-high vacuum (UHV). Several groups have reported on the structures and physical properties of sandwich-type tetrapyrrole rare-earth complexes on various substrates. In this section, we give an overview of the morphologies and magnetic properties of double-decker and triple-decker complexes on different substrates. Since 2008, many examples of **Ln(Pc)$_2$** and/or **Ln$_2$(Pc)$_3$** complexes on various substrates, including non-magnetic metals (Cu(100),[267] Cu(111),[372,373] Cu(001),[374] Au(111),[232,302] Ag(111),[375] Ir(111),[376] MgO/Ag(100),[377] CuO/Cu(110)[378]), magnetic metals (Co/Ir(111),[379] Co/Cu(100),[380] Co/Au(111),[299] Ni/Cu(100),[381] Ni/Ag(100),[381] Fe/Cu(100),[382] FeMn/Cu(100),[382] CoO/Ag(100),[383] Mn/Ag(100),[383] Ni(111)[384]), carbon-based substrates (HOPG,[385–387] graphite(0001),[388] graphene/SiC(0001),[389] graphene/Ni(111)[390]), silicon-based substrates (SiO_2(100)[391]), perovskite ($LaSrMnO_3/SrTiO_3$,[380] $SrVO_3$(001)[392]), and composite substrates,[393,394] have been reported. Moreover, materials of sandwich-type tetrapyrrole rare-earth metal complexes combined with carbon nanotubes (CNT)/fullerene are shown in Chapter 3.8. In general, eight lobes for both **Ln(Pc)$_2$** and/or **Ln$_2$(Pc)$_3$** are observed in topographic STM images,[301] which reflects the electronic state of the Pc ligand on the vacuum side. On the other hand, for **Ln(Pc)^x/Au(111)**, four lobes are observed in the topographic image.[232] In addition, the STM height profiles for **Ln(Pc)^x**, **Ln(Pc)$_2$**, and **Ln$_2$(Pc)$_3$** on substrates reflect the molecular structure (crystal structure).[301]

In recent years, physical properties of surfaces have been actively studied to advance the research on applications, and together with the progress of nanotechnology, the academic and social importance have increased. Precise control is possible at the atomic level, and organic–inorganic hybrid compounds can be prepared with the surfaces acting as reaction fields. Atoms and molecules adsorbed on surfaces can arrange into various dimensional structures (zero dimensional (0D), one dimensional (1D), two dimensional (2D), and three dimensional (3D)) which exhibit different properties. For example, 2D substances have multifunctional properties. Due to the electronic state of graphene, spin-polarised electron bands form for non-magnetic materials. In addition, graphene is used for molecular spintronics because it utilizes spin–orbit interactions which increases when the π–d orbitals mix at the interface with magnetic metal electrodes.[395] At the interface, charge transfer bring about the alteration of the electronic structure, thereby affecting or even quenching the magnetic moment of the molecules. Recently, such spin current control at the interface at the molecular level has become known as spinterface.[396] In principle, it is possible to use the spin for quantum information processing (QIP), and spin detection and evaluation are important for realising a quantum computer (QC) and/or spintronic devices.[258] Electron spin resonance (ESR), reported by E. Zaboisky in 1945, is one such detection method.

At the same time, scanning tunnelling microscopy (STM) and scanning tunnelling spectroscopy (STS) can be used to identify one magnetic atom adsorbed on a substrate surface and directly observe the density of states (DOS). Thus, they have been attracting attention as a method for single spin detection. STM and STS play a major role in directly investigating the relationship between morphology and electronic structure. For example, for **CoPc** adsorbed on an Au surface, a symmetric Kondo resonance is observed because only the direct tunnel process from the probe to the substrate is suppressed by the Pc ligand.[397] It is possible to study the interactions between magnetic atoms and non-magnetic/magnetic metals or those between magnetic atoms on an atomic scale.[398] The Kondo effect, which is the principle of Kondo resonance, was proposed by Jun Kondo in 1964. As the temperature of a metal decreases, its electrical resistance decreases. However, the electrical resistance increases when the temperature is lowered below a certain temperature due to trace amounts of magnetic impurities contained in the metal. This is a phenomenon in which the spins of metallic conduction electrons and the spins of magnetic impurities finally form a Kondo–Yoshida singlet, which has a higher resistance than the metallic state and the electrical resistance remains constant. In this process, as a result of the spin exchange process between the conduction electrons and the magnetic impurities, a resonance state is observed as a sharp peak at the Fermi level (0 V). The temperature at which the electrical conductivity becomes constant at low temperatures is defined as the Kondo temperature (T_K), and in the case of STS, it is proportional to the peak width at half maximum of the Kondo resonance obtained from tunnelling current spectroscopy. By applying the Kondo effect to the conduction electrons, it is possible that the conductance changes, and this phenomenon has been attracting attention again recently because of its high utility in spintronics. As a result, the Kondo resonance should be observed even for **M(Pc)$_2$**, which has a spin source.

A Kondo resonance for a delocalized π radical on the ligand due to the electronic state of **Tb(Pc)$_2$** adsorbed on a substrate has been reported, and it is clear that the Kondo resonance observed on Au(111) depends on the molecular conformation (Fig. 31a–c and 32a, b).[302,399] In other words, the Kondo resonance can be switched off by changing θ by $<8^\circ$. In addition, when Cs is deposited on **Tb(Pc)$_2$/Au(111)**, the electronic structure of the molecule changes.[400] This is probably

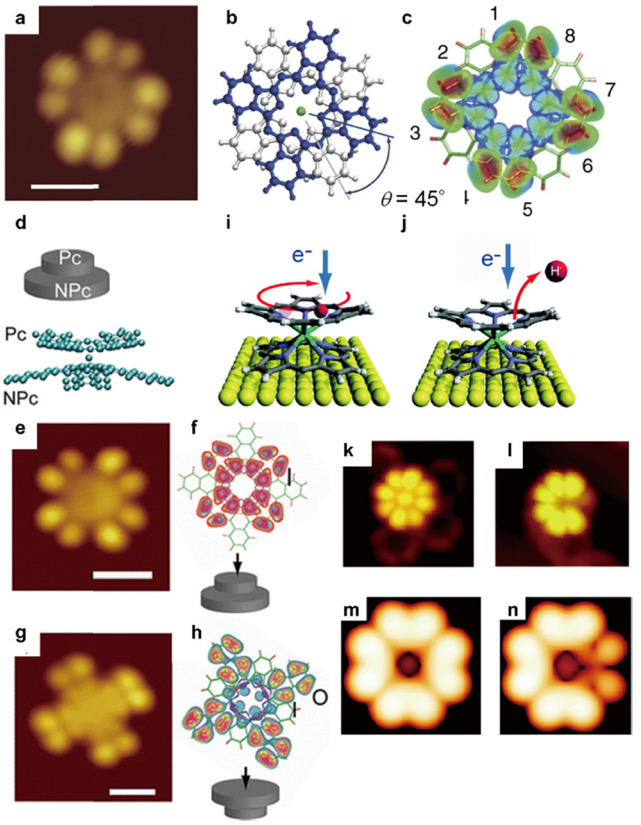

Fig. 31 STM image of the sandwich-type tetrapyrrole rare-earth metal complexes on the Au(111) surface. (a) STM image of an Isolated **Tb(Pc)$_2$** molecule. (b) Molecular structure of **Tb(Pc)$_2$** which is shown in the upper (lower) Pc ligand is coloured in blue (silver). (c) A simulated STM image of **Tb(Pc)$_2$** obtained by using DFT calculations. (d) Molecular structure of **(Nc)Tb(Pc)**. (e–h) STM and DFT simulated STM images of isolated Pc-up and Nc-up ligands of **(Nc)Tb(Pc)**. White bars in (a), (e), and (g) are 1 nm. (i and j) A schematic model of the operation caused by the injection of tunnelling electrons into a **(HOEP)Tb(OEP)**. (i) Proton (H) atom hopping and (j) H atom desorption. (k–n) STM and DFT simulated STM images of isolated (k and m) **Tb(OEP)$_2$** and (l and n) **(HOEP)Tb(OEP)**. Topographic images, which is similar to those in (k) and (l), observed by the operations in (i) and (j). Reproduced from (a–c) ref. 302. Copyright 2011, Nature Research. Adapted with permission from (d–h) ref. 135. Copyright 2013, American Chemical Society. Reproduced from (i–n) ref. 307. Copyright 2018, Royal Society of Chemistry.

because charge transfer occurs when Cs is added, switching on the Kondo resonance. On the other hand, for **Tb(Pc)$_2$/Ag(111)**, Kondo resonance is silent in the first layer of **Tb(Pc)$_2$** but active in that of the second layer.[375] The π radical recovers by decoupling at the interface. Since the Kondo resonance is silent even for **Tb(Pc)$_2$/Cu(111)**, the interactions between the substrate and **Tb(Pc)$_2^0$** are important for understanding the Kondo resonance.[372] In other words, it is possible to control the spin state of **Tb(Pc)$_2^0$** *via* the interface. In addition, since Kondo resonances depend on the electronic state of ligands, the T_K values of delocalized π radicals of Nc^{2-} (naphthalocyaninato) and Pc^{2-} ligands of **(Nc)Tb(Pc)/Au(111)** differ (Fig. 31d–h).[135] Furthermore, for **Tb(OEP)$_2$** (OEP^{2-} = 2,3,9,10,16,17,23,24-octaethylporphyrinato)/**Au(111)**, the electronic structure changes significantly due to the addition and desorption of proton at the isoindole nitrogen (N_{iso}) position, meaning that the Kondo resonance could be switched on and off (Fig. 31i–n).[307] Moreover, Kondo resonances have been detected for **Tb(Pc)^x/Au(111)** and **Tb$_2$(Pc)$_3$/Ag(111)** (Fig. 32d).[232,401] However, a Kondo resonance for **Y$_2$(Pc)$_3$/Au(111)** has not been observed under the same conditions as those used for **Y(Pc)$_2$/Au(111)** (Fig. 32c).[302] It has been shown that interactions with a Cu(111) substrate quench the unpaired π electron of **Tb(Pc)$_2^0$**, explaining the lack of a Kondo resonance. In addition, it has been shown that the unpaired π electron expected for an isolated molecule of **Dy(Pc)$_2^0$** is quenched upon adsorption onto Cu(001). In the case of **Nd(Pc)$_2$/Cu(100)**, quenching occurs due to charge rearrangement at the interface.[402] On the other hand, a 4f metal centre of **Dy(Pc)$_2$/Cu(001)** contributes to the Kondo resonance.[374] From density functional theory (DFT) calculations, the Kondo resonance occurs due to the coupling between the Dy^{3+} ion and the Cu electron bath which is mediated by strong hybridization between Dy d and f orbitals.

Research on the Kondo resonance induced at the interface between a light rare-earth tetrapyrrole sandwich compounds

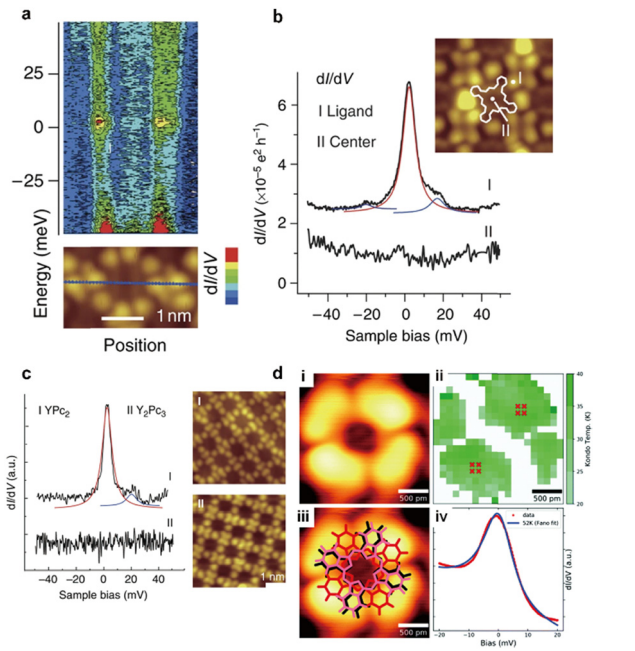

Fig. 32 STS measurement of the sandwich-type tetrapyrrole rare-earth metal complexes on a metal substrate near the Fermi level. (a) Change in the Kondo peak height of **Tb(Pc)$_2$/Au(111)** when the tip position is moved along the blue line (bottom) in the STM topography panel. The different colours correspond to the d*I*/d*V* intensity, described above the figure. (b) d*I*/d*V* spectra measured at the upper Pc ligand of **Tb(Pc)$_2$/Au(111)** at positions I (centre) and II (ligand) of the molecule. (c) d*I*/d*V* spectra and STM topography of **Y(Pc)$_2$/Au(111)** (I) and **Y$_2$(Pc)$_3$/Au(111)** (II). (d) STM topography (i) and topography with staggered three Pc ligands (iii) of **Tb$_2$(Pc)$_3$/Ag(111)**. (ii) Map of the fitted Kondo temperature (T_K) on a single **Tb$_2$(Pc)$_3$/Ag(111)**. (iv) Averaged point spectra showing the Kondo peak (red x's on ii) on a single **Tb$_2$(Pc)$_3$/Ag(111)**. Reproduced from (a–c) ref. 302. Copyright 2011, Nature Research. Reproduced from (d) ref. 401. Copyright 2018, Royal Society of Chemistry.

has been reported. For **(Pc)Ce(TPP)^0** and **Ce(Pc)$_2^0$**, the formal charge of Ce^{4+} resulting from the donation of four negative charges to both Pc^{2-} and TPP^{2-} anions causes a $4f^0$ electronic configuration.[403,404] In this case, no Kondo resonance is expected. However, **(Pc)Ce(TPP)/Ag(111)** exhibits a Kondo resonance but **(Pc)Ce(TPP)/Cu(111)** does not.[403] Thus, a formal 3 +/4+ oxidation state would result in one electron in the 4f orbital and one unpaired π electron in a radical state ($^\bullet-$)/2− in the ligand for a valence fluctuating system, such as **Ce(Pc)$_2^0$**, in which the Ce ion has a valence charge of about 3.57 estimated from Ce L_{III}-edge X-ray absorption near edge structure spectrum (XANES).[403] These systems with fluctuating valences could lead to a ligand-spin induced Kondo resonance similar to those observed for **Cu(Pc)/Ag(100)** and **Tb(Pc)^x/Au(111)**.[405] Intermediate valence states make it difficult to explain the presence of a Kondo resonance. Strong hybridization of the molecular orbitals and substrate could result in the quenching of the spin at the interface, eliminating the Kondo resonance. In addition, ligand–ligand interactions in Pc based molecules have been shown to reduce molecule–substrate coupling *via* the modification of the molecule/substrate distance or charge transfer and therefore to reduce or even quench T_K.[135,405] For example, the competition between the Kondo effect and Ruderman–Kittel–Kasuya–Yosida (RKKY) coupling in 1D and 2D lattices has been reported.[135,406] Thus, theoretical and experimental results are needed to fully understand the spin states at the interface involved in the Kondo process.

The magnetic anisotropy and coercivity can be investigated using soft X-ray magnetic circular dichroism (XMCD) measurements on **Ln(Pc)$_2$** (Ln^{3+} = Tb and Dy) on a substrate (Fig. 33).[267] Moreover, the magnetic properties of rare-earth metal ions three-dimensionally surrounded by organic ligands in an element-selective manner can be analysed, and the origin of the magnetic anisotropy of SMMs can be determined from the viewpoint of their electronic states. Soft XMCD can be used on a single atomic layer when synchrotron radiation is used. The uniaxial magnetic anisotropy of the Tb^{3+} ion of **Tb(Pc)$_2$** can be determined by measuring the change in the XMCD spectrum when the magnetic field is applied in different directions (vertical and in-plane directions to the substrate). By performing sum-rule analysis on the obtained spectrum, magnetic hysteresis can be obtained from the quantitative evaluation of the Tb 4f magnetic moment and the magnetisation curve for each element. In addition, by applying the sum rule to the XMCD (and/or XAS) spectra, the orbital magnetic moment L_z and spin magnetic moment $2S_z$ of the Tb^{3+} ions can be calculated separately. Studies on the magnetic properties of **Ln(Pc)$_2$** (Ln^{3+} = Tb and Dy) on various substrates using XMCD have been reported.[345,380,387,391] The ferromagnetic Ni layer forms out-of-plane (OP)/Cu(111) and in-plane (IP)/Ag(100), depending on the type of substrate (Fig. 33d–g).[381] When **Tb(Pc)$_2$** is adsorbed on these Ni layers, the elemental decomposition hysteresis loop changes according to the magnetisation direction of the ferromagnetic Ni layer due to the magnetic interaction between **Tb(Pc)$_2$** and Ni layer. **Tb(Pc)$_2$/Fe/Cu(111)** has the same antiferromagnetic relationship as the Ni system.[382] When Li is deposited, the ferromagnetic exchange interactions change probably because charge transfer occurs when Li is added. Furthermore, it has been reported that the SMM characteristics of **Tb(Pc)$_2$** and **Dy(Pc)$_2$** adsorbed on the MgO substrate are better (Fig. 33c).[377,407] The improvement in the SMM properties is believed to be due to the effects of spin-phonon coupling on the magnetic stabilities of surface-adsorbed SMMs. This suggests that the use of substrates with low phonon density of states is beneficial for the construction of molecular-based spintronics devices and for further increases in the blocking temperature (T_B) of surface-adsorbed **Ln(Pc)$_2$** (Ln^{3+} = Tb and Dy).

Spintronics of SMMs, like **Tb(Pc)$_2$** on a substrate, has been prepared using the spin state control. With respect to **Tb(Pc)$_2$** adsorbed on a ferromagnetic Co layer grown on an Ir(111), the spin-polarised tunnel current changes according to the application direction (parallel/antiparallel) of the external magnetic

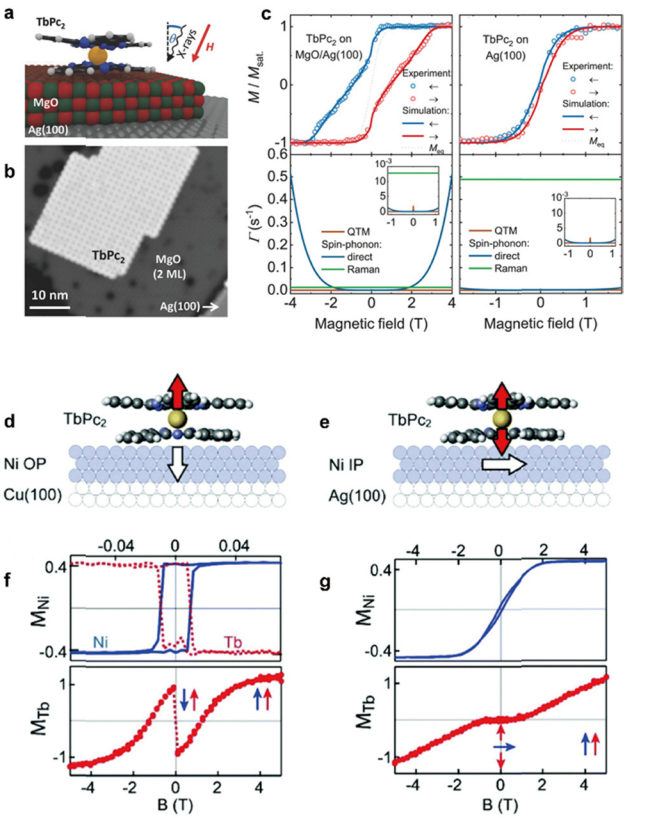

Fig. 33 XMCD hysteresis curves for **Tb(Pc)$_2$** on a metal substrate. (a) Schematic illustration of a **Tb(Pc)$_2$** on an ultrathin MgO film on Ag(100). (b) STM image of a 2D film of **Tb(Pc)$_2$** on a double-layer film of MgO on Ag(100). (c) Hysteresis loop obtained with XMCD at 3 K and the best fit calculations of magnetisation dynamics for **Tb(Pc)$_2$/MgO/Ag(100)** and **Tb(Pc)$_2$/Ag(100)**. (d) Schematic illustration of the magnetic anisotropy axis of **Tb(Pc)$_2$/Ni(OP)/Cu(100)** and (f) elemental Ni and Tb resolved hysteresis loops from XMCD at 8 K. (e) Schematic illustration of the magnetic anisotropy axis of **Tb(Pc)$_2$/Ni(IP)/Ag(100)** and (g) elemental Ni and Tb resolved hysteresis loops from XMCD at 8 K. Adapted with permission from (a and b) ref. 377. Copyright 2016, Wiley-VCH. Reproduced from (c) ref. 407. Copyright 2019, Wiley-VCH. Reproduced from (d–g) ref. 305. Copyright 2016, Royal Society of Chemistry.

field (B_{ext}) (Fig. 34a).[379] It depends on the magnetisation direction of the chip and the sample, and the pattern of spin polarisation of the molecular orbital is observed (Fig. 34b–d). It has been shown that the spin of **Tb(Pc)$_2$** is antiferromagnetically coupled to the magnetisation of Co-islands grown on Au(111) regardless of the adsorption site of the **Tb(Pc)$_2$**.[299] Both edge and flat-lying molecules exhibit a stable spin direction opposite to the magnetisation direction of the Co-islands to which they are attached (Fig. 34e). More importantly, the spin state of **Tb(Pc)$_2$** can be switched independently of the Co island by applying B_{ext} (Fig. 34f). The magnetic asymmetries of edge and flat molecules are reversed due to the difference in the DOS due to the **Tb(Pc)$_2$-Co**-island interactions between the two different adsorption configurations. Stable spin polarisation is inferred from the substantial hysteresis observed in the magnetisation curve of the **Tb(Pc)$_2$** SMM even with the frozen magnetization of the Co island (Fig. 34g). The observation of significant openings of the hysteresis in the magnetisation curves suggests suppression of the quantum tunnelling of the magnetisation (QTM) process.

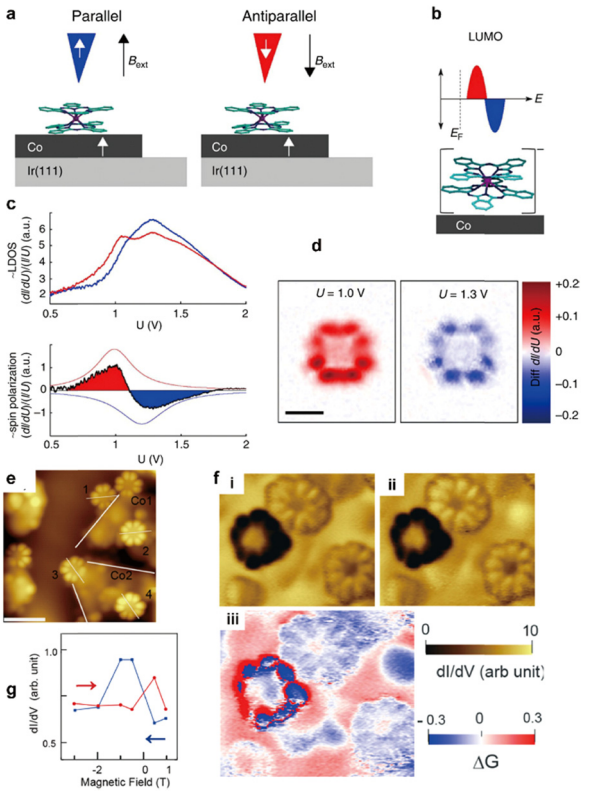

Fig. 34 Spin state control of **Tb(Pc)$_2$** on a ferromagnetic Co layer. (a) Schematic illustration of the SP-STM experimental setting of a **Tb(Pc)$_2$/Co/Ir(111)** by applying an external magnetic field (B_{ext}) which is parallel (right) and antiparallel to the magnetisation direction (left). (b) Schematic illustration of the spin-split on the LUMO of **Tb(Pc)$_2$** on the ferromagnetic Co layer. (c) Spin-resolved point-mode spectroscopy. The parallel (blue line) and the antiparallel magnetisation directions (red line) (above). Difference in the spectroscopic curves (below). (d) The spin polarisation of the molecular orbitals which have opposite spin polarisations: red (U = +1.0 V) and blue (U = +1.3 V). (e) STM topographic image of **Tb(Pc)$_2$/Co/Au(111)**, which is grouped in islands Co 1 and Co 2. (f) Conductance mapping for **Tb(Pc)$_2$/Co/Au(111)** obtained with V_s = −600 mV and B_{ext} = +1 T (i) and −1 T (ii). (iii) Difference mapping ΔG (+1 T, −1 T). The scale of dI/dV (top) and the ΔG (bottom) are shown in the colour bar scales. (g) dI/dV signal measured as a function of external magnetic field (B_{ext}) for **Tb(Pc)$_2$/Co/Au(111)**, which are shown in (f). The hysteresis loops of dI/dV shown in both edge and flat-lying molecular positions. Adapted with permission from (a–d) ref. 379. Copyright 2012, Nature Research. Adapted with permission from (e–g) ref. 299. Copyright 2019, American Institute of Physics.

SMMs and/or molecular nano magnets (MNM) have potential for technological applications in magnetic storage and for implementing qubits in the quantum computing (QC).[266] The application in magnetic storage requires high anisotropic energy barriers for spin reversal (U_{eff}) and QTM suppression, whereas QC requires a QTM process, such as a spin cascade $|S = 1/2\rangle\,|J = 6\rangle\,|I = 3/2\rangle$ in the **Tb(Pc)$_2^0$** system, for qubit reading and manipulation (the spin cascade mechanism for qubit is described in Section 3.2).[270] Therefore, both applications can be achieved using organic–inorganic hybrid materials by developing viable means for coordinating the QTM process in a controlled manner. An approach that uses the hybrid materials to control and enhance the properties of sandwich-type tetrapyrrole rare-earth metal SMMs will accelerate further research towards the realisation of spintronic devices made of functional sandwich-type tetrapyrrole rare-earth metal complexes.

3.8 Rare-earth phthalocyaninato sandwich complex/carbon nanotube hybrid materials

The internal nanospace of carbon nanotubes (CNTs) can be regarded as a reaction vessel that is 1/1000 smaller than a microreactor.[408] Therefore, these chemical reaction fields, which have a diameter range of 1–3 nm (100 nm to 0.1 mm in length), are expected to have a great influence on reaction chemistry and/or nanoelectronics research in the 21st century.[409–412] It has been shown that atoms and molecules can be contained in the nanospace of CNTs.[413–418] Focusing on the use of the stable one-dimensional nanospace of a CNT as a host for host–guest structures, various SMM–CNT hybrid materials (*i.e.*, with single-walled CNTs (SWCNTs): internal diameter of *ca.* 3 nm and multi-walled CNTs (MWCNTs): internal diameters of (5–50 nm)) have been reported for nanoelectronics and spintronics research.[344,419–421]

In 2009, Kyatskaya *et al.* first reported a **[(Pyrene)Pc]Tb(Pc)–SWCNT** hybrid material, in which a **[(Pyrene)Pc]Tb(Pc)** (one Pc ligand is substituted with three hexyl groups and one 4-(4-pyren-1-ylbutoxy) group) was attached to the outside of a SWCNT, along with its magnetic properties.[114] **[(Pyrene)Pc]Tb(Pc)–SWCNT** shows a Coulomb blockade in which a **Tb(Pc)$_2$** derivative and a SWCNT act as a quantum dot in a field-effect-transistor (FET) device. In the spin valves of **[(Pyrene)Pc]Tb(Pc)–SWCNT**, the maximum magnetic resistance ratio between the parallel state and the antiparallel state is approximately 300% at submillikelvin temperatures.[117,312] In 2011, in a related study, Urdampilleta *et al.* reported hybrid devices that consist of chemical vapor deposition (CVD)-grown CNT

transistors decorated with **Tb(Pc)$_2$** SMMs.[269,309] The devices were achieved by tailoring the supramolecular π–π interactions between the **Tb(Pc)$_2$** SMMs and CNTs (**Tb(Pc)$_2$–CNT**) (Fig. 35a). Magnetoresistance measurements revealed steep steps, which were related to the magnetisation reversal of the individual **Tb(Pc)$_2$** SMMs. The electron-transport properties of these devices are strongly dependent on the relative magnetisation orientation of the grafted SMMs. In this material, the **Tb(Pc)$_2$** SMMs act as a local spin polarizer and analyser on the CNT electron-conduction channel. As a result, reluctance ratios of up to several hundred percent were observed at submillikelvin temperatures. These results suggest that a spin valve with a larger magnetoresistance ratio can be prepared by using SMMs as the spin source instead of ferromagnets. These systems were demonstrated to detect differential conductance (dI/dV) by taking advantage of the switching of the QTM steps by the corresponding magnetic field ($\mu_0 H_z < \pm 50$ mT). In other words, readout of the nuclear spin state was realized using **Tb(Pc)$_2$** SMMs.

In 2019, Abd El-Mageed *et al.* reported a supramolecular structure formed by a **Tb(BDP)$_2$–SWCNT** hybrid material, in which Tb^{3+}-5,15-bisdodecylporphyrin (BDP) double-decker SMMs were attached to the outside of an SWCNT.[423] Scanning tunneling microscopy (STM) confirmed an ordered, self-organized spiral array on the SWCNT surface stabilized by non-sharing (π-stacking) interactions. In addition, atomic force microscopy (AFM) images exhibited a distinctive debundling effect due to the adsorption of the **Tb(BDP)$_2^0$** SMMs on the SWCNT surface with some helical array structures. The SMM properties of **Tb(BDP)$_2$–SWCNT** were investigated, and the hybrid materials interestingly showed larger butterfly-shaped hysteresis loops than the **Tb(BDP)$_2^0$** SMMs alone, indicating a slow τ for **Tb(BDP)$_2$–SWCNT**. So far, electron-transport properties have not yet been reported for **Tb(BDP)$_2$–SWCNT**.

In 2021, Katoh *et al.* first reported the encapsulation of **Tb(Pc)$_2$** SMMs in the internal nanospace of SWCNTs (**Tb(Pc)$_2$SMM@SWCNT**).[422] The magnetic and electronic properties of the **Tb(Pc)$_2$SMM@SWCNT** hybrids (Fig. 35e) were investigated in detail using DC and AC magnetic susceptibility measurements, transition electron microscopy (TEM), scanning electron microscopy (SEM), STM, and STS. By arranging the **Tb(Pc)$_2$** SMMs in the 1D internal nanospaces of the SWCNTs, it is possible to investigate the essential SMM characteristics of **Tb(Pc)$_2$** without considering LF effects. Moreover, it appears that the electron correlation between **Tb(Pc)$_2$** and the SWCNT can affect the electron transport and/or electromagnetic properties. Since bandgap modulation was observed due to the encapsulation of **Tb(Pc)$_2$** in SWCNTs, these materials should be useful in FETs. Furthermore, as the stable internal nanospace of SWCNTs is used, it is thought that the density of the SMMs in the SMM–SWCNT hybrid material can be controlled, and the hybrids should be usable as spin valves. This strategy may pave the way for the construction of SMM–SWCNT hybrid materials for operable molecular spintronic devices using the quantum effects of individual SMMs.

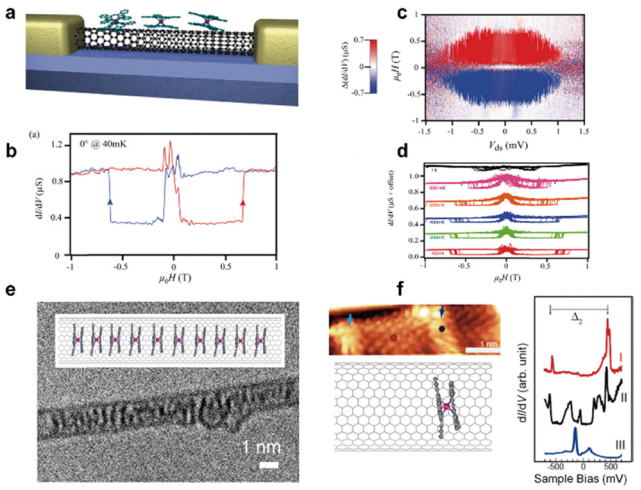

Fig. 35 Supramolecular spin valves based on the **Tb(Pc)$_2$–SWCNT** hybrid device. (a) Schematic illustration of the device. (b) Conductance hysteresis loops of **Tb(Pc)$_2$–SWCNT**. dI/dV measured at 40 mK with an in-plane magnetic field applied along the easy axial direction (0°). Bias and temperature dependences of the conductance hysteresis loops of **Tb(Pc)$_2$–SWCNT**. (c) Scale map of the dI/dV hysteresis as a function of the in-plane magnetic field and source drain voltage (V_{ds}). (d) Temperature dependence of the conductance hysteresis loops. (e) Supramolecular structure of the **Tb(Pc)$_2$@SWCNT** hybrid material. TEM image and schematic illustration of **Tb(Pc)$_2$@SWCNT**. (f) STM image showing empty (red dot) and filled (black dot) regions. Comparative STS spectra measured at the red and black dotted points in STM image. The STS of **Tb(Pc)$_2$** adsorbed on an Au(111) surface is illustrated as plot III (blue) in (f) as a reference. Reprinted from (a–d) ref. 269. Copyright 2011, MDPI. Reproduced from (e and f) ref. 422. Copyright 2021, Royal Society of Chemistry.

4. Semiconducting materials based on REE sandwich complexes

Discovery of semiconducting properties of phthalocyanines reported by the group of J. Simon in 1987 on the examples of radical complexes **LiPc** and **Lu(Pc)$_2$** is definitely one of important milestones not only for tetrapyrrolic compounds, but for all organic electronics in general.[35] This discovery nearly coincided with the first report on organic field effect transistors (OFETs) made in 1986 by Tsumura *et al.* with polythiophene conducting layer,[424] thus no surprise that the same year **Lu(Pc)$_2$** was introduced into OFET technology.

OFETs attract increasing research interest since they were first reported due to their potential for application in flexible displays, integrated circuits and low-cost electronic devices. A typical OFET device consists of an organic semiconducting layer, a dielectric layer, and three electrodes (source, drain, and gate electrodes). Three key parameters define the performance of an OFET device, namely charge carrier mobility (μ), current on/off ratio, and threshold voltage (V_T). The organic semiconducting layer is the most important part to determining the OFET performance, though other factors, such as the device configuration, the interfaces, and the materials for electrodes and insulators, also can affect the performance.[425,426]

π-Conjugated tetrapyrrole derivatives, including porphyrins (Pors) and phthalocyanines (Pcs), are important organic semiconducting materials for OFETs because of their unique molecular and electronic structures.[427,428] For rare-earth based tetrapyrrolic sandwiches, the molecular energy levels are highly disturbed by the intramolecular π–π interactions between tetrapyrrolic rings, typically possessing destabilized HOMOs and stabilized LUMOs, thus having decreased molecular energy gaps in comparison to the constituent monomeric tetrapyrroles. This is desirable for improving the semiconducting properties of tetrapyrrolic materials, as demonstrated by Guillaud *et al.* for **Lu(Pc)$_2$** and **Tm(Pc)$_2$** based OFETs.[429] The molecular energy levels of tetrapyrrolic sandwiches can be further tuned by choosing different ligands and rare-earth metal ions, adjusting the number of deckers, and incorporating various substitutes on tetrapyrrolic ligands.[1,7] The intermolecular interactions and solubility of sandwiches are also adjustable by such chemical modifications, which can provide further opportunity for the fabrication of solution-processable and high quality films for OFET devices.

Moreover, specific substitution of sandwich complexes may allow for the formation of supramolecular structures that provide intrinsic dielectric insulation at the molecular level. For example, ultrathin solid films of structurally similar octabutoxy and tetra-crown-ether substituted Eu(III) bisphthalocyaninates, **Eu[(BuO)$_8$Pc]$_2$** and **Eu[(15C5)$_4$Pc]$_2$**, were formed and their transversal conductivity and, consequently, electrochemical activity were studied in an aqueous electrolyte.[430] Excellent transfer of charge through monomolecular ultrathin films of crown-substituted complex was observed enabling its redox-multistability, which can be utilized in molecular logic and information storage devices. However, transversal charge transfer was inhibited in the films formed by octa-butoxy-substituted complex, which might be promising for OFET applications.

Depending on the correlation between the molecular energy levels of the semiconducting layer and the work function of source–drain electrodes, holes or electrons can be preferentially injected from the source electrode to the semiconducting layer, and transported to the drain electrode, leading to p- or n-type transporting modes, respectively. If both types of charge carriers can be injected and transported, an ambipolar OFET device is achieved, which, however, is of great importance in complementary metal oxide semiconductor (CMOS) logic circuits.[431] Most tetrapyrrolic sandwiches can exhibit p-type OFET performance in air with usual source–drain electrodes (such as Au, with a work function of 5.1 eV), because of the suitable HOMO energy levels of sandwiches for hole injection (Table 1). However, unipolar n-type operations are often detected under an inert (or reducing) gas atmosphere, because of the relatively high LUMO energy levels of sandwiches, which cannot resist the air-derived electron traps. On the other hand, due to the versatility of tuning the HOMO and LUMO energy levels of tetrapyrrolic sandwiches by molecular design,[432] single-component air-stable ambipolar OFET devices based on tetrapyrrolic sandwiches have become the research focus in recent years (Table 2).

4.1 p-Type OFETs

In 2005, Su *et al.* reported LB film-based OFETs by using heteroleptic bis(phthalocyaninato) rare earth complexes

Table 1 Performance of sandwich complexes based p-type OFET devices

Compounds/deposition method	Hole mobility [cm^2 V^{-1} s^{-1}]	V_T [V]	I_{on}/I_{off}	L and W [μm]	Source–drain electrode	Gate electrode	Insulator	Ref.
[(OctO)$_8$Pc]Tb(Pc)/LB	6.4×10^{-4}		5.5×10^4	240 and 28 600	Au	Si	SiO_2	433
[(OctO)$_8$Pc]Lu(Pc)/LB	1.7×10^{-3}		10^2					
Lu[(α-Oct)$_8$Pc]$_2$/SC	1.5×10^{-3}	−25	10^3	10 and 2000	Au/Cr	n-Type Si	SiO_2/OTS	434
Lu[(α-Oct)$_8$Pc]/SC, TA	8.0×10^{-3}	−12.5	10^5	10 and 2000	Au/Cr	n-Type Si	SiO_2/OTS	
Gd[(α-C$_8$H$_{17}$)$_8$Pc]$_2$/SC	7.47×10^{-5}	−28.9	10^3	5 and 20 000	Au	Si	SiO_2/OTS	435
Gd[Pc(α-C$_8$H$_{17}$)$_8$]$_2$/SC	1.96×10^{-5}	−27.6	2×10^2	20 and 20 000	Au	Si	SiO_2/OTS	
[(OctO)$_8$Pc]Eu[(15C5)$_4$Pc]Eu[(15C5)$_4$Pc]/LB	0.60	—	1.4×10^5	240 and 28 600	Au	Si	SiO_2	436
[(OctO)$_8$Pc]Ho[(15C5)$_4$Pc]Ho[(15C5)$_4$Pc]/LB	0.40	—	—			Si		
[(OctO)$_8$Pc]Lu[(15C5)$_4$Pc]Lu[(15C5)$_4$Pc]/LB	0.24	—	—			Si		
[(BuO)$_8$Pc]Eu[(15C5)$_4$Pc]Eu[(15C5)$_4$Pc]/LB	0.0032	—	9.3×10	240 and 28 600	Au	Si	SiO_2	437
[(HexO)$_8$Pc]Eu[(15C5)$_4$Pc]Eu[(15C5)$_4$Pc]/LB	0.014	—	8.2×10^3					
[(DecO)$_8$Pc]Eu[(15C5)$_4$Pc]Eu[(15C5)$_4$Pc]/LB	0.21	—	9.7×10^4					
[(C$_{12}$H$_{25}$O)$_8$Pc]Eu[(15C5)$_4$Pc]Eu[(15C5)$_4$Pc]/LB	0.053	—	3.9×10					
[(HexO)$_8$Pc]Eu[(DEGOMe)$_8$Pc]Eu[(DEGOMe)$_8$Pc]/LB	0.46	—	1.01×10^2	240 and 28 600	Au	Si	SiO_2	438
[(OctO)$_8$Pc]Eu[(DEGOMe)$_8$Pc]Eu[(DEGOMe)$_8$Pc]/LB	0.17	—	1.02×10^3					
[(DecO)$_8$Pc]Eu[(DEGOMe)$_8$Pc]Eu[(DEGOMe)$_8$Pc]/LB	0.096	—	3.85×10^4					
[(C$_{12}$H$_{25}$O)$_8$Pc]Eu[(DEGOMe)$_8$Pc]Eu[(DEGOMe)$_8$Pc]/LB	0.014	—	1.15×10^2					
[(OctO)$_8$Pc]Eu[(12C4)$_4$Pc]Eu[(12C4)$_4$Pc]/LB	0.03	—	2.32×10^3	240 and 28 600	Au	Si	SiO_2	439
	0.31	—	8.59×10^4				SiO_2/HMDS	
	0.33	—	7.91×10^5				SiO_2/OTS	
[(OctO)$_8$Pc]Eu[(18C6)$_4$Pc]Eu[(18C6)$_4$Pc]/LB	0.02	—	5.5×10^3	240 and 28 600	Au	Si	SiO_2	
	0.28	—	1.73×10^5				SiO_2/HMDS	
[(Dec)$_4$Por]Eu[(15C5)$_4$Pc]Eu[(15C5)$_4$Pc]/LB	0.78	−3.84	2.20×10^4	240 and 28 600	Au	Si	SiO_2/HMDS	440
	0.04	−4.02	4.94×10^3				SiO_2/OTS	
[(*p*-PentOPh)$_4$Por]Eu[(15C5)$_4$Pc]Eu[(15C5)$_4$Pc]/LB	0.05	−1.19	1.48×10^4				SiO_2/HMDS	
	0.03	−4.34	1.03×10^4				SiO_2/OTS	
Tb$_2$[(BuO)$_8$Pc]$_3$/DC	$1–2 \times 10^{-5}$	—	—	20 and 150	—	Si	SiO_2	441

Table 2 Performance of sandwich complexes based ambipolar-type OFET devices

Compounds/deposition method	Hole mobility [$cm^2 V^{-1} s^{-1}$]	I_{on}/I_{off}	Electron mobility [$cm^2 V^{-1} s^{-1}$]	I_{on}/I_{off}	$-V_T$ [V]	L and W [μm]	Source–drain electrode	Gate electrode	Insulator	Ref.
Y(Pc)$_2$/DFT	0.034		0.031	—	—	—	Au	—	—	432
La(Pc)$_2$/DFT	0.17		0.088	—	—	—	Au	—	—	
[(PhO)$_8$Pc]Ho(Pc)/QLS film	1.7×10^{-4} in air		—	10^3	−21	240 and 28 600	Au	Si	SiO_2	442
Ho[(PhO)$_8$Pc]$_2$/QLS film	—		0.54 in N_2	10^4	12	240 and 28 600	Au	Si	SiO_2	
Eu[(NaphO)$_8$Pc]$_2$/QLS film	0.10 in air	10^4	0.01 in N_2	10^2		240 and 28 600	Au	Au	PMMA	38
Eu[(SPh)$_8$Pc]$_2$/QLS film	1.1×10^{-4} in air	—	0.11 in N_2	—	—	—	Au	Si	SiO_2/HMDS	443
Ho[Pc(SPh)$_8$]$_2$/QLS film	4.9×10^{-7} in air		3.0×10^{-3} in N_2							
[(PhS)$_8$Pc]Eu(Pc)/QLS film	4.4×10^{-3}									
[(PhS)$_8$Pc]Ho(Pc)/QLS film	2.6×10^{-3}									
(Pc)Eu[f-Pc$_2$]Eu(Pc)^{OBu}/QLS film	0.8 in air	—	2.3 in N_2	—	−3 + 12	240 and 28 600	Au	Si	SiO_2/HMDS	221
(TPP)Eu[(PhO)$_8$Pc]Eu[(PhO)$_8$Pc]/QLS film	0.04 in air	10^5	0.08 in N_2	10^5	—	240 and 28 600	Au	Si	SiO_2/HMDS	444
Eu$_2$[(*p*-FPhO)$_8$Pc]$_3$/QLS film	0.24	—	0.042	—	−1.1 + 13	W = 28.6 mm, L = 240 μm, W/L = 119	Au	Si	SiO_2/HMDS	44
[(PhO)$_8$Pc]Eu[(PhO)$_8$Pc]Eu(Pc)/QLS film	0.68	—	0.014	—	—	240 and 28 600	Au	Si	SiO_2/HMDS	42
Eu$_2$[(PhO)$_8$Pc]$_3$/QLS film	0.041	—	0.0026	—	—					
Eu$_2$[(NaphO)$_8$Pc]$_3$/QLS film	2.5×10^{-6}	10^2	2.3×10^{-6}	10^2	−8 + 10	240 and 28 600	Au	Si	SiO_2/HMDS	40
Solvent-vapor annealing 60 °C	2.6×10^{-7}	10^2	2.3×10^{-8}	10^2	−1 + 3					
Solvent-vapor annealing 80 °C	4.9×10^{-4}	10^3	7.1×10^{-5}	10^2	−20 + 18					
Solvent-vapor annealing 100 °C	0.11	10^5	0.06	10^5	−3 + 9					
Solvent-vapor annealing 120 °C	1.1×10^{-2}	10^4	9.6×10^{-3}	10^4	−4 + 5					
[(PhO)$_8$Pc]Eu[(PhO)$_8$Pc]Eu[(C≡CCOOH)Por]/QLS film	7.0×10^{-7}	10^2	7.5×10^{-7}	10^2	−8 + 8	240 and 28 600	Au	Si	SiO_2/HMDS	445
[(PhO)$_8$Pc]Eu[(PhO)$_8$Pc]Eu[(C≡CCOOH)Por]/nanoribbon	0.11	10^6	4×10^{-4}	10^4	−3 + 17					
CdEu$_2$[(HexS)$_8$Pc]$_4$/QLS film	5.6×10^{-3}	10	1.2×10^{-3}	10	—	—	—	—	—	206
(Pc)$_2$Eu$_2$[f-Pc$_2$]Eu$_2$(Pc)$_2^{SHex}$/single crystal microsheets	18	10^3–10^4	0.3	10^3–10^4	—	—	Au	Si	SiO_2/HMDS	223
[(Py$_4$Por)Eu[(PhO)$_8$Pc]Eu[(PhO)$_8$Pc]]/QLS film	6.9×10^{-7}	10^2	3.07×10^{-5}	10^2	—	—	Au	Si	SiO_2/HMDS	446
[(Py$_4$Por)Eu[(PhO)$_8$Pc]Eu[(PhO)$_8$Pc]]/CdS hybrid QLS film	0.09	10^4	0.01	10^3	—					
(TClPP)Y(Pc) and fullerene C_{60} cocrystals	3.72	10^2	2.22	10^2	—	240 and 28 600	Au	Si	SiO_2	447
(TFPP)Eu[(PhO)$_8$Pc]Eu[(PhO)$_8$Pc]/QLS film	6.0×10^{-5}	—	1.4×10^{-4}	—	−20 + 38	240 and 28 600	Au	Si	SiO_2	448
(TFPP)Eu[(PhO)$_8$Pc]Eu[(PhO)$_8$Pc]/QLS film/CuPc VCD film:	0.16	—	0.30	—	−13 + 25					
[(*p*-HOPh)$_4$Por]Eu(Pc)Eu(Pc)/QLS film	4.85×10^{-8}	10^2–10^3	2.33×10^{-8}	10^2–10^3	—	240 and 28 600	Au	Si	SiO_2/HMDS	449
[(*p*-HOPh)$_4$Por]Eu(Pc)Eu(Pc)/rGO/QLS film	25.53	10^3–10^4	0.77	10^3–10^4	—					
[(*p*-HOPh)$_4$Por]Eu[(PhO)$_8$Pc]Eu[(PhO)$_8$Pc]/QLS film	2.14×10^{-6}	10^2–10^3	2.33×10^{-8}	10^2–10^3	—					
[(*p*-HOPh)$_4$Por]Eu[(PhO)$_8$Pc]Eu[(PhO)$_8$Pc]/rGO/QLS film	30.9	10^3–10^4	39.6	10^3–10^4	—					

[(OctO)$_8$Pc]M(Pc), M = Tb and Lu as the electroactive components, which showed hole mobilities of 6.4×10^{-4} and 1.7×10^{-3} $cm^2 V^{-1} s^{-1}$, respectively, on a SiO_2 dielectric layer with top contacted Au source–drain electrodes.[433] Chen *et al.* designed amphiphilic tris(phthalocyaninato) rare earth complexes **[(OctO)$_8$Pc]M[(15C5)$_4$Pc]M[(15C5)$_4$Pc]**, M = Eu, Ho and Lu, and fabricated LB film-based OFETs with SiO_2/Si substrates and top contacted Au source–drain electrodes.[436] The devices exhibited highly improved hole mobilities in the range of 0.24–0.60 $cm^2 V^{-1} s^{-1}$ with an on/off current ratio of 10^5, which was ascribed to the intramolecular π–π stacking among Pc rings and the J-aggregation in the LB films.[437]

In order to study the substituent effect on the assembling properties and OFET performance of tris(phthalocyaninato) triple-deckers **[(C$_n$H$_{2n+1}$O)$_8$Pc]Eu[(15C5)$_4$Pc]Eu[(15C5)$_4$Pc]**, n = 4, 6, and 8, different lengths of alkoxy chains were connected to one of the outer phthalocyanine ligands.[437] The results indicated that the molecular packing and intermolecular

interaction in LB films are closely related to the length of hydrophobic side chains, thus leading to the change of hole mobilities within 0.0032–0.60 $cm^2\ V^{-1}\ s^{-1}$.

A similar trend was observed for another series of amphiphilic tris(phthalocyaninato) rare earth complexes **[($C_nH_{2n+1}O$)$_8$Pc]Eu[(DEGOMe)$_8$Pc]Eu[(DEGOMe)$_8$Pc]**, DEGOMe = $(OC_2H_4)_2OCH_3$, n = 6, 8, 10 and 12.[438] In the OFET devices with bottom contacted Au source–drain electrodes, the LB films of those triple-deckers also displayed hole mobilities in the range of 0.014–0.46 $cm^2\ V^{-1}\ s^{-1}$, depending on the length of hydrophobic alkoxy chains.

The hydrophilic sides of tris(phthalocyaninato) rare earth complexes were also modified with different crown ether substituents.[439] Replacing the 15-crown-5 rings of **[(OctO)$_8$Pc]M[(15C5)$_4$Pc]M[(15C5)$_4$Pc]** (Fig. 36a) with 12-crown-4 or 18-crown-6 moieties resulted in different packing modes in LB films. Thus, 12-crown-4 and 15-crown5-substituted complexes formed edge-to-edge connected J-aggregates, providing a charge transfer channel parallel to the Pc rings. In contrast, 18-crown-6-substituted complex formed face-to-face connected H-aggregates in LB films, providing a channel along the long axis of the assemblies (Fig. 36b and c). In addition, the authors found that the surface treatment of the SiO_2/Si substrate by hexamethyldisilazane (HMDS) or octadecyltrichlorosilane (OTS) can significantly improve the quality of the LB film, thus leading to an increased carrier mobility.

Mixed-ligand (phthalocyaninato)(porphyrinato) Eu(III) triple-deckers **(Por*)Eu[(15C5)$_4$Pc]Eu[(15C5)$_4$Pc]** where Por* = tetra-*meso*-decylporphyrinate or tetra-*meso*-(*p*-pentyloxyphenyl) porphyrinate were synthesized and tested in LB film-based OFET devices.[440] These triple-deckers adopt a "face-to-face" connected "edge-on" orientation on HMDS- or OTS-treated SiO_2/Si surfaces, leading to the effective intramolecular π–π stacking in films. As a result, the hole mobility of OFET devices can reach 0.78 $cm^2\ V^{-1}\ s^{-1}$, with an on/off ratio of 2.2×10^4 and a threshold voltage of −3.84 V.

In addition to LB films, drop-casted and spin-coated films of tetrapyrrolic sandwiches have also been applied for OFET devices. By using spin-coated films of a liquid crystalline bis(phthalocyaninato) lutetium complex **Lu[(α-Oct)$_8$Pc]$_2$**, Ray *et al.* fabricated bottom gated OFET devices, which showed a hole mobility of 1.5×10^{-3} $cm^2\ V^{-1}\ s^{-1}$ with an on/off current ratio of 10^3 at a threshold voltage of −25 V.[434] After thermal annealing, the hole mobility was improved to 8.0×10^{-3} $cm^2\ V^{-1}\ s^{-1}$, together with an increased on/off ratio by two orders of magnitude and a reduced threshold voltage to half of that of the as-deposited films. Recently, through the study of spin-coated films of the gadolinium complex **Gd[(α-Oct)$_8$Pc]$_2$**,[435] Ray *et al.* revealed that the OFET performance decreases along with scaling down the channel length of devices. The electronic transport properties of drop-casted films of a triple-decker complex **Tb$_2$[(BuO)$_8$Pc]$_3$** were reported by Yamashita *et al.*, which also show p-type mobilities in the range of 1–2 × 10^{-5} $cm^2\ V^{-1}\ s^{-1}$.[441]

4.2 Ambipolar OFETs

The ambipolar semiconducting properties of unsubstituted bis(phthalocyaninato) rare earth complexes were initially reported by Simon and co-workers in 1990s.[450] The high intrinsic conductivity of **Lu(Pc)$_2$** and **Tm(Pc)$_2$** was ascribed to the narrow molecular energy gaps associated with their radical nature.[429] The ambipolar charge transfer properties of **M(Pc)$_2$**, M = Y or La were also studied by density functional theory (DFT) calculations, which suggest that the delocalized radical can

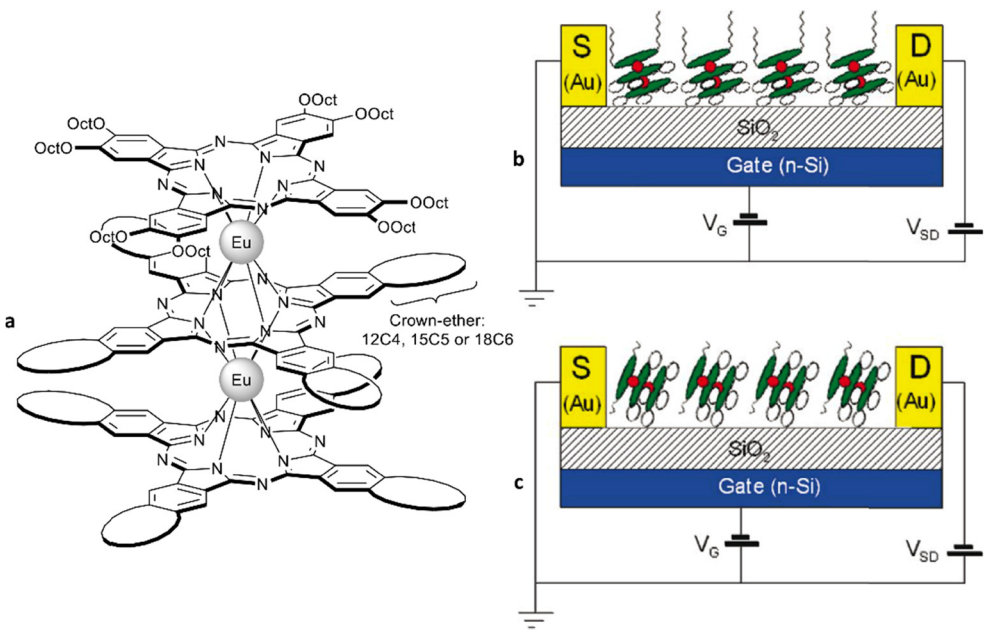

Fig. 36 (a) Amphiphilic Eu(III) crown-phthalocyaninates **[(OctO)Pc]Eu[(crown)$_4$Pc]Eu[(crown)$_4$Pc]** and schematic arrangement of complexes **[(OctO)$_8$Pc]Eu[(12C4)$_4$Pc]Eu[(12C4)$_4$Pc]** – (b) and **[(OC_8H_{17})$_8$Pc]Eu[(18C6)$_4$Pc]Eu[(18C6)$_4$Pc]** – (c) in the LB film-based OFET devices. Adapted with permission from ref. 439. Copyright 2009, American Chemical Society.

induce a high HOMO level and a low LUMO level, leading to a small ionization potential and a large electronic affinity. As a result, small injection barriers for both hole and electron from source–drain electrodes (Au) can be expected for these neutral double-deckers.[432] The DFT study also revealed small charge reorganization energy and large transfer integral values in the crystal of $M(Pc)_2$, thus predicted promising ambipolar charge transfer properties. However, in experimental studies, single-component bis(phthalocyaninato) rare earth complex-based OFET devices usually show p-type transporting properties in air, the corresponding n-type operations only can be detected under an inert or reducing atmosphere.

By connecting electron withdrawing phenoxyl groups onto one or both Pc rings of rare earth double-deckers, heteroleptic **[(PhO)$_8$Pc]Ho(Pc)** and homoleptic **Ho[(PhO)$_8$Pc]$_2$** were obtained, which exhibit p- and n-type transporting properties, respectively, in the quasi-Langmuir–Shäfer (QLS) film-based OFET devices.[442] Introducing other electron withdrawing groups, such as naphthoxyl[38] and phenylthiol,[443] to the Pc rings of rare earth double-deckers can lead to transforming their semiconducting nature from p-type to ambipolar type by tuning their HOMO/LUMO energy levels.[37] A dimeric phthalocyanine ligand was incorporated into rare earth sandwiches, leading to the formation of a yttrium(III) double-decker dimer **(Pc)Y[f-Pc$_2$]Y(Pc)^{OBu}** (*cf.* Section 2.6.2),[216] which exhibits a unique biradical state and can be fabricated into high quality QLS films, thus displaying very high carrier mobilities of 2.3 and 0.8 cm^2 V^{-1} s^{-1} for electrons and holes in air and N_2, respectively (Table 2).[221]

Molecular orbital (MO) levels of sandwiches can be adjusted by the addition of another tetrapyrrolic ring to double-deckers. In this way, a mixed (phthalocyaninato)(porphyrinato) europium(III) triple-decker complex **(TPP)Eu[(OPh)$_8$Pc]Eu[(OPh)$_8$Pc]** was prepared and fabricated into QLS film-based OFET devices, which displayed balanced hole and electron mobilities in air and N_2, respectively.[444]

Tetrapyrrolic sandwich-based air-stable ambipolar OFET devices were first achieved by using a partially fluorinated tris(phthalocyaninato) europium complex **Eu$_2$[(*p*-FPhO)$_8$Pc]$_3$**.[44] The introduction of electron-withdrawing 4-fluoro-phenoxy groups on the peripheral sites resulted in finely controlled HOMO (−5.27 eV) and LUMO (−4.17 eV) levels; both facilitate charge carrier injection from Au electrodes. In particular, the LUMO level is suitable for electron transport under ambient conditions. The triple-decker molecules also form H-aggregates and adopt an "edge-on" conformation in the QLS films, which can provide intense intermolecular interaction and π-electron delocalization. As a result, the QLS film-based single-component OFET devices display an average hole mobility of 0.24 cm^2 V^{-1} s^{-1} and an average electron mobility of 0.042 cm^2 V^{-1} s^{-1} in air, with relatively low threshold voltages of −1.1 and +13 V for holes and electrons, respectively. By taking a similar optimizing strategy, tris(phthalocyaninato) europium complexes **[(PhO)$_8$Pc]Eu[(PhO)$_8$Pc]Eu(Pc)**, **Eu$_2$[(PhO)$_8$Pc]$_3$** and **Eu$_2$[(NaphO)$_8$Pc]$_3$** were obtained. The HOMO and LUMO levels of these triple-deckers were also successfully tuned into the range for air-stable ambipolar semiconductors by the introduction of electron-withdrawing phenoxy[42] or naphthoxy subsititutes.[40]

Triple-decker complex **Eu$_2$[(NaphO)$_8$Pc]$_3$** was used to fabricate ambipolar OFET device by QLS technique, and nanoparticles of the pristine QLS film could be converted into well-defined microstructures using solvent vapour annealing with *o*-dichlorobenzene (Fig. 37).[40] Fragment-like irregular polygons, quasi-four-corner sheets, 2D squares, and clovers were obtained at different temperatures (60, 80, 100 and 120 °C, respectively), providing access to the tuning of OFET device performance due the carrier mobilities depending on morphologies and crystallinities. The best result was achieved for the most crystalline 2D squares-based devices with the carrier mobilities of 0.11 ± 0.03 cm^2 V^{-1} s^{-1} for holes and 0.06 ± 0.02 cm^2 V^{-1} s^{-1} for electrons.

A further modification was performed by replacing one of the outer Pc ligands with an amphiphilic low-symmetry porphyrin ring (Fig. 38a).[445] The resulting triple-decker can form 1-D nanoribbons *via* a "phase-transfer" process (Fig. 38b), which show improved air-stable ambipolar semiconducting properties with mobilities of 0.11 and 4 × 10^{-4} cm^2 V^{-1} s^{-1} for holes and electrons, respectively, 3 to 6 orders higher than those of non-crystalline QLS film (Fig. 38c).

Further extension of sandwiches was beneficial for their OFET behaviour. Thus a quadruple-decker complex **Eu$_2$Cd[(HexS)$_8$Pc]$_4$** exhibited air-stable ambipolar semiconducting characters due to the extended π-system and narrowed bandgap[206] The best result for phthalocyanine-based OFETs was achieved with a dimeric phthalocyanine ligand involved sandwich-type triple-decker complex **(Pc)$_2$Eu$_2$[f-Pc$_2$]Eu$_2$(Pc)$_2^{SHex}$**.[223] This special sandwich can be fabricated into single crystal microsheets, which display high hole and electron mobilities of 18 and 0.3 cm^2 V^{-1} s^{-1}, respectively, with on/off ratios of 10^3–10^4.

Another approach for ambipolar OFETs is the fabrication of bicomponent films and/or cocrystals with triple-decker complexes as one of the components. For example, bicomponent thin film transistors of **(TPyP)Eu[(OPh)$_8$Pc]Eu[(OPh)$_8$Pc]/CdS**

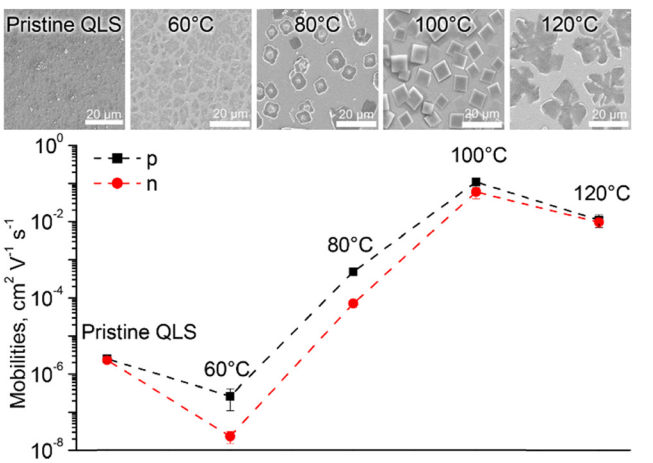

Fig. 37 The carrier mobilities for holes and electrons in pristine QLS film of **Eu$_2$[(NaphO)$_8$Pc]$_3$** and microstructures obtained by solvent vapour annealing at different temperatures together with SEM images of the corresponding films. Adapted from ref. 40, Copyright (2018) with permission Elsevier.

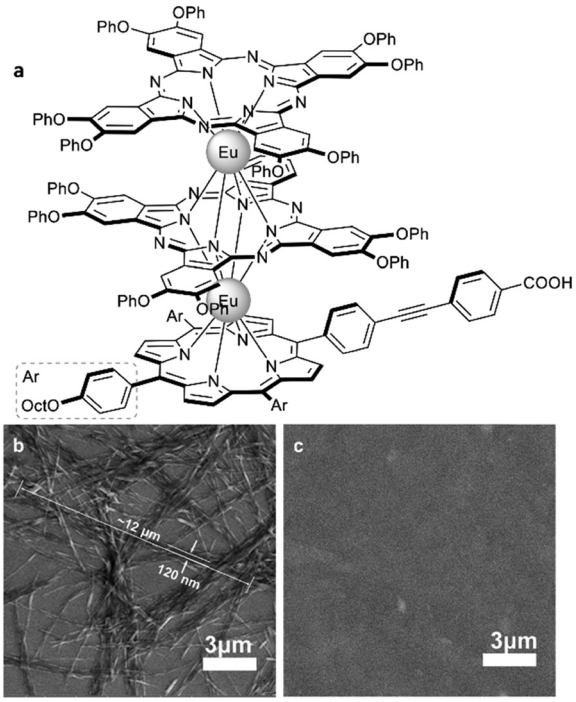

Fig. 38 (a) Amphiphilic mixed-ligand Eu(III) complex and SEM images of films showing crystallinity of films formed by the "phase transfer" process – (b) and non-crystalline films obtained by the quasi-Langmuir–Shäfer process – (c) Adapted with permission from ref. 445. Copyright 2016, American Chemical Society.

show highly improved charge mobilities for holes (0.09 $cm^2\ V^{-1}\ s^{-1}$) and electrons (0.01 $cm^2\ V^{-1}\ s^{-1}$) relative to those of single-component thin film transistors of **(TPyP)Eu[(PhO)$_8$Pc]Eu[(PhO)$_8$Pc]** for holes (6.9×10^{-7} $cm^2\ V^{-1}\ s^{-1}$) and electrons (3.07×10^{-5} $cm^2\ V^{-1}\ s^{-1}$).[446] OFET devices based on the cocrystals of **(TClPP)Y(Pc)Y(Pc)** and C_{60} also display very high mobilities of 3.72 and 2.22 $cm^2\ V^{-1}\ s^{-1}$ for holes and electrons, respectively, which is proposed to be due to similar LUMO energy levels of the two components and the low reorganization energy values for holes and electrons at the interface.[447] On the other hand, ambipolar OFETs have been achieved with a bilayer heterojunction configuration by using triple-decker complexes as air-stable ambipolar semiconductors. The QLS films of **(TFPP)Eu[(PhO)$_8$Pc]Eu[(PhO)$_8$Pc]** were obtained on vacuum deposited (VCD) CuPc templates, and fabricated into two-component bilayer thin film transistors.[448] The devices possess charge mobilities of 0.16 and 0.30 $cm^2\ V^{-1}\ s^{-1}$ for holes and electrons, respectively, which are 10^3–10^5 times of those of the single-component based devices. The improvement of the performance can be attributed to the heterojunction effect and the H-aggregation of triple-deckers on **CuPc** films. Bilayer heterojunction FETs were also fabricated by QLS films of **[TP(OH)P]Eu(Pc)Eu(Pc)** and **[TP(OH)P]Eu[(PhO)$_8$Pc]Eu[(PhO)$_8$Pc]**, as the top layers, and reduced graphene oxide (rGO) film as the sublayers. The obtained devices exhibit very high and balanced carrier mobilities of 30.9 and 39.6 $cm^2\ V^{-1}\ s^{-1}$ for holes and electrons, respectively, again due to the heterojunction effect.[449]

4.3 Supramolecular assembling of semiconductive materials based on sandwich crown-substituted complexes

The relationship between morphology and conductivity of layers formed by tetrapyrrole sandwiches in electronic devices makes it possible to apply supramolecular tools to control these factors. For this purpose, molecular blocks capable of exhibiting various types of intermolecular interactions, such as hydrophobic and stacking interactions, as well as hydrogen bonds, were synthesized and studied. However, the assembly of such molecules is a trial-and-error method, since the morphology and conductivity of the film cannot be predicted *a priori*. To some extent, this problem can be solved by applying cation-induced assembly of crown-substituted phthalocyanines, where well-established cooperative effects govern the formation of well-defined supramolecular architectures (*cf.* Section 3.3.1).

Thus, Zvyagina *et al.* used homoleptic crown-substituted bisphthalocyaninates **M[(15C5)$_4$Pc]$_2$**, M = Ce, Tb, and Lu as potential molecular blocks for cation-induced formation of 1D supramolecular polymers **{M[(15C5)$_4$Pc]$_2$·4$^+$}$_n$** where enhanced conductivity was expected (Fig. 39a).[451] Noteworthy, this possibility was envisaged in 1994 by Toupance *et al.* in one of keystone papers on the construction of ionoelectronic materials based on crown-substituted phthalocyanines; however, experimental verification of this hypothesis was reported only in 2021.

Indeed, interaction of Lu(III) complex with $KBPh_4$ in chloroform–acetonitrile mixture resulted in the intermolecular binding of potassium cations which connect neighbouring double-deckers in a cofacial manner, yielding nanowires with a thickness of 10–50 nm and a length of up to 50 μm. The four-probe

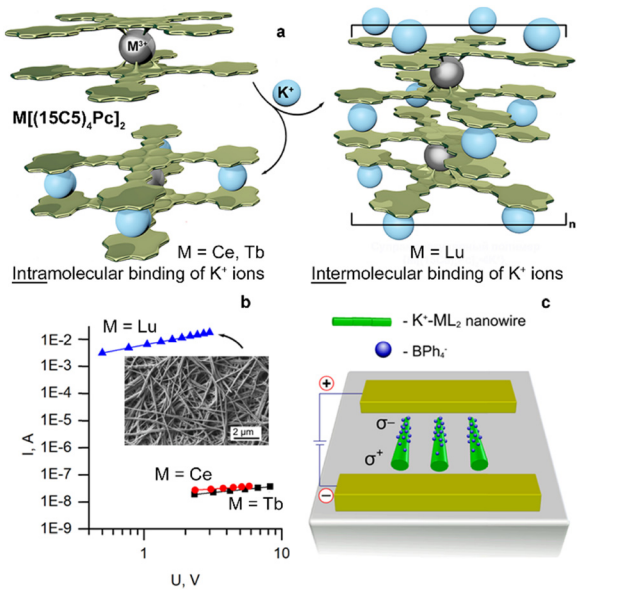

Fig. 39 (a) Modes of interaction of **M[(15C5)$_4$Pc]$_2$** with potassium cations – intramolecular for M = Tb and Ce *vs.* intermolecular for M = Lu. (b) The current–voltage characteristic of the drop-cast films of the assemblies formed by **M[(15C5)$_4$Pc]$_2$** and $KBPh_4$. Inset shows SEM image of nanowires formed by Lu(III) complex. (c) Schematic illustration of the mechanism of alignment of the **{Lu[(15C5)$_4$Pc]$_2$·4KBPh$_4$}$_n$** nanowires. Adapted with permission from ref. 451. Copyright 2021, American Chemical Society.

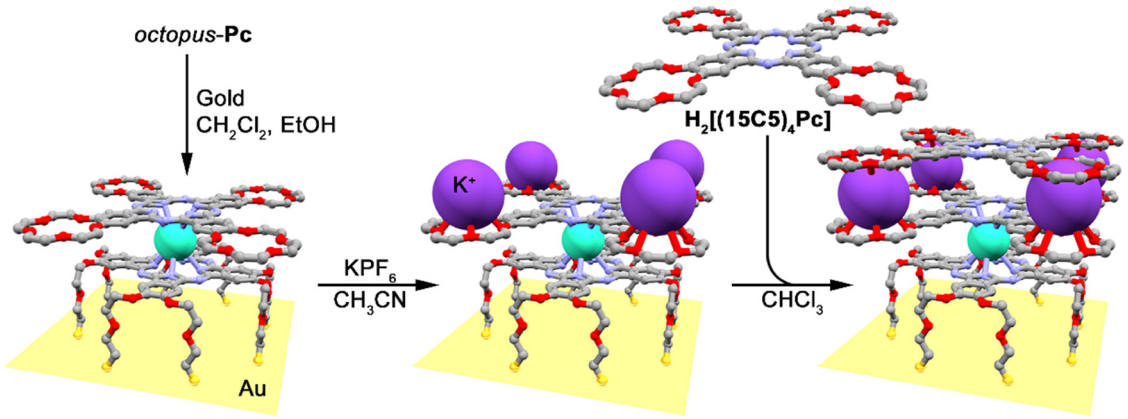

Fig. 40 Formation of a bilayer composed of **H_2[(15C5)$_4$Pc]** molecules appended to *octopus*-**Pc** SAM on gold *via* supramolecular assembly. Adapted with permission from ref. 73. Copyright 2022, Wiley-VCH.

technique in a four-stripe layout revealed the superior conductivity of these wires up to 11.4 S cm^{-1}, the highest among them being reported for phthalocyanine assemblies (Fig. 39b). The electric properties of these 1D assemblies made it possible to use technologically feasible methods for their controlled alignment on surfaces under an applied electric field (Fig. 39c).

In striking contrast, cerium- and terbium-based complexes underwent mainly intramolecular cation binding without the formation of conductive nanowires (Fig. 39a and b). Apparently, this is associated with a larger interligand distance in these complexes allowing potassium cations to intercalate between crown-substituted ligands.[452] The films, formed by the resulting assemblies had 8 orders of magnitude lower conductivity due to the lack of intermolecular interactions.

The way to controllable immobilization of supramolecular assemblies onto the electroactive surfaces was paved by Shokurov *et al.*, who used the octopus-like double-decker anchor, *octopus*-**Pc** (Scheme 4) which can form self-assembled monolayer (SAM) on the surface of Au electrodes (Fig. 40).[73] Face-on orientation of the anchors allowed for the subsequent binding of crown-phthalocyanine molecules **H_2[(15C5)$_4$Pc]** *via* potassium ion bridges. This chemistry was utilized to form a heterogeneous bilayer, in which a single molecule thick adlayer brought an additional redox-state to the system, thus expanding the multistability of the system as a whole. All four redox states available to this system exhibited characteristic absorbance in the visible range, allowing for the switching to be easy read out using optical density measurements. It is expected that the proposed approach can be used in a wide range of switchible materials – single-molecule magnets, conductive and optical devices, *etc.*

5. Non-linear optical materials based on REE sandwich complexes

Metalloporphyrins (MPor) and metallophthalocyanines (MPcs) are important organic nonlinear optical (NLO) materials due to their two-dimensional π-system.[453,454] Among practically relevant properties optical limiting (OL) is particularly interesting as it can be used to protect eyes from damage caused by laser irradiation.

Upon the formation of sandwich complexes with rare earth metals, the π-conjugation systems can be further extended along the axial direction of tetrapyrrol plane, leading to three-dimensionally conjugated molecules, which is desirable for improving the NLO response by regulating the intramolecular charge transfer transitions and/or constructing dipolar and multipolar systems.[3]

5.1 Second-order nonlinear optical materials

For materials having second-order NLO responses at the molecular level, noncentrosymmetric molecules with strong intramolecular dipolar charge distribution are required. Heteroleptic double-decker tetrapyrrolic complexes generally meet this requirement. However, reports in this field are still very rare. The sole example of heteroleptic double-decker complexes studied for the second-order NLO properties is a mixed porphyrin and tetraazaporphyrin zirconium(IV) complex **(OEP)Zr(OETAP)**.[455] A negative hyperpolarizability β [$(-83 \pm 43) \times 10^{-30}$ esu] was obtained at 1907 nm by the electric field-induced second harmonic (EFISH) measurements.

An interesting trial for second-order NLO materials has been extended to homoleptic double-decker complexes with "cubic" octupolar architectures (*cf.* Section 2.2.2 for structures of complexes). In this regard, Ayhan *et al.* developed ABAB homoleptic bis(phthalocyaninato) rare earth complexes **M[(SHex)$_4$Pc]$_2$**, M = Nd, Eu, Dy, Y and Lu,[109,110] which represent a new class of cubic molecules with an octupolar charge distribution. Their second-order NLO properties were studied by Hyper–Rayleigh Scattering (HRS) measurements at 1907 nm in chloroform solution. The first molecular hyperpolarizabilities (β_{HLS}) were evaluated to be in the range of 3010×10^{-30} esu to 5760×10^{-30} esu for Y(III) and Lu(III) complexes, respectively, which are among the largest values ever reported for nondipolar molecules. Furthermore, it was found that the β_{HLS} values of these complexes are depended on the number of 4f electrons and ionic radii of the sandwiched lanthanide(III) ions, thus providing opportunity to

regulate the second-order NLO responses. Another ABAB homoleptic bis(phthalocyaninato) rare earth complex **Lu[(α-PentO)$_4$Cl$_4$Pc]$_2$**, containing alternating pentyloxy and chloro substituents on phthalocyanine ligands, was reported by Cao *et al.*,[111] which also showed a high molecular hyperpolarizability (β_{HLS} = 1240 × 10^{-30} esu at 1907 nm, in chloroform).

By applying a porphyrin ligand with di(phenylamino)phenyl and carboxymethyl–phenylethynyl *meso*-substituents as typical electron-donating and electron-accepting groups, respectively, Sun *et al.* synthesized the first octupolar bis(porphyrinato) rare earth complex **[HTb(DADAPor)$_2$]** (Scheme 15).[113] Because of the reduced protonated nature, this compound does not have any absorption in the near-IR range beyond 800 nm. Consequently, an off-resonant hyperpolarizability (β_{HLS} = 1700 × 10^{-30} esu at 1907 nm, in chloroform) was obtained for this compound, which is the largest off-resonant hyperpolarizability for octupolar molecular materials.

Density functional theory (DFT) studies were also conducted to clarify the nature of the second-order NLO properties of octupolar homoleptic bis(phthalocyaninato) rare earth complexes.[456] A series of cubic molecules based on the bis(phthalocyaninato) yttrium **Y(Pc)$_2$** skeleton, containing two couples of electron-donating and electron-withdrawing groups in an alternate manner (Fig. 41a), were investigated. According to the calculation results: (1) the static hyperpolarizability (β_{HLS}, 10^3–10^4 a.u.) increases along with increasing electronegativity of the peripheral substituents; (2) a dynamic perturbation (excitation) will induce a resonance effect with a much higher dynamic β_{HLS} (10^4–10^6 a.u.), which is also positively correlated with the electronegativity of peripheral substituents; (3) the molecular conformation affects the second-order NLO properties. The maximal static β_{HLS} appears at a rotation angle θ of 70°, but not 90°, because **Y(Pc)$_2$** molecule employs a cuboid instead of a standard cube (Fig. 41b and c). These findings are useful for the design of new octupolar NLO materials, given that the theoretically predicted maximal β_{HLS} values can reach 10^5 × 10^{-30} esu for such octupolar molecules.

5.2 Third-order nonlinear optical materials

The tetrapyrrol macrocycles are very suitable for the third-order NLO materials due to three special advantages, including (1) the large number of free π electrons playing the role of oscillators driven by an external periodically vibrating electromagnetic field; (2) the extended delocalized π-system acting as a broad oscillating space; and (3) the huge polarizing/hyperpolarizing moments due to the long distance between the peripheral electron-donating and withdrawing substituents. The double-decker and multi-decker tetrapyrrols further improves the total three advantages in comparison with the single-decker ones.

The study of third-order NLO materials based on double-decker phthalocyanines started from 1990s. Shirk and coworkers investigated the third-order NLO performance of double-deckers **M(Pc)$_2$** (M = Sc, Y, Eu, Gd, Lu) using the degenerate four-wave mixing (DFWM) method.[457] The second-order hyper-polarizabilities (γ) and third-order susceptibility $\chi^{(3)}$ values of **M(Pc)$_2$** are about an order of magnitude higher than those of typical monomeric metallophthalocyanines. Among these double-deckers, the third-order NLO performance of **Sc(Pc)$_2$**, **Lu(Pc)$_2$** and **Yb(Pc)$_2$** are better than others. This therefore suggests that the large increase in the hyperpolarizabilities of bis(phthalocyaninato) complexes over those of the monophthalocyaninato compounds could not be simply attributed to the extended delocalization length from monomers to double-deckers.

In the past 20 years, the Z-scan method was widely used in most third-order NLO experiments. Sheng and coworkers studied a series of homoleptic bis(phthalocyaninato) rare earth

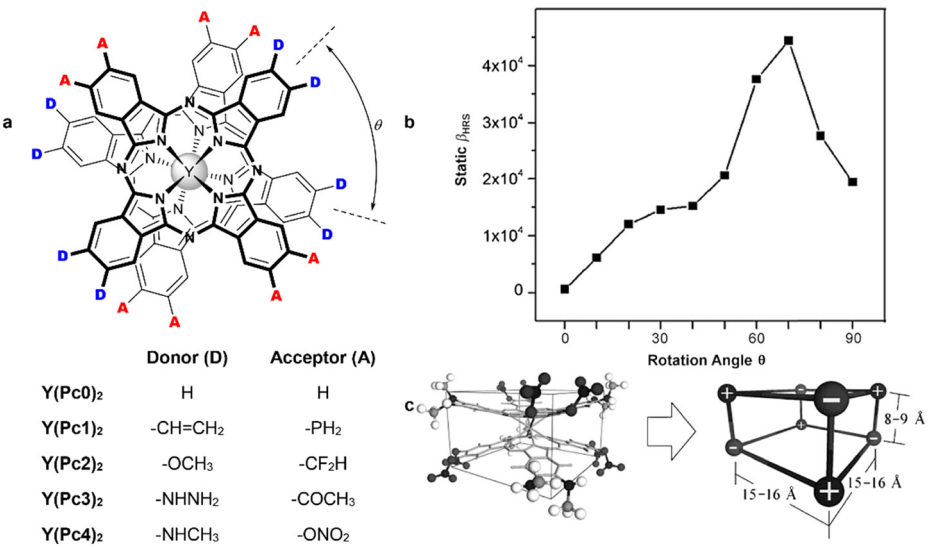

	Donor (D)	Acceptor (A)
Y(Pc0)$_2$	H	H
Y(Pc1)$_2$	-CH=CH$_2$	-PH$_2$
Y(Pc2)$_2$	-OCH$_3$	-CF$_2$H
Y(Pc3)$_2$	-NHNH$_2$	-COCH$_3$
Y(Pc4)$_2$	-NHCH$_3$	-ONO$_2$

Fig. 41 (a) Molecular structures of the series of bis(phthalocyaninato) yttrium double-decker skeletons used for DFT modelling. (b) Plot of the calculated static β_{HRS} as a function of the rotation angle θ for the complex **Y(Pc4)$_2$**. (c) Cuboid structure of the bis(phthalocyaninato) yttrium double-decker skeleton with a rotation angle of 90°. Adapted with permission from ref. 456. Copyright 2015, Wiley-VCH.

complexes **M[(OctO)$_8$Pc]$_2$**, M = Pr, Ce, Sm, and Lu.[458–460] The NLO performance of these compounds are tested using the exciting laser wavelength of 800 nm (Z-scan, 170 ns). The two-photon absorption cross-section σ_{2PA} values of this series are in the range of (3–254) $\times$ 10^3 GM, showing their strong nonlinear optical response. More importantly, the authors measured the real part of the second-order molecular hyperpolarizability (γ_R) of the neutral complex **Pr[(OctO)$_8$Pc]$_2^{0\bullet}$** together with its anion **Pr[(OctO)$_8$Pc]$_2^-$** and cation **Pr[(OctO)$_8$Pc]$_2^+$**. They found that the γ_R values of neutral, anionic and cationic forms are 440 $\times$ 10^{-32}, 180 $\times$ 10^{-32}, and 220 $\times$ 10^{-32} esu, respectively.[460] This is a key experimental phenomenon which shows the free single electron in the neutral radical molecule can be used as a good oscillator in the NLO response. When this free single electron is paired in the anionic form or removed in the cationic form, the NLO response will be significantly weakened. Following a similar mentality, Plekhanov *et al.* examined another complex **Lu[(SHex)$_8$Pc]$_2$**.[461] Using a similar Z-scan test (300 ns) at an exciting laser wavelength of 1550 nm, the complex achieved a remarkable nonlinear refractive index (n_2) value of (300 $\pm$ 3) $\times$ 10^{-5} cm^2 GW^{-1}. They found that the n_2 for unsubstituted complex **Lu(Pc)$_2$** is only (228 $\pm$ 3) $\times$ 10^{-5} cm^2 GW^{-1}, which is a quarter lower than that of **Lu[(SHex)$_8$Pc]$_2$**. This comparative investigation revealed that the peripheral electron-withdrawing substituents are beneficial to the NLO response because they could provide more free electrons to the π conjugated system.

Karpo *et al.* studied the NLO properties of a series of butyl-substituted complexes **M(Bu$_8$Pc)$_2$**, M = Eu, Dy, Er, and Lu in THF solution using the open aperture z-scan technique with 350 ps laser pulses at 532 nm.[462] All the compounds exhibited reverse saturable absorption (RSA), and application or rate equations formalism evidenced that RSA is mainly contributed by the triplet state absorption. Absorption cross-sections from the ground state (σ_0), excited singlet and triplet (σ_1 and σ_2) were deduced, evidencing that $\sigma_2 \gg \sigma_0 > \sigma_1$, the largest ratio σ_2/σ_0 was found for erbium complex.

Sekhosana *et al.* conducted a series of comparative studies on the NLO properties of double-decker phthalocyanines with electron-withdrawing pyridin-4-yloxy substituents (PyO).[47,463–466] They found that the imaginary part of the third-order susceptibility $\chi_I^{(3)}$ value is 106 $\times$ 10^{-12} esu for **Yb[(α-OPy)$_4$Pc]$_2$** and 338 $\times$ 10^{-12} esu for **Yb[(β-OPy)$_4$Pc]$_2$** (**Y20**) under the Z-scan test (10 ns, in DMSO) at the wavelength of 532 nm. When the –OR substituents are linked onto the macrocycle α-sites, there will be a p–π-super-conjugation between the p$_z$(O) and π(Pc) orbitals. When the –OR substituents are connected on the β-sites instead of the α-sites, the oscillation space of π electrons will be more effectively extended, which is positive to the periodic oscillation in the nonlinear forced vibration.

Another interesting discovery is that the $\chi_I^{(3)}$ value for the neutral complex **Nd[(*t*BuPhO)$_4$Pc]$^{0\bullet}$** is 377 $\times$ 10^{-12} esu, but it gains spectacular increase to 1280 $\times$ 10^{-12} esu for the ionic complex **Nd[(*t*BuPhO)$_4$Pc]$^-$Nd(OAc)$_2^+$**.[47] Although the latter complex does not have unpaired π-electrons, a huge positive/negative ion-pair is constructed by the bisphthalocyaninate anion and its counter-ion, rendering it as a (δ^+)–(δ^-) pair with a very strong dipole moment, which shows an improved NLO property.

Throughout the investigations on various RE(Pc)$_2$ molecules, it is easy to find out two rules to get the double-decker tetrapyrrols with high NLO performance: (1) the neutral radical **M(Pc)$_2^{0\bullet}$** is a good NLO material due to the additional free single π electron. When this radical complex is oxidized/reduced and then this free single π electron is removed/paired, it lowers the overall NLO response. However, it still can be improved by ion pair formation.[47] (2) The peripheral electron-donating substituents, especially the –OR groups, are beneficial to NLO response because they could provide more free electrons to the π conjugated system. If the –OR groups are linking at the β-sites, they will provide an extended oscillating space, and thus an improved NLO response. In comparison with these positions, the efficiency of substitution at α-sites is not obvious.

Sheng and coworkers also tested a series of heteroleptic double-deckers **[(OctO)$_8$Pc]M(Pc)**, M = Y, Ho, Er, Yb, and found that their σ_{2PA} is in the range of (126–183) $\times$ 10^3 GM,[467] which is still at the same level of **M[(OctO)$_8$Pc]$_2$**, M = Pr, Ce, Sm, and Lu series.[458–460]

Jiang and coworkers explored binuclear phthalocyanine-containing sandwich-type rare-earth complexes.[468] They revealed that the $\chi_I^{(3)}$ value of **(Pc)M[f-Pc$_2$]M(Pc)^{SHex}** (18.6 $\times$ 10^{-12} esu) is higher than that of **Pr[(SHex)$_8$Pc]$_2$** (15.6 $\times$ 10^{-12} esu), due to the enlarged π-conjugation by incorporating a binuclear phthalocyanine ligand.

Chen *et al.* conducted another comparative study on a series of porphyrin-appended europium(III) bis(phthalocyaninato) complexes (Fig. 42a).[469] The $\chi_I^{(3)}$ values for **[(α-ZnPor)Pc]Eu(Pc)**, **[(β-ZnPor)Pc]Eu(Pc)** and **[(β-ZnPor)$_2$Pc]Eu(Pc)** are 111 $\times$ 10^{-22}, 74 $\times$ 10^{-22}, and 133 $\times$ 10^{-22} m^2 V^{-2} which are in cases smaller than $\chi_I^{(3)}$ for the unsubstituted Eu(Pc)$_2$ complex (194 $\times$ 10^{-22} m^2 V^{-2}). This result shows that the using of larger ligands is not always beneficial to NLO properties. In the porphyrin-appended Pc ligands, there is no unified conjugating system between the Por and Pc macrocycles, which cannot provide a channel for electron oscillation. So the effective electron oscillating space is still located at the **Eu(Pc)$_2$** part.

In order to improve the third-order NLO responses of rare-earth based tetrapyrrolic sandwiches, multi-deckers were constructed to extend the delocalized π-system and increase the oscillating space. However, the $\chi_I^{(3)}$ value of a homoleptic triple-decker **Nd$_2$[(β-*t*BuPhO)$_4$Pc]$_3$** is found to be 350 $\times$ 10^{-12} esu,[470] which is slightly lower than that of the corresponding double-decker **Yb[(β-*t*BuPhO)$_4$Pc]$_2$** ($\chi_I^{(3)}$ = 420 $\times$ 10^{-12} esu) in the same Z-scan test (10 ns, 0.3 mmol L^{-1} in DMF).[465] Similar results were also obtained in the comparison of mixed (phthalocyaninato)(porphyrinato) europium triple- and double-decker complexes, in which γ_R for **[(Pyr)$_4$Por]Eu(Pc)Eu(Pc)** is also lower than γ_R for **[(Pyr)$_4$Por]Eu(Pc)** (Fig. 42b and c).[31]

However, Oluwole *et al.* showed that symmetrical **Eu$_2$[(BuO)$_8$Pc]$_3$** has a higher $\chi_I^{(3)}$ value in comparison with **Eu[(BuO)$_8$Pc]$_2$**.[101] NLO response and OL properties can be improved by lowering the molecular symmetry *via* the

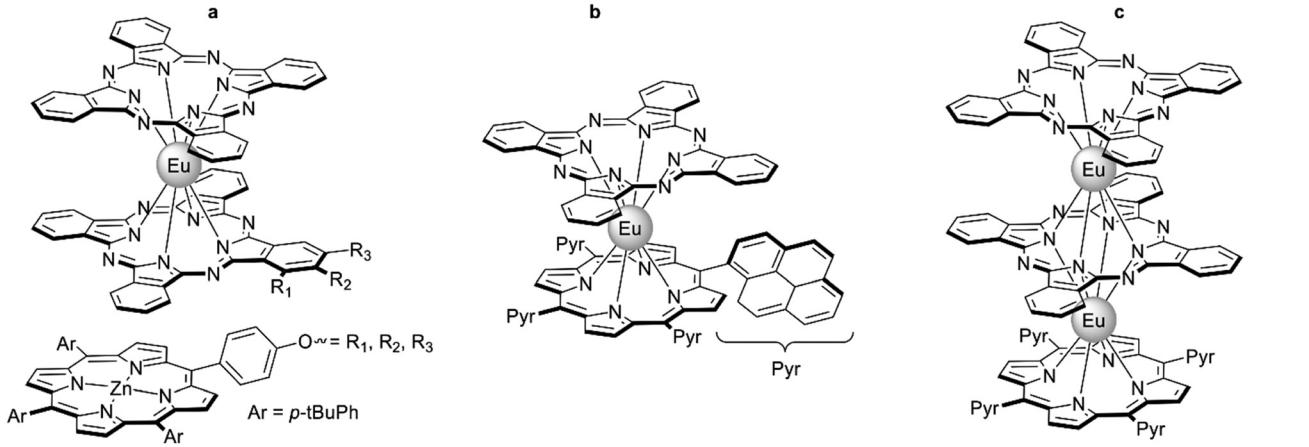

Fig. 42 Examples of π-extended sandwich complexes used for NLO studies: (a) Eu(III) bisphthalocyaninates with appended porphyrin units;[469] (b and c) double- and triple-decker complexes with *meso*-pyrenyl-substituted porphyrin ligands.[31]

introduction of diethyleneglycol substituents (Scheme 11), which in turn can be used to graft complexes to quantum dot surfaces gaining even more spectacular improvement of OL characteristics.

The third-order NLO properties of multi-decker sandwiches with more than a three layered structure were also examined by using Z-scan technique.[48,209,471–473] Along with expanding the π–π interaction system in the order of triple-, quadruple-, quintuple-, and sextuple-deckers, as expected, the NLO responses are gradually improved due to the extended oscillating space. Remarkable $\chi_I^{(3)}$ and γ_R values of 4910 × 10^{-12} and 12 700 × 10^{-30} esu were recorded for a sextuple-decker **$Nd_3Cd_2[(tBuPhO)_4Pc]_6$** in the Z-scan test (10 ns, 532 nm, 3.0 × 10^{-4} M in CH_2Cl_2),[48] suggesting the great potential for application.

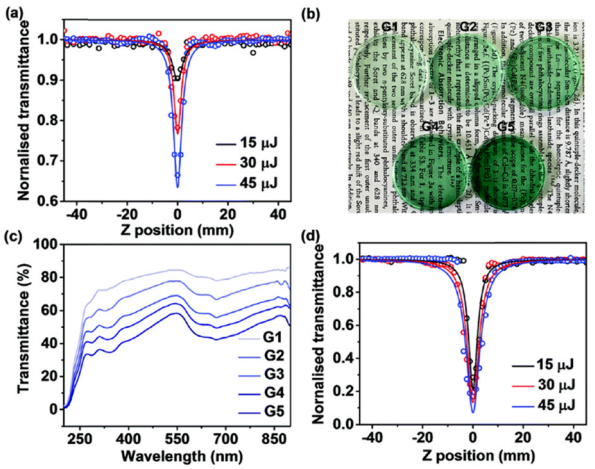

Fig. 43 (a) NLO properties of **(Pc)Sm(Pc)Cd(Pc*)Cd(Pc*)Cd(Pc)Sm(Pc)** in $CHCl_3$ at a concentration of 2.0 × 10^{-5} mol L^{-1} at different incident intensities. (b) Photographs of the gel glass of the complex with different concentrations, G1–G5 where the number corresponds to weight percentage of the complex. (c) Transmittance spectra of glasses G1–G5. (d) NLO properties of gel glass G1 at different incident intensities. Reproduced from ref. 474 with permission from the Royal Society of Chemistry.

While solution measurements provide fundamental NLO characteristics of synthesized complexes, their practical application requires immobilization of molecules on surfaces or incorporation into polymeric matrices for coating fabrication. The latter approach was used by Liu *et al.* to form optical limiters based on heteroleptic sextuple-decker complex **(Pc)Sm(Pc)Cd(Pc*)Cd(Pc*)Cd(Pc)Sm(Pc)**, where Pc* = $(BuO)_8Pc$.[474] Due to RSA mechanism this complex showed excellent OL characteristics in chloroform solution (Fig. 43a), which inspired the authors to probe its practical application. Thus, this complex was dispersed in gel glass formed by methyltriethoxysilane polycondensation (Fig. 43b), affording materials capable of efficient optical limiting – while linear transmittance of a glass sample containing 1 mass% of complex was 84% (Fig. 43c), the minimum normalized transmittances decreased to 10% (Fig. 43d).

6. Conclusions

The data presented in this review showed that tetrapyrrole sandwich complexes based on rare earth elements are a unique molecular platform for targeted design of functional materials. Over the last 20 years, the field of REE sandwich complexes has made great progress in both basic and applied research. The variety of architectures and properties of sandwiches presented in this review shows fantastic opportunities for their application in advanced technologies, particularly SMM-based quantum information storage and processing, where spins are used as information carriages and quantum effects play an important role.

We can expect that the prospects for the use of REE tetrapyrrolic sandwiches will greatly expand in the coming years both with the further development of their synthetic chemistry and further elaboration of approaches to hybrid materials and thin film-based devices. The latter aspect is particularly important in terms of application, as the requirements in small amounts of complexes needed for the fabrication of such devices partially alleviate the need in large scale synthesis.

Thus, despite the rather large number of papers already published and reviewed, this area of research still has many avenues for further development, so the authors are confident that this review will encourage scientists from various fields of chemistry and materials science to tackle this exciting and promising topic.

List of abbreviations

3*n*C*n*, *n* = 4, 5, 6	3*n*-crown-*n*-ether
acac$^-$	Acetylacetonate
ClN	Chloronaphthalene
c-Pc$_2$	Clamshell-bisphthalocyanine
DClB	Dichlorobenzene
dpm$^-$	Dipivaloylmethanate
DZPc	Diazepinoporphyrazine
f-Pc$_2$	Fused bisphthalocyanine
Hp	Hemiporphyrazine
LF	Ligand-field
Ln	Lanthanide
Menth	Menthyl
Naph	Naphthyl
Nc	Naphthalocyanine
NLO	Nonlinear optics
OFET	Organic field-effect transistor
P or Por	Porphyrin
Pc	Phthalocyanine
Pz	Porphyrazine
QT	Quantum technology
QTM	Quantum tunneling of magnetization
REE	Rare earth element
SB	Schiff base
SMM	Single-molecule magnet
SOC	Spin–orbit coupling
SWNT	Single-wall nanotube
TAnP	Tetra-*p*-anisylpoprhyrin
TBP	Tetrabenzoporphyrin
TBTAP	Tetrabenzotriazporphyrin
TClB	1,2,4-Trichlorobenzene
TClPP	Tetra-*p*-chlorophenylpoprhyrin
TM	Transition metal
TTP	Tetra-*p*-tolylporphyrin

Conflicts of interest

There are no conflicts to declare.

Acknowledgements

A. G. Martynov (Chapter 2) thanks Russian Science Foundation (18-73-10174-P). Y. Horii thanks the JSPS KAKENHI Grant Number JP21K14645. K. Katoh thanks the JSPS KAKENHI Grant Number JP24750119, JP15K05467. Y. Bian thanks the Financial support from the National Natural Science Foundation of China (22271012) and Beijing Natural Science Foundation (2202028). J. Jiang thanks the Financial support from the National Natural Science Foundation of China (22235001, 22175020), M. Yamashita thanks the JSPS KAKENHI Grant Number JP19H05631, JP20225003, CREST (JPMJCR12L3) from JST, the National Natural Science Foundation of China (NSFC, 22150710513), and the 111 project (B18030) from China.

Notes and references

1 D. K. P. Ng and J. Jiang, *Chem. Soc. Rev.*, 1997, **26**, 433–442.
2 J. W. Buchler and D. K. P. Ng, in *The Porphyrin Handbook*, ed. K. M. Kadish, K. M. Smith and R. Guilard, Academic Press, New York, 2000, vol. 3, pp. 245–294.
3 J. Jiang, K. Kasuga and D. P. Arnold, in *Supramolecular Photosensitive and Electroactive Materials*, ed. H. S. Nalwa, Elsevier, 2001, pp. 113–210.
4 R. Weiss and J. Fischer, in *The Porphyrin Handbook*, ed. K. M. Kadish, K. M. Smith and R. Guilard, Academic Press, New York, 2003, vol. 16, pp. 171–246.
5 V. E. Pushkarev, L. G. Tomilova and V. N. Nemykin, *Coord. Chem. Rev.*, 2016, **319**, 110–179.
6 V. E. Pushkarev, L. G. Tomilova and Y. V. Tomilov, *Russ. Chem. Rev.*, 2008, **77**, 875–907.
7 J. Jiang and D. K. P. Ng, *Acc. Chem. Res.*, 2009, **42**, 79–88.
8 M. Bouvet, P. Gaudillat and J.-M. M. Suisse, *J. Porphyrins Phthalocyanines*, 2013, **17**, 628–635.
9 H. Wang, B. W. Wang, Y. Bian, S. Gao and J. Jiang, *Coord. Chem. Rev.*, 2016, **306**, 195–216.
10 W. L. Chan, C. Xie, W. S. Lo, J. C. G. Bünzli, W. K. Wong and K. L. Wong, *Chem. Soc. Rev.*, 2021, **50**, 12189–12257.
11 X. Tang, Q. Liu, C. Wei, X. Lv, Z. Jin, Y. Chen and J. Jiang, *J. Rare Earths*, 2021, **39**, 113–120.
12 P. A. Barrett, C. E. Dent and R. P. Linstead, *J. Chem. Soc.*, 1936, 1719.
13 I. S. Kirin, P. N. Moskalev and Y. A. Makashev, *Russ. J. Inorg. Chem.*, 1965, **10**, 1065–1066.
14 G. A. Corker, B. Grant and N. J. Clecak, *J. Electrochem. Soc.*, 1979, **126**, 1339–1343.
15 D. Markovitsi, T.-H. Tran-Thi, R. Even and J. Simon, *Chem. Phys. Lett.*, 1987, **137**, 107–112.
16 R. Rousseau, R. Aroca and M. L. Rodríguez-Méndez, *J. Mol. Struct.*, 1995, **356**, 49–62.
17 L. G. Tomilova, E. V. Chernykh, N. A. Ovchinnikova, E. V. Bezlepko, V. M. Mizin and E. A. Lukyanets, *Opt. Spectrosc.*, 1991, **70**, 775–778.
18 K. Kasuga, M. Ando, H. Morimoto and M. Isa, *Chem. Lett.*, 1986, 1095–1098.
19 M. M'Sadak, J. Roncali and F. Garnier, *J. Chim. Phys.*, 1986, **83**, 211–216.
20 K. Kasuga, M. Tsutsui, R. C. Petterson, K. Tatsumi, N. Van Opdenbosch, G. Pepe and E. F. Meyer, *J. Am. Chem. Soc.*, 1980, **102**, 4835–4836.
21 S. I. Troyanov, L. A. Lapkina, V. E. Larchenko and A. Y. Tsivadze, *Dokl. Chem.*, 1999, **367**, 192–196.

22 A. De Cian, M. Moussavi, J. Fischer and R. Weiss, *Inorg. Chem.*, 1985, **24**, 3162–3167.
23 K. Takahashi, Y. Tomita, Y. Hada, K. Tsubota, M. Handa, K. Kasuga, K. Sogabe and T. Tokii, *Chem. Lett.*, 1992, 759–762.
24 K. Takahashi, M. Itoh, Y. Tomita, K. Nojima, K. Kasuga and K. Isa, *Chem. Lett.*, 1993, 1915–1918.
25 L. A. Lapkina, E. Niskanen, H. Rönkkömäki, V. E. Larchenko, K. I. Popov and A. Y. Tsivadze, *J. Porphyrins Phthalocyanines*, 2000, **4**, 588–590.
26 I. V. Nefedova, Y. G. Gorbunova, S. G. Sakharov and A. Y. Tsivadze, *Russ. J. Inorg. Chem.*, 2005, **50**, 165–173.
27 J. W. Buchler, H.-G. Kapellmann, M. Knoff, K.-L. Lay and S. Pfeifer, *Zeitschrift für Naturforsch. B*, 1983, **38**, 1339–1345.
28 J. W. Buchler, K. Elsässer, M. Kihn-Botulinski and B. Scharbert, *Angew. Chem., Int. Ed. Engl.*, 1986, **25**, 286–287.
29 J. W. Buchler, A. De Cian, J. Fischer, M. Kihn-Botulinski, H. Paulus and R. Weiss, *J. Am. Chem. Soc.*, 1986, **108**, 3652–3659.
30 J. W. Buchler, A. De Cian, J. Fischer, M. Kihn-Botulinski and R. Weiss, *Inorg. Chem.*, 1988, **27**, 339–345.
31 J. K. Duchowski and D. F. Bocian, *J. Am. Chem. Soc.*, 1990, **112**, 8807–8811.
32 H. Heiner, A. Tutaß, M. Göldner, U. Cornelissen and H. Homborg, *Z. Anorg. Allg. Chem.*, 2001, **627**, 485–497.
33 L. A. Lapkina, S. G. Sakharov, N. Y. Konstantinov, V. E. Larchenko, Y. G. Gorbunova and A. Y. Tsivadze, *Russ. J. Inorg. Chem.*, 2007, **52**, 1758–1768.
34 M. Moussavi, A. De Cian, J. Fischer and R. Weiss, *Inorg. Chem.*, 1986, **25**, 2107–2108.
35 P. Turek, P. Petit, J. J. Andre, J. Simon, R. Even, B. Boudjema, G. Guillaud and M. Maitrot, *J. Am. Chem. Soc.*, 1987, **109**, 5119–5122.
36 N. Ishikawa, M. Sugita, T. Ishikawa, S.-Y. Koshihara and Y. Kaizu, *J. Am. Chem. Soc.*, 2003, **125**, 8694–8695.
37 G. Lu, M. Bai, R. Li, X. Zhang, C. Ma, P.-C. Lo, D. K. P. Ng and J. Jiang, *Eur. J. Inorg. Chem.*, 2006, 3703–3709.
38 X. Kong, Q. Jia, F. Wu and Y. Chen, *Dyes Pigm.*, 2015, **115**, 67–72.
39 X. Kong, Z. Dong, Y. Wu, X. Li, Y. Chen and J. Jiang, *Chin. J. Chem.*, 2016, **34**, 975–982.
40 X. Kong, G. Lu, X. Zhang, X. Li, Y. Chen and J. Jiang, *Dyes Pigm.*, 2017, **143**, 203–210.
41 X. Kong, X. Zhang, D. Gao, D. Qi, Y. Chen and J. Jiang, *Chem. Sci.*, 2015, **6**, 1967–1972.
42 D. Li, H. Wang, J. Kan, W. Lu, Y. Chen and J. Jiang, *Org. Electron.*, 2013, **14**, 2582–2589.
43 T. V. Dubinina, A. D. Kosov, E. F. Petrusevich, S. S. Maklakov, N. E. Borisova, L. G. Tomilova and N. S. Zefirov, *Dalton Trans.*, 2015, **44**, 7973–7981.
44 J. Kan, Y. Chen, D. Qi, Y. Liu and J. Jiang, *Adv. Mater.*, 2012, **24**, 1755–1758.
45 K. E. Sekhosana, E. Amuhaya, J. Mack and T. Nyokong, *J. Mater. Chem. C*, 2014, **2**, 5431–5437.
46 K. E. Sekhosana, M. H. Manyeruke and T. Nyokong, *J. Mol. Struct.*, 2016, **1121**, 111–118.
47 K. E. Sekhosana, R. Nkhahle and T. Nyokong, *ChemistrySelect*, 2018, **3**, 6671–6682.
48 K. E. Sekhosana and T. Nyokong, *Dyes Pigm.*, 2020, **172**, 107836.
49 C. R. Ganivet, B. Ballesteros, G. de la Torre, J. M. Clemente-Juan, E. Coronado and T. Torres, *Chem. – Eur. J.*, 2013, **19**, 1457–1465.
50 T. V. Dubinina, K. V. Paramonova, S. A. Trashin, N. E. Borisova, L. G. Tomilova and N. S. Zefirov, *Dalton Trans.*, 2014, **43**, 2799–2809.
51 T. V. Dubinina, M. S. Belousov, S. S. Maklakov, V. I. Chernichkin, M. V. Sedova, V. A. Tafeenko, N. E. Borisova and L. G. Tomilova, *Dyes Pigm.*, 2019, **170**, 107655.
52 N. Kobayashi and A. B. P. Lever, *J. Am. Chem. Soc.*, 1987, **109**, 7433–7441.
53 O. E. Sielcken, M. M. Van Tilborg, M. F. M. Roks, R. Hendriks, W. Drenth and R. J. M. Nolte, *J. Am. Chem. Soc.*, 1987, **109**, 4261–4265.
54 T. Toupance, V. Ahsen and J. Simon, *J. Am. Chem. Soc.*, 1994, **116**, 5352–5361.
55 T. Toupance, H. Benoit, D. Sarazin and J. Simon, *J. Am. Chem. Soc.*, 1997, **119**, 9191–9197.
56 Y. G. Gorbunova, L. A. Lapkina, A. G. Martynov, I. V. Biryukova and A. Y. Tsivadze, *Russ. J. Coord. Chem.*, 2004, **30**, 245–251.
57 A. May, P. Majumdar, A. G. Martynov, L. A. Lapkina, S. I. Troyanov, Y. G. Gorbunova, A. Y. Tsivadze, J. Mack and T. Nyokong, *J. Porphyrins Phthalocyanines*, 2020, **24**, 589–601.
58 Y. G. Gorbunova, A. G. Martynov and A. Y. Tsivadze, in *Handbook of Porphyrin Science*, ed. K. M. Kadish, K. M. Smith and R. Guilard, World Scientific Publishing, 2012, vol. 24, pp. 271–388.
59 K. P. Birin, Y. G. Gorbunova and A. Y. Tsivadze, *J. Porphyrins Phthalocyanines*, 2006, **10**, 931–936.
60 A. G. Martynov, E. A. Safonova, A. Y. Tsivadze and Y. G. Gorbunova, *Coord. Chem. Rev.*, 2019, **387**, 325–347.
61 S. L. Selektor, A. V. Shokurov, V. V. Arslanov, Y. G. Gorbunova, K. P. Birin, O. A. Raitman, F. Morote, T. Cohen-Bouhacina, C. Grauby-Heywang and A. Y. Tsivadze, *J. Phys. Chem. C*, 2014, **118**, 4250–4258.
62 A. V. Shokurov, D. S. Kutsybala, A. G. Martynov, A. V. Bakirov, M. A. Shcherbina, S. N. Chvalun, Y. G. Gorbunova, A. Y. Tsivadze, A. V. Zaytseva, D. Novikov, V. V. Arslanov and S. L. Selektor, *Langmuir*, 2020, **36**, 1423–1429.
63 D. S. Kutsybala, A. V. Shokurov, A. G. Martynov, A. V. Yagodin, V. V. Arslanov, Y. G. Gorbunova and S. L. Selektor, *Symmetry*, 2022, **14**, 340.
64 S. P. Babailov, M. A. Polovkova, G. A. Kirakosyan, A. G. Martynov, E. N. Zapolotsky and Y. G. Gorbunova, *Sens. Actuators, A*, 2021, **331**, 112933.
65 S. P. Babailov, M. A. Polovkova, E. N. Zapolotsky, G. A. Kirakosyan, A. G. Martynov and Y. G. Gorbunova, *J. Porphyrins Phthalocyanines*, 2022, **26**, 334–339.
66 R. J. Holmberg, M. A. Polovkova, A. G. Martynov, Y. G. Gorbunova and M. Murugesu, *Dalton Trans.*, 2016, **45**, 9320–9327.

67 Y. Horii, S. Kishiue, M. Damjanović, K. Katoh, B. K. Breedlove, M. Enders and M. Yamashita, *Chem. – Eur. J.*, 2018, **24**, 4320–4327.
68 A. G. Martynov, A. V. Bykov, Y. G. Gorbunova and A. Y. Tsivadze, *Russ. Chem. Bull.*, 2018, **67**, 2195–2200.
69 A. G. Martynov, O. V. Zubareva, Y. G. Gorbunova, S. G. Sakharov, S. E. Nefedov, F. M. Dolgushin and A. Y. Tsivadze, *Eur. J. Inorg. Chem.*, 2007, 4800–4807.
70 A. G. Martynov, E. A. Safonova, Y. G. Gorbunova and A. Y. Tsivadze, *Russ. J. Inorg. Chem.*, 2010, **55**, 347–354.
71 A. Y. Tsivadze, A. G. Martynov, M. A. Polovkova and Y. G. Gorbunova, *Russ. Chem. Bull.*, 2011, **60**, 2258–2262.
72 M. A. Polovkova, A. G. Martynov, K. P. Birin, S. E. Nefedov, Y. G. Gorbunova and A. Y. Tsivadze, *Inorg. Chem.*, 2016, **55**, 9258–9269.
73 A. V. Shokurov, A. V. Yagodin, A. G. Martynov, Y. G. Gorbunova, A. Y. Tsivadze and S. L. Selektor, *Small*, 2022, **18**, 2104306.
74 H. Zhou, K. Wang, D. Qi and J. Jiang, *Dalton Trans.*, 2014, **43**, 1699–1705.
75 W. Lv, P. Zhu, Y. Bian, C. Ma, X. Zhang and J. Jiang, *Inorg. Chem.*, 2010, **49**, 6628–6635.
76 W. Zheng, B.-B. Wang, J.-C. Lai, C.-Z. Wan, X.-R. Lu, C.-H. Li and X.-Z. You, *J. Mater. Chem. C*, 2015, **3**, 3072–3080.
77 M. Gonidec, F. Luis, À. Vílchez, J. Esquena, D. B. Amabilino and J. Veciana, *Angew. Chem., Int. Ed.*, 2010, **49**, 1623–1626.
78 E. A. Kuzmina, T. V. Dubinina and L. G. Tomilova, *New J. Chem.*, 2019, **43**, 9314–9327.
79 Y. Chen, W. Cao, K. Wang and J. Jiang, *Inorg. Chem.*, 2015, **54**, 9962–9967.
80 Y. Chen, F. Ma, X. Chen, B. Dong, K. Wang, S. Jiang, C. Wang, X. Chen, D. Qi, H. Sun, B. Wang, S. Gao and J. Jiang, *Inorg. Chem. Front.*, 2017, **4**, 1465–1471.
81 Y. Chen, F. Ma, X. Chen, B. Dong, K. Wang, S. Jiang, C. Wang, X. Chen, D. Qi, H. Sun, B. Wang, S. Gao and J. Jiang, *Inorg. Chem.*, 2017, **56**, 13889–13896.
82 C. Liu, M. Li, Y. Zhang, H. Tian, Y. Chen, H. Wang, J. Dou and J. Jiang, *Eur. J. Inorg. Chem.*, 2019, 2940–2946.
83 Y. Chen, F. Ma, Y. Zhang, L. Zhao, K. Wang, D. Qi, H. Sun and J. Jiang, *Inorg. Chem. Front.*, 2018, **5**, 2006–2012.
84 S. Takamatsu, T. Ishikawa, S. Koshihara and N. Ishikawa, *Inorg. Chem.*, 2007, **46**, 7250–7252.
85 D. V. Konarev, S. S. Khasanov, M. S. Batov, A. G. Martynov, I. V. Nefedova, Y. G. Gorbunova, A. Otsuka, H. Yamochi, H. Kitagawa and R. N. Lyubovskaya, *Inorg. Chem.*, 2019, **58**, 5058–5068.
86 M. Gonidec, D. B. Amabilino and J. Veciana, *Dalton Trans.*, 2012, **41**, 13632.
87 M. Gonidec, I. Krivokapic, J. Vidal-Gancedo, E. S. Davies, J. McMaster, S. M. Gorun and J. Veciana, *Inorg. Chem.*, 2013, **52**, 4464–4471.
88 A. Şenocak, B. Köksoy, E. Demirbaş and M. Durmuş, *J. Phys. Org. Chem.*, 2019, **32**, e3907.
89 F. Bertani, N. Cristiani, M. Mannini, R. Pinalli, R. Sessoli and E. Dalcanale, *Eur. J. Org. Chem.*, 2015, 7036–7042.
90 E. A. Kuzmina, T. V. Dubinina, N. E. Borisova, B. N. Tarasevich, V. I. Krasovskii, I. N. Feofanov, A. V. Dzuban and L. G. Tomilova, *Dyes Pigm.*, 2020, **174**, 108075.
91 E. A. Kuzmina, T. V. Dubinina, P. N. Vasilevsky, M. S. Saveliev, A. Y. Gerasimenko, N. E. Borisova and L. G. Tomilova, *Dyes Pigm.*, 2021, **185**, 108871.
92 E. A. Safonova, A. G. Martynov, S. E. Nefedov, G. A. Kirakosyan, Y. G. Gorbunova and A. Y. Tsivadze, *Inorg. Chem.*, 2016, **55**, 2450–2459.
93 R. Wang, R. Li, Y. Bian, C.-F. Choi, D. K. P. Ng, J. Dou, D. Wang, P. Zhu, C. Ma, R. D. Hartnell, D. P. Arnold and J. Jiang, *Chem. – Eur. J.*, 2005, **11**, 7351–7357.
94 Y. Chen, F. Ma, X. Chen, Y. Zhang, H. Wang, K. Wang, D. Qi, H.-L. Sun and J. Jiang, *Inorg. Chem.*, 2019, **58**, 2422–2429.
95 Y. Gao, R. Li, S. Dong, Y. Bian and J. Jiang, *Dalton Trans.*, 2010, **39**, 1321–1327.
96 M. Damjanović, Y. Horie, T. Morita, Y. Horii, K. Katoh, M. Yamashita and M. Enders, *Inorg. Chem.*, 2015, **54**, 11986–11992.
97 Y. Horii, Y. Horie, K. Katoh, B. K. Breedlove and M. Yamashita, *Inorg. Chem.*, 2018, **57**, 565–574.
98 J. Mack and N. Kobayashi, *Chem. Rev.*, 2011, **111**, 281–321.
99 N. Ishikawa and Y. Kaizu, *Chem. Lett.*, 1998, 183–184.
100 S. Alpugan, Ü. İşci, F. Albrieux, C. Hirel, A. G. Gürek, Y. Bretonnière, V. Ahsen and F. Dumoulin, *Chem. Commun.*, 2014, **50**, 7466.
101 D. O. Oluwole, A. V. Yagodin, N. C. Mkhize, K. E. Sekhosana, A. G. Martynov, Y. G. Gorbunova, A. Y. Tsivadze and T. Nyokong, *Chem. – Eur. J.*, 2017, **23**, 2820–2830.
102 V. E. Pushkarev, A. Y. Tolbin, N. E. Borisova, S. A. Trashin and L. G. Tomilova, *Eur. J. Inorg. Chem.*, 2010, 5254–5262.
103 A. Pedrini, M. Perfetti, M. Mannini and E. Dalcanale, *ACS Omega*, 2017, **2**, 517–521.
104 V. E. Pushkarev, A. Y. Tolbin, F. E. Zhurkin, N. E. Borisova, S. A. Trashin, L. G. Tomilova and N. S. Zefirov, *Chem. – Eur. J.*, 2012, **18**, 9046–9055.
105 Y. Horii, K. Katoh, B. K. Breedlove and M. Yamashita, *Chem. Commun.*, 2017, **53**, 8561–8564.
106 Y. S. Korostei, V. G. Tarasova, V. E. Pushkarev, N. E. Borisova, A. K. Vorobiev and L. G. Tomilova, *Dyes Pigm.*, 2018, **159**, 573–575.
107 K. P. Birin, A. I. Poddubnaya, E. V. Isanbaeva, Y. G. Gorbunova and A. Y. Tsivadze, *J. Porphyrins Phthalocyanines*, 2017, **21**, 406–415.
108 W. Lu, C. Wang, X. Li, X. Zhan, D. Qi and Y. Bian, *Inorg. Chem. Commun.*, 2017, **81**, 18–21.
109 M. M. Ayhan, A. Singh, C. Hirel, A. G. Gürek, V. Ahsen, E. Jeanneau, I. Ledoux-Rak, J. Zyss, C. Andraud and Y. Bretonnière, *J. Am. Chem. Soc.*, 2012, **134**, 3655–3658.
110 M. M. Ayhan, A. Singh, E. Jeanneau, V. Ahsen, J. Zyss, I. Ledoux-Rak, A. G. Gürek, C. Hirel, Y. Bretonnière and C. Andraud, *Inorg. Chem.*, 2014, **53**, 4359–4370.
111 W. Cao, K. Wang, I. Ledoux-Rak and J. Jiang, *Inorg. Chem. Front*, 2016, **3**, 1146–1151.
112 Q. Zhi, F. Ma, C. Wang, Y. Chen, H. Wang, H. Sun and J. Jiang, *Eur. J. Inorg. Chem.*, 2019, 1329–1334.

113 J. Sun and Y. Han, *RSC Adv.*, 2017, **7**, 22855–22859.
114 S. Kyatskaya, J. R. Galán Mascarós, L. Bogani, F. Hennrich, M. Kappes, W. Wernsdorfer and M. Ruben, *J. Am. Chem. Soc.*, 2009, **131**, 15143–15151.
115 S. Klyatskaya, A. Eichhöfer and W. Wernsdorfer, *Eur. J. Inorg. Chem.*, 2014, 4179–4185.
116 O. Hampe, S. Klyatskaya, T. Karpuschkin, M. Vonderach, P. Weis, M. Ruben and M. M. Kappes, *Int. J. Mass Spectrom.*, 2012, **325–327**, 183–188.
117 M. Urdampilleta, S. Klyatskaya, J.-P. Cleuziou, M. Ruben and W. Wernsdorfer, *Nat. Mater.*, 2011, **10**, 502–506.
118 B. Ballesteros, G. de la Torre, A. Shearer, A. Hausmann, M. Â. Ã. Herranz, D. M. Guldi and T. Torres, *Chem. – Eur. J.*, 2010, **16**, 114–125.
119 H. Pan, L. Gong, W. Liu, C. Lin, Q. Ma, G. Lu, D. Qi, K. Wang and J. Jiang, *Dyes Pigm.*, 2018, **156**, 167–174.
120 K. Wang, H. Pan and J. Jiang, *Chem. – Eur. J.*, 2015, **21**, 18461–18465.
121 Y. Li, Y. Bian, M. Yan, P. S. Thapaliya, D. Johns, X. Yan, D. Galipeau and J. Jiang, *J. Mater. Chem.*, 2011, **21**, 11131.
122 S. Sakaue, A. Fuyuhiro, T. Fukuda and N. Ishikawa, *Chem. Commun.*, 2012, **48**, 5337.
123 K. P. Birin, Y. G. Gorbunova, A. Y. Tsivadze and A. Y. Tsivadze, *J. Porphyrins Phthalocyanines*, 2009, **13**, 283.
124 K. P. Birin, Y. G. Gorbunova and A. Y. Tsivadze, *Magn. Reson. Chem.*, 2010, **48**, 505–515.
125 K. P. Birin, Y. G. Gorbunova and A. Y. Tsivadze, *Macroheterocycles*, 2010, **3**, 210–217.
126 K. P. Birin, K. a Kamarova, Y. G. Gorbunova and A. Y. Tsivadze, *J. Porphyrins Phthalocyanines*, 2013, **17**, 1027–1034.
127 K. P. Birin, Y. G. Gorbunova and A. Y. Tsivadze, *Dalton Trans.*, 2011, **40**, 11539–11549.
128 K. P. Birin, A. I. Poddubnaya, Y. G. Gorbunova and A. Y. Tsivadze, *Macroheterocycles*, 2017, **10**, 514–519.
129 K. P. Birin, Y. G. Gorbunova and A. Y. Tsivadze, *Dalton Trans.*, 2012, **41**, 23–28.
130 H.-G. Jin, X. Jiang, I. A. Kühne, S. Clair, V. Monnier, C. Chendo, G. Novitchi, A. K. Powell, K. M. Kadish and T. S. Balaban, *Inorg. Chem.*, 2017, **56**, 4864–4873.
131 D. González-Lucas, S. C. Soobrattee, D. L. Hughes, G. J. Tizzard, S. J. Coles and A. N. Cammidge, *Chem. – Eur. J.*, 2020, **26**, 10724–10728.
132 P. Zhu, X. Zhang, H. Wang, Y. Zhang, Y. Bian and J. Jiang, *Inorg. Chem.*, 2012, **51**, 5651–5659.
133 X. Wu, W. Lv, Q. Wang, H. Wang, X. Zhang and J. Jiang, *Dalton Trans.*, 2011, **40**, 107–113.
134 J. Lu, L. Zhou, Q. Meng, H. Sui, Y. Li and X. Tai, *Dyes Pigm.*, 2015, **113**, 138–144.
135 T. Komeda, H. Isshiki, J. Liu, K. Katoh, M. Shirakata, B. K. Breedlove and M. Yamashita, *ACS Nano*, 2013, **7**, 1092–1099.
136 K. Katoh, S. Yamashita, N. Yasuda, Y. Kitagawa, B. K. Breedlove, Y. Nakazawa and M. Yamashita, *Angew. Chem., Int. Ed.*, 2018, **57**, 9262–9267.
137 T. V. Dubinina, A. D. Kosov, E. F. Petrusevich, N. E. Borisova, A. L. Trigub, G. V. Mamin, I. F. Gilmutdinov, A. A. Masitov, S. V. Tokarev, V. E. Pushkarev and L. G. Tomilova, *Dalton Trans.*, 2019, **48**, 13413–13422.
138 R. Stefak, N. Ratel-Ramond and G. Rapenne, *Inorg. Chim. Acta*, 2012, **380**, 181–186.
139 Y. Zhang, H. Kersell, R. Stefak, J. Echeverria, V. Iancu, U. G. E. Perera, Y. Li, A. Deshpande, K.-F. Braun, C. Joachim, G. Rapenne and S.-W. Hla, *Nat. Nanotechnol.*, 2016, **11**, 706–712.
140 N. Giménez-Agulló, C. S. de Pipaón, L. Adriaenssens, M. Filibian, M. Martínez-Belmonte, E. C. Escudero-Adán, P. Carretta, P. Ballester and J. R. Galán-Mascarós, *Chem. – Eur. J.*, 2014, **20**, 12817–12825.
141 E. N. Tarakanova, P. A. Tarakanov, V. E. Pushkarev and L. G. Tomilova, *J. Porphyrins Phthalocyanines*, 2014, **18**, 149–154.
142 P. A. Tarakanov, E. N. Tarakanova, P. V. Dorovatovskii, Y. V. Zubavichus, V. N. Khrustalev, S. A. Trashin, K. De Wael, M. E. Neganova, D. V. Mischenko, J. L. Sessler, P. A. Stuzhin, V. E. Pushkarev and L. G. Tomilova, *Dalton Trans.*, 2018, **47**, 14169–14173.
143 E. N. Tarakanova, S. A. Trashin, A. O. Simakov, T. Furuyama, A. V. Dzuban, L. N. Inasaridze, P. A. Tarakanov, P. A. Troshin, V. E. Pushkarev, N. Kobayashi and L. G. Tomilova, *Dalton Trans.*, 2016, **45**, 12041–12052.
144 E. N. Tarakanova, S. A. Trashin, P. A. Tarakanov, V. E. Pushkarev and L. G. Tomilova, *Dyes Pigm.*, 2015, **117**, 61–63.
145 E. N. Tarakanova, O. A. Levitskiy, T. V. Magdesieva, P. A. Tarakanov, V. E. Pushkarev and L. G. Tomilova, *New J. Chem.*, 2015, **39**, 5797–5804.
146 E. N. Tarakanova, P. A. Tarakanov, A. O. Simakov, T. Furuyama, N. Kobayashi, D. V. Konev, O. A. Goncharova, S. A. Trashin, K. De Wael, I. V. Sulimenkov, V. V. Filatov, V. I. Kozlovskiy, L. G. Tomilova, P. A. Stuzhin and V. E. Pushkarev, *Dalton Trans.*, 2021, **50**, 6245–6255.
147 T. V. Dubinina, D. V. Dyumaeva, S. A. Trashin, M. V. Sedova, A. S. Dudnik, N. E. Borisova, L. G. Tomilova and N. S. Zefirov, *Dyes Pigm.*, 2013, **96**, 699–704.
148 J. H. Helberger, A. von Rebay and D. B. Hevér, *Justus Liebigs Ann. Chem.*, 1938, **533**, 197–215.
149 H. Y. Xu, C. H. Hu, Q. F. Liu, W. X. Zhao and Y. Liu, *Appl. Mech. Mater.*, 2012, **190–191**, 571–574.
150 Q. F. Liu, *Adv. Mater. Res.*, 2013, **750–752**, 1816–1821.
151 Q. F. Liu, *Adv. Mater. Res.*, 2013, **690–693**, 573–576.
152 N. E. Galanin and G. P. Shaposhnikov, *Russ. J. Org. Chem.*, 2012, **48**, 851–857.
153 A. I. Koptyaev, N. E. Galanin and G. P. Shaposhnikov, *Russ. J. Org. Chem.*, 2019, **55**, 944–950.
154 A. I. Koptyaev, N. E. Galanin, V. V. Travkin and G. L. Pakhomov, *Dyes Pigm.*, 2021, **186**, 108984.
155 A. I. Koptyaev, M. I. Bazanov and N. E. Galanin, *Russ. J. Org. Chem.*, 2020, **56**, 788–796.
156 N. E. Galanin, L. A. Yakubov and G. P. Shaposhnikov, *Russ. J. Org. Chem.*, 2011, **47**, 941–947.
157 V. E. Pushkarev, V. V. Kalashnikov, S. A. Trashin, N. E. Borisova, L. G. Tomilova and N. S. Zefirov, *Dalton Trans.*, 2013, **42**, 12083.

158 V. E. Pushkarev, V. V. Kalashnikov, A. Y. Tolbin, S. A. Trashin, N. E. Borisova, S. V. Simonov, V. B. Rybakov, L. G. Tomilova and N. S. Zefirov, *Dalton Trans.*, 2015, **44**, 16553–16564.
159 Z. Gross, N. Galili and I. Saltsman, *Angew. Chem., Int. Ed.*, 1999, **38**, 1427–1429.
160 S. Nardis, F. Mandoj, M. Stefanelli and R. Paolesse, *Coord. Chem. Rev.*, 2019, **388**, 360–405.
161 H. L. Buckley, M. R. Anstey, D. T. Gryko and J. Arnold, *Chem. Commun.*, 2013, **49**, 3104.
162 K. C. Armstrong, S. Hohloch, T. D. Lohrey, R. A. Zarkesh, J. Arnold and M. R. Anstey, *Dalton Trans.*, 2016, **45**, 18653–18660.
163 G. Lu, S. Yan, M. Shi, W. Yu, J. Li, W. Zhu, Z. Ou and K. M. Kadish, *Chem. Commun.*, 2015, **51**, 2411–2413.
164 G. Lu, C. He, K. Wang, J. Sun, D. Qi, L. Gong, C. Wang, Z. Ou, S. Yan, S. Zeng and W. Zhu, *Inorg. Chem.*, 2017, **56**, 11503–11512.
165 G. Lu, J. Li, S. Yan, C. He, M. Shi, W. Zhu, Z. Ou and K. M. Kadish, *Dyes Pigm.*, 2015, **121**, 38–45.
166 G. Lu, J. Li, X. Jiang, Z. Ou and K. M. Kadish, *Inorg. Chem.*, 2015, **54**, 9211–9222.
167 G. Lu, J. Li, S. Yan, W. Zhu, Z. Ou and K. M. Kadish, *Inorg. Chem.*, 2015, **54**, 5795–5805.
168 G. Lu, C. He, Y. Fang, L. Wang and W. Zhu, *New J. Chem.*, 2018, **42**, 2498–2503.
169 H. Furuta, T. Asano and T. Ogawa, *J. Am. Chem. Soc.*, 1994, **116**, 767–768.
170 H. Furuta, H. Maeda and A. Osuka, *Chem. Commun.*, 2002, 1795–1804.
171 W. Cao, H. Wang, X. Wang, H. K. Lee, D. K. P. Ng and J. Jiang, *Inorg. Chem.*, 2012, **51**, 9265–9272.
172 Y. Zhang, W. Cao, K. Wang and J. Jiang, *Dalton Trans.*, 2014, **43**, 9152.
173 W. Cao, C. Gao, Y.-Q. Zhang, D. Qi, T. Liu, K. Wang, C. Duan, S. Gao and J. Jiang, *Chem. Sci.*, 2015, **6**, 5947–5954.
174 H. Wang, W. Cao, T. Liu, C. Duan and J. Jiang, *Chem. – Eur. J.*, 2013, **19**, 2266–2270.
175 Q. Ma, X. Feng, W. Cao, H. Wang and J. Jiang, *CrystEngComm*, 2013, **15**, 10383.
176 H. Wang, C. Liu, T. Liu, S. Zeng, W. Cao, Q. Ma, C. Duan, J. Dou and J. Jiang, *Dalton Trans.*, 2013, **42**, 15355.
177 Z. Li, F. Gao, Z. Xiao, G. Ao, X. Wu, Y. Fang, Z. Nie, T. H. Wei, J. Yang, Y. Wang, X. Zhang, J. Zuo and Y. Song, *Dyes Pigm.*, 2015, **119**, 70–74.
178 Z. Li, F. Gao, Z. Xiao, X. Wu, J. Zuo and Y. Song, *Opt. Laser Technol.*, 2018, **103**, 42–47.
179 F. Gao, X.-M. Zhang, L. Cui, K. Deng, Q.-D. Zeng and J.-L. Zuo, *Sci. Rep.*, 2015, **4**, 5928.
180 F. Gao, X. Feng, L. Yang and X. Chen, *Dalton Trans.*, 2016, **45**, 7476–7482.
181 A. Santria, A. Fuyuhiro, T. Fukuda and N. Ishikawa, *Inorg. Chem.*, 2017, **56**, 10625–10632.
182 K. Kizaki, M. Uehara, A. Fuyuhiro, T. Fukuda and N. Ishikawa, *Inorg. Chem.*, 2018, **57**, 668–675.
183 A. Santria, A. Fuyuhiro, T. Fukuda and N. Ishikawa, *Dalton Trans.*, 2019, **48**, 7685–7692.
184 A. Santria and N. Ishikawa, *Inorg. Chem.*, 2020, **59**, 14326–14336.
185 K. Kizaki, A. Santria and N. Ishikawa, *Inorg. Chem.*, 2021, **60**, 2037–2044.
186 R. H. Platel, T. Teixeira Tasso, W. Zhou, T. Furuyama, N. Kobayashi and D. B. Leznoff, *Chem. Commun.*, 2015, **51**, 5986–5989.
187 J. A. Elvidge and R. P. Linstead, *J. Chem. Soc.*, 1952, 5008.
188 W. Liu, H. Pan, Z. Wang, K. Wang, D. Qi and J. Jiang, *Chem. Commun.*, 2017, **53**, 3765–3768.
189 W. Liu, S. Zeng, X. Chen, H. Pan, D. Qi, K. Wang, J. Dou and J. Jiang, *Inorg. Chem.*, 2018, **57**, 12347–12353.
190 F. Gao, M.-X. Yao, Y.-Y. Li, Y.-Z. Li, Y. Song and J.-L. Zuo, *Inorg. Chem.*, 2013, **52**, 6407–6416.
191 J. Y. Hu, Y. Ning, Y. S. Meng, J. Zhang, Z. Y. Wu, S. Gao and J. L. Zhang, *Chem. Sci.*, 2017, **8**, 2702–2709.
192 G. Q. Jin, Y. Ning, J. X. Geng, Z. F. Jiang, Y. Wang and J. L. Zhang, *Inorg. Chem. Front.*, 2020, **7**, 289–299.
193 S. Sarwar, S. Sanz, J. van Leusen, G. S. Nichol, E. K. Brechin and P. Kögerler, *Dalton Trans.*, 2020, **49**, 16638–16642.
194 H. Sugimoto, T. Higashi, A. Maeda, M. Mori, H. Masuda and T. Taga, *J. Chem. Soc., Chem. Commun.*, 1983, 1234–1235.
195 H. Sugimoto, T. Higashi, A. Maeda, Y. Hirai, J. Teraoka, M. Mori, H. Masuda and T. Taga, *J. Less Common Met.*, 1985, **112**, 387–392.
196 A. Maeda and H. Sugimoto, *J. Chem. Soc., Faraday Trans. 2*, 1986, **82**, 2019.
197 S. Tsuchiya, A. Fuyuhiro, T. Fukuda and N. Ishikawa, *J. Porphyrins Phthalocyanines*, 2014, **18**, 933–936.
198 J.-Y. Ge, H.-Y. Wang, J. Li, J.-Z. Xie, Y. Song and J.-L. Zuo, *Dalton Trans.*, 2017, **46**, 3353–3362.
199 J. Ge, Y. Qiu, H. Wang, J. Su, P. Wang and Z. Chen, *Chem. – Asian J.*, 2020, **15**, 3013–3019.
200 J.-Y. Ge, L. Cui, J. Li, F. Yu, Y. Song, Y.-Q. Zhang, J.-L. Zuo and M. Kurmoo, *Inorg. Chem.*, 2017, **56**, 336–343.
201 J.-Y. Ge, H.-Y. Wang, J. Su, J. Li, B.-L. Wang, Y.-Q. Zhang and J.-L. Zuo, *Inorg. Chem.*, 2018, **57**, 1408–1416.
202 T. Fukuda, T. Biyajima and N. Kobayashi, *J. Am. Chem. Soc.*, 2010, **132**, 6278–6279.
203 T. Fukuda, K. Hata and N. Ishikawa, *J. Am. Chem. Soc.*, 2012, **134**, 14698–14701.
204 T. Fukuda and N. Ishikawa, *J. Porphyrins Phthalocyanines*, 2014, **18**, 615–629.
205 H. Wang, K. Qian, K. Wang, Y. Bian, J. Jiang and S. Gao, *Chem. Commun.*, 2011, **47**, 9624–9626.
206 G. Lu, X. Kong, H. Wang, Y. Y. Chen, C. Wei, Y. Y. Chen and J. Jiang, *New J. Chem.*, 2019, **43**, 15763–15767.
207 H. Wang, K. Wang, Y. Bian, J. Jiang and N. Kobayashi, *Chem. Commun.*, 2011, **47**, 6879.
208 H. Wang, N. Kobayashi and J. Jiang, *Chem. – Eur. J.*, 2012, **18**, 1047–1049.
209 H. Wang, D. Qi, Z. Xie, W. Cao, K. Wang, H. Shang and J. Jiang, *Chem. Commun.*, 2013, **49**, 889–891.

210 C. Liu, W. Yang, Y. Zhang and J. Jiang, *Inorg. Chem.*, 2020, **59**, 17591–17599.
211 K. Katoh, Y. Horii, N. Yasuda, W. Wernsdorfer, K. Toriumi, B. K. Breedlove and M. Yamashita, *Dalton Trans.*, 2012, **41**, 13582–13600.
212 Y. Horii, K. Katoh, N. Yasuda, B. K. Breedlove and M. Yamashita, *Inorg. Chem.*, 2015, **54**, 3297–3305.
213 Y. Horii, K. Katoh, G. Cosquer, B. K. Breedlove and M. Yamashita, *Inorg. Chem.*, 2016, **55**, 11782–11790.
214 Y. Horii, M. Damjanović, M. R. Ajayakumar, K. Katoh, Y. Kitagawa, L. Chibotaru, L. Ungur, M. Mas-Torrent, W. Wernsdorfer, B. K. Breedlove, M. Enders, J. Veciana and M. Yamashita, *Chem. – Eur. J.*, 2020, **26**, 8621–8630.
215 N. Kobayashi, H. Lam, W. A. Nevin, P. Janda, C. C. Leznoff, T. Koyama, A. Monden and H. Shirai, *J. Am. Chem. Soc.*, 1994, **116**, 879–890.
216 K. Wang, D. Qi, H. Wang, W. Cao, W. Li, T. Liu, C. Duan and J. Jiang, *Chem. – Eur. J.*, 2013, **19**, 11162–11166.
217 T. Morita, M. Damjanović, K. Katoh, Y. Kitagawa, N. Yasuda, Y. Lan, W. Wernsdorfer, B. K. Breedlove, M. Enders and M. Yamashita, *J. Am. Chem. Soc.*, 2018, **140**, 2995–3007.
218 C. Wei, G. Lu, C. Guo, X. Lv, X. Tang, Q. Liu, X. Cai, Y. Chen and J. Jiang, *Org. Electron.*, 2021, **93**, 106151.
219 T. Morita, K. Katoh, B. K. Breedlove and M. Yamashita, *Inorg. Chem.*, 2013, **52**, 13555–13561.
220 K. Katoh, T. Morita, N. Yasuda, W. Wernsdorfer, Y. Kitagawa, B. K. Breedlove and M. Yamashita, *Chem. – Eur. J.*, 2018, **24**, 15522–15528.
221 G. Lu, K. Wang, X. Kong, H. Pan, J. Zhang, Y. Chen and J. Jiang, *ChemElectroChem*, 2018, **5**, 605–609.
222 X. Cai, C. Wei, J. Dong, Q. Liu, Y. Wu, G. Lu, Y. Chen and J. Jiang, *J. Mater. Sci.: Mater. Electron.*, 2019, **30**, 1976–1983.
223 G. Lu, X. Kong, J. Sun, L. Zhang, Y. Chen and J. Jiang, *Chem. Commun.*, 2017, **53**, 12754–12757.
224 S. Lee, K. ichi Yamashita, N. Sakata, Y. Hirao, K. Ogawa and T. Ogawa, *Chem. – Eur. J.*, 2019, **25**, 3240–3243.
225 W. Wernsdorfer, N. Aliaga-Alcalde, D. N. Hendrickson and G. Christou, *Nature*, 2002, **416**, 406–409.
226 R. Sessoli, D. Gatteschi, A. Caneschi and M. A. Novak, *Nature*, 1993, **365**, 141–143.
227 D. Gatteschi and R. Sessoli, *Angew. Chem., Int. Ed.*, 2003, **42**, 268–297.
228 ed. *Molecular Nanomagnets and Related Phenomena*, S. Gao, Springer Berlin Heidelberg, Berlin, Heidelberg, 2015, vol. 164.
229 J. D. Rinehart and J. R. Long, *Chem. Sci.*, 2011, **2**, 2078–2085.
230 D. N. Woodruff, R. E. P. Winpenny and R. A. Layfield, *Chem. Rev.*, 2013, **113**, 5110–5148.
231 A. R. Farrell, J. A. Coome, M. R. Probert, A. E. Goeta, J. A. K. Howard, M.-H. Lemée-Cailleau, S. Parsons and M. Murrie, *CrystEngComm*, 2013, **15**, 3423–3429.
232 K. Katoh, Y. Yoshida, M. Yamashita, H. Miyasaka, B. K. Breedlove, T. Kajiwara, S. Takaishi, N. Ishikawa, H. Isshiki, Y. F. Zhang, T. Komeda, M. Yamagishi and J. Takeya, *J. Am. Chem. Soc.*, 2009, **131**, 9967–9976.
233 N. Ishikawa, M. Sugita, T. Okubo, N. Tanaka, T. Iino and Y. Kaizu, *Inorg. Chem.*, 2003, **42**, 2440–2446.
234 F. S. Guo, B. M. Day, Y. C. Chen, M. L. Tong, A. Mansikkamäki and R. A. Layfield, *Science*, 2018, **362**, 1400–1403.
235 S. G. McAdams, A.-M. Ariciu, A. K. Kostopoulos, J. P. S. Walsh and F. Tuna, *Coord. Chem. Rev.*, 2017, **346**, 216–239.
236 M. Feng and M.-L. Tong, *Chem. – Eur. J.*, 2018, **24**, 7574–7594.
237 F. Habib and M. Murugesu, *Chem. Soc. Rev.*, 2013, **42**, 3278–3288.
238 H. L. C. Feltham and S. Brooker, *Coord. Chem. Rev.*, 2014, **276**, 1–33.
239 S. Demir, I. R. Jeon, J. R. Long and T. D. Harris, *Coord. Chem. Rev.*, 2015, **289–290**, 149–176.
240 P. Zhang, Y. N. Guo and J. Tang, *Coord. Chem. Rev.*, 2013, **257**, 1728–1763.
241 X.-Y. Wang, C. Avendaño and K. R. Dunbar, *Chem. Soc. Rev.*, 2011, **40**, 3213–3238.
242 C. Benelli and D. Gatteschi, *Introduction to Molecular Magnetism. From Transition Metals to Lanthanides*, 2015.
243 *Lanthanides and Actinides in Molecular Magnetism*, ed. R. A. Layfield and M. Murugesu, 2015.
244 M. Yamashita and K. Katoh, *Molecular Magnetic Materials*, Wiley-VCH Verlag GmbH & Co. KGaA, Weinheim, Germany, 2016, pp. 79–101.
245 D. Gatteschi, R. Sessoli and J. Villain, *Molecular Nanomagnets*, Oxford University Press, 2006.
246 K. S. Cole and R. H. Cole, *J. Chem. Phys.*, 1941, **9**, 341–351.
247 A. Abragam and B. Bleaney, *Electron paramagnetic resonance of transition ions*, Oxford University Press, 2012.
248 A. Lunghi, F. Totti, R. Sessoli and S. Sanvito, *Nat. Commun.*, 2017, **8**, 14620.
249 L. Gu and R. Wu, *Phys. Rev. Lett.*, 2020, **125**, 117203.
250 M. Briganti, F. Santanni, L. Tesi, F. Totti, R. Sessoli and A. Lunghi, *J. Am. Chem. Soc.*, 2021, **143**, 13633–13645.
251 J. M. Zadrozny, M. Atanasov, A. M. Bryan, C.-Y. Lin, B. D. Rekken, P. P. Power, F. Neese and J. R. Long, *Chem. Sci.*, 2013, **4**, 125–138.
252 N. Ishikawa, M. Sugita, T. Ishikawa, S. Y. Koshihara and Y. Kaizu, *J. Phys. Chem. B*, 2004, **108**, 11265–11271.
253 W. Wernsdorfer, M. Murugesu and G. Christou, *Phys. Rev. Lett.*, 2006, **96**, 3–6.
254 L. Gunther, *Quantum Tunneling of Magnetization—QTM '94*, Springer Netherlands, Dordrecht, 1995, pp. 413–434.
255 J. R. Friedman, M. P. Sarachik, J. Tejada and R. Ziolo, *Phys. Rev. Lett.*, 1996, **76**, 3830–3833.
256 S. Bertaina, S. Gambarelli, T. Mitra, B. Tsukerblat, A. Müller and B. Barbara, *Nature*, 2008, **453**, 203–206.
257 E. Burzurí, F. Luis, B. Barbara, R. Ballou, E. Ressouche, O. Montero, J. Campo and S. Maegawa, *Phys. Rev. Lett.*, 2011, **107**, 097203.
258 W. Wernsdorfer and R. Sessoli, *Science*, 1999, **284**, 133–135.
259 M. N. Leuenberger and D. Loss, *Nature*, 2001, **410**, 789–793.

260 S. Sproules, *Electron Paramagnetic Resonance*, 2017, vol. 25, pp. 61–97.
261 M. J. Graham, J. M. Zadrozny, M. S. Fataftah and D. E. Freedman, *Chem. Mater.*, 2017, **29**, 1885–1897.
262 A. Gaita-Ariño, F. Luis, S. Hill and E. Coronado, *Nat. Chem.*, 2019, **11**, 301–309.
263 M. Atzori and R. Sessoli, *J. Am. Chem. Soc.*, 2019, **141**, 11339–11352.
264 J. Bartolomé, F. Luis and J. F. Fernández, *Molecular magnets: physics and applications*, Springer-Verlag/Sci-Tech/Trade, 2013.
265 F. Aquilante, J. Autschbach, R. K. Carlson, L. F. Chibotaru, M. G. Delcey, L. De Vico, I. F. Galván, N. Ferré, L. M. Frutos, L. Gagliardi, M. Garavelli, A. Giussani, C. E. Hoyer, G. Li Manni, H. Lischka, D. Ma, P. Å. Malmqvist, T. Müller, A. Nenov, M. Olivucci, T. B. Pedersen, D. Peng, F. Plasser, B. Pritchard, M. Reiher, I. Rivalta, I. Schapiro, J. Segarra-Martí, M. Stenrup, D. G. Truhlar, L. Ungur, A. Valentini, S. Vancoillie, V. Veryazov, V. P. Vysotskiy, O. Weingart, F. Zapata and R. Lindh, *J. Comput. Chem.*, 2016, **37**, 506–541.
266 E. Coronado, *Nat. Rev. Mater.*, 2020, **5**, 87–104.
267 S. Stepanow, J. Honolka, P. Gambardella, L. Vitali, N. Abdurakhmanova, T. C. Tseng, S. Rauschenbach, S. L. Tait, V. Sessi, S. Klyatskaya, M. Ruben and K. Kern, *J. Am. Chem. Soc.*, 2010, **132**, 11900–11901.
268 S. Lumetti, A. Candini, C. Godfrin, F. Balestro, W. Wernsdorfer, S. Klyatskaya, M. Ruben and M. Affronte, *Dalton Trans.*, 2016, **45**, 16570–16574.
269 M. Urdampilleta, N. V. Nguyen, J. P. Cleuziou, S. Klyatskaya, M. Ruben and W. Wernsdorfer, *Int. J. Mol. Sci.*, 2011, **12**, 6656–6667.
270 S. Thiele, F. Balestro, R. Ballou, S. Klyatskaya, M. Ruben and W. Wernsdorfer, *Science*, 2014, **344**, 1135–1138.
271 A. L. Thomas, *Phthalocyanine Research and Applications*, Taylor & Francis Inc, 1990.
272 N. Ishikawa, J. Jiang, O. Bekaroğlu, J. Liu, P. Lo and D. K. P. Ng, *Functional Phthalocyanine Molecular Materials*, Springer Berlin Heidelberg, Berlin, Heidelberg, 2010, vol. 135.
273 J. W. Perry, K. Mansour, I. S. Lee, X. Wu, P. V. Bedworth, C. Chen, D. Ng, S. R. Marder, P. Miles, T. Wada, M. Tian and H. Sasabe, *Science*, 1996, **273**, 1533–1536.
274 E. Palomares, M. V. Martı and J. R. Durrant, *Chem. Commun.*, 2004, 2112–2113.
275 B. Lim, G. Y. Margulis, J.-H. Yum, E. L. Unger, B. E. Hardin, M. Grätzel, M. D. McGehee and A. Sellinger, *Org. Lett.*, 2013, **15**, 784–787.
276 N. Ishikawa, M. Sugita and W. Wernsdorfer, *Angew. Chem., Int. Ed.*, 2005, **44**, 2931–2935.
277 N. Ishikawa, M. Sugita, N. Tanaka, T. Ishikawa, S. Koshihara and Y. Kaizu, *Inorg. Chem.*, 2004, **43**, 5498–5500.
278 M. Damjanovic, T. Morita, K. Katoh, M. Yamashita and M. Enders, *Chem. – Eur. J.*, 2015, **21**, 14421–14432.
279 K. M. Kadish, K. M. Smith and R. Guilard, *The porphyrin handbook*, Phthalocyanines: spectroscopic and electrochemical characterization, Academic Press, 2003, vol. 16.
280 R. Sessoli, *Nature*, 2017, **548**, 400–401.
281 L. Escalera-Moreno, J. J. Baldoví, A. Gaita-Ariño and E. Coronado, *Chem. Sci.*, 2018, **9**, 3265–3275.
282 F.-S. Guo, B. M. Day, Y.-C. Chen, M.-L. Tong, A. Mansikkamäki and R. A. Layfield, *Angew. Chem., Int. Ed.*, 2017, **56**, 11445–11449.
283 C. A. P. Goodwin, F. Ortu, D. Reta, N. F. Chilton and D. P. Mills, *Nature*, 2017, **548**, 439–442.
284 N. Ishikawa, T. Iino and Y. Kaizu, *J. Phys. Chem. A*, 2002, **106**, 9543–9550.
285 J. L. Liu, Y. C. Chen, Y. Z. Zheng, W. Q. Lin, L. Ungur, W. Wernsdorfer, L. F. Chibotaru and M. L. Tong, *Chem. Sci.*, 2013, **4**, 3310–3316.
286 J. L. Liu, Y. C. Chen and M. L. Tong, *Chem. Soc. Rev.*, 2018, **47**, 2431–2453.
287 L. Sorace, C. Benelli and D. Gatteschi, *Chem. Soc. Rev.*, 2011, **40**, 3092–3104.
288 K. W. H. Stevens, *Proc. Phys. Soc., London, Sect. A*, 1952, **65**, 209–215.
289 J. Sievers, *Z. Phys. Chem.*, 1982, **45**, 289–296.
290 D. Schmitt, *J. Phys.*, 1986, **47**, 677–681.
291 C. Görller-Walran and K. Binnemans, *Handbook on the physics and chemistry of rare earths*. *Volume 23*, Elsevier, North-Holland, Amsterdam, 1996.
292 L. F. Chibotaru, in *Molecular Nanomagnets and Related Phenomena*, ed. S. Gao, Springer Berlin Heidelberg, Berlin, Heidelberg, 2015, pp. 185–229.
293 L. Ungur and L. F. Chibotaru, *Chem. – Eur. J.*, 2017, **23**, 3708–3718.
294 A. L. Wysocki and K. Park, *Inorg. Chem.*, 2020, **59**, 2771–2780.
295 G. Taran, E. Bonet and W. Wernsdorfer, *J. Appl. Phys.*, 2019, **125**, 142903.
296 G. Taran, E. Bonet and W. Wernsdorfer, *Phys. Rev. B*, 2019, **99**, 180408.
297 D. Tanaka, T. Inose, H. Tanaka, S. Lee, N. Ishikawa and T. Ogawa, *Chem. Commun.*, 2012, **48**, 7796.
298 N. Ishikawa, T. Iino and Y. Kaizu, *J. Am. Chem. Soc.*, 2002, **124**, 11440–11447.
299 F. Ara, H. Oka, Y. Sainoo, K. Katoh, M. Yamashita and T. Komeda, *J. Appl. Phys.*, 2019, **125**, 183901.
300 K. Katoh, H. Isshiki, T. Komeda and M. Yamashita, *Coord. Chem. Rev.*, 2011, **255**, 2124–2148.
301 K. Katoh, H. Isshiki, T. Komeda and M. Yamashita, *Chem. – Asian J.*, 2012, **7**, 1154–1169.
302 T. Komeda, H. Isshiki, J. Liu, Y.-F. Zhang, N. Lorente, K. Katoh, B. K. Breedlove and M. Yamashita, *Nat. Commun.*, 2011, **2**, 217.
303 R. Vincent, S. Klyatskaya, M. Ruben, W. Wernsdorfer and F. Balestro, *Nature*, 2012, **488**, 357–360.
304 A. Candini, S. Klyatskaya, M. Ruben, W. Wernsdorfer and M. Affronte, *Nano Lett.*, 2011, **11**, 2634–2639.
305 E. Moreno-Pineda, T. Komeda, K. Katoh, M. Yamashita and M. Ruben, *Dalton Trans.*, 2016, **45**, 18417–18433.
306 T. Komeda, K. Katoh and M. Yamashita, *Single molecule magnet for quantum information process*, 2019.

307 T. Inose, D. Tanaka, J. Liu, M. Kajihara, P. Mishra, T. Ogawa and T. Komeda, *Nanoscale*, 2018, **10**, 19409–19417.
308 E. Moreno-Pineda, C. Godfrin, F. Balestro, W. Wernsdorfer and M. Ruben, *Chem. Soc. Rev.*, 2018, **47**, 501–513.
309 M. Ganzhorn, S. Klyatskaya, M. Ruben and W. Wernsdorfer, *ACS Nano*, 2013, **7**, 6225–6236.
310 M. Urdampilleta, S. Klayatskaya, M. Ruben and W. Wernsdorfer, *ACS Nano*, 2015, **9**, 4458–4464.
311 E. Moreno-Pineda, M. Damjanović, O. Fuhr, W. Wernsdorfer and M. Ruben, *Angew. Chem., Int. Ed.*, 2017, **56**, 9915–9919.
312 I. V. Krainov, J. Klier, A. P. Dmitriev, S. Klyatskaya, M. Ruben, W. Wernsdorfer and I. V. Gornyi, *ACS Nano*, 2017, **11**, 6868–6880.
313 C. Godfrin, S. Thiele, A. Ferhat, S. Klyatskaya, M. Ruben, W. Wernsdorfer and F. Balestro, *ACS Nano*, 2017, **11**, 3984–3989.
314 E. Moreno-Pineda, S. Klyatskaya, P. Du, M. Damjanović, G. Taran, W. Wernsdorfer and M. Ruben, *Inorg. Chem.*, 2018, **57**, 9873–9879.
315 C. Godfrin, R. Ballou, E. Bonet, M. Ruben, S. Klyatskaya, W. Wernsdorfer and F. Balestro, *npj Quantum Inf.*, 2018, **4**, 53.
316 N. Koike, H. Uekusa, Y. Ohashi, C. Harnoode, F. Kitamura, T. Ohsaka and K. Tokuda, *Inorg. Chem.*, 1996, **35**, 5798–5804.
317 K. Katoh, B. K. Breedlove and M. Yamashita, *Chem. Sci.*, 2016, **7**, 4329–4340.
318 J. Kan, H. Wang, W. Sun, W. Cao, J. Tao and J. Jiang, *Inorg. Chem.*, 2013, **52**, 8505–8510.
319 K. Katoh, T. Kajiwara, M. Nakano, Y. Nakazawa, W. Wernsdorfer, N. Ishikawa, B. K. Breedlove and M. Yamashita, *Chem. – Eur. J.*, 2011, **17**, 117–122.
320 H. Wang, K. Wang, J. Tao and J. Jiang, *Chem. Commun.*, 2012, **48**, 2973.
321 K. Katoh, N. Yasuda, M. Damjanović, W. Wernsdorfer, B. K. Breedlove and M. Yamashita, *Chem. – Eur. J.*, 2020, **26**, 4805–4815.
322 B. Cirera, J. Matarrubia, T. Kaposi, N. Giménez-Agulló, M. Paszkiewicz, F. Klappenberger, R. Otero, J. M. Gallego, P. Ballester, J. V. Barth, R. Miranda, J. R. Galán-Mascarós, W. Auwärter and D. Ecija, *Phys. Chem. Chem. Phys.*, 2017, **19**, 8282–8287.
323 T. Orlando, M. Filibian, S. Sanna, N. Giménez-Agullo, C. S. De Pipaón, P. Ballester, J. R. Galán-Mascarós and P. Carretta, *J. Phys.: Condens. Matter*, 2016, **28**, 386002.
324 N. Ishikawa, M. Sugita and W. Wernsdorfer, *J. Am. Chem. Soc.*, 2005, **127**, 3650–3651.
325 T. Fukuda, W. Kuroda and N. Ishikawa, *Chem. Commun.*, 2011, **47**, 11686–11688.
326 Y. Horii, K. Katoh, K. Sugimoto, R. Nakanishi, B. K. Breedlove and M. Yamashita, *Chem. – Eur. J.*, 2019, **25**, 3098–3104.
327 N. Ishikawa, S. Otsuka and Y. Kaizu, *Angew. Chem., Int. Ed.*, 2005, **44**, 731–733.
328 H. Wang, T. Liu, K. Wang, C. Duan and J. Jiang, *Chem. – Eur. J.*, 2012, **18**, 7691–7694.
329 T. Fukuda, K. Matsumura and N. Ishikawa, *J. Phys. Chem. A*, 2013, **117**, 10447–10454.
330 K. Katoh, R. Asano, A. Miura, Y. Horii, T. Morita, B. K. Breedlove and M. Yamashita, *Dalton Trans.*, 2014, **43**, 7716–7725.
331 A. Y. Tolbin, V. E. Pushkarev, L. G. Tomilova and N. S. Zefirov, *Mendeleev Commun.*, 2009, **19**, 78–80.
332 N. Ishikawa and Y. Kaizu, *Chem. Phys. Lett.*, 1993, **203**, 472–476.
333 A. G. Martynov, M. A. Polovkova, G. S. Berezhnoy, A. A. Sinelshchikova, F. M. Dolgushin, K. P. Birin, G. A. Kirakosyan, Y. G. Gorbunova and A. Y. Tsivadze, *Inorg. Chem.*, 2020, **59**, 9424–9433.
334 A. G. Martynov, M. A. Polovkova, G. S. Berezhnoy, A. A. Sinelshchikova, V. N. Khrustalev, K. P. Birin, G. A. Kirakosyan, Y. G. Gorbunova and A. Y. Tsivadze, *Inorg. Chem.*, 2021, **60**, 9110–9121.
335 Y. Chen, C. Liu, F. Ma, D. Qi, Q. Liu, H.-L. Sun and J. Jiang, *Chem. – Eur. J.*, 2018, **24**, 8066–8070.
336 H. Zhang, R. Wang, P. Zhu, Z. Lai, J. Han, C.-F. Choi, D. K. P. Ng, X. Cui, C. Ma and J. Jiang, *Inorg. Chem.*, 2004, **43**, 4740–4742.
337 J. D. Rinehart, M. Fang, W. J. Evans and J. R. Long, *J. Am. Chem. Soc.*, 2011, **133**, 14236–14239.
338 J. D. Rinehart, M. Fang, W. J. Evans and J. R. Long, *Nat. Chem.*, 2011, **3**, 538–542.
339 K. Katoh, K. Kagesawa and M. Yamashita, *Materials and Energy*, World Scientific Publishing, 2018, vol. 10, pp. 271–344.
340 K. Katoh, T. Komeda and M. Yamashita, *Chem. Rec.*, 2016, **16**, 987–1016.
341 K. Katoh, Y. Aizawa, T. Morita, B. K. Breedlove and M. Yamashita, *Chem. – Eur. J.*, 2017, **23**, 15377–15386.
342 T. Sato, S. Matsuzawa, K. Katoh, B. K. Breedlove and M. Yamashita, *Magnetochemistry*, 2019, **5**, 65.
343 D. Pinkowicz, R. Podgajny and B. Sieklucka, *Molecular Magnetic Materials*, Wiley-VCH Verlag GmbH & Co. KGaA, Weinheim, Germany, 2016, pp. 279–300.
344 L. Bogani and W. Wernsdorfer, *Nat. Mater.*, 2008, **7**, 179–186.
345 L. Margheriti, D. Chiappe, M. Mannini, P. E. Car, P. Sainctavit, M. A. Arrio, F. B. De Mongeot, J. C. Cezar, F. M. Piras, A. Magnani, E. Otero, A. Caneschi and R. Sessoli, *Adv. Mater.*, 2010, **22**, 5488–5493.
346 A. Hofmann and Z. Salman, *J. Phys.: Conf. Ser.*, 2014, **551**, 012055.
347 T. Yamabayashi, K. Katoh, B. K. Breedlove and M. Yamashita, *Molecules*, 2017, **22**, 1–11.
348 T. Sato, B. K. Breedlove, M. Yamashita and K. Katoh, *Angew. Chem., Int. Ed.*, 2021, **60**, 21179–21183.
349 M. S. Haghighi, M. Rath, H. W. Rotter and H. Humborg, *Z. Anorg. Allg. Chem.*, 1993, **619**, 1887–1896.
350 G. Ostendorp, H. W. Rotter and H. Homborg, *Zeitschrift für Naturforsch. B*, 1996, **51**, 567–573.
351 G. Ostendorp, H. W. Rotter and H. Homborg, *Z. Anorg. Allg. Chem.*, 1996, **622**, 235–244.

352 J. Janczak, R. Kubiak and A. Jezierski, *Inorg. Chem.*, 1999, **38**, 2043–2049.
353 R. Kubiak and J. Janczak, *Inorg. Chim. Acta*, 2010, **363**, 2461–2466.
354 M. A. Lebedeva, T. W. Chamberlain and A. N. Khlobystov, *Chem. Rev.*, 2015, **115**, 11301–11351.
355 P. D. W. Boyd and C. A. Reed, *Acc. Chem. Res.*, 2005, **38**, 235–242.
356 D. Sun, F. S. Tham, C. A. Reed, L. Chaker and P. D. W. Boyd, *J. Am. Chem. Soc.*, 2002, **124**, 6604–6612.
357 A. L. Litvinov, D. V. Konarev, A. Y. Kovalevsky, I. S. Neretin, P. Coppens and R. N. Lyubovskaya, *Cryst. Growth Des.*, 2005, **5**, 1807–1819.
358 M. Suzuki, Z. Slanina, N. Mizorogi, X. Lu, S. Nagase, M. M. Olmstead, A. L. Balch and T. Akasaka, *J. Am. Chem. Soc.*, 2012, **134**, 18772–18778.
359 T. Ishii, N. Aizawa, R. Kanehama, M. Yamashita, K. ichi Sugiura and H. Miyasaka, *Coord. Chem. Rev.*, 2002, **226**, 113–124.
360 H. Wang, K. Qian, D. Qi, W. Cao, K. Wang, S. Gao and J. Jiang, *Chem. Sci.*, 2014, **5**, 3214–3220.
361 H. Iwami, J. Xing, R. Nakanishi, Y. Horii, K. Katoh, B. K. Breedlove, K. Kawachi, Y. Kasama, E. Kwon and M. Yamashita, *Chem. Commun.*, 2020, **56**, 12785–12788.
362 N. Ishikawa, Y. Mizuno, S. Takamatsu, T. Ishikawa and S. Koshihara, *Inorg. Chem.*, 2008, **47**, 10217–10219.
363 S. Takamatsu and N. Ishikawa, *Polyhedron*, 2007, **26**, 1859–1862.
364 R. Pederson, A. L. Wysocki, N. Mayhall and K. Park, *J. Phys. Chem. A*, 2019, **123**, 6996–7006.
365 Y. Horii, M. Damjanović, K. Katoh and M. Yamashita, *Dalton Trans.*, 2021, **50**, 9719–9724.
366 M. Gonidec, E. S. Davies, J. McMaster, D. B. Amabilino and J. Veciana, *J. Am. Chem. Soc.*, 2010, **132**, 1756–1757.
367 T. Inose, D. Tanaka, H. Tanaka, O. Ivasenko, T. Nagata, Y. Ohta, S. De Feyter, N. Ishikawa and T. Ogawa, *Chem. – Eur. J.*, 2014, **20**, 11362–11369.
368 D. Tanaka, N. Sumitani, T. Inose, H. Tanaka, N. Ishikawa and T. Ogawa, *Chem. Lett.*, 2015, **44**, 668–670.
369 N. Sun, H. Wang, T. Liu, D. Qi and J. Jiang, *Dalton Trans.*, 2019, **48**, 1586–1590.
370 L. Ruan, J. Tong, F. Luo, G. Qin, F. Tian, X. Jiao and X. Zhang, *Inorg. Chem.*, 2021, **125**, 10165–10172.
371 M. Dailey and C. Besson, *CrystEngComm*, 2021, **23**, 7151–7161.
372 L. Vitali, S. Fabris, A. M. Conte, S. Brink, M. Ruben, S. Baroni and K. Kern, *Nano Lett.*, 2008, **8**, 3364–3368.
373 Z. Deng, S. Rauschenbach, S. Stepanow, S. Klyatskaya, M. Ruben and K. Kern, *Phys. Scr.*, 2015, **90**, 98003.
374 B. Warner, F. El Hallak, N. Atodiresei, P. Seibt, H. Prüser, V. Caciuc, M. Waters, A. J. Fisher, S. Blügel, J. van Slageren and C. F. Hirjibehedin, *Nat. Commun.*, 2016, **7**, 12785.
375 F. Ara, Z. K. Qi, J. Hou, T. Komeda, K. Katoh and M. Yamashita, *Dalton Trans.*, 2016, **45**, 16644–16652.
376 Y. S. Fu, J. Schwöbel, S. W. Hla, A. Dilullo, G. Hoffmann, S. Klyatskaya, M. Ruben and R. Wiesendanger, *Nano Lett.*, 2012, **12**, 3931–3935.
377 C. Wäckerlin, F. Donati, A. Singha, R. Baltic, S. Rusponi, K. Diller, F. Patthey, M. Pivetta, Y. Lan, S. Klyatskaya, M. Ruben, H. Brune and J. Dreiser, *Adv. Mater.*, 2016, **28**, 5195–5199.
378 Y. Zhang, Y. Wang, P. Liao, K. Wang, Z. Huang, J. Liu, Q. Chen, J. Jiang and K. Wu, *ACS Nano*, 2018, **12**, 2991–2997.
379 J. Schwöbel, Y. Fu, J. Brede, A. Dilullo, G. Hoffmann, S. Klyatskaya, M. Ruben and R. Wiesendanger, *Nat. Commun.*, 2012, **3**, 953.
380 L. Malavolti, L. Poggini, L. Margheriti, L. Chiappe, P. Graziosi, B. Cortigiani, V. Lanzilotto, F. Buatier de Mongeot, P. Ohresser, E. Otero, F. Choueikani, P. Sainctavit, I. Bergenti, V. A. Dediu, M. Mannini and R. Sessoli, *Chem. Commun.*, 2013, **49**, 11506–11508.
381 A. Lodi Rizzini, C. Krull, T. Balashov, J. J. Kavich, A. Mugarza, P. S. Miedema, P. K. Thakur, V. Sessi, S. Klyatskaya, M. Ruben, S. Stepanow and P. Gambardella, *Phys. Rev. Lett.*, 2011, **107**, 177205.
382 C. Nistor, C. Krull, A. Mugarza, S. Stepanow, C. Stamm, M. Soares, S. Klyatskaya, M. Ruben and P. Gambardella, *Phys. Rev. B: Condens. Matter Mater. Phys.*, 2015, **92**, 184402.
383 A. Lodi Rizzini, C. Krull, T. Balashov, A. Mugarza, C. Nistor, F. Yakhou, V. Sessi, S. Klyatskaya, M. Ruben, S. Stepanow and P. Gambardella, *Nano Lett.*, 2012, **12**, 5703–5707.
384 A. Candini, D. Klar, S. Marocchi, V. Corradini, R. Biagi, V. De Renzi, U. Del Pennino, F. Troiani, V. Bellini, S. Klyatskaya, M. Ruben, K. Kummer, N. B. Brookes, H. Huang, A. Soncini, H. Wende and M. Affronte, *Sci. Rep.*, 2016, **6**, 1–8.
385 J. Gómez-Segura, I. Díez-Pérez, N. Ishikawa, M. Nakano, J. Veciana and D. Ruiz-Molina, *Chem. Commun.*, 2006, 2866–2868.
386 M. Gonidec, R. Biagi, V. Corradini, F. Moro, V. De Renzi, U. Del Pennino, D. Summa, L. Muccioli, C. Zannoni, D. B. Amabilino and J. Veciana, *J. Am. Chem. Soc.*, 2011, **133**, 6603–6612.
387 D. Klar, A. Candini, L. Joly, S. Klyatskaya, B. Krumme, P. Ohresser, J.-P. Kappler, M. Ruben and H. Wende, *Dalton Trans.*, 2014, **43**, 10686–10689.
388 L. Smykalla, P. Shukrynau and M. Hietschold, *J. Phys. Chem. C*, 2012, **116**, 8008–8013.
389 G. Serrano, E. Velez-Fort, I. Cimatti, B. Cortigiani, L. Malavolti, D. Betto, A. Ouerghi, N. B. Brookes, M. Mannini and R. Sessoli, *Nanoscale*, 2018, **10**, 2715–2720.
390 S. Marocchi, A. Candini, D. Klar, W. Van Den Heuvel, H. Huang, F. Troiani, V. Corradini, R. Biagi, V. De Renzi, S. Klyatskaya, K. Kummer, N. B. Brookes, M. Ruben, H. Wende, U. Del Pennino, A. Soncini, M. Affronte and V. Bellini, *ACS Nano*, 2016, **10**, 9353–9360.
391 M. Mannini, F. Bertani, C. Tudisco, L. Malavolti, L. Poggini, K. Misztal, D. Menozzi, A. Motta, E. Otero, P. Ohresser, P. Sainctavit, G. G. Condorelli, E. Dalcanale and R. Sessoli, *Nat. Commun.*, 2014, **5**, 1–8.
392 H. Oka, K. Katoh, Y. Okada, D. Oka, T. Hitosugi, M. Yamashita and T. Fukumura, *Chem. Lett.*, 2021, **50**, 1489–1492.

393 M. Serri, M. Mannini, L. Poggini, E. Vélez-Fort, B. Cortigiani, P. Sainctavit, D. Rovai, A. Caneschi and R. Sessoli, *Nano Lett.*, 2017, **17**, 1899–1905.
394 F. Pineider, E. Pedrueza-Villalmanzo, M. Serri, A. M. Adamu, E. Smetanina, V. Bonanni, G. Campo, L. Poggini, M. Mannini, C. De Julián Fernández, C. Sangregorio, M. Gurioli, A. Dmitriev and R. Sessoli, *Mater. Horiz.*, 2019, **6**, 1148–1155.
395 A. Dahal and M. Batzill, *Nanoscale*, 2014, **6**, 2548–2562.
396 M. Cinchetti, V. A. Dediu and L. E. Hueso, *Nat. Mater.*, 2017, **16**, 507–515.
397 A. Zhao, Q. Li, L. Chen, H. Xiang, W. Wang, S. Pan, B. Wang, X. Xiao, J. Yang, J. G. Hou and Q. Zhu, *Science*, 2005, **309**, 1542–1544.
398 V. Madhavan, W. Chen, T. Jamneala, M. F. Crommie and N. S. Wingreen, *Science*, 1998, **280**, 567–569.
399 T. Komeda, H. Isshiki, J. Liu, K. Katoh and M. Yamashita, *ACS Nano*, 2014, **8**, 4866–4875.
400 R. Robles, N. Lorente, H. Isshiki, J. Liu, K. Katoh, B. K. Breedlove, M. Yamashita and T. Komeda, *Nano Lett.*, 2012, **12**, 3609–3612.
401 J. Hellerstedt, A. Cahlík, M. Švec, B. De La Torre, M. Moro-Lagares, T. Chutora, B. Papoušková, G. Zoppellaro, P. Mutombo, M. Ruben, R. Zbořil and P. Jelinek, *Nanoscale*, 2018, **10**, 15553–15563.
402 S. Fahrendorf, N. Atodiresei, C. Besson, V. Caciuc, F. Matthes, S. Blügel, P. Kögerler, D. E. Bürgler and C. M. Schneider, *Nat. Commun.*, 2013, **4**, 2425.
403 J. Granet, M. Sicot, B. Kierren, S. Lamare, F. Chérioux, F. Baudelet, Y. Fagot-Revurat, L. Moreau and D. Malterre, *Nanoscale*, 2018, **10**, 9123–9132.
404 H. Isago and M. Shimoda, *Chem. Lett.*, 1992, 147–150.
405 A. Mugarza, C. Krull, R. Robles, S. Stepanow, G. Ceballos and P. Gambardella, *Nat. Commun.*, 2011, **2**, 490.
406 N. Tsukahara, S. Shiraki, S. Itou, N. Ohta, N. Takagi and M. Kawai, *Phys. Rev. Lett.*, 2011, **106**, 187201.
407 M. Studniarek, C. Wäckerlin, A. Singha, R. Baltic, K. Diller, F. Donati, S. Rusponi, H. Brune, Y. Lan, S. Klyatskaya, M. Ruben, A. P. Seitsonen and J. Dreiser, *Adv. Sci.*, 2019, **6**, 1901736.
408 S. Iijima, *Nature*, 1991, **354**, 56–58.
409 M. Menon and D. Srivastava, *Phys. Rev. Lett.*, 1997, **79**, 4453–4456.
410 S. J. Tans, A. R. M. Verschueren and C. Dekker, *Nature*, 1998, **393**, 49–52.
411 V. I. Preprint, S. W. Emmons and A. M. Leroi, *Nature*, 1999, **402**, 253–254.
412 W. Lu and C. M. Lieber, *Nat. Mater.*, 2007, **6**, 841–850.
413 P. M. Ajayan, T. W. Ebbesen, T. Ichihashi, S. Iijima, K. Tanigaki and H. Hiura, *Nature*, 1993, **362**, 522–525.
414 E. Dujardin, T. W. Ebbesen, H. Hiura and K. Tanigaki, *Science*, 1994, **265**, 1850–1852.
415 B. W. Smith, M. Monthioux and D. E. Luzzi, *Nature*, 1998, **396**, 323–324.
416 T. Pichler, H. Kuzmany, H. Kataura and Y. Achiba, *Phys. Rev. Lett.*, 2001, **87**, 267401.
417 S. Bandow, M. Takizawa, K. Hirahara, M. Yudasaka and S. Iijima, *Chem. Phys. Lett.*, 2001, **337**, 48–54.
418 R. Kitaura, N. Imazu, K. Kobayashi and H. Shinohara, *Nano Lett.*, 2008, **8**, 693–699.
419 M. del Carmen Giménez-López, F. Moro, A. La Torre, C. J. Gómez-García, P. D. Brown, J. van Slageren and A. N. Khlobystov, *Nat. Commun.*, 2011, **2**, 407.
420 R. Nakanishi, M. Yatoo, K. Katoh, B. Breedlove and M. Yamashita, *Materials*, 2016, **10**, 7.
421 R. Nakanishi, J. Satoh, K. Katoh, H. Zhang, B. K. Breedlove, M. Nishijima, Y. Nakanishi, H. Omachi, H. Shinohara and M. Yamashita, *J. Am. Chem. Soc.*, 2018, **140**, 10955–10959.
422 K. Katoh, J. Sato, R. Nakanishi, F. Ara, T. Komeda, Y. Kuwahara, T. Saito, B. K. Breedlove and M. Yamashita, *J. Mater. Chem. C*, 2021, **9**, 10697–10704.
423 A. I. A. Abd El-Mageed and T. Ogawa, *RSC Adv.*, 2019, **9**, 28135–28145.
424 A. Tsumura, H. Koezuka and T. Ando, *Appl. Phys. Lett.*, 1986, **49**, 1210–1212.
425 C. A. Di, G. Yu, Y. Liu and D. Zhu, *J. Phys. Chem. B*, 2007, **111**, 14083–14096.
426 C. Wang, H. Dong, W. Hu, Y. Liu and D. Zhu, *Chem. Rev.*, 2012, **112**, 2208–2267.
427 M. H. Hoang, Y. Kim, M. Kim, K. H. Kim, T. W. Lee, D. N. Nguyen, S. J. Kim, K. Lee, S. J. Lee and D. H. Choi, *Adv. Mater.*, 2012, **24**, 5363–5367.
428 Y. Zhang, X. Cai, Y. Bian and J. Jiang, in *Functional Phthalocyanine Molecular Materials*, ed. J. Jiang, Springer Berlin Heidelberg, Berlin, Heidelberg, 2010, vol. 135, pp. 275–322.
429 G. Guillaud, M. Al Sadoun, M. Maitrot, J. Simon and M. Bouvet, *Chem. Phys. Lett.*, 1990, **167**, 503–506.
430 A. V. Shokurov, D. S. Kutsybala, A. G. Martynov, O. A. A. Raitman, V. V. V. Arslanov, Y. G. G. Gorbunova, A. Y. Tsivadze and S. L. Selektor, *Thin Solid Films*, 2019, **692**, 137591.
431 F. S. Kim, E. Ahmed, S. Subramaniyan and S. A. Jenekhe, *ACS Appl. Mater. Interfaces*, 2010, **2**, 2974–2977.
432 Y. Zhang, X. Cai, D. Qi, Y. Bian and J. Jiang, *J. Phys. Chem. C*, 2008, **112**, 14579–14588.
433 W. Su, J. Jiang, K. Xiao, Y. Chen, Q. Zhao, G. Yu and Y. Liu, *Langmuir*, 2005, **21**, 6527–6531.
434 N. B. Chaure, J. L. Sosa-Sanchez, A. N. Cammidge, M. J. Cook and A. K. Ray, *Org. Electron.*, 2010, **11**, 434–438.
435 S. Barard, D. Mukherjee, S. Sarkar, T. Kreouzis, I. Chambrier, A. N. Cammidge and A. K. Ray, *J. Mater. Sci.: Mater. Electron.*, 2020, **31**, 265–273.
436 Y. Chen, W. Su, M. Bai, J. Jiang, X. Li, Y. Liu, L. Wang and S. Wang, *J. Am. Chem. Soc.*, 2005, **127**, 15700–15701.
437 Y. Chen, R. Li, R. Wang, P. Ma, S. Dong, Y. Gao, X. Li and J. Jiang, *Langmuir*, 2007, **23**, 12549–12554.
438 R. Li, P. Ma, S. Dong, X. Zhang, Y. Chen, X. Li and J. Jiang, *Inorg. Chem.*, 2007, **46**, 11397–11404.
439 Y. Gao, P. Ma, Y. Chen, Y. Zhang, Y. Bian, X. Li, J. Jiang and C. Ma, *Inorg. Chem.*, 2009, **48**, 45–54.

440 P. Ma, Y. Chen, N. Sheng, Y. Bian and J. Jiang, *Eur. J. Inorg. Chem.*, 2009, 954–960.
441 K. Katoh, K. Yamamoto, T. Kajiwara, J. Takeya, B. K. Breedlove and M. Yamashita, *J. Phys.: Conf. Ser.*, 2011, **303**, 012035.
442 Y. Chen, D. Li, N. Yuan, J. Gao, R. Gu, G. Lu and M. Bouvet, *J. Mater. Chem.*, 2012, **22**, 22142–22149.
443 Y. Chen, X. Kong, G. Lu, D. Qi, Y. Wu, X. Li, M. Bouvet, D. Sun and J. Jiang, *Mater. Chem. Front.*, 2018, **2**, 1009–1016.
444 X. Zhang and Y. Chen, *Inorg. Chem. Commun.*, 2014, **39**, 79–82.
445 G. Lu, X. Kong, P. Ma, K. Wang, Y. Chen and J. Jiang, *ACS Appl. Mater. Interfaces*, 2016, **8**, 6174–6182.
446 X. Zhang, L. Liu, J. Xiao, Z. Sun and P. Li, *J. Mater. Res. Technol.*, 2020, **9**, 13682–13691.
447 C. Wang, D. Qi, G. Lu, H. Wang, Y. Chen and J. Jiang, *Inorg. Chem. Front.*, 2019, **6**, 3345–3349.
448 D. Gao, X. Zhang, X. Kong, Y. Chen and J. Jiang, *ACS Appl. Mater. Interfaces*, 2015, **7**, 2486–2493.
449 X. Kong, G. Lu, X. Wang, S. Zhao, D. Sun, X. Li, Y. Chen and J. Jiang, *J. Mater. Sci.: Mater. Electron.*, 2019, **30**, 12437–12446.
450 R. Madru, G. Guillaud, M. Al Sadoun, M. Maitrot, J. J. André, J. Simon and R. Even, *Chem. Phys. Lett.*, 1988, **145**, 343–346.
451 A. I. Zvyagina, A. E. Aleksandrov, A. G. Martynov, A. R. Tameev, A. E. Baranchikov, A. A. Ezhov, Y. G. Gorbunova and M. A. Kalinina, *Inorg. Chem.*, 2021, **60**, 15509–15518.
452 A. G. Martynov, Y. G. Gorbunova and A. Y. Tsivadze, *Prot. Met. Phys. Chem. Surfaces*, 2011, **47**, 465–470.
453 M. O. Senge, M. Fazekas, E. G. A. Notaras, W. J. Blau, M. Zawadzka, O. B. Locos and E. M. N. Mhuircheartaigh, *Adv. Mater.*, 2007, **19**, 2737–2774.
454 G. de la Torre, P. Vazquez, F. Agullo-Lopez and T. Torres, *Chem. Rev.*, 2004, **104**, 3723–3750.
455 J. P. Collman, J. L. Kendall, J. L. Chen, T. A. Eberspacher and C. R. Moylan, *Inorg. Chem.*, 1997, **36**, 5603–5608.
456 D. Qi and J. Jiang, *ChemPhysChem*, 2015, **16**, 1889–1897.
457 J. S. Shirk, J. R. Lindle, F. J. Bartoli, Z. H. Kafafi, A. W. Snow and M. E. Boyle, *J. Nonlinear Opt. Phys. Mater.*, 1992, **01**, 699–726.
458 J. L. Wu, B. Gu, N. Sheng, D. Liu and Y. Cui, *Appl. Phys. Lett.*, 2014, **105**, 171113.
459 N. Sheng, D. Liu, B. Gu, J. He and Y. Cui, *Dyes Pigm.*, 2015, **122**, 346–350.
460 B. Ren, N. Sheng, B. Gu, Y. Wan, G. Rui, C. Lv and Y. Cui, *Dyes Pigm.*, 2017, **139**, 788–794.
461 A. I. Plekhanov, T. V. Basova, R. G. Parkhomenko and A. G. Gürek, *Opt. Mater.*, 2017, **64**, 13–17.
462 A. B. Karpo, V. E. Pushkarev, V. I. Krasovskii and L. G. Tomilova, *Chem. Phys. Lett.*, 2012, **554**, 155–158.
463 K. E. Sekhosana and T. Nyokong, *Opt. Mater.*, 2014, **37**, 139–146.
464 K. E. Sekhosana and T. Nyokong, *Opt. Mater.*, 2015, **47**, 211–218.
465 K. E. Sekhosana and T. Nyokong, *Inorg. Chim. Acta*, 2016, **450**, 87–91.
466 K. E. Sekhosana, M. Shumba and T. Nyokong, *Polyhedron*, 2017, **138**, 154–160.
467 N. Sheng, B. Gu, B. Ren, Y. Wang, L. Han, J. Wang, H. Cao, M. Guan, X. Zhai and J. Sha, *Dyes Pigm.*, 2017, **136**, 553–558.
468 C. Huang, K. Wang, J. Sun and J. Jiang, *Eur. J. Inorg. Chem.*, 2014, 1546–1551.
469 L. Chen, R. Hu, J. Xu, S. Wang, X. Li, S. Li and G. Yang, *Spectrochim. Acta, Part A*, 2013, **105**, 577–581.
470 K. E. Sekhosana, E. Amuhaya, S. Khene and T. Nyokong, *Inorg. Chim. Acta*, 2015, **426**, 221–226.
471 H. Shang, H. Wang, K. Wang, J. Kan, W. Cao and J. Jiang, *Dalton Trans.*, 2013, **42**, 1109–1115.
472 K. E. Sekhosana and T. Nyokong, *RSC Adv.*, 2019, **9**, 16223–16234.
473 X. Chen, D. Qi, C. Liu, H. Wang, Z. Xie, T. W. Chen, S. M. Chen, T. W. Tseng and J. Jiang, *RSC Adv.*, 2019, **10**, 317–322.
474 C. Liu, W. Yang, J. Wang, X. Ding, H. Ren, Y. Chen, Z. Xie, T. Sun and J. Jiang, *Dalton Trans.*, 2021, **50**, 13661–13665.